The University Of Sheffield.

Dual Rotor Magnetically Geared Power Split Device for Hybrid Electric Vehicles

Petr Chmelicek

Department of Electronic and Electrical Engineering

University of Sheffield

A thesis submitted for the degree of

Doctor of Philosophy

August 2019

Abstract

This thesis summarizes the main findings of research into novel dual-rotor magnetically geared power split device for automotive hybrid electric drivetrain application. The device represents a functional integration of conventional permanent magnet synchronous machine with concentric magnetic gear. As both functional elements share the same magnetic circuit, the design and analysis of the device presents many challenges, some of which are addressed in this thesis.

Firstly, fundamental principles upon which the device is based are explained with particular attention to harmonic content of both air gaps which is key for further analysis of its performance. Furthermore, it is shown how interfacing the gear element with the electrical machine stator imposes limitations on selection of feasible configurations and how design of each principle element affects torque transmission.

Secondly, negative influence of axial leakage on performance of the device and importance of considering its effects during design are explained. Both the axial leakage and the aforementioned air gap harmonic content are key in analysing electromagnetic efficiency of the devices as both contribute to different loss mechanisms in ways which are not common in conventional electrical machines.

Lastly, results of experimental validation on full scale prototype of the device are presented and discussed.

List of Publications

Journal papers

P. Chmelicek, S. D. Calverley, R. S. Dragan and K. Atallah, "Dual Rotor Magnetically Geared Power Split Device for Hybrid Electric Vehicles," in IEEE Transactions on Industry Applications, vol. 55, no. 2, pp. 1484-1494, March-April 2019. doi: 10.1109/TIA.2018.2883547

Conference publications and presentations

P. Chmelicek, S. D. Calverley, R. S. Dragan and K. Atallah, "Dual rotor magnetically geared power split device for hybrid electric vehicles," 2017 IEEE International Electric Machines and Drives Conference (IEMDC), Miami, FL, 2017, pp. 1-6. doi: 10.1109/IEMDC.2017.8002192

P. Chmelicek, S. D. Calverley, R.E. Clark, "Design Optimisation of MAGSPLIT® - a Magnetic Power Split e-CVT," Opera European User Group Meeting 2014, Woodstock, 29. May 2014.

Patents

P. Chmelicek, D. J. Powell, "Magnetically geared apparatus and a pole piece for such apparatus," UK Patent application GB 2545154 (A), Filed Aug. 24, 2015, Published Jun. 14, 2017

P. Chmelicek, S. D. Calverley, " An electrical machine and a method of operating an electrical machine," UK Patent application GB 2558660 (A), Filed Jan. 16, 2017, Published Jul. 18, 2018

Acknowledgment

I would like to express my sincere thanks to Professor Kais Atallah for his guidance, and support in the course of this research project. Without his encouragement and many words of wisdom I would not have made it this far.

I would also like to thank to Magnomatics ltd. for the sponsorship of this research project and for the opportunity to work there alongside a truly world class engineering team. The years I spent there shaped me in many ways and allowed me to grow as an engineer. I feel particularly indebted to Dr Stuart Calverley for his advice, support and for the many invaluable discussions we had over the years, although thanks are due to the entire Magnomatics team as almost everyone contributed to the project in some way.

I would also like to thank to my former colleagues at Romax Technology ltd. who provided warm and friendly atmosphere at work and encouragement during the period when I was writing the thesis. It was difficult to say goodbye.

Finally, I would like to thank to my family and all my friends both in the UK and in the Czech Republic for their love and endless support.

Contents

Nomenclature

Abbreviation	Definition
HEV	Hybrid Electric Vehicle
EV	Electric Vehicle
ICE	Internal Combustion Engine
PMSM	Permanent Magnet Synchronous Machine
NdFeB	Neodymium-Iron-Boron magnet
SmCo	Samarium-Cobalt magnet
PM	Permanent Magnet
UMP	Unbalance Magnetic Pull
SMC	Soft Magnetic Composites
MG	Motor Generator
ECU	Engine Control Unit
FEA	Finite Element Analysis
PPR	Pole Piece Rotor
EMF	Electro Motive force
MMF	Magneto motive force
GHG	Green house gas
EU	European Union
REEV	Range extender electric vehicle
IM	Induction machine
SPM	Surface mounted permanent magnet
PDD	Pseudo Direct Drive

Symbol	Definition
ω_s	Angular velocity of sun gear (rad·s-1)
ω_r	Angular velocity of ring gear (rad·s-1)
ω_c	Angular velocity of planet carrier (rad·s-1)
n_r	Number of teeth of ring gear (-)
n_s	Number of teeth of sun gear (-)
T_r	Torque acting on ring gear (Nm)
T_s	Torque acting on sun gear (Nm)
T_c	Torque acting on planet carrier (Nm)
p_{out}	Number of pole pairs of outer magnet array (-)
p_{ppr}	Number of pole pieces (-)
p_{in}	Number of pole pairs of inner magnet array (-)
ω_{ppr}	Angular velocity of pole pieces (rad·s-1)
ω_{out}	Angular velocity of outer magnet array (rad·s-1)
ω_{in}	Angular velocity of inner magnet array (rad·s-1)
ω_{cont}	Angular velocity of control rotor (rad·s-1)
ω_{output}	Angular velocity of output rotor (rad·s-1)
p_{output}	Number of pole pairs of output rotor (-)
T_{cont}	Torque acting on control rotor (Nm)
T_{ppr}	Torque acting on pole piece rotor (Nm)
T_{output}	Torque acting on output rotor (Nm)
T_{in}	Torque acting on inner rotor (Nm)
T_g	Transmittable torque of magnetic gear (Nm)
B_{r_pm}	Radial flux density (T)
ϑ	Angular position (rad)
t	Time (sec)
b_{rn}	Fourier coefficient of radial flux density distribution (T)
B_{r_mod}	Modulated radial flux density (T)
δ	Load angle (rad)
ϑ_{ppr}	Pole piece angular position (rad)

ϑ_{in}	Inner array angular position (rad)
ϑ_{out}	Outer array angular position (rad)
G_{r1}	Intrinsic gear ratio 1 (-)
G_{r2}	Intrinsic gear ratio 2 (-)
ψ	Flux linkage (Wb)
k_w	Winding factor (-)
k_{pv}	Pitch factor (-)
k_{dv}	Distribution factor (-)
m	Number of phases (-)
W	Coil pitch (-)
N_{slots}	Number of slots (-)
τ_p	Pole pitch (-)
f	Frequency (Hz)
l	Length (m)
r	Radius (m)
k	Harmonic order (-)
n_k	Fourier coefficient of winding function (-)
B_{p_k}	Peak flux density (T)
E_{1rms_k}	Rms EMF induced by k-th harmonic (V)
N	Number of conductors (-)
B_k	Amplitude of flux density of k-th harmonic (T)
n_k	Amplitude of conductor density of k-th harmonic (T)
ψ_k	Flux linkage of k-th harmonic (Wb)
n_q	Number of conductors in slot q (-)
$k_{w,k}$	Winding factor for k-th harmonic (-)
ψ_{pm}	Flux linkage due to PM (Wb)
I_d	Direct axis current (A)
I_q	Quadrature axis current (A)
L_d	Direct axis inductance (H)
L_q	Quadrature axis inductance (H)
p_{stat}	Stator pole pairs (-)
p_m	Magnet rotor pole pairs (-)

ψ_{con}	Flux linkage due to control space harmonic (Wb)
T_m	Magnet rotor torque (Nm)
ϑ_c	Control space harmonic angular position (rad)
ϑ_m	Magnet rotor angular position (rad)
ω_m	Magnet rotor speed (rad·s-1)
f_{stat}	Stator frequency (Hz)
$x_{s1} - x_{s4}$	Symmetry factors (-)
f_r	Radial force density (Nm-1)
V_r	Rotor volume (m3)
σ	Shear stress (Nm-2)
D_r	Rotor outer diameter (m)
L_{fe}	Active axial length (m)
A_{rms}	Electrical loading (Am-1)
B_{peak}	Peak flux density (T)
k_{ppr_c}	Pole piece rotor control modulation factor (-)
B_m	Peak inner air gap flux density (T)
B_{cont}	Peak control harmonic air gap flux density (T)
V_{ppr}	Pole piece rotor volume (m3)
D_{ppr}	Pole piece rotor outer diameter (m)
λ	Split ratio (-)
k_{fe}	Steel stacking factor (-)
k_ρ	Stator leakage factor (-)
B_{para}	Peak parasitic harmonic air gap flux density (T)
k_{ppr_p}	Pole piece rotor parasitic modulation factor (-)
P_{cu}	Copper loss (W)
ρ_{cu}	Copper resistivity (Ωm)
k_{cu}	Slot fill factor (-)
L_{ew}	Length of end winding (m)
J_{rms_slot}	RMS value of slot current density (Am-2)
b_t	Back iron thickness (m)
t_w	Tooth width (m)
B_{fe_max}	Maximal steel flux density (T)

B_{og}	Outer air gap average flux density (T)
g_{out}	Outer air gap length (m)
g_{in}	Inner air gap length (m)
h_{ppr}	Pole piece radial height (m)
n_{turns}	Number of turns (-)
A_{slot}	Slot area (mm^2)
ϕ_{coil}	Coil flux (Wb)
ψ_{coil}	Coil flux linkage (Wb)
A_{avg_go}	Magnetic vector potential in return slot (A)
A_{avg_return}	Magnetic vector potential in return slot (A)
ω_{base}	Base speed ($rad \cdot s^{-1}$)
U_{max}	Maximal voltage (V)
I_{max}	Maximal current (A)
l_{fe}	Lamination thickness (m)
l_{insul}	Insulation thickness (m)
l_{stack}	Stack length (m)
k_{fe}	Steel packing factor (-)
μ_{fe}	Relative permeability of steel (-)
μ_0	Permeability of vaccum (Hm^{-1})
B_{stack}	Stack flux density (T)
H_{stack}	Stack field strength (Am^{-1})
$\emptyset_{stackt}$	Stack flux (Wb)
$\emptyset_{Fe}$	Steel flux (Wb)
$\emptyset_{insul}$	Insulation flux (Wb)
R_{fe}	Reluctance of lamination ($ATWb^{-1}$)
R_{insul}	Reluctance of insulation layer ($ATWb^{-1}$)
μ_n	Equiv. permeability in normal direction (-)
μ_t	Equiv. permeability in tangential direction (-)
A_{ppr}	Pole piece surface area (m^2)
B_z	Z axis flux density (T)
B_{z_avg}	Average axial z axis flux density (T)
P_{fe}	Iron loss (W)

k_e	Eddy current loss coefficient (-)
k_h	Hysteresis loss coefficient (-)
k_{exc}	Excess loss coefficient (-)
σ_{fe}	Steel conductivity (Sm^{-1})
f_{ppr}	Pole piece rotor frequency (Hz)
f_{fe_mag}	Magnet rotor passing frequency (Hz)
f_{fe_slots}	Slots passing frequency (Hz)
P_{sc}	Stator iron loss due to control harmonic (W)
P_{sm}	Stator iron loss due to parasitic harmonic (W)
P_{ppr}	Pole piece rotor iron loss (W)
P_m	Magnet rotor iron loss (W)
P_{stray_eddy}	Stray eddy current loss (W)
H_{x_lam}	Lamination field strength (Am^{-1})
B_{z_lam}	Z axis lamination flu density (T)
P_{stray_ppr}	Pole piece rotor stray loss (W)
n_{lam}	Number of pole piece laminations (-)
I_{ph}	Phase current (A)
η	Efficiency (-,%)
P_{in}	Total input power (W)
P_{loss}	Total power loss (W)
P_{stat}	Stator power (W)
P_{ppr}	Pole piece rotor power (W)

Chapter 1 Introduction

1.1 Motivation

Electrification of personal mobility has been given a lot of attention in the past decade with most of the developed countries launching national programmes to support and to provide framework for mass deployment of more sustainable modes of transportation. Currently, partially electrified vehicles, also known as hybrid electric vehicles (HEV), are widely available while imminent mass production of fully electric vehicles has been announced by number of leading car manufacturers [1]. For instance, Volvo announced that all vehicle models manufactured after 2019 will be either hybrid or electric while Toyota is aiming to electrify the entire vehicle portfolio by 2025. The shift from internal combustion engine (ICE) based drivetrains towards electrified propulsion systems is driven by the need to reduce greenhouse gas emissions on a global level, increase energy security and minimize local noxious emissions in urban areas [2]. Additionally, drivetrain electrification could be used to improve driveability, safety and vehicle performance [3].

It is generally believed that one of the main factors contributing to climate change is increase of greenhouse gases (GHG), such as carbon dioxide, in the earth's atmosphere [4]. Carbon dioxide is one of the main contributors to so called greenhouse effect, a process by which a planet's surface and lower atmosphere is warmed by infrared radiation absorbed and reflected by gasses in the upper atmosphere. While naturally occurring greenhouse effect is essential for supporting life on earth, it is believed that human activities, such as burning of fossil fuels, could intensify this phenomenon and lead to unwanted increase in global temperature. This theory is supported by historical data of temperature measurements in Fig. 1-1 which show steady increase in global temperature since 1960 and correlate with global CO_2

emissions shown in Fig. 1-2. In 2016, road transport contributed approximately 21% of CO_2 emissions in the EU [5].

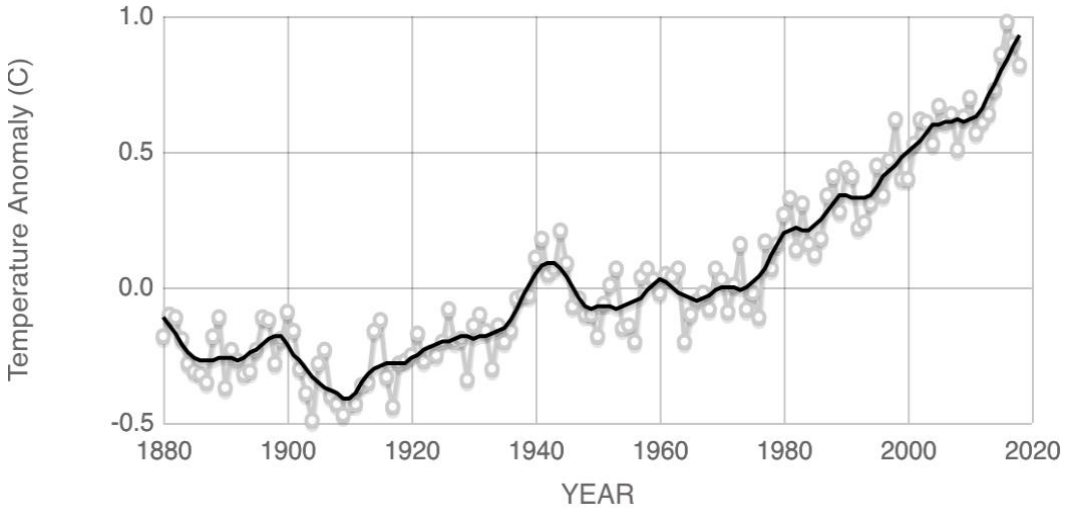

Fig. 1-1 Change of global temperature between 1880 and 2019 relative to the average temperature between 1951 and 1980 [6]

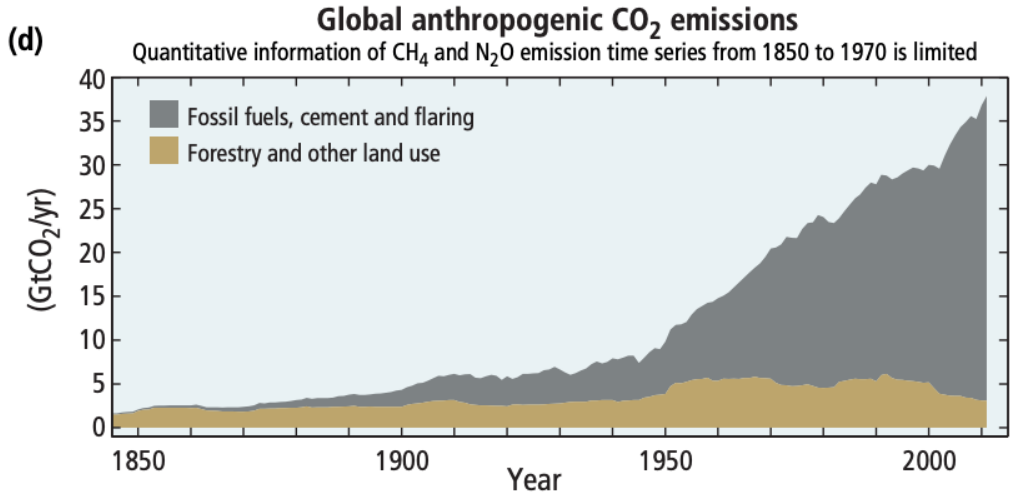

Fig. 1-2 Global CO_2 emissions as a function of time [4]

On the local level, transportation sector can be a source of noxious emissions affecting public health, particularly in urban areas with high population density, where vehicle pollutants can be linked to various respiratory diseases and even lung cancer [7]. Furthermore, World Health Organisation reports that exhaust emissions

are responsible for more deaths than traffic accidents. Another important impact of electrification on urban areas is reduction of noise emitted by vehicles, which is the most important contributor to urban noise, as noise from vehicles driven by electric motors is mainly limited to noise due to air drag and tire rolling. Both localized noise and pollution are a major bone of contention in large cities such as London, Paris and Shanghai. London, for instance, has already introduced low and zero emission zones restricting access for vehicles with internal combustion engines, and some cities are planning on banning them altogether in the not so distant future.

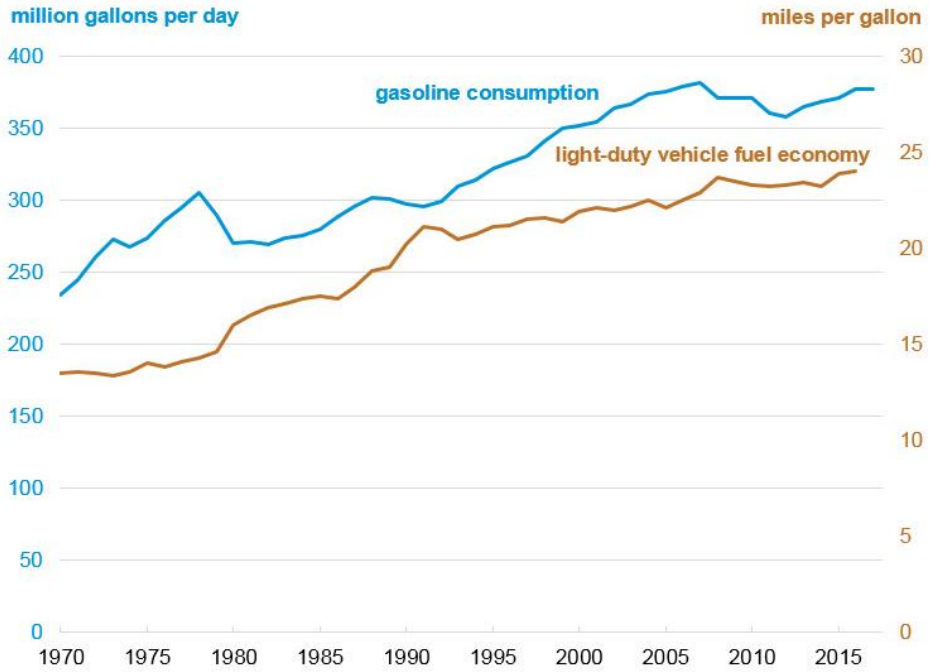

Fig. 1-3: Motor gasoline consumption for transportation and light-duty vehicle fuel economy in U.S between 1970 and 2017 [8]

All developed economies depend heavily on finite reserves of fossil fuels as a source of primary energy. Growing energy demand and dependence on less stable countries for the fuel supply create economic and political concerns. Transport sector in the EU, using ICE equipped vehicles, consumes approximately 73% of all imported oil [7]. Mass deployment of electrified vehicles could reduce the dependence on fossil fuels as electricity can be generated using various energy sources including renewables such as solar or wind. Additionally, electrification

could increase transport efficiency and lessen primary energy demand [9]. Fig. 1-3 illustrates the rise in gasoline consumption in the U.S. and light duty vehicle fuel economy between 1970 and 2017. It is apparent that despite the fact that the fuel economy of light duty vehicles has been steadily improving over the years, this has not stopped the rise of gasoline consumption as the total number of vehicles on the roads has increased [8]. The only times when gasoline consumption decreased were the periods of global economic downturn, for instance the period of global financial crisis between 2008 and 2010. Growth of gasoline consumption is closely linked with economic prosperity. In order to reduce the consumption, either number of vehicles need to be restricted or their fuel efficiency must be considerably improved.

1.2 Role of drivetrain hybridisation

Vehicle drivetrain electrification is trying to address the problems mentioned in the previous section and while fully electric vehicles may be the future of personal transportation, HEVs will play key role in the transition period, as illustrated in Fig. 1-4, and are expected to remain relevant beyond 2030 since without them current air quality and emissions targets cannot be met [10]. Current battery equipped fully electric vehicles suffer from unsatisfactory operating range, compared to traditional ICE based vehicles, which in combination with undeveloped charging infrastructure and cost limits their deployment on large scale [11], although considerable progress has been made in the last years. HEVs combine the advantages of two propulsion systems allowing vehicles to drive on long distances while considerably reducing fuel consumption and exhaust emissions or, depending on a specific architecture, even drive in pure electric mode with zero exhaust emission and low noise in densely populated areas. Furthermore, intelligent drivetrain control strategies could improve fuel consumption and emissions without compromising vehicles performance and driveability [9].

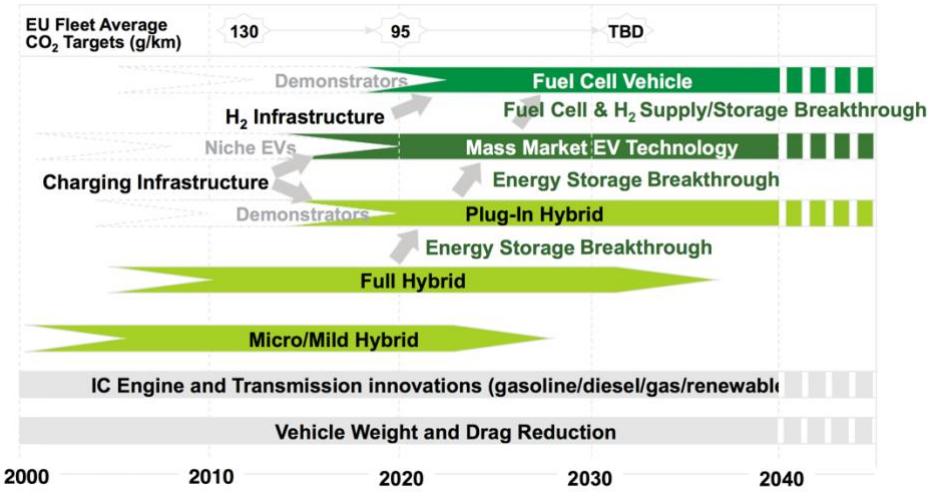

Fig. 1-4: Role of HEVs in the transitioning towards full EVs [12]

Current generation of HEVs, which are either available or are presently entering the market, mostly belong to the category of adapted hybrids, vehicles designed for conventional drivetrain which were later hybridized by integrating electrical machines into their existing drivetrains. The next generation is expected to have higher level of system integration, term dedicated hybrid is often used to describe them [13], and aims to compete and eventually replace conventional cars. Unlike the adapted hybrids, these vehicles will be designed with hybrid propulsion in mind and will be able to fully utilize the advantages of such systems while minimising the potential drawbacks, such as increase in drivetrain complexity, mass and cost.

1.3 Classification of hybrid drivetrains

Hybrid electric drivetrain is an electromechanical system comprising ICE, one or more electric machines with power electronic inverters and, typically, one or more mechanical gear sets. Two storages of energy are used to drive an HEV, one being a tank of fossil fuel and the other a battery pack. In broad terms, hybridised power trains could be split into two categories based on the degree of hybridisation, and the way electrical machines in the drivetrain are used [14]:

1) Micro/Mild hybrid: Micro and mild hybrids are quite similar and the distinction between them is vague. Typically, micro hybrids use 12V battery while mild hybrids rely on 48V system. The defining characteristic for both is

that electric machines don't tend to be used to drive the vehicle, rather to assist the engine [15]. Their power rating, compared to the ICE, tends to be much smaller. Typically, ICE in mild hybrid drivetrains is downsized and electrical machines are used for transient power boosting and energy recuperation. An example of 48V products for mild hybridisation are electrified turbochargers and compressors which can be integrated with an existing engine to improve its transient response, torque production and reduce emissions [16].

2) Full hybrid: Full hybrid employs two sources of propulsion, each able to propel the vehicle on its own. Full hybrid drive train is a much more complex and integrated system than micro or mild hybrid but it has the greatest potentional of reducing emision and fuel consumption. Battery packs of full hybrid vehicles have higher voltage to support high power electrical systems, typically either 400V or 800V for particularly high power applications [14]. Rating of electrical machines in full hybrids tends to be in tens of kilowats. The most well known example of full hybrid electric vehicle is Toyota Prius equiped with two motors rated at 60kW (2010 model year) [17]

Micro and mild hybrids present a relatively cheap and simple way of hybridising existing engines in order to improve their performance, reduce fuel consumption and emission. Vehicles equipped with these technologies are becoming more common and represent important step towards highly integrated and optimized full hybrids. While the transmission system described in this thesis could be used in certain mild/micro hybrid applications, the aim of this research project is development of transmission system for a full HEV. Micro and mild hybrids are, therefore, outside of the scope of this thesis and are mentioned only for the sake of completeness. It is worth mentioning that typical mild hybrid technologies such as electric turbochargers could be included in full hybrid drivetrains alongside high power traction motors. For instance, an ICE could be integrated with an electric turbocharger as well as high power traction motor.

1.4 Overview of full hybrid electric drivetrains

As mentioned before, full hybrid drivetrains utilize electrical machines with typical power rating in tens of kilowatts which could be used to propel a vehicle without any contribution from the ICE. Full hybrid drive trains come in various architectures and could share some features of micro/mild hybrids. From the passenger car perspective, there are three dominant families of full hybrid drivetrain architectures [18], the most prevalent of which is the so called power split drivetrain and Fig. 1-5 shows the US market for 2014 model year HEV's which has 80% of vehicle volume attributed to power split architecture.

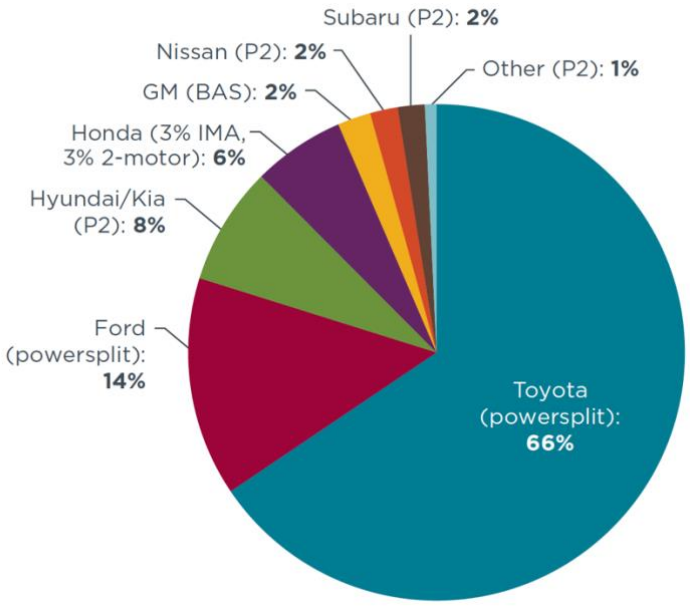

Fig. 1-5: Market share of 2014 model HEVs in USA [18]

Power split hybrid drive train uses a combination of two electrical machines combined with epicyclic gear box (planetary gear set) to control the flow of power coming from the engine to the wheels. There are two paths for the power flow, the direct mechanical and the indirect through the electrical systems and the battery pack. A basic block diagram showing the main components and power flow paths can be seen in Fig. 1-6 b). The system allows for regenerative braking, reduces drive train complexity replacing traditional multi speed gearbox with fixed ratio transmission, removes the need for additional starter generator and allows the engine to operate near its optimal fuel economy curve by controlling the ratio of power

passing through the two power flow paths. This architecture is particularly important for the research described in this thesis. It will, therefore, be discussed in greater detail in the next sections. An example of passenger car power split drivetrain is Toyota Synergy drive used in a number of Toyota vehicles, the most famous of which is Prius.

Parallel hybrid drivetrain, in Fig. 1-6 a) called P2, is the direct competitor of the power split drivetrain and because of its lower manufacturing and development cost is preferred by some major car manufacturers for whom hybrid sales do not justify the cost of developing a dedicated hybrid platform [18]. P2 configuration is a subset of parallel hybrid architecture in which an electric motor is sandwiched between ICE and a conventional multi speed gear box and can be decoupled from the engine by a clutch so as to allow for pure electric drive with engine shut down. Number 2 in the name P2 defines the electric motor position within the parallel drivetrain, Fig. 1-6 a), and number of other possible configurations exist ranging from P0 representing an integrated starter generator permanently coupled to the engine to P4 which is an independent electrified axle. VW group is among vehicle manufacturers that produce parallel hybrids [19] with P2 configuration being the most common.

The series architecture, Fig. 1-6 c), is one of the oldest hybrid drivetrains and while it is less common in automotive industry it is widely used in diesel-electric locomotives and ships. In this configuration, IEC is not mechanically coupled to the wheels and only generates electricity to charge batteries and to drive the traction motor. Term range-extender electric vehicle (REEV) is sometimes used since they are essentially EVs capable of recharging their own batteries by low power ICEs. Range extender version of BMW i3 is an example of such vehicle architecture.

Term “Plug-in hybrid” is used in Fig. 1-4 to denote vehicles which could be charged from the grid and are less dependent on the energy generated by the ICE. From the drivetrain architecture standpoint, they are not significantly different from standard HEVs, the only difference can be larger battery pack and sometimes more powerful electric motor. Both parallel and power split drivetrains can be deployed in plug-in HEVs.

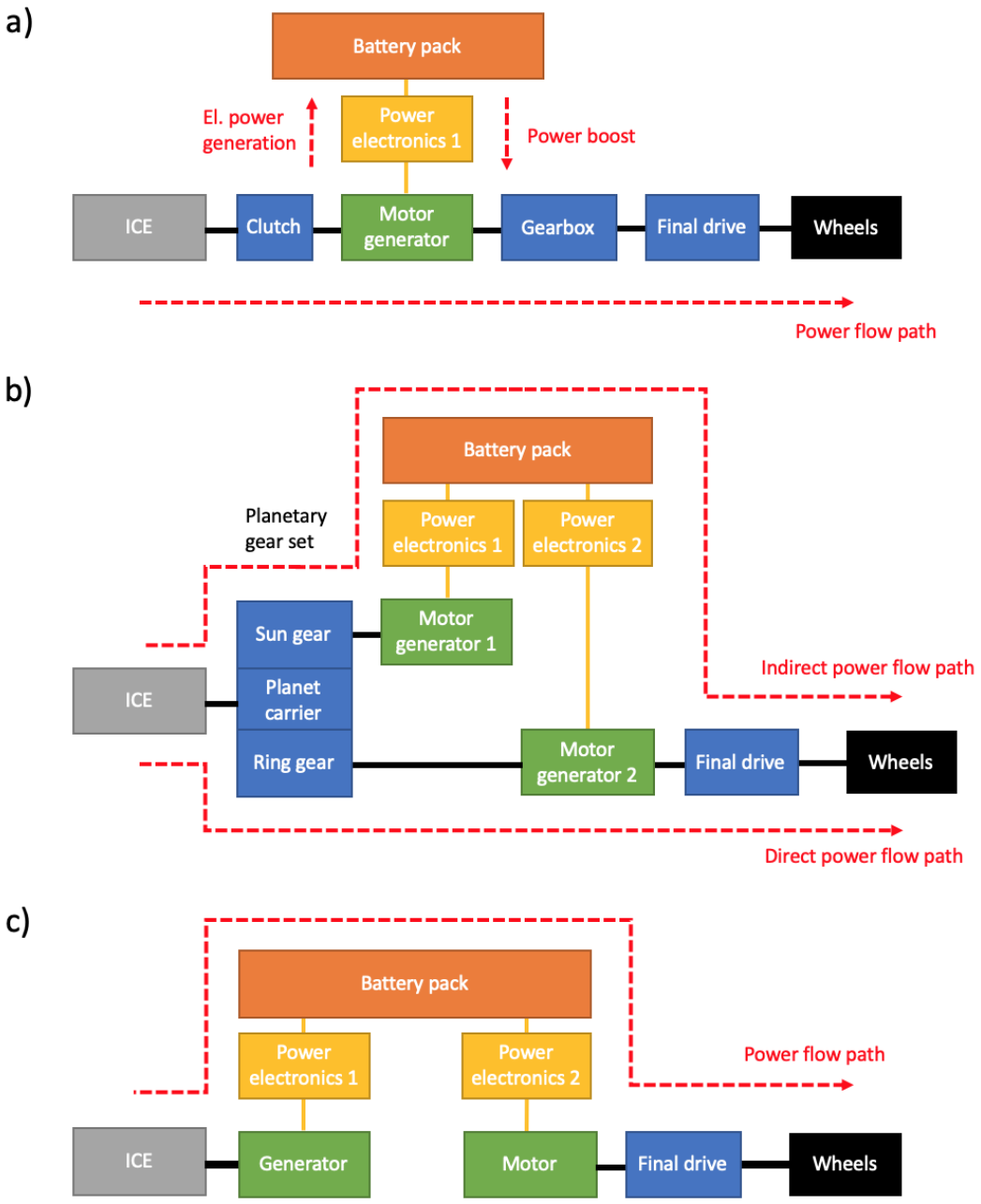

Fig. 1-6 Three dominant hybrid power train architectures: a) Parallel P2, b) power split, c) series

1.5 Power split hybrid drivetrain

The so-called power split hybrid drivetrain mentioned in the previous section, pioneered by Toyota, is the most common and commercially successful hybrid platform [18]. Since its introduction in 1997, more than 7 million vehicles equipped with it have been sold worldwide. Because the electrical sub-systems are highly

integrated with the rest of the drivetrain, it satisfies the definition of dedicated hybrid transmission introduced in [13]. It consists of an Atkinson cycle ICE specifically tailored for hybrid operation, two motor-generators MG1 and MG2, planetary gear set used for power splitting, high voltage battery pack and two electronic motor controllers connected to common DC link via boost DC converter [17].

1.5.1 Role of planetary gear set in the power split drivetrain

The key component of the power split hybrid drivetrain, which allows splitting of power between the two power flow paths, is the planetary gear set, as depicted in Fig. 1-7. Unlike simple spur gear with two rotating parts, a planetary gear set has three principal components, each of which can carry torque and rotate. The three principal components are sun gear located in the centre of the gear set, ring gear defining the outer diameter and planets which are held by planet carrier and mechanically connect the sun with the ring.

In the hybrid power split drivetrain shown in Fig. 1-7, the ICE is coupled to the planet carrier, MG1 to the sun gear and MG2 to the ring gear. Following equations describe torque and speed relationships between all three components at steady state operation:

$$n_s \cdot \omega_s + n_r \cdot \omega_r = (n_s + n_r) \cdot \omega_c \qquad (1\text{-}1)$$

$$T_r = T_c \frac{n_r}{n_r + n_s} \qquad (1\text{-}2)$$

$$T_s = T_c \frac{n_s}{n_s + n_r} \qquad (1\text{-}3)$$

where n_s and n_r are number of teeth of sun and ring gear respectively, T_r, T_c and T_s are torques acting on ring, carrier and sun gear shafts respectively, ω_r, ω_s and ω_c are angular velocities of ring, carrier and sun gear shafts respectively. It is apparent from equation (1-1) that fixed gear ratio operation is possible when one of the three shafts is held stationary while the other two are free to rotate. Continuous variable gearing is achieved when all three components are free to rotate with gear ratio being defined by angular velocities of all three shafts. In order to fully define an operating

point of a particular planetary gear set, three variables must be known: speed of two shafts and torque acting on one.

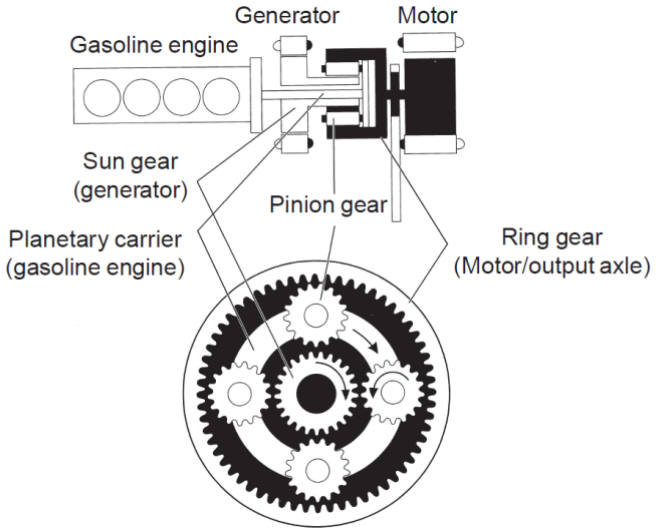

Fig. 1-7: Epicyclic (planetary) gear set in a power split drivetrain [20]

The internal combustion engine delivers power to the epicyclic (planetary) gear which splits the flow of power between MG1 and MG2, as explained in the previous section. MG1 acts as a generator, providing power to the battery pack, but can also start the engine in motoring mode. Consequently, the ability of MG1 to start the engine eliminates the need for conventional alternator. MG2 fulfils the role of primary drive motor and is, through final drive gearing and differential, coupled to the wheels. It can also be used for regenerative breaking where it converts kinetic energy of the vehicle into electric energy supplied to the battery pack. In this configuration, the ICE speed is completely independent of speed of the vehicle and can follow (or be as close as possible) the curve of optimal fuel efficiency, which can be seen in power vs. speed characteristic of a typical ICE in Fig. 1-8. The whole drive train acts as a continuously variable transmission system; term e-CVT is sometimes used, removing the need for conventional multi speed gearbox. Sophisticated control system is used to ensure efficient operation of the drivetrain whilst minimizing influence of the driver. The engine control unit (ECU) gathers various inputs, such as acceleration pedal position and state of charge of the battery pack and provides real time power flow control whilst trying to keep each element of the drivetrain within its band of highest efficiency.

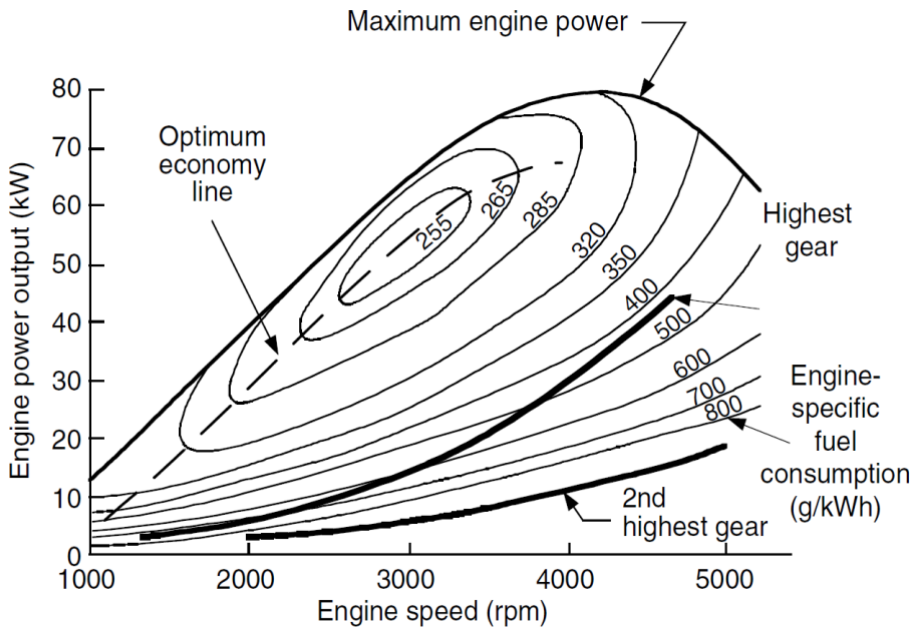

Fig. 1-8: Power vs. speed characteristic of a typical ICE with lines of constant specific fuel consumption [21]

1.5.2 Modes of operation of power split drivetrain

Fig. 1-9 shows nomogram of power split hybrid drivetrain. The flow of power is controlled by adjusting the speed of MG1, MG2 and the internal combustion engine. Line (A) represents a situation when the vehicle is at standstill, no power is being delivered from the engine and no fuel is being consumed. MG1 starts the engine and begins to generate electrical energy for MG2 to propel the vehicle at (B). Line (C) is normal driving condition when little electrical power needs to be generated and most of the power from the engine goes straight to the wheels. Engine could be assisted by MG2 during sudden acceleration, consuming energy from the battery pack. MG1 could be also used to increase load of the engine thus maintaining its operating point near the line of optimum fuel economy (D). The generated electrical power is used by the MG2 to drive the vehicle together with the engine. It is worth noting that the ICE in Prius produces relatively low torque at low speed, but the vehicle acceleration is not compromised since it can be assisted by the MG2. This allows the ICE to be optimized for overall efficiency rather than dynamic performance of the vehicle.

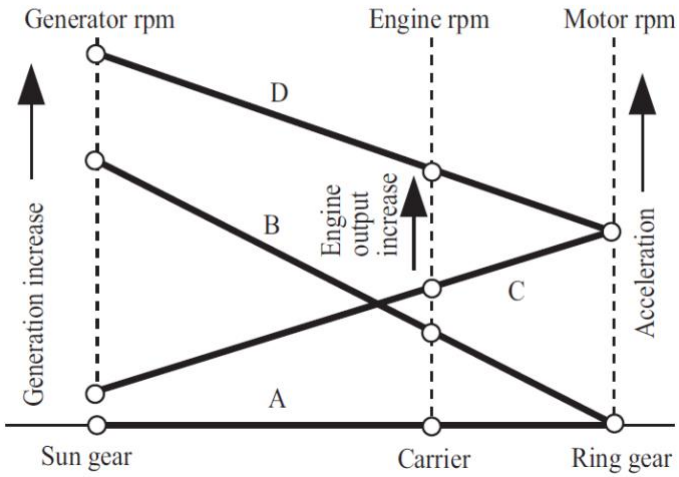

Fig. 1-9:Operating modes of power split hybrid drivetrain [20]

MG2 is the main source of tractive power and it, therefore, must be sized according to required dynamic performance of the vehicle. On the other hand, MG1, fulfilling the role of primary generator can have lower rating. Both machines are typically designed so that they could be overloaded for short periods of time up to twice of their continuous power rating. High voltage battery pack in Toyota Prius has a nominal voltage of only 201V but boost converter is used to increase DC link voltage up to 650V to allow for high speed and high power operation of both machines [17].

1.6 Magnetic gearing and its application in HEV

Magnetic gearing, where torque transmission is achieved via interaction of magnetic fields rather than physical contact offers several advantages over conventional mechanical gears. For instance, since there is no mechanical contact in the active portion of the gear between the rotating components, there is no need for lubrication. Each magnetic gear design is defined by the maximal torque which the gear can transmit; however, if the limit is exceeded, the gear will slip and re-engage when the excessive load torque is removed.

1.6.1 Introduction to magnetic gearing

The simplest construction of a magnetic gear is a mechanical gear where teeth were replaced by permanent magnets, each magnetic pole representing one mechanical tooth. Such construction is feasible but suffers from poor utilisation of magnets and consequently poor torque density. A novel concentric magnetic gear was first proposed in [22], showing that by employing rare earth magnets and arranging the rotating components concentrically, high torque density, in excess of 100kNm/m3, and efficiency could be achieved, making the gear suitable for high performance applications [23]. The concept was further examined [24], [25] and tests were performed on a prototype verifying its performance. Since its introduction, the concentric magnetic gear has attracted a lot of attention and is now a well-established and accepted technology. The topology of a concentric magnetic gear can be seen in Fig. 1-10. It consists of two arrays of permanent magnets, having a different number of pole pairs, between which ferromagnetic pole pieces are sandwiched.

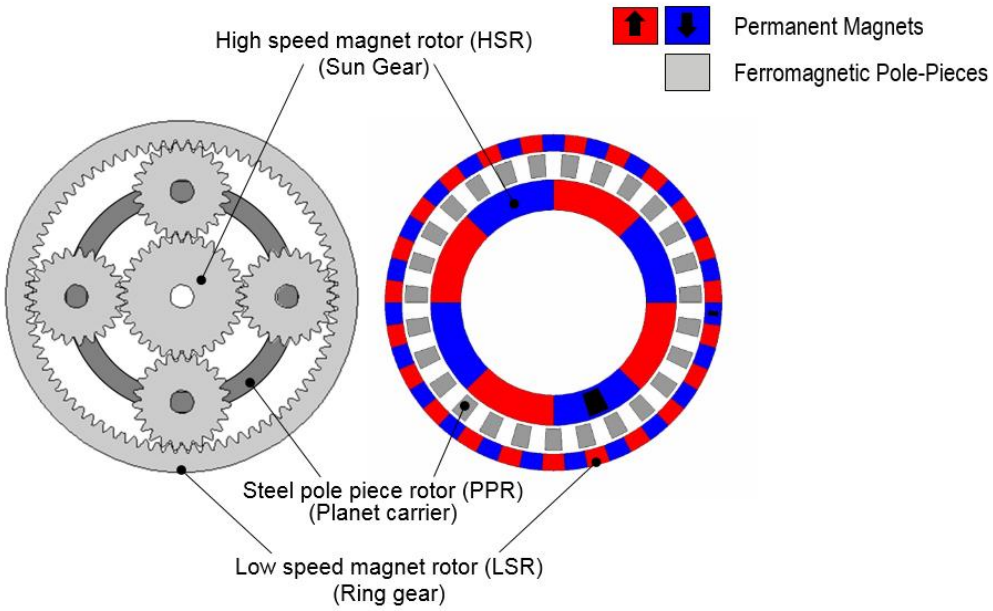

Fig. 1-10: Magnetic (right) and mechanical (left) planetary gear equivalence

The inner array of PMs creates a magnetic field in the inner air gap with corresponding number of pole pairs. The set of ferromagnetic pole pieces modulates the field in the inner air gap creating several harmonic components in the outer air gap, one of which must have the same number of pole pairs as the outer array of PMs

allowing for mutual coupling and torque transmission. The relationship between number of pole pairs of both arrays and number of pole pieces is governed by following equation:

$$p_{out} = p_{ppr} - p_{in} \quad (1\text{-}4)$$

where p_{out} is number of pole pairs of the outer array, p_{inner} is number of pole pairs of the inner array and p_{ppr} is number of ferromagnetic pole pieces. Angular velocities of all three components are related by:

$$(p_{ppr} - p_{in}) \cdot \omega_{out} = p_{ppr} \cdot \omega_s - p_{in} \cdot \omega_{in} \quad (1\text{-}5)$$

where ω_{out} is speed of the outer array, ω_{in} is speed of the inner array and ω_s is speed of pole pieces. It is apparent from equations (1-4) and (1-5) that magnetic gear is a magnetic equivalent of mechanical planetary gear as illustrated in Fig. 1-10 and can be used in a power split HEV drivetrain in the same manner [26].

1.6.2 Construction of the concentric magnetic gear

In terms of its construction, magnetic gear can be realized using various structures commonly found in electrical machines. For instance, the PM arrays can be embedded in steel laminations [27], use spoke type topology or be arranged in halbach patterns eliminating the need for backing iron. Optimal two dimensional electromagnetic design of magnetic gears is discussed in [28]. Authors conclude that designs with the highest torque density are not always feasible due to possible demagnetisation of PM arrays and that multi-dimensional optimisation must be performed in the initial design stage. Apart from increasing the amount of active materials, torque density can also be improved by optimising shape and size of the pole pieces, thus improving their ability to modulate the fields generated by PMs [29].

1.6.3 Cogging torque and radial force

Since the principle of concentric magnetic gear relies on interaction between arrays of PMs and salient pole pieces, the transmitted torque could be distorted by cogging torque. In addition, magnetic asymmetry between components could cause unbalanced magnetic pull. Similar approach to that introduced in [30] for conventional PM motors could be used for cogging torque and unbalance pull analysis of a magnetic gear. Goodness factors give a good indication whether particular combination of number of pole pairs of PM arrays and pole pieces is prone to cogging torque or radial force. Generally, it is impossible to completely eliminate both cogging and radial force without using skewing [31]. Authors suggest that optimal approach is to select a combination with zero radial force and then minimize cogging by step skewing one of the PM arrays. Experimental cogging torque analysis [32] shows that amplitude of torque in respective air gaps depends on the gearing ratio between the two PM arrays.

1.6.4 Three dimensional effects

Significant difference between peak torque obtained by 2D analysis and measured was reported in [24] and in [25]. The reduction in torque was believed to be caused by three-dimensional end-effects and axial leakage in the relatively large effective air gap between the magnet arrays, needed to accommodate the pole pieces. Sensitivity of end-effects on various design parameters was studied in [33] by means of 2D and 3D finite element analysis (FEA). It was reported that the difference is typically in the range between 10 to 20% and depends on many design variables, making 2D design methods relatively inaccurate and unreliable. As expected, the most affected by end-field fringing affects are gear designs with short axial length and large outer diameter. In addition, mechanical supporting structure used to hold pole pieces in place can further exacerbate axial leakage, Fig. 1-11, and, if made of conductive materials such as aluminium, can dramatically reduce gears efficiency [34]. Moreover, optimal length of pole pieces differs from stack length of both PM arrays and different permeability of laminated structure in the plane of lamination must be considered. Pole pieces are subject to complex forces and torques acting on each one

of them [35]. Consequently, optimal design is a compromise between mechanical rigidity and electromagnetic performance.

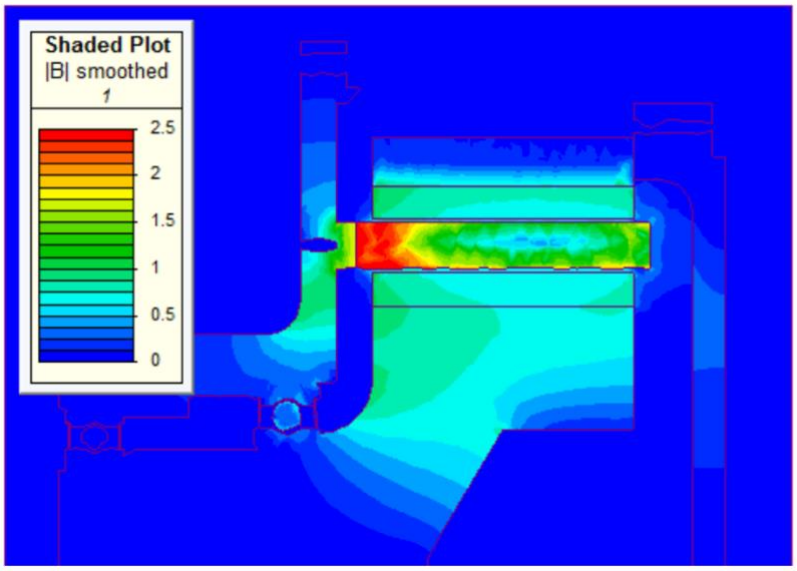

Fig. 1-11: Leakage field in the supporting structure of a magnetic gear [33]

1.6.5 Efficiency of magnetic gears

Loss mechanisms present in a PM excited magnetic gear are speed dependant since the device itself is passive, not requiring supply of electrical energy. Among the main losses are windage and friction losses in bearings, iron losses in the pole pieces and back iron of the PM arrays and eddy current losses in magnets. General approach to minimisation of all these loss mechanisms, apart from mechanical losses, is axial segmentation. This means using laminated electrical steel, or alternatively SMC, for all ferromagnetic parts and cutting magnet blocks into axially short slices. As discussed in the previous paragraph, varying axial leakage field passing through conductive supporting structures has significant impact on efficiency of the device [25] and can be substantially larger than all other losses of electromagnetic nature. Furthermore, axial lamination of magnetic circuit is ineffective if the field has large axial component, which it usually does in a magnetic gear. Despite all this, high efficiency exceeding 97% can be achieved [24].

Various improvements and modifications to the original concept of concentric (or coaxial) magnetic gear have been proposed, such as three-dimensional pole pieces utilizing the axial leakage to produce torque [36] or pole pieces with integrated PMs [37]. However, all these variants are based on the principles described above. For application in EV or HEV, magnetic gear could be integrated within an electric motor resulting in dual rotor machine with exceptionally high torque density, suitable for low speed high torque operation [38]. The gear element is used in fixed gear ratio configuration with outer PM array being attached to the inner bore of a wound field stator Fig. 1-12. Of particular interest to the research described in this thesis is the continuously variable magnetic transmission [39] which can replace the planetary gear and the MG1 in a typical power-split drivetrain by a single unit. Next section will describe its construction and operation in detail.

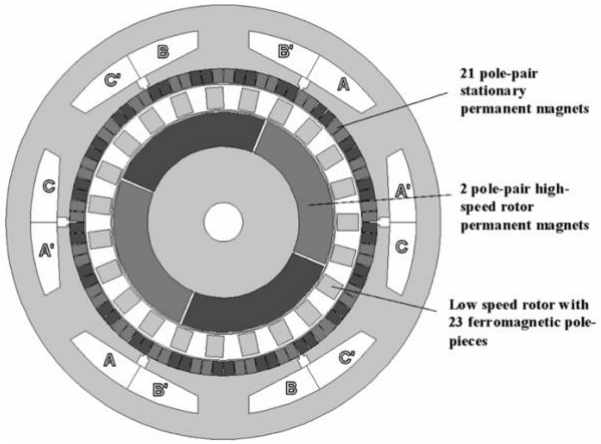

Fig. 1-12: Magnetically geared brushless PM motor [38]

1.7 Magnetically geared power split device

1.7.1 Triple rotor power split device

As shown in the previous sections, power split hybrid drivetrain relies on a planetary gear to split the flow of power from ICE between direct mechanical and indirect electrical path to the driven wheels. While the planetary gear could be directly replaced with a concentric magnetic gear, continuous variable magnetic

transmission device introduced in [39] provides a higher level of integration and drivetrain simplification. In essence, the device can be seen as a conventional surface mounted PMSM with integrated magnetic gear inside of its rotor, Fig. 1-13.

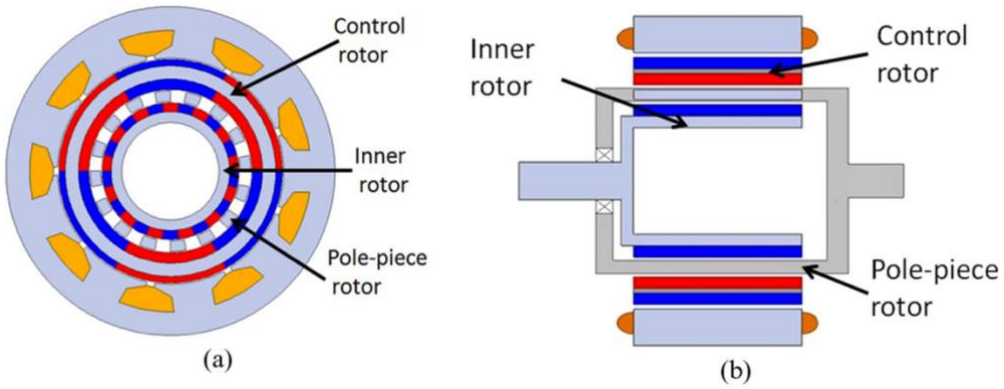

Fig. 1-13: Radial (a) and axial (b) cross section of triple rotor continuously variable transmission device [39]

First shaft is mechanically coupled to the innermost PM array (inner rotor) while the second shaft is connected to the pole pieces (pole piece rotor or PPR). The gear ratio between the two shafts can be varied by controlling speed of the outermost PM array (control rotor) which is shared between the gear and the PMSM. Since the machine has three physical rotating components and is used to split power, the term triple rotor power split device will be used to refer to it. Similarly to the mechanical planetary gear, one torque and two speeds must be known to fully describe an operating point of the device. Assuming that the pole piece rotor is coupled to the input shaft and the inner rotor to the output shaft, required speed of control rotor for any given combination of input and output speeds can be calculated as follows:

$$\omega_{cont} = \frac{p_{ppr} \cdot \omega_{ppr} - p_{output} \cdot \omega_{output}}{\left(p_{ppr} - p_{output}\right)} \qquad (1\text{-}6)$$

where p_{output} is number of pole pairs of the output rotor, ω_{ppr} is speed of the pole piece rotor, ω_{cont} is speed of control rotor and ω_{output} is speed of output rotor. Torques acting on control and output rotor are given by:

$$T_{cont} = T_{ppr} \frac{p_{output}}{p_{ppr}} \qquad (1\text{-}7)$$

$$T_{out} = T_{ppr} \frac{(p_{ppr} - p_{output})}{p_{ppr}} \quad (1\text{-}8)$$

where T_{ppr}, T_{cont} and T_{output} are pole piece rotor, control rotor and output rotor torque respectively. Assuming lossless operation, power balance between input and outputs can be expresses as:

$$T_{ppr} \cdot \omega_{ppr} = T_{cont} \cdot \omega_{cont} + T_{output} \cdot \omega_{output} \quad (1\text{-}9)$$

It is apparent that with constant speed and torque input from the ICE, division of power between control and output rotor is realised by varying the control rotor speed, Fig. 1-14. The role of the PMSM stator is to control speed and to react torque applied to the control rotor by the gear element.

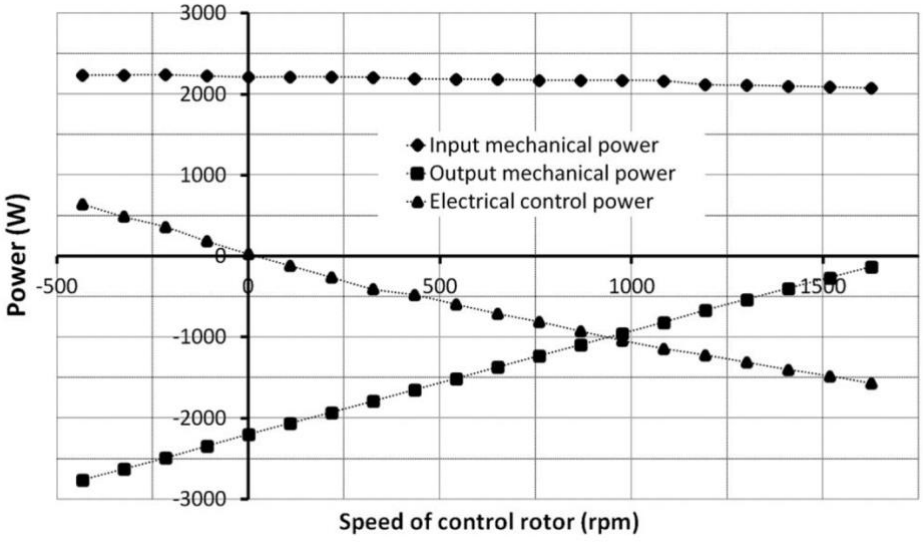

Fig. 1-14: Power flow control controlled by control rotor speed [39]

It can be seen in Fig. 1-15 how triple rotor power split device fits into a power split hybrid drivetrain where it combines function of MG1 and planetary mechanical gear. Tests performed on a prototype revealed that the device can reach 97.5% efficiency and is able to control the flow of power as expected [39]. While it does simplify overall layout of a power split drivetrain, it is relatively complex device requiring several sets of bearings and careful mechanical design of all three rotating

components. Mechanical retention, demagnetisation and thermal management of the control rotor magnets present significant design challenges.

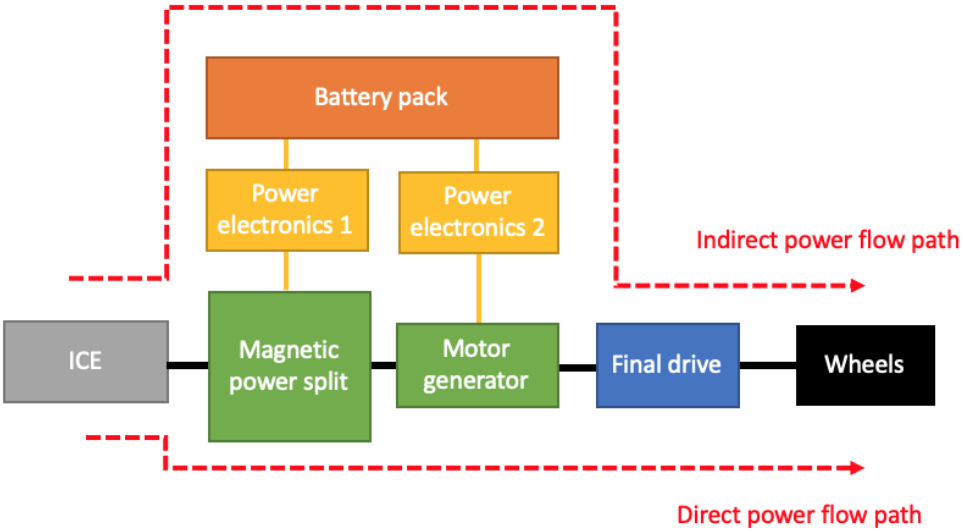

Fig. 1-15: Power split hybrid drivetrain equipped with the magnetic power split device

1.7.2 Dual rotor power split device

The control rotor of the device illustrated in Fig. 1-13 consists of ferromagnetic ring onto which outer and inner array of permanent magnets are mounted. The ring fulfils the function of a mechanical support for the magnets and, from principle of operation perspective, is not necessary. Furthermore, since both control rotor PM arrays have the same number of pole pairs, they can be eliminated, and the wound field stator can be directly coupled to the field created by the magnetic gear element. This novel arrangement, Fig. 1-16, creates dual rotor power split which retains the functionality of the triple rotor device whilst removing one of the rotating components and its corresponding set of bearings.

Directly interfacing the magnetic gear and the stator without the intermediate set of magnets will likely result in change of performance. For instance, relying on the wound field stator for magnetisation of the magnetic gear will likely decrease continuous transmittable torque density and negatively affect power factor, however, short term overload is now a possibility. Moreover, the stator of the dual rotor device

is exposed to air gap flux density harmonics produced by the gear which could have negative impact on efficiency and may even cause EMF distortion.

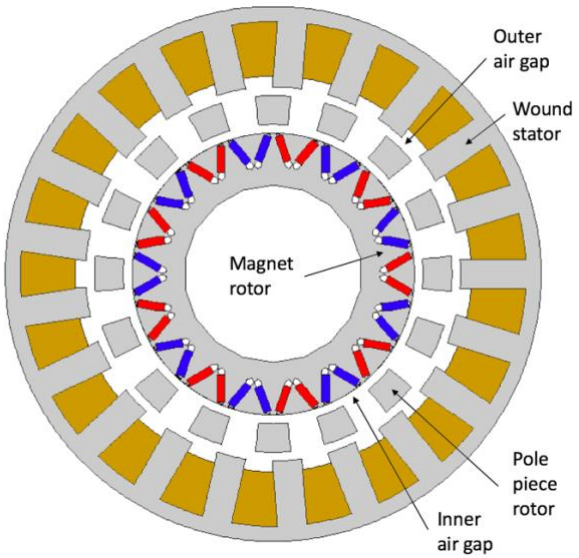

Fig. 1-16: Dual rotor power split device

Although the concept is novel, a few papers have been recently published addressing some of the concerns [40] [41]. EMF distortion and high cogging torque were reported [40] and it was shown that both problems can be minimized by dividing both rotors into axial segments and rotating them with respect to each other, Fig. 1-17. EMF distortion is a direct cause of rich spectrum of flux density harmonics in the outer air gap of the dual rotor device while cogging is present due to inherent symmetry in the selected pole combination. The performance of other pole combinations and winding patterns has not been reported.

From a magnetic circuit perspective, overload capability depends on magnetic loading of electrical steel and its saturation point. Linear relationship between torque and stator current density of a dual rotor machine is presented in [41], suggesting good overload capability. However, utilisation of magnetic steel at and below rated load is likely poor if the impact of saturation is negligible. In addition, a good match between results obtained by 2D FEA and test are reported. Authors mention using 3D FEA to estimate end winding leakage inductance, which is later used to correct 2D FEA results, however, axial leakage of both rotors is not considered.

Since the physical control rotor is omitted, the position of outer air gap fields cannot be directly measured by encoders and must be calculated from the position of both rotors so that the stator can be synchronised with the magnetic gear. Tests on a prototype showed very high efficiency, exceeding 98% [42], and excellent field weakening capability [41] likely resulting from relatively high leakage inductance. The efficiency computation has not been presented in any publication so far and remains one of the key areas for future research.

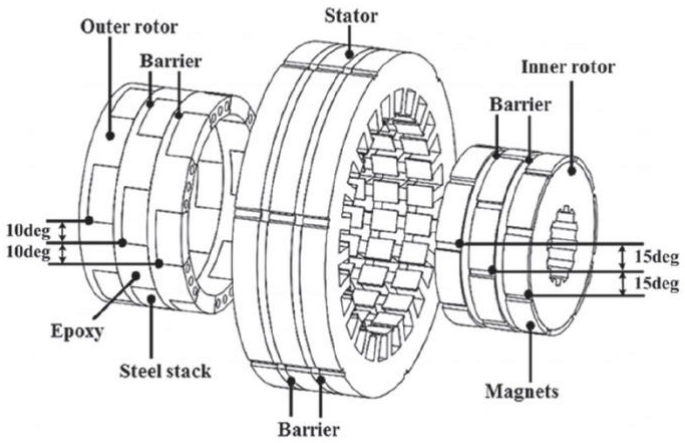

Fig. 1-17: Axially segmented and stepped skewed concept of dual rotor power split device [40]

1.8 Trends in electrical machine technology in HEV

As it was mentioned earlier, electrical machines in full hybrid drivetrains of typical passenger cars tend to be rated at tens of kilowatts so that they can propel the vehicle without any input form ICE. Robustness, ease of mass manufacture, cost and high efficiency over wide speed and torque range are among the main requirements for these machines [43]. While each currently available hybrid drivetrain uses unique electrical machine design, there are certain design trends worth discussing in detail.

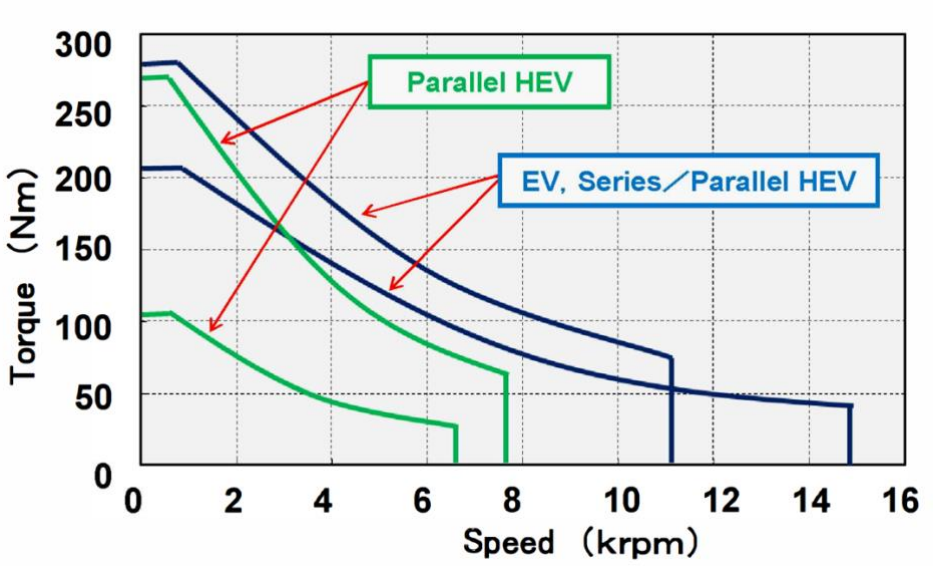

Fig. 1-18: Torque speed characteristics of traction motors used in HEVs produced by Toyota, Nissan and Honda. [44]

1.8.1 Torque and speed rating

Typical torque speed envelopes of traction motors used in current parallel and series/parallel (series/parallel refers to power split drivetrain) HEVs can be seen in Fig. 1-18. In parallel hybrid drivetrains, the motor is directly coupled to the engine and hence its maximum speed is limited by the maximum speed of the engine, typically around 7000rpm. In drivetrains where motors are independent of engine speed, the motor speed tends to be higher and often exceeds 10000rpm. The main reason for high speed in traction electrical machines is the need for compact size and low weight expressed in form of high-power density requirement. It is well known that size of an electrical machine is driven by its torque requirement, assuming constant magnetic and electrical loading. Since output power is given by multiplication of shaft torque and speed, the only way to increase output power of a machine designed for a specific torque is to increase its operating speed thus increasing power density. Trend of increasing speed of traction motors in order to reduce their size is apparent in the industry. For instance traction motors used in 3rd generation of Toyota Prius drivetrain have 20% higher power rating whilst being considerably smaller than those used in the 2nd generation [44]. For high speed operation consideration of mechanical robustness of rotors, torsional vibration and

frequency dependant loss mechanisms, such as AC copper and iron loss, is particularly important.

1.8.2 Topology and windings

Due to their high torque and power density, radial field permanent magnet synchronous machines (PMSM) currently dominate, especially in HEVs where system size and weight reduction are of prime importance. Restricted space envelope comes from limitations imposed by the vehicle layout and it tends to favour machines with relatively large diameter and short axial length, especially in vehicles with transversally mounted engines [44]. Consequently, fractional slot concentrated windings have become popular due to the short end winding, making it possible to achieve high torque density and efficiency in small volume. Segmented stators are often used together with coils which are pre-wound on bobbins and then inserted onto individual teeth. Pre-wound coils are easily manufacturable by automated winding machines and a very high slot fill factor can be achieved. Halo bus bar arrangement is often used to connect the individual coils into single three phase winding with multiple parallel paths. Practical example of such machine can be seen in Fig. 1-19 and detailed description can be found in [45].

Fig. 1-19: Integrated motor generator developed by Bosh, currently used in parallel hybrids manufactured by VW group [45]

Distributed overlapping winding has generally longer end-winding and, due to its random positioning of conductors in the slots, could suffers from lower slot fill factor in comparison to precision wound concentrated winding. However, higher fundamental winding factor can be achieved and, because this type of winding is essentially the same as that of a typical induction machine, well developed and mature coil manufacturing techniques can be employed. Moreover, bar wound distributed winding, Fig. 1-20, attracted a lot of interest in recent years as it combines high slot fill factor, relatively compact end-winding, better high voltage insulation properties and enhanced thermal performance due to improved copper to steel heat transfer [46]. Similar winding technology have been used by Toyota for the traction motor used in the latest generation of Prius and 10% reduction of end-winding length compared to conventional distributed winding was reported [44]. High slot fill factor ensures low DC copper loss; however, large cross-sectional area of individual conductors can exhibit significant skin effect at high stator frequencies.

Fig. 1-20: Detail of distributed bar (hairpin) wound stator end-winding [47]

1.8.3 Material of magnetic circuit

Laminated electrical steel, in the range from 0.2 to 0.35 mm thickness, is commonly used for stators and rotors of traction machines. Since they tend to have high number of poles and are expected to operate in wide speed range, careful material selection is essential to minimize frequency dependant iron loss and to

ensure mechanical robustness of rotors [44]. In order to further boost torque density, high flux density steel with increased saturation point can be used but is reported to be substantially more expensive [48] making it less attractive for mass production in automotive industry. Soft magnetic composites (SMC) present more exotic alternative to laminated steel and are particularly suitable for axial field PMSM [49] and other machines with three dimensional magnetic circuits.

1.8.4 Rotor construction and source of excitation

Modern high performance NdFeB permanent magnets, having high remanent flux density and coercive force, make it possible to achieve air gap flux densities above 1T without generating copper losses in the rotor. Since the machines are located in the engine bay and often share liquid cooling circuit with the engine, high temperature grades, typically SH or UH, must be used to prevent unwanted demagnetisation during normal operation. General trend in machine design leads towards magnet content [50] and rare earth material[46] reduction. SmCo magnets could be used but are not as common in vehicular applications since their very high sustainable operating temperature is not required and are more costly than NdFeB magnets.

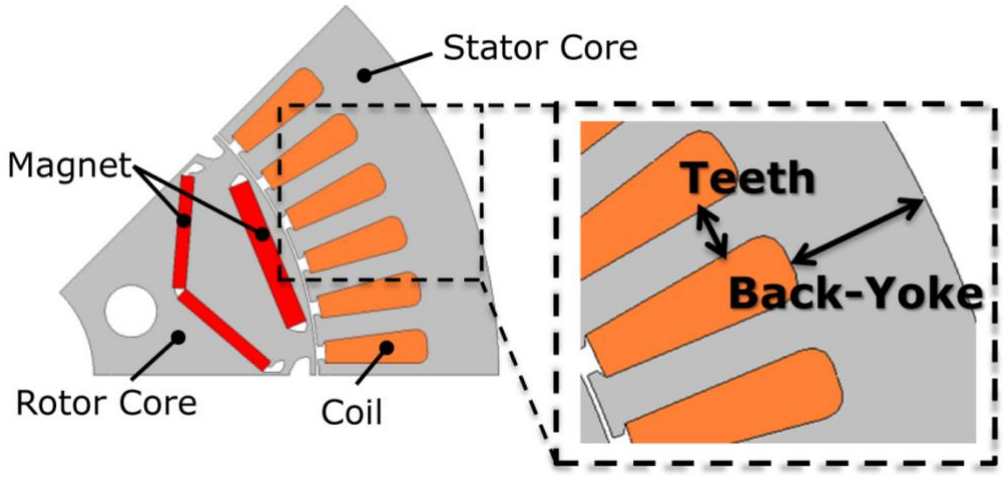

Fig. 1-21: Flux focused interior PM machine for an EV [51]

Benefits of interior and surface mounted PM rotors are comprehensively discussed in [52]. Surface mounted rotor tends to produce higher air gap flux density,

and consequently higher torque, but interior permanent magnet rotors are known for their inverse saliency, having higher inductance in quadrature axis. This is often exploited in the field weakening region of the torque speed characteristic, where negative d-axis current is applied to supress magnet flux, as the inverse salient machines produce positive reluctance torque increasing the machines torque capability in wide speed range. It has been reported in [43] that reluctance torque component at some operating points can be significantly higher than torque due to PMs interacting with the stator field. In addition, magnets embedded in the rotor steel are better protected against demagnetising air gap fields and don't have to rely on metallic or carbon fibre sleeves for mechanical retention. Special case of interior PM rotors are rotors utilising flux focusing to increase air gap flux density, saliency and to reduce magnet mass [50]. Flux focused rotors utilize two or more magnet blocks per pole arranged in spoke or V type pattern. Such topology, Fig. 1-21, has been successfully deployed in several HEVs and EVs produced by Toyota, Nisan [44] and Chevrolet [46] [47].

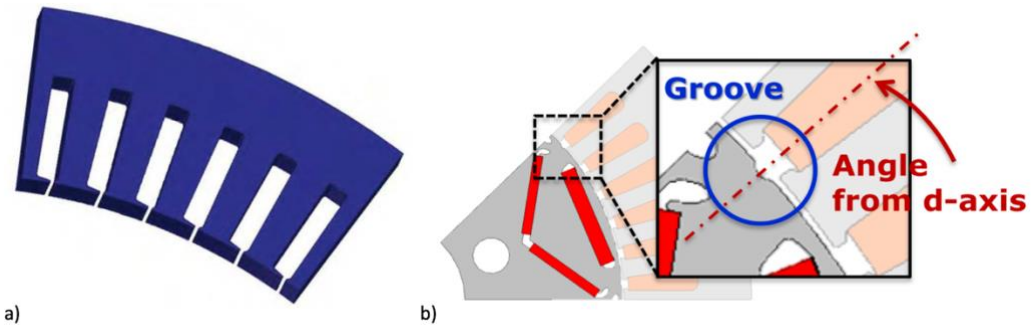

Fig. 1-22: Design techniques to reduce noise and cogging torque: a) asymmetrical tooth tips [47], b) non-uniform air gap [51]

1.8.5 Noise and vibration aspects

Another important topic in traction machine design is noise and vibration. Air gap magnetic fields interacting with salient structure of the stator can be a source of unwanted torque pulsation known as cogging torque and of on-load torque ripple. In addition, radial force acting on the lamination stack manifests itself as stator vibration and acoustic noise and could even lead to premature failure of winding

insulation due to friction. Cogging torque and unbalanced magnetic pull (UMP) can be analysed at the initial design stage by evaluating so called goodness factors [30]. This method doesn't predict cogging torque or UMP explicitly but allows for elimination of particularly poor performing designs early in the design stage. In order to minimize certain harmonic components of the air gap flux density, causing the torque ripples and radial force, various design techniques have been proposed. In [51] rotor lamination profile and magnet shape were optimized for minimal noise and authors conclude that the traction motor must be design in conjunction with the rest of the drivetrain, otherwise real world noise and vibration performance is difficult to predict. Stator slot openings could modulate air gap flux density distribution and add to its harmonic content. However, they can also be used to eliminate unwanted harmonics as presented in [47] where asymmetric tooth tips were shown to reduce radial force and cogging. Step skewing, where rotor is split into several axial sections which are rotated with respect to each other, is effective [53], although it comes at a cost of decreased machine performance due to inherent increase in leakage inductance.

1.8.6 Alternative machine topologies

Induction machines (IM) are still seen as standard against which all other machine topologies are compared. IM is a mature and well-established technology known for its robustness and simple manufacturing. They are neither as efficient nor as power dense as PMSMs but the fact that they don't rely on volatile prices of high performance permanent magnets makes them attractive, especially in pure EVs where space and weight restriction are not as strict [54]. Furthermore, higher efficiency could be achieved by employing rotor cage made of copper instead of aluminium [55]. Among other promising traction motor technologies are switched reluctance machines, however, they are not as widespread and their benefits, compared to PMSM, don't always counterbalance their disadvantages, namely poor noise performance and expensive controllers [56].

1.9 Aims and objectives

As is apparent from the preceding review, drivetrain electrification is a topic paramount to the future of sustainable personal transportation in Europe and worldwide. Hybrid electric vehicles, combining two propulsion systems in a single drivetrain, represent key technology allowing the transition from internal combustion engines to fully electric vehicles and enabling fulfilment of current legislative demands aimed at reducing greenhouse and noxious gas emissions as well as lessening the dependence of transportation sector on fossil fuels. Development of the next generation of HEV drivetrains is highly relevant from academic as well as industrial perspective and is expected to have significant impact on the future of personal mobility.

Emerging technologies, such as magnetically geared electromechanical devices, could have a major impact on the next generation of hybridized drivetrains, improving their performance and increasing the level of integration. This thesis addresses some key issues associated with design, analysis and operation of the novel dual rotor magnetically geared power split device with particular emphasis on the following:

- Selection of feasible configuration
- Sizing for a target application
- Magnetic circuit optimisation
- Effects of axial leakage
- Efficiency and loss
- Test and validation of a full-scale prototype

The research presented in this thesis was carried out under combined industrial and academic supervision and was sponsored by Magnomatics limited, leader in commercialization of products based on magnetic gear technology. The project aims to expand current understanding of the topic as well as to deliver a full-scale prototype of the aforementioned dual rotor device for a mid-sized passenger vehicle.

1.10 Outline of the thesis

The thesis is organized as follows:

Chapter 2: Principle of operation

The chapter describes the principle of operation of the proposed device and its application in hybrid electric drivetrain.

Chapter 3: Configuration selection and sizing

Limitations related to feasible configuration selection and electromagnetic sizing of the dual rotor device for a target automotive application are described.

Chapter 4: Effects of axial leakage

The proposed device is prone to axial leakage which negatively affects its performance. Influence of axial leakage on torque transmission and possible ways of reducing it are discussed in this chapter.

Chapter 5: Electromagnetic efficiency

All main loss mechanisms of electromagnetic nature present in the proposed device are discussed and evaluated for a range of input and output speeds and input torque.

Chapter 6: Experimental validation

Full scale prototype of the proposed device is presented together with test rig setup up and test results validating the theoretical discussions presented in chapters 2, 3, 4 and 5.

Chapter 7: Conclusion

The final chapter summarizes the main findings of the research presented in the thesis and proposes several areas for future research related to the dual rotor device.

Chapter 2 Principle of operation

2.1 Introduction

The dual rotor power split device, introduced in the first chapter, is based on the magnetic gearing principle, whereby magnetic field with a certain number of pole pairs is modulated by an array of ferromagnetic pole pieces in order to create space harmonic with a different number of pole pairs moving asynchronously with respect to the modulated magnetic field. Since understanding of this phenomenon is crucial for many of the discussion in this thesis, this chapter describes the fundamental principles in greater detail.

Firstly, the magnetic gearing effect is explained on an example of a passive magnetic gear with particular attention to air gaps flux density harmonic content. Torque and speed ratios between all principle components of the magnetic gear are described together with continuous variable gear ratio operation. Practical realisations of continuously variable gear ratio in forms of triple and dual rotor power split devices are discussed and advantages of the dual rotor solution highlighted.

Secondly, constraints imposed on windings of the dual rotor power split device by presence of two dominant space harmonics in the air gap adjacent to the stator are outlined. Degree of coupling between the windings and the space harmonics is evaluated by means of winding factor calculation based on harmonic analysis of so-called winding function describing distribution of conductors in stator slots.

Finally, torque transmission and control of power flow through the dual rotor device is discussed emphasizing the differences compared to passive magnetic gear. Throughout the chapter, results of FE simulations are used to illustrate and validate some of the theoretical assumptions.

2.2 Magnetic gearing effect

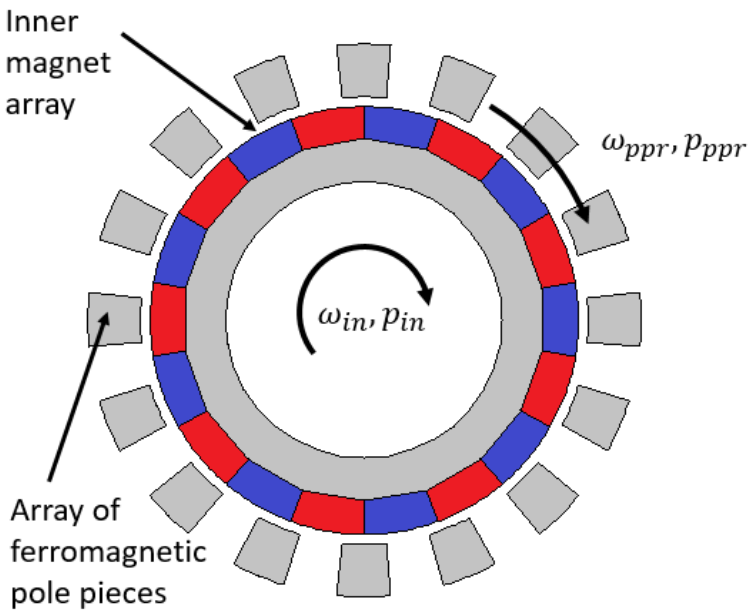

Fig. 2-1: Concentric arrangement of 9 pole pair magnet array and 16 pole pieces

Let us have a concentric arrangement of a magnet array and pole pieces as depicted in Fig. 2-1. The radial component of air gap flux density distribution due to the inner magnet array, having number of pole pairs equal to p_{in}, can be expressed as follows:

$$B_{r\_pm}(\vartheta) = \sum_{n=1,3,5}^{\infty} b_{rn} \cdot \sin(n \cdot p_{in}(\vartheta + \omega_{in} \cdot t) + n \cdot p_{in} \cdot \vartheta_0) \qquad (2\text{-}1)$$

where ω_{in} is angular velocity of the inner magnet array and b_{rn} is the Fourier coefficient for the radial flux density distribution. The array of ferromagnetic pole pieces acts as a modulator. The flux density waveform described by equation (2-1) is faced with series of highly permeable pole pieces and gaps filled with air between them which, in simple terms, behave like gates and barriers for the flux. Assuming the pole pieces are infinitely permeable, magnetic flux cannot pass through the gaps between them in radial direction and there is no flux leakage in circumferential direction, the modulating function can be expressed as a simple square wave function with amplitude of 1. Such function is expressed as follows:

$$\delta_{ppr}(\vartheta) = \frac{1}{2} + \sum_{m=1,2,3}^{\infty} \frac{2}{m \cdot \pi} \cdot sin\left(\frac{m \cdot \pi}{2}\right) \cdot \sin\left(m \cdot p_{ppr}(\vartheta + \omega_{ppr} \cdot t)\right) \quad (2\text{-}2)$$

where p_{ppr} is number of ferromagnetic pole pieces and ω_{ppr} is angular velocity of the pole piece array. Such modulating function represents an ideal modulator which, in practice, is impossible to construct and is only used here to illustrate basic principles. Modulated flux density waveform can be calculated by multiplying the original field distribution, expressed by equation (2-1), by the modulating function in equation (2-2). Derivation of modulated flux density function can be found in Appendix A. Assuming higher order harmonics of both functions are not present, i.e. coefficients m and n are equal to 1, modulated flux density distribution is given by:

$$\begin{aligned} B_{r\_mod}(\vartheta) &= \frac{2 \cdot B_r}{\pi} \cdot \sin\left(p_{in}(\vartheta + \omega_{in} \cdot t)\right) \\ &+ \frac{4 \cdot B_r}{\pi^2} cos\left[\left(p_{ppr} - p_{in}\right)\left(\vartheta + t\frac{\left(p_{ppr}\omega_{ppr} - p_{in}\omega_{in}\right)}{\left(p_{ppr} - p_{in}\right)}\right)\right] \\ &- \frac{4 \cdot B_r}{\pi^2} cos\left[\left(p_{ppr} + p_{in}\right)\left(\vartheta + t\frac{\left(p_{ppr}\omega_{ppr} + p_{in}\omega_{in}\right)}{\left(p_{ppr} + p_{in}\right)}\right)\right] \end{aligned} \quad (2\text{-}3)$$

It is apparent from equation (2-3) that three dominant harmonic components exist. One of the space harmonics has the same number of pole pairs as the inner array of permanent magnets and rotates at the same angular velocity while the other two have different number of pole pairs and rotate asynchronously with respect to the inner magnet array. Number of pole pairs of the two asynchronous harmonics is given by:

$$p = p_{ppr} \pm p_{in} \quad (2\text{-}4)$$

While angular velocity of the asynchronous space harmonics is given by:

$$\omega = \frac{\left(p_{ppr} \cdot \ \omega_{ppr} \pm p_{in} \cdot \omega_{in}\right)}{\left(p_{ppr} \pm p_{in}\right)} \quad (2\text{-}5)$$

The inner magnet array of the arrangement in Fig. 2-1 creates space harmonic with nine pole pairs. Modulation of this space harmonic by 16 pole pieces results in two dominant asynchronous space harmonics having 7 and 25 pole pairs, both having the same amplitude.

Fig. 2-2 and Fig. 2-4 show the flux density distribution at inner and outer periphery of the pole piece array obtained by FEA analysis while Fig. 2-3 and Fig. 2-5 show their corresponding harmonic spectra. Fields at both inner and outer periphery of the pole piece array contain space harmonics as predicted by (2-3), however, their relative amplitudes are different. This is due to the pole piece array being non-ideal modulator. In addition, some higher order harmonics, which were neglected in the above analysis, are present. It is apparent, from Fig. 2-3, that 9 pole pair harmonic has significantly higher amplitude than the 25 pole pair one and it is, therefore the space harmonic used in magnetic gears.

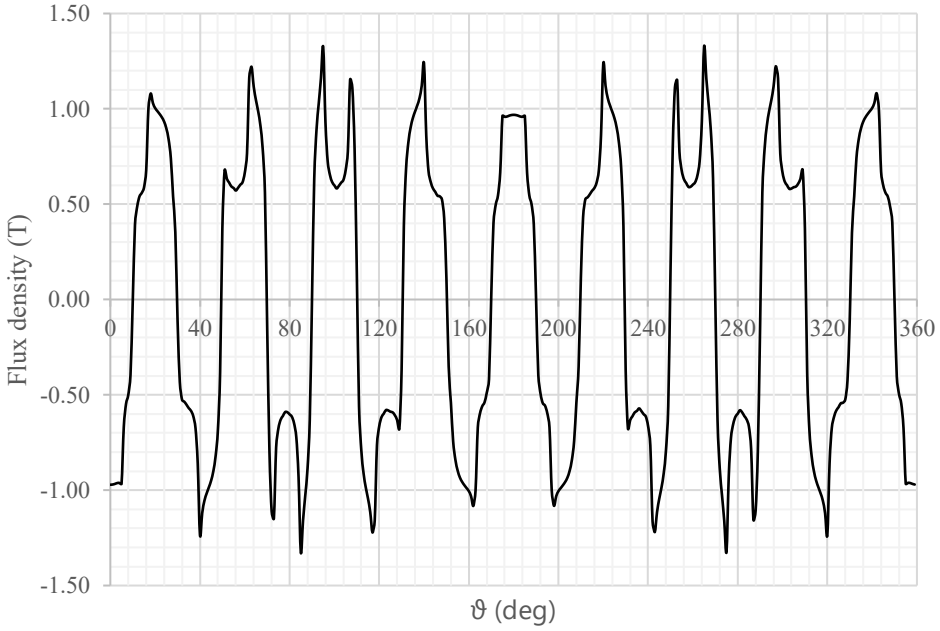

Fig. 2-2 Radial component of flux density at inner periphery of the pole piece array

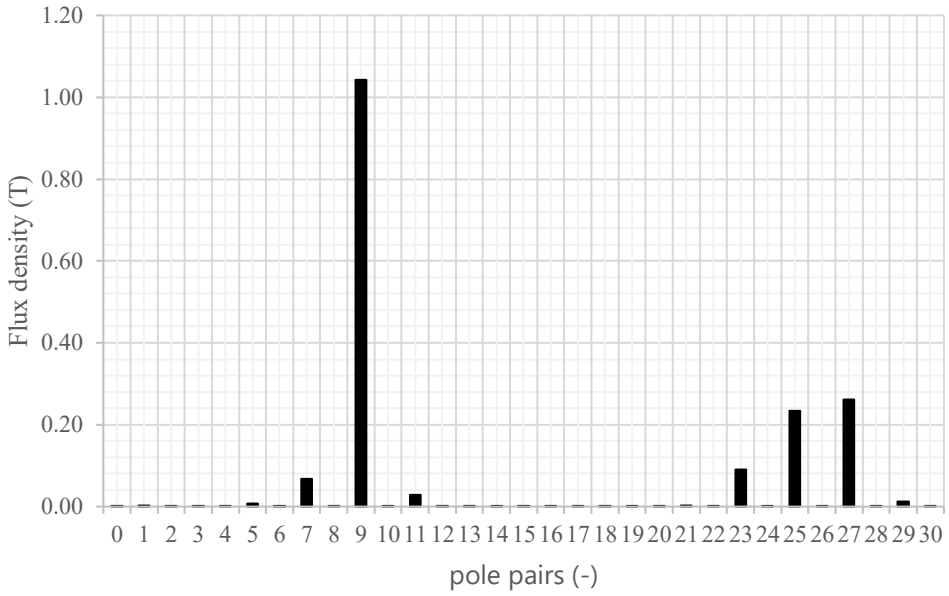

Fig. 2-3 Spectrum of flux density waveform at inner periphery of the pole piece array showing dominant 9 pole pair space harmonic

Fig. 2-4 Radial component of flux density at outer periphery of the pole piece array

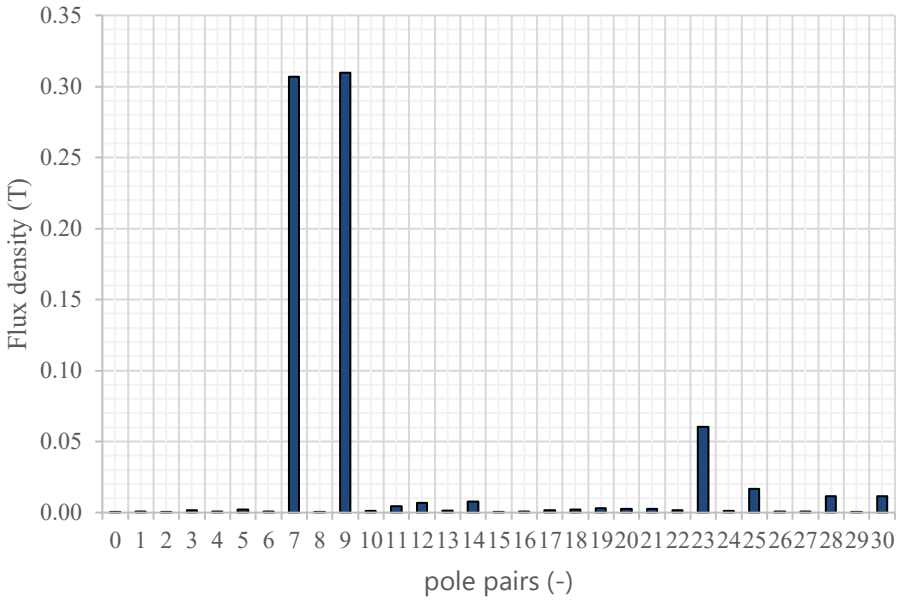

Fig. 2-5 Spectrum of flux density waveform at outer periphery of the pole piece array showing dominant 7 and 9 pole pair space harmonics

In order to construct a magnetic gear, the third component, able to couple to the 7-pole pair asynchronous harmonic, must be provided. Complete gear can be seen in Fig. 2-6, showing all three principal components of a magnetic gear.

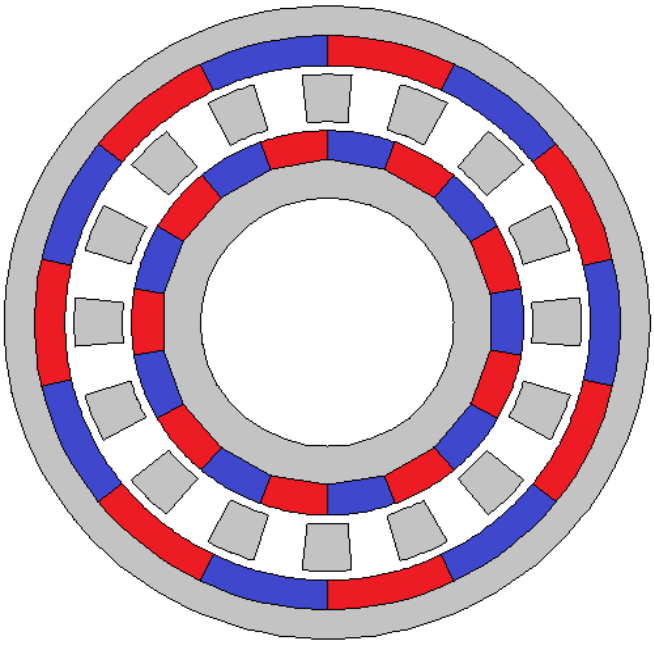

Fig. 2-6 Concentric magnetic gear with 9 pole pair inner magnet array, 7 pole pair outer magnet array and 16 pole pieces

2.3 Torque and speed ratios of magnetic gears

In steady state condition, torques acting on all three components are given by:

$$T_{ppr} = -T_g \cdot \sin(\delta) \quad (2\text{-}6)$$

$$T_{out} = T_g \cdot \left(\frac{p_{out}}{p_{ppr}}\right) \cdot \sin(\delta) \quad (2\text{-}7)$$

$$T_{in} = T_g \cdot \left(\frac{p_{in}}{p_{ppr}}\right) \cdot \sin(\delta) \quad (2\text{-}8)$$

where T_{in}, T_{out} and T_{ppr} are torque acting on inner magnets, outer magnets and pole pieces respectively, δ is internal load angle and T_g is peak transmittable torque. Peak transmittable torque of a magnetic gear is a function of its design and, in case of gears using permanent magnets, it cannot be increased. Any further increase of load beyond this value would result in gear slippage and loss of synchronism between the magnet arrays and the space harmonics with which they couple. Internal load angle is composed of angular positions of individual components expressed in electrical degrees and is given by:

$$\delta = \vartheta_{in} \cdot p_{in} + \vartheta_{out} \cdot p_{out} - \vartheta_{ppr} \cdot p_{ppr} \quad (2\text{-}9)$$

where ϑ_{in}, ϑ_{out} and ϑ_{ppr} are angular position of inner and outer magnet arrays and pole piece array respectively. Peak transmittable torque is reached when internal load angle equals π/2. It is apparent from equations (2-6) to (2-8) that relationship between torques acting on all three components can be expressed as follows:

$$|T_{ppr}| = \left(\frac{p_{ppr}}{p_{out}}\right) \cdot |T_{out}| = \left(\frac{p_{ppr}}{p_{in}}\right) \cdot |T_{in}| \quad (2\text{-}10)$$

At steady state, torque applied to the pole pieces is reacted by torques acting on both magnet arrays such that the system is in equilibrium. From equation (2-10), two torque ratios within the magnetic gear can be defined:

$$G_{r1} = \left(\frac{p_{ppr}}{p_{in}}\right) \quad (2\text{-}11)$$

$$G_{r2} = \left(\frac{p_{ppr}}{p_{out}}\right) \quad (2\text{-}12)$$

It is apparent from equations (2-11) and (2-12) that both torque ratios only depend on specific combination of pole pairs and pole pieces. They are, therefore, inherent to a specific gear design and cannot be altered without physically modifying the gear.

Any magnetic gear can be operated as a fixed gear ratio transmission when one of the three principal components of the gear is mechanically constrained so that its angular velocity remains zero regardless of applied load. Assuming lossless operation, sum of mechanical power entering and leaving the gear must be zero:

$$T_{in} \cdot \omega_{in} + T_{out} \cdot \omega_{out} + T_{ppr} \cdot \omega_{ppr} = 0 \quad (2\text{-}13)$$

If angular velocity of one the components of the magnetic gear is zero, gear ratio between the other components can be derived using equations (2-13). For instance, if the outer array of permanent magnets is fixed, gear ratio between the pole piece array and the inner magnets can be calculated as follows:

$$G_r = \frac{\omega_{in}}{\omega_{ppr}} = \frac{p_{ppr}}{p_{in}} = \frac{T_{ppr}}{T_{in}} \quad (2\text{-}14)$$

Similarly, a fixed gear ratio could also be defined for a situation where the pole pieces are mechanically grounded, and the two magnet arrays are free to rotate. It is important to note that, in the case of fixed transmission operation, both speed and torque ratios are constant.

2.4 Continuous variable transmission operation of magnetic gears

Of particular interest to the research presented in this thesis is continuous variable transmission operation of magnetic gears. Any combination of input and output speed between any two of the principal components can be realized as long as the third, controlling, component is free to rotate, and the following equation is satisfied:

$$\omega_{out} \cdot (p_{ppr} - p_{in}) = p_{ppr}\omega_{ppr} - p_{in}\omega_{in} \qquad (2\text{-}15)$$

where ω_{out} is angular velocity of the outer magnet array. It is important to note that while the speed ratio between the two components can be varied, the torque ratios are still function of the combination of poles and pole pieces and remain constant. Hence the speed of the controlling component not only changes the speed ratio between shafts but also power flow through the gear according to equation (2-13). In variable transmission mode, a magnetic gear works as a power split device.

It is apparent from equation (2-15) and (2-10) that to fully describe the operating point of a magnetic gear working as a continuous variable transmission, speed of two components and torque acting on one must be known.

2.4.1 Practical realisation of continuous variable gear

Practical realisation of continuous variable transmission system, employing magnetic gear technology, was first introduced in [39] and was briefly discussed in the previous chapter. Cross sectional view of the device can be seen in Fig. 2-7. It has two shafts, one coupled to pole pieces and the other to the inner magnet array. One of the shafts is used as a mechanical power input while the second as a power output. Angular velocity of the outer array, called control rotor, is controlled by a conventional synchronous machine stator such that speed ratio between input and output shaft can be varied and electrical power can be either removed or injected into the system. The control rotor provides magnetic flux for both the intermediate and the outermost air gap and has lower number of pole pairs than the inner rotor. This configuration is preferable since the array with lower number of poles carries lower

torque and therefore requires lower electrical loading of the stator. In total, the device has three rotating components, hence the name triple rotor power split device.

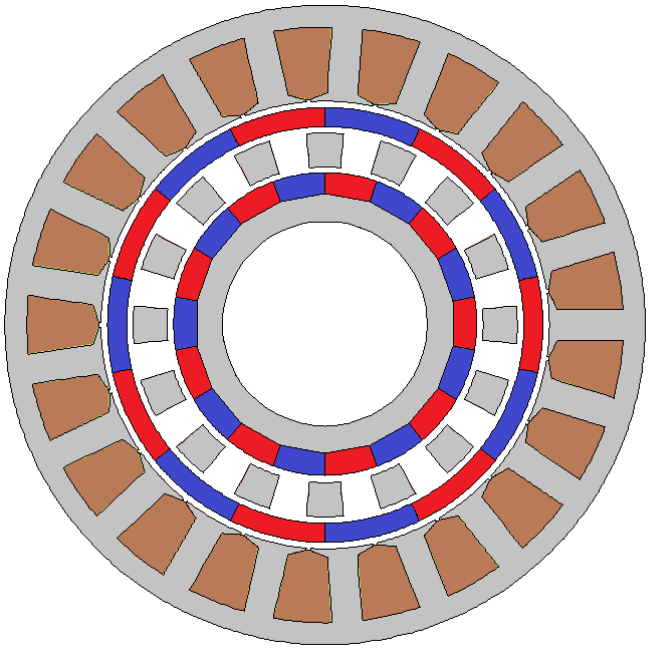

Fig. 2-7 Continuously variable magnetic gear with three rotors

Both mechanical and electromagnetic design of the control rotor present significant challenge. The control rotor magnets need to be retained against centrifugal forces which is often achieved by employing composite or metallic retaining sleeves, increasing effective length of the outer most air gap. In order to achieve high torque density, magnetic gears rely on rare earth permanent magnets which are electrically conductive and can be source of power loss when exposed to asynchronous space harmonics introduced by, for example, stator slotting. This power loss is relatively difficult to remove since the retaining sleeve, depending on its material, could act as a thermal insulator. Consequently, higher operating temperature of the magnets leads to adoption of heavy rare earth rich materials which add considerable cost. Having relatively large effective air gaps on either side of the control rotor could also increase risk of permanent demagnetisation of the magnets at higher operating temperatures. Additionally, three concentric rotating components require relatively complicated mechanical arrangement and a large number of bearings.

Having discussed some of the design challenges presented by the triple rotor power split device, it is apparent that its wider adoption may be limited especially in industries where cost, robustness and simplicity is preferred. Since the asynchronous space harmonic created by interaction of the inner magnet array and pole pieces has the same number of pole pairs as the stator, it could be directly coupled to it without the need for another magnet array, thus creating dual rotor power split device which is the main subject of the research presented in this thesis. Cross sectional view of the dual rotor power split device can be seen in

Fig. 2-8. There are only two rotating components, the array of pole pieces, for which term ‘pole piece rotor’ or abbreviation ‘ppr’ will be used, and the inner magnet array named ‘magnet rotor’. The outer magnet array in the triple rotor device was called ‘control rotor’ since by controlling its speed, speed ratio between the input and the output shaft was controlled. In the dual rotor device, the useful space harmonic in the outer air gap resulting from interaction of pole pieces and magnet rotor replaces the control rotor. Since the useful space harmonic has the same function as the control rotor it will be referred to as ‘control’ space harmonic.

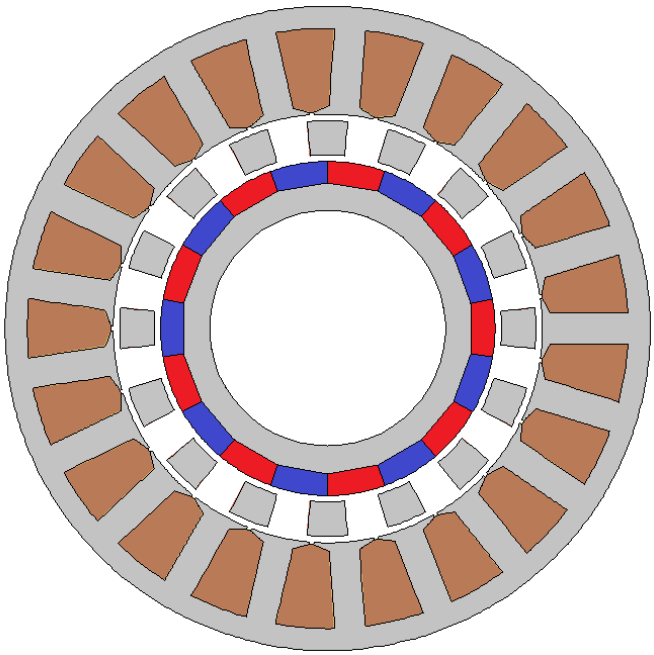

Fig. 2-8 Dual rotor power split device

2.5 Winding selection for the dual rotor device

Appropriate winding pattern selection is particularly important in case of the dual rotor device, since there are two dominant space harmonics in the air gap adjacent to the stator. Interaction between the parasitic harmonic and the winding is generally undesirable, hence windings with no coupling are preferable. The degree of coupling between a winding and a flux density space harmonic is expressed by winding factor, which must be evaluated for all space harmonics interacting with the winding. The following sections describe general method of winding factor calculation and examples of windings suitable for the dual rotor device.

2.5.1 Winding factor calculation

A winding of a rotating synchronous electrical machine has typically a number of phases connected in either star or delta configuration, each having one or more coils embedded in stator slots and connected together to form one or more parallel paths. According to the induction law, time variation of magnetic fields intersecting the stator winding induces electromotive force which can be measured at the winding terminals and is given by:

$$emf = \frac{d\psi}{dt} = \omega \cdot \psi \cdot k_w \qquad (2\text{-}16)$$

where ψ is flux linkage, ω is angular velocity and k_w is winding factor. In classical electrical machine theory, idealized stator winding, having perfect sinusoidal distribution of conductors and no chording, is often used to explain fundamental principles. However, such winding is purely theoretical and cannot be physically constructed. Winding factor is used to expresses reduction of induced EMF due to non-ideal nature of a particular winding and is defined as follows:

$$k_w = \frac{emf\ of\ actual\ winding}{emf\ of\ equivalent\ full\ pitch\ ideal\ winding} \qquad (2\text{-}17)$$

Winding factor is often expressed as a product of distribution and pitch factor. Distribution factor accounts for non-sinusoidal distribution of conductors in stator slots and pitch factor for coils chording. A classical method of determining both factors is explained for example in [57] and following equation is derived:

$$k_{wv} = k_{pv} \cdot k_{dv} = \sin\left(v \cdot \frac{W}{\tau_p} \cdot \frac{\pi}{2}\right) \cdot \frac{2 \cdot \sin\left(\frac{v}{m} \cdot \frac{\pi}{2}\right)}{\frac{N_{slots}}{m \cdot p} \sin\left(v \cdot \pi \cdot \frac{p}{N_{slots}}\right)} \qquad (2\text{-}18)$$

where k_{pv} is pitch factor, k_{dv} distribution factor, v is harmonic order, W is coil pitch, τ_p is pole pitch, N_{slots} is number of stator slots, m is number of stator phases and p number of winding pole pairs. While equation (2-18) is valid for most common winding configurations, it is not completely general and cannot be used for fractional slot, asymmetrical or windings with varying number of conductors in each slot. In addition, the winding factor can only be calculated for fundamental harmonic and its integer multiples.

In order to assess suitability of a particular winding for the dual rotor device, its winding factor for both space harmonics must be evaluated. Optimal winding configuration would have a winding factor of 1 for the useful asynchronous space harmonic whilst having no coupling, i.e. winding factor equal to 0, for the parasitic one. Since both space harmonics are not necessarily integer multiples of each other, it is apparent that more general approach for winding factor calculation is needed.

Several alternative methods of winding factor calculation have been developed over the years and they are comprehensively summarized in [58]. Authors came to the conclusion that the most general approach to winding factor calculation is to perform harmonic analysis on so called winding function which describes a distribution of conductors along stator periphery. A generalized formula for winding factor calculation of any arbitrary winding is derived and used for analysis of several complicated winding patterns. In addition, it is shown that the results of Fourier analysis can be also used to compute harmonic leakage factor, i.e. ratio of magnetizing to harmonic leakage inductance. Similar approach was adopted in [59] and applied to a fractional slot winding design in [60], although the winding function

is called conductor density function. Both publications provide detailed mathematical derivation of general formulas and also explore different ways of representing the winding function. Additionally, it is shown that the Fourier series representation of conductor distribution is suitable not only for calculation of winding factors of arbitrary windings but also for analysis of harmonic distortion of air gap magnetic fields generated by the windings. The effect of steel saturation on air gap flux density is, however, neglected.

Detailed mathematical derivation of the general winding factor formula can be found in the aforementioned publications, only general principles will, therefore be described here. Let us have a straight conductor in a rotating magnetic field. Effective value of EMF induced in the conductor by the rotating field is given by:

$$E_{1rms\_k} = \frac{\sqrt[2]{2} \cdot \pi \cdot f \cdot r \cdot l \cdot B_{p\_k}}{k} \qquad (2\text{-}19)$$

where f is frequency, r is radial position of the conductor, l is length, B_{p_k} is peak flux density of k-th space harmonic of the magnetic field and k is harmonic order. Phase of a winding consists of number of conductors and total phase EMF is given by sum of EMFs induced in all conductors connected in series. In case of ideal winding, EMFs induced in individual conductors are in phase and, therefore, total EMF can be calculated simply by multiplying EMF induced in a single conductor by total number of conductors in series.

As it was mentioned previously, conductors of a real winding are spatially distributed in number of slots and EMFs of individual conductors are not necessarily in phase. According to [58], each phase of a winding can be described by a winding function which can be expressed as a Fourier series:

$$n(\vartheta) = \sum_{k=1}^{\infty} n_k \cdot \cos(k \cdot \vartheta + \vartheta_0) \qquad (2\text{-}20)$$

where n_k is Fourier coefficient of the winding function. Example of winding function of a single phase of 7 pole pair 18 slot winding can be seen in Fig. 2-10. Rotating flux density distribution in the air gap can be described in similar manner:

$$B(\vartheta, t) = \sum_{k=1}^{\infty} B_k \cdot \cos(k \cdot \vartheta + k \cdot \omega \cdot t + \vartheta_0) \qquad (2\text{-}21)$$

where B_k is Fourier coefficient of the air gap flux density distribution. Flux linkage of a phase conductors described by equation (2-20) interacting with rotating flux density distribution according to equation (2-21) is given by following equation:

$$\psi(t) = \int_0^{2\pi} [B(\vartheta, t) \cdot r \cdot l \cdot n(\vartheta)] d\vartheta \qquad (2\text{-}22)$$

By solving the integral and rearranging the results, the equation for peak value of flux linkage of harmonic order k is obtained:

$$\psi_k = \pi \cdot R \cdot l \cdot B_k \cdot n_k \qquad (2\text{-}23)$$

where B_k and n_k are amplitude of flux and conductor density functions of harmonic order k. Effective value of EMF of harmonic order k induced in a phase is time derivative of flux linkage:

$$E_{w,k} = \frac{d\psi_k}{dt} = \omega \cdot \psi_k = \sqrt[2]{2} \cdot \pi^2 \cdot f \cdot B_k \cdot n_k \cdot r \cdot l \qquad (2\text{-}24)$$

Having established formulas for calculation of EMF induced in ideal sinusoidally distributed and real winding, winding factor can be calculated from direct comparison of equations (2-19) and (2-24) :

$$k_{w,k} = \frac{E_{w,k}}{2 \cdot N \cdot E_{1rms\_k}} \qquad (2\text{-}25)$$

$$k_{w,k} = \frac{\pi \cdot n_k \cdot k}{2 \cdot N} \qquad (2\text{-}26)$$

where N is total number of conductors in a phase of the analysed winding and can be calculated by integrating absolute value of the winding function or simply by summing all conductors belonging to the phase in all slots.

$$N = \int_0^{2\pi} |n(\vartheta)| d\vartheta = \sum_{q=1}^{N_{slots}} n_q \qquad (2\text{-}27)$$

where n_q is number of conductors in slot q. Equation (2-27) is general formula for winding factor calculation of single phase of any arbitrary winding regardless of how complex the distribution of conductors is. Its only limitation lies in the necessity to accurately compute amplitudes of winding function harmonic components which can be done either numerically or analytically. It is worth noting that for the purpose of initial winding analysis and selection, absolute number of conductors in stator slots does not need to be known, relative conductor distribution function may be used.

The value of winding factor obtained by harmonic analysis of winding function inherently contains both the distribution and the pitch factor and these two factors cannot be separated. However, in practice there is no need for separation of these two factors. In addition, the method doesn't take into consideration reduction of EMF due to stator or rotor skewing which needs to be analysed separately. For the purpose of initial winding selection this effect can be neglected.

2.5.2 Winding pattern selection

Winding factor calculation method introduced in the previous section can be used to analyse various winding patterns and to identify suitable configurations. As an example, highlighting the potential issue arising from selecting an unsuitable winding pattern, 7 pole pair 18 slot double layer fractional slot winding was analysed.

Fig. 2-9 shows distribution of conductors of a single phase in stator slots and its corresponding winding function (Fig. 2-10). Winding factors for the first 20 harmonic orders can be calculated by performing harmonic analysis of the conductor density function and applying equation (2-26) to calculate winding factors. This winding

may seem as an attractive choice for a dual rotor device with 9 pole pair magnet rotor and 16 pole pieces since it has relatively high winding factor for the operating 7 pole pair harmonic, Fig. 2-11. However, winding factor for 9 pole pairs is even higher. EMF measured at the terminals of this winding would, therefore, be distorted by the parasitic harmonic. If, however, the parasitic harmonic had 10 pole pairs instead of 9, there would be no coupling with the winding and no EMF distortion. Such configuration would, however, require 17 pole pieces.

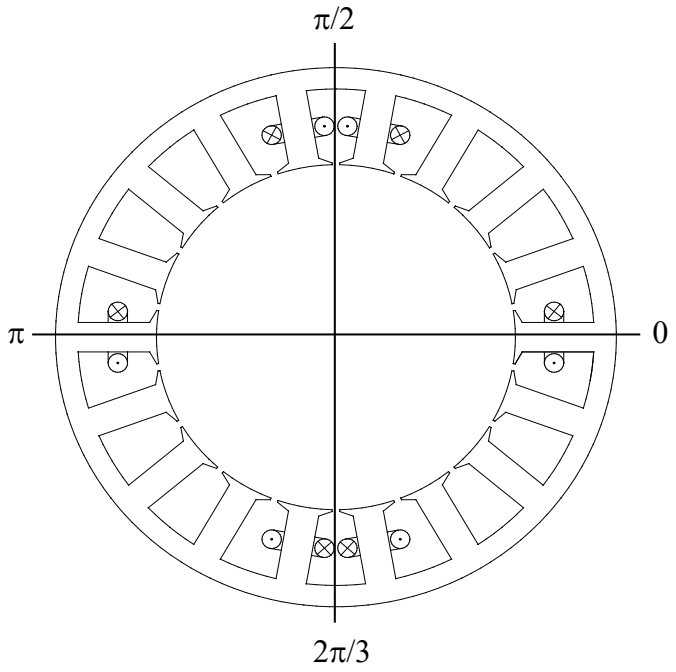

Fig. 2-9: 18 slot 7 pole pair concentrated double layer winding: A phase coils

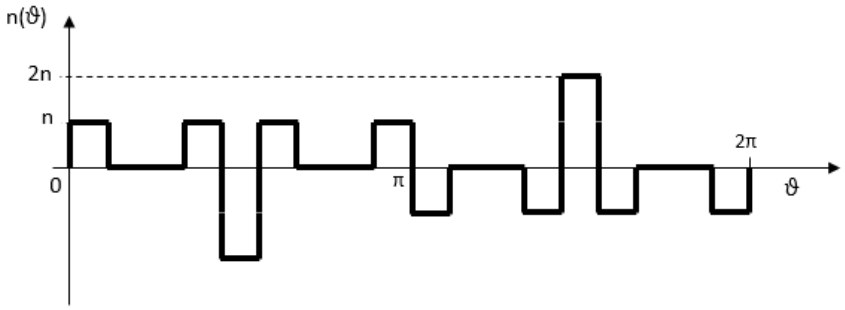

Fig. 2-10 Phase winding function of 18 slot 7 pole pair double layer concentrated winding describing average conductor density distribution around stator periphery

The 7 pole 18 slot winding is an example of fractional slot concentrated windings which have become popular in modern traction motors since they have considerably shorter overhang length whilst having high fundamental winding factor. Short overhang reduces copper loss in the passive portion of the winding and it also lowers the overall axial length of the machine thus improving volumetric power density. On the other hand, windings with low number of slots per pole and phase tend to produce more MMF harmonics since they do not approximate the ideal sinusoidally distributed winding as well. In addition, interaction between air gap space harmonics and the relatively salient structure of a fractional slot stator could introduce considerable torque ripple or unbalanced pull [57]. Since the dual rotor device in an HEV drivetrain is directly coupled to an ICE, a strong source of torsional vibration, cogging torque may be considered less important while both high power density and efficiency are desirable.

Fig. 2-12 shows winding factors for 7 and 9 pole pairs for number of fractional slot double layer windings. It is apparent that only windings with 9 and 21 slots have zero winding factor for the 9-pole pair harmonic. Windings with 12, 15 and 18 slots have very high fundamental winding factor but would suffer from EMF distortion and possibly torque ripples.

Winding factors for number of integer and fractional overlapping windings can be seen in Fig. 2-13. 42 slot single layer integer slot winding has the highest achievable winding factor whilst having zero winding factor for the 9-pole pair harmonic, however, since it is a full pitched winding it will likely have the longest winding overhang. In practice, integer slot windings are often constructed as double layer and short pitched so that overhang length can be reduced, and short pitching could also eliminate EMF harmonics. For instance, double layer integer slot winding with 2/3 pitch is known to eliminate odd multiples of third harmonic and for that reason is widely used. Most of the fractional slot overlapping windings don't satisfy the requirement of zero winding factor for the 9 pole harmonic, apart from 63 slot winding having 0.953 fundamental winding factor.

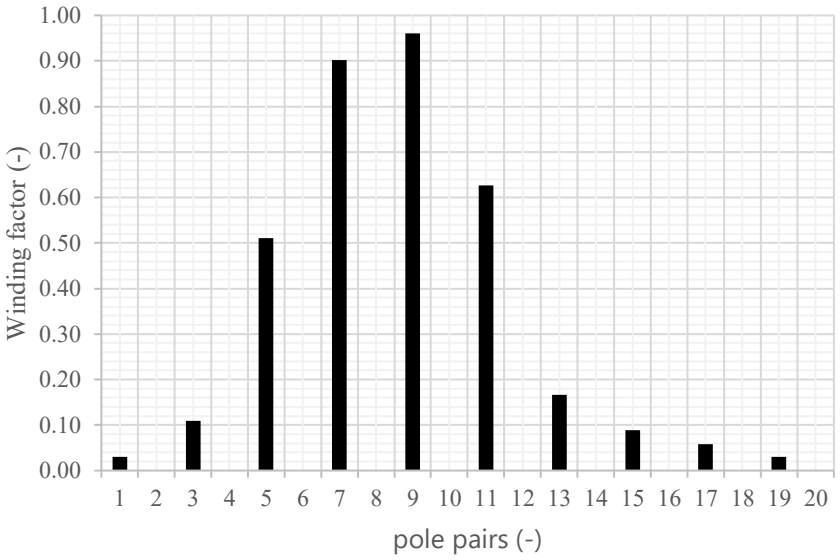

Fig. 2-11 Winding factors for 7 pole pair concentrated double layer winding with 18 slots

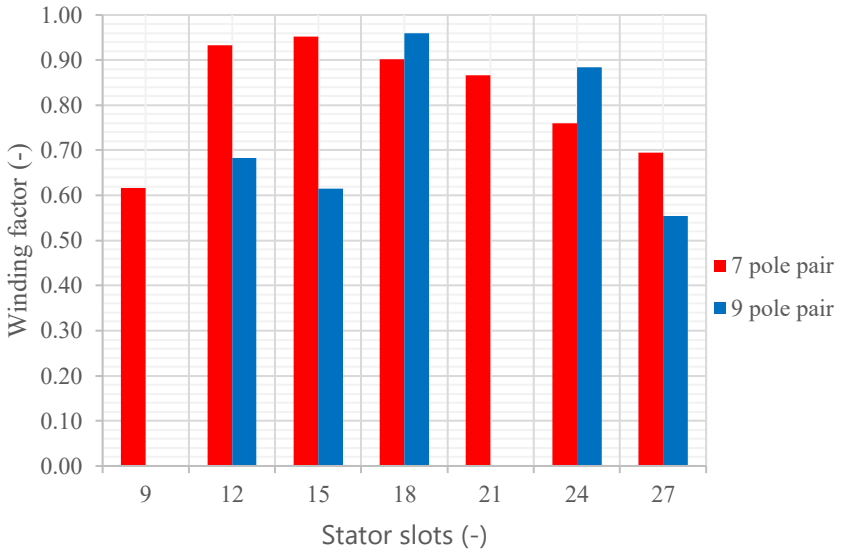

Fig. 2-12 Winding factors for 7 and 9 pole pair harmonics for double layer concentrated windings

It can be concluded that number of suitable windings for the dual rotor device is relatively limited. Generally, windings with symmetry equal to number of pole pairs of the useful space harmonic (i.e. the winding pattern repeating itself as many times as there are fundamental pole pairs) have zero winding factor for the parasitic one, unless both harmonics are direct multiple of each other. Tab. 2-1 summarizes the suitable windings for the dual rotor device with 9 pole pair magnet rotor and 16 pole pieces. The list of windings is not exhaustive, since other windings with even higher

number of slots exist. For instance, integer slot winding with 84 slots. However, increasing number of slots beyond certain value for a given stator diameter may lead to increase in slot leakage since slot circumferential width becomes similar to radial thickness of the air gap between pole piece rotor and the stator. Influence of stator leakage on performance of the dual rotor device will be discussed in one of the following chapters.

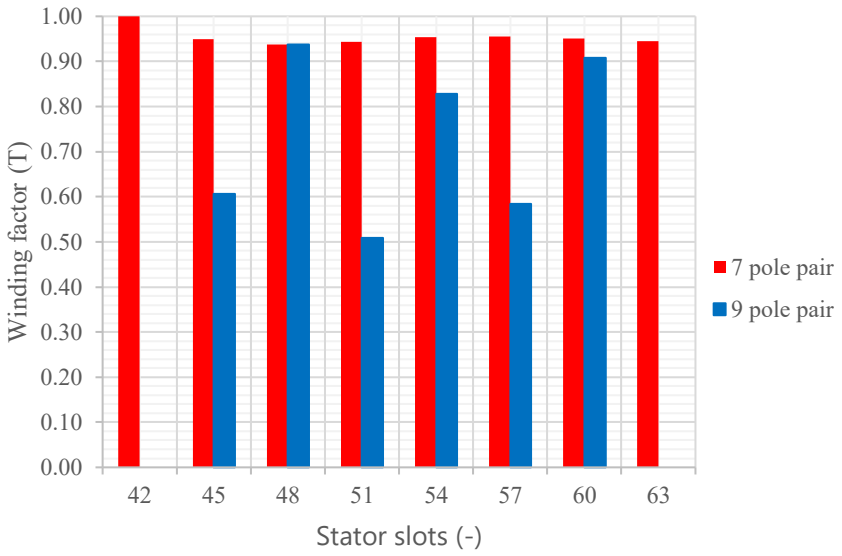

Fig. 2-13 Winding factors for 7 and 9 pole pair harmonics for double layer overlapping windings

Tab. 2-1 Suitable windings for dual rotor device with 9 pole pair magnet rotor and16 pole pieces

Slots	Type	Layers	Coil pitch	7 pp winding factor
9	Fractional slot concentrated	2	1	0.617
21	Fractional slot concentrated	2	1	0.866
42	Integer slot	1	3	1
42	Integer slot	2	2	0.866
63	Fractional slot overlapping	2	4	0.953

As an example of EMF generated at the terminals of appropriately selected winding, device shown in Fig. 2-8 was simulated by FEA at two different operating points. The device has 21 slot dual layer winding with fundamental winding factor of

0.866 which according to Fig. 2-12 has no coupling with the parasitic space harmonic. Space harmonics in the outer air gap are the same as shown in Fig. 2-5. At operating point 1 pole piece rotor rotates at 3000rpm and magnet rotor at 2000rpm. This leads to stator fundamental frequency of 500Hz while the 9-pole pair parasitic harmonic oscillates at 300Hz. It can be seen in Fig. 2-14 that EMF generated at winding terminals has negligible harmonic distortion and period of 0.002 seconds. In case of operating point 2, pole piece rotor was rotated at 2250rpm and magnet rotor at 4000rpm. In this situation, the useful space harmonic is stationary while the parasitic one rotates at the magnet rotor speed having electrical frequency of 600Hz. Despite relatively high amplitude and frequency, the parasitic harmonic does not generate significant EMF.

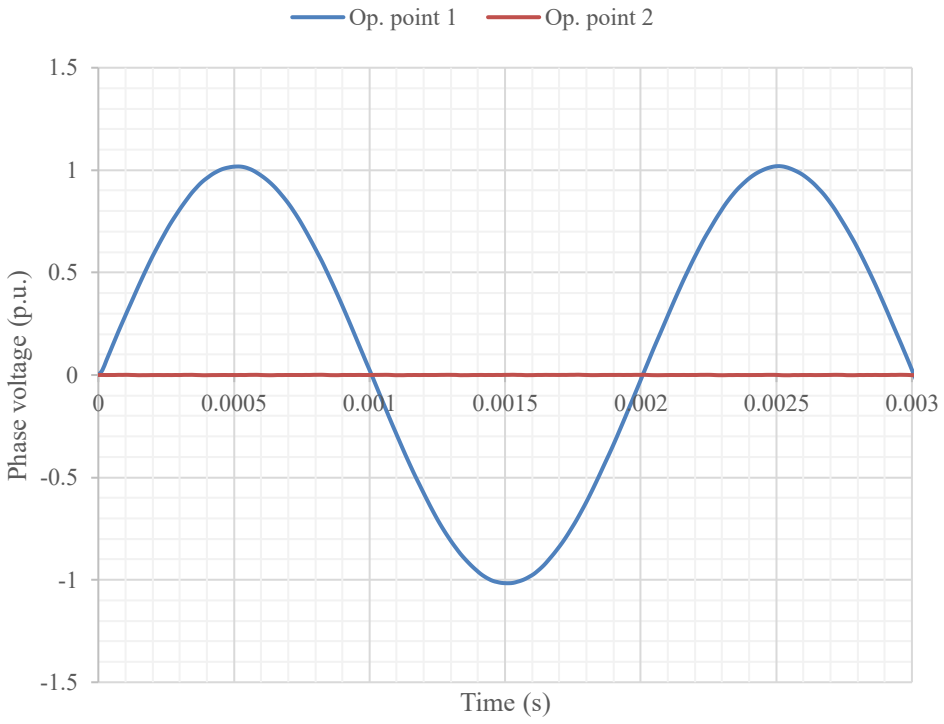

Fig. 2-14 Phase EMF of 21 slot 7 pole pair double layer winding at two operating points

Authors in [40] analysed a dual rotor device with similar topology, albeit with different number of poles and pole pieces, and came to the conclusion that EMF distortion is inherently caused by asymmetry of the device and can only be remedied by pole piece and magnet rotor skewing. However, results of the above-mentioned

analysis clearly demonstrate that sinusoidal EMF with negligible level of harmonic distortion can be achieved.

2.5.3 Paralleling of phase coils

In practice, coils belonging to a single phase are not necessarily connected in series and each phase may have a number of parallel paths. Since amplitude of EMF is proportional to the number of turns connected in series, paralleling of stator coils makes it possible to either increase number of turns per coil without increasing total phase EMF or to reduce EMF in order to match power supply with lower voltage. While paralleling of stator coils is widely adopted in industry, it could negatively affect performance of an electrical machine, since it relies on coils being physically identical (i.e. having the same impedance and conductor distribution in a slot) and being exposed to flux linkage with the same amplitude and phase. Neither of these requirements can be ensured in an industrial environment but the negative effects, usually in a form of current circulation between winding elements of unequal electric potential, tend to be negligible as authors point out in [61]. While imbalances caused by manufacturing could be neglected, the effect of parasitic space harmonic present in the dual rotor device on parallel connected winding needs to be taken into account.

As it was demonstrated in the previous section, EMF measured at the terminals of appropriately selected winding is not distorted by presence of the parasitic space harmonic. However, EMF induced in individual coils will still show signs of distortion with amplitude being a function of output rotor speed. Fig. 2-15 shows EMF of two randomly selected coils in 21 slot 7 pole pair winding obtained by FEA simulation of the same operating point as described in the previous section with frequency of 500Hz and 300Hz of the useful and parasitic harmonic respectively. It is apparent that at any given time, voltage difference between the coils exists. It is worth noting that the distortion is only observable when the output rotor is rotating.

Since coils belonging to the same phase have different potential, connecting them in parallel would lead to current circulation between them and, consequently, to increase in stator copper loss. Fig. 2-16 shows cross sectional view of two configurations of dual rotor power split device with A-phase coils, each having different number of pole pair, pole pieces and stator slots. Both machines have

double layer fractional slot concentrated winding which does not couple with the parasitic space harmonic and has fundamental winding factor of 0.866.

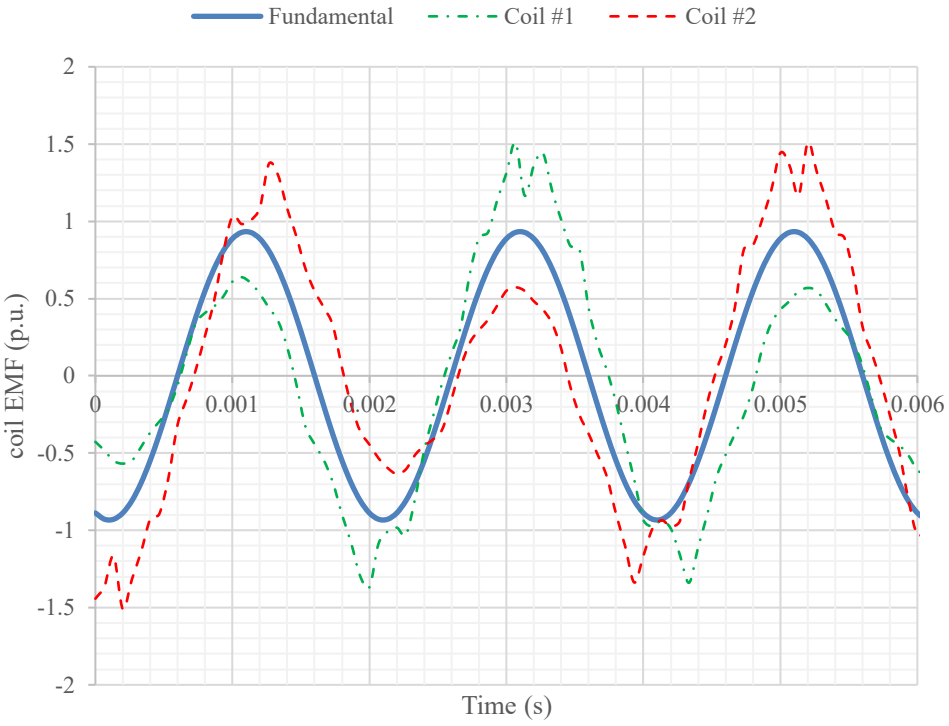

Fig. 2-15 EMF induced in individual coils by two space harmonics

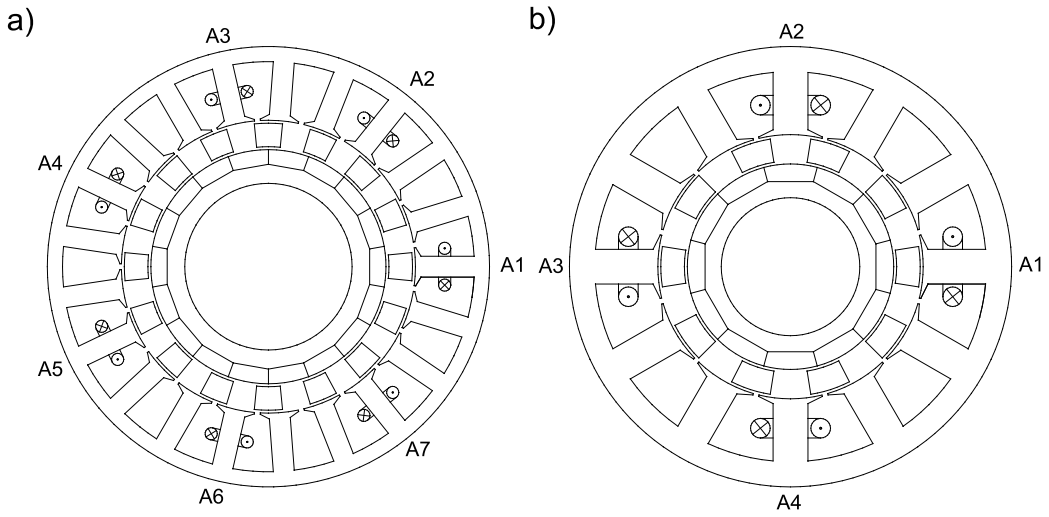

Fig. 2-16 Dual rotor device with a) 16 pole pieces, 9 pole pair magnet rotor, 7 pole pair stator b) 10 pole pieces, 6 pole pair magnet rotor, 4 pole pair stator

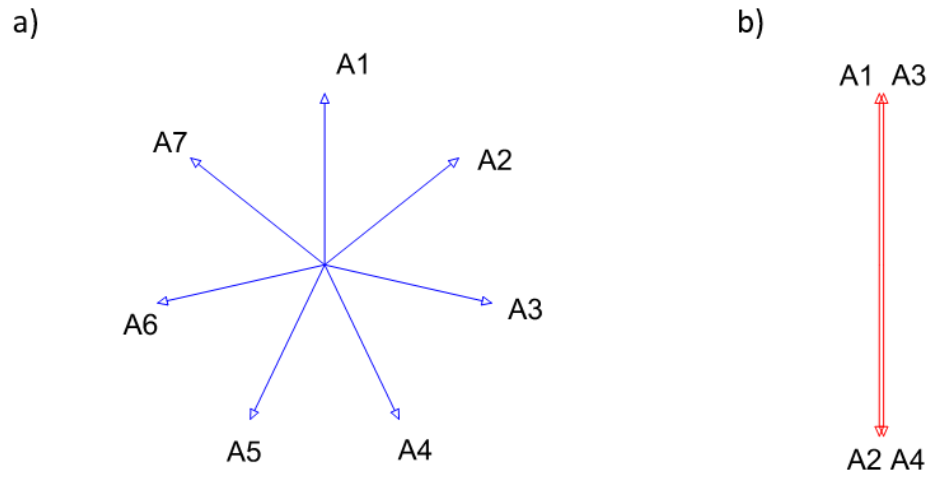

Fig. 2-17 Phasor diagrams of EM induced by the parasitic harmonic in phase coils of a) 21 slot 7 pole pair and b) 12 slot 4 pole pair winding

The machine in Fig. 2-16 a) has 9 pole pair output rotor, 16 pole pieces and 7 pole pair 21 slot stator with 7 concentrated coils per phase. EMFs induced in phase coils by the parasitic 9 pole pair field have the same amplitude but are phase shifted by 51.43 electrical degrees, as shown by phasor diagram in Fig. 2-17. It is apparent that connecting any of the coils in parallel will inevitable result in current circulation between them. However, there are configurations which allow for parallel connection such as the one in Fig. 2-16 b) which has 6 pole pair output rotor, 10 pole pieces and 4 pole pair 12 slot stator. It is apparent that symmetry between the output rotor, generating the parasitic space harmonic, and the stator winding exists. Parasitic EMFs induced in two out of four phase coils are in phase, and therefore the winding can have two parallel paths without the risk of current circulation. Phasor diagram for this configuration can be seen in Fig. 2-17 b).

2.6 Torque transmission and control of the dual rotor device

General expressions for electromagnetic torque acting on a rotor of a synchronous PM machine is given by:

$$T = \frac{3}{2} \cdot p\big((\psi_{pm} \cdot I_q + \big(L_d - L_q\big) \cdot I_q \cdot I_d\big) \qquad (2\text{-}28)$$

where ψ_{pm} is flux linkage provided by rotor magnets, L_d and L_q are *d* and *q* axis inductances respectively and I_d and I_q are *d* and *q* axis current respectively. Apart from torque created by the interaction between *q* axis current and flux linkage due to permanent magnets, equation (2-28) also contains so called reluctance torque component which only exists in machines with electromagnetically salient rotors, having different *d* and *q* axis inductance. Embedded PM rotors, for instance, are inherently salient and their ability to produce positive reluctance torque when negative, i.e. demagnetizing, *d* axis current is applied is exploited in many modern hybrid electric power trains particularly at high speed operation [17].

Similar equation can be used to express electromagnetic reaction torque produced by the stator of the dual rotor device, however, the reluctance torque component can be omitted since the difference in *d* and *q* axis inductance is negligible. This is not because the dual rotor device has surface mounted magnet rotor, any rotor topology including embedded can be used to provide excitation, but because there is no reluctance variation, created by a physical rotor, travelling at the same speed as the useful space harmonic. Neither pole piece rotor nor magnet rotor rotate at the same angular velocity as the armature reaction field. As a result of this, peak torque produced by the stator for a given current is always achieved when *d* axis current is zero, i.e. the armature reaction current is in phase with EMF, Fig. 2-18. D axis current cannot produce any reluctance torque, however, it can still be used for field weakening at high speed operation the same way it would be used in case of motor with surface mounted rotor magnets. It is worth noting at this point that definition of *d* and *q* axis is not as straightforward as in normal synchronous machine since the rotating dq reference frame is not directly associated with a physical rotor. In a normal machine, *d* axis is the middle of a physical rotor pole, however, in the dual rotor device it can only be defined as a position where flux linkage due to the useful space harmonic is at its peak or, alternatively and more practically, position where induced EMF wave crosses zero. When effect of magnetic gearing is taken into account, pole piece rotor torque can be expressed as follows:

$$T_{ppr} = \left(\frac{p_{ppr}}{p_{stat}}\right) \cdot \frac{3}{2} \cdot p_{stat} \cdot \psi_{con} \cdot I_q = \left(\frac{p_{ppr}}{p_m}\right) \cdot T_m \qquad (2\text{-}29)$$

where p_{stat} is number of stator pole pairs, ψ_{con} flux linkage due to control space harmonic, T_m is magnet rotor torque and p_m is number of magnet rotor pole pairs.

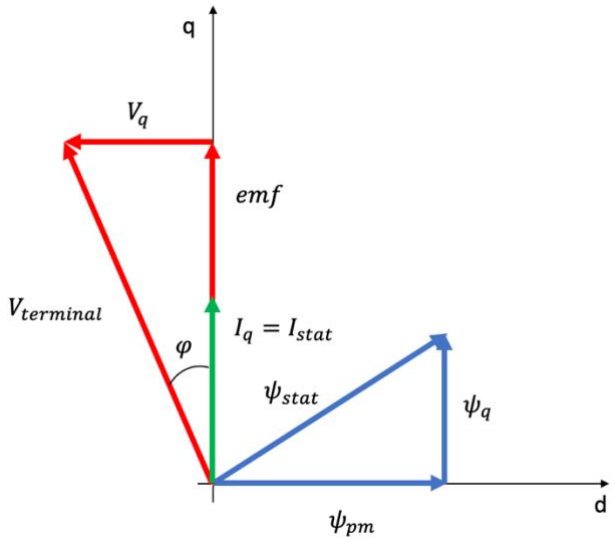

Fig. 2-18 Phasor diagram of the dual rotor device operating at Id=0 control strategy

Fig. 2-19 shows variation of torque acting on all three components of the dual rotor device as a function of internal load angle. The variation was obtained by 2D FE analysis of the device shown in

Fig. 2-8 but serves only illustrative purpose, hence the per unit notation. While the equation for the internal load angle of the dual rotor device is identical to equation (2-9) referring to a passive magnetic gear, position of the outer magnet array must be replaced by position of the armature reaction field produced by the stator. Inner rotor and stator torques are negative as they are reacting torque applied to the pole piece rotor to maintain equilibrium.

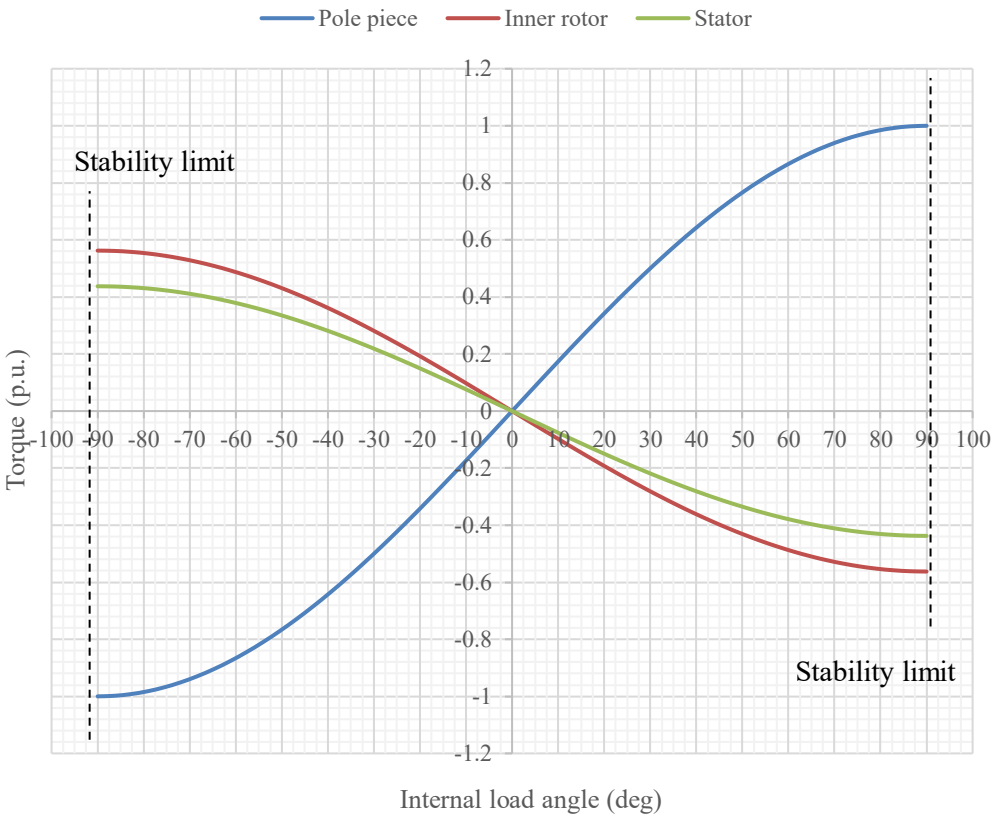

Fig. 2-19 Torque acting on each component of the dual rotor device as a function of internal load angle

Pole piece rotor torque as a function of stator MMF, assuming $\pi/2$ internal load angle, is shown in Fig. 2-20 for linear and non-linear magnetic circuit. It is apparent that the shape of the non-linear curve is influenced by saturation of the magnetic circuit at higher levels of electrical loading. Peak transmittable torque of the dual rotor device is therefore limited by three parameters. Firstly, by amplitude of the useful space harmonic in the outer air gap, secondly by achievable electrical loading of the stator windings and lastly by magnetic loading of the stator magnetic circuit. While peak and continuous transmittable torque of a passive magnetic gear are identical, peak transmittable torque of the dual rotor device may not be sustainable indefinitely due to stator heating. However, the dual rotor device can be temporarily overloaded, as long as the magnetic circuit is not already deeply saturated.

Fig. 2-21 shows spectra of outer air gap flux density at no load and when stator windings were fed with current for the device depicted in Fig. 2-16 a). While the 21-slot double layer winding only interacts with the useful 7 pole harmonic, it is

apparent that the amplitude of the parasitic 9 pole harmonic decreases slightly when electrical load is applied. This can be attributed to increase in saturation of both the stator and the pole pieces. It is also apparent that the fractional slot winding creates additional flux density harmonics in the outer air gap.

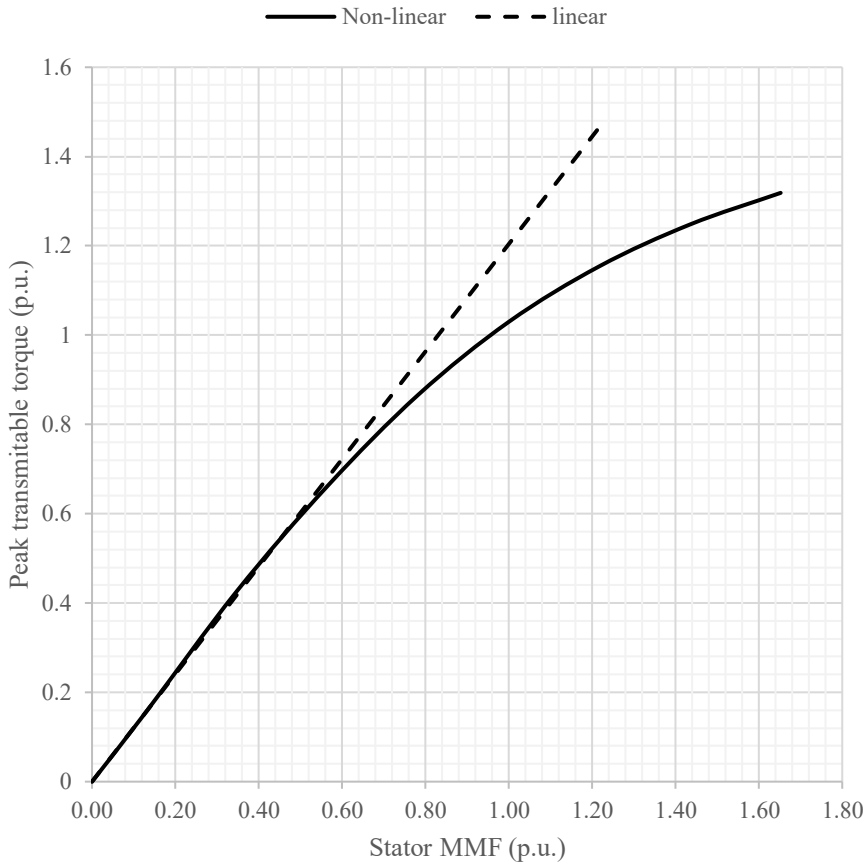

Fig. 2-20 Peak transmittable torque of a dual rotor power split device as a function of stator electrical loading with linear and non-linear magnetic circuit

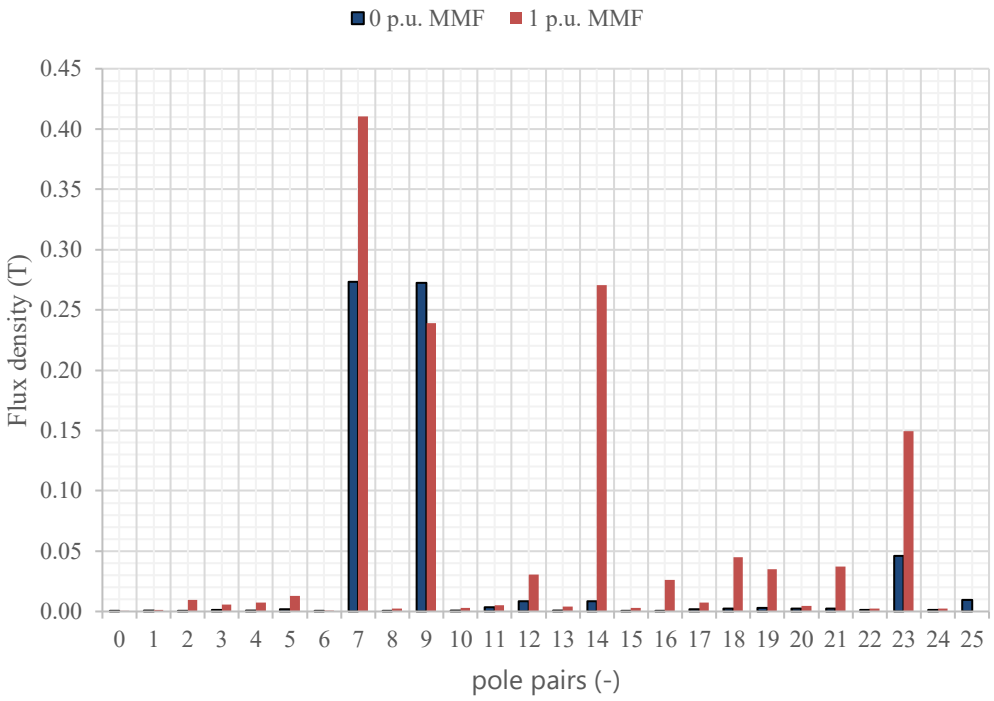

Fig. 2-21 Outer air gap flux density spectrum at 0 and 1 p.u. electrical load

2.6.1 Control of armature reaction commutation

Principally, control of the dual rotor device is identical to control of a synchronous permanent magnet machine with surface mounted magnets, where currents in stator windings are commutated in such a way that desired angle between rotor field and armature reaction is maintained. Typically, some sort of position sensor is used to provide position feedback for the AC controller although sensorless methods of position estimation exist. Since armature reaction interacts with the useful space harmonic not associated with a physical rotor its position cannot be measured by a conventional position sensor and, therefore, needs to be calculated from measured positions of pole piece and magnet rotors:

$$\vartheta_c = \frac{\left(p_{ppr} \cdot \vartheta_{ppr} - p_m \cdot \vartheta_m\right)}{\left(p_{ppr} - p_m\right)} \qquad (2\text{-}30)$$

where ϑ_c, ϑ_{ppr} and ϑ_m are angular positions of control space harmonic, pole piece rotor and inner rotor respectively.

Fig. 2-22 shows a simple schematic of the dual rotor device and its supporting electrical systems. DC/AC inverter is fed from a source of DC voltage (in a HEV represented by a battery pack) and allows for bi-directional flow of electrical power. Position of both rotors is measured and fed back to the control system of the DC/AC inverter which then estimates position of the control space harmonic and commutates phase currents accordingly.

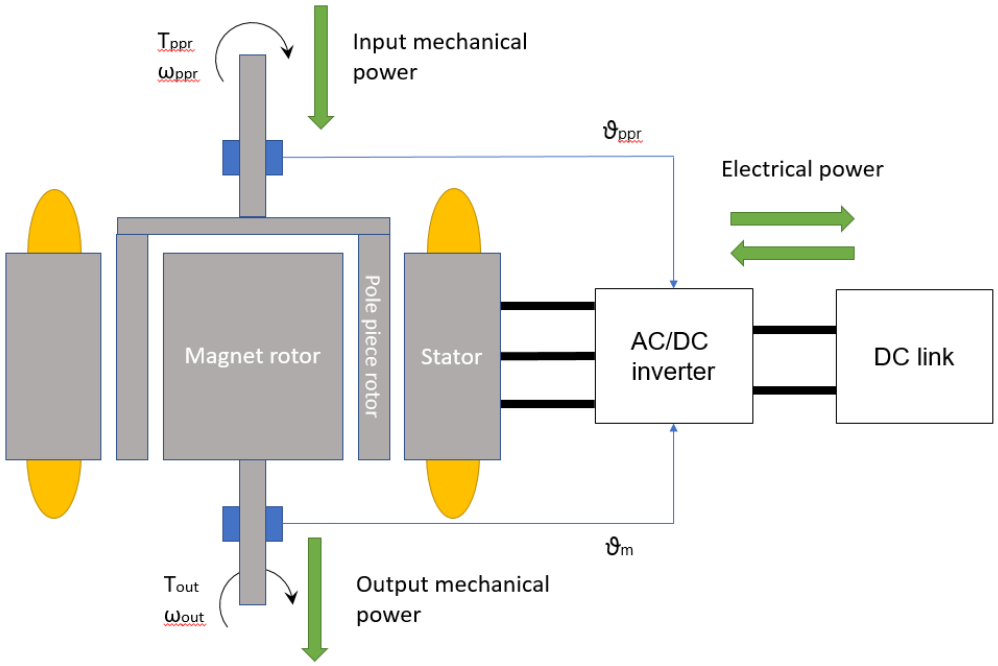

Fig. 2-22 Power flow schematic of the dual rotor device

Torque acting on all three principal components as a function of pole piece rotor angular position during steady state operation at constant load and rotor speeds can be seen in Fig. 2-23. Stator phase currents were commutated based on control harmonic position as described in the previous paragraphs. The results were obtained by time stepping FE analysis and it is apparent that torque acting on all three components is almost constant, exhibiting only low level of torque ripple. However, torque transmitted through a magnetic gear is not inherently ripple free, as pointed out in [31], rather it results from careful design and pole/pole piece selection which will be discussed in the following chapters.

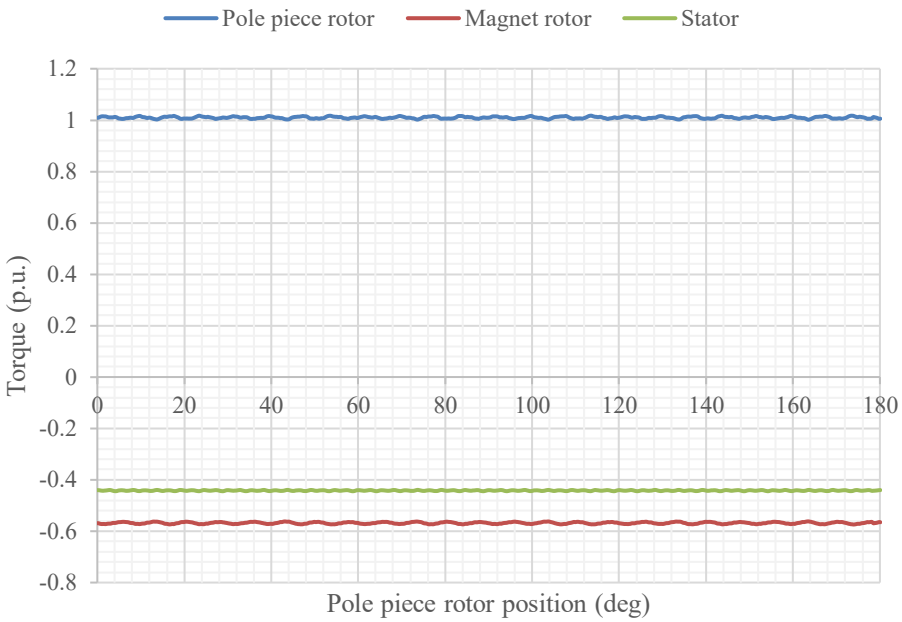

Fig. 2-23 Torque acting on all three principal components of the dual rotor device as a function of pole piece rotor position

2.7 Power flow through the dual rotor device

As it was mentioned in the section describing continuously variable operation of magnetic gears, varying speed ratio between input and output shaft of the dual rotor device also affects the flow of power since torque ratios are constant. In configuration depicted in Fig. 2-22, pole piece rotor shaft serves as mechanical input and magnet rotor shaft as mechanical output. Power balance, assuming lossless operation, is given by:

$$T_{ppr} \cdot \omega_{ppr} = T_m \cdot \omega_m + \frac{3}{2} \cdot p_{stat} \cdot \psi_{con} \cdot I_q \cdot \omega_{con} \qquad (2\text{-}31)$$

Speed of the control space harmonic for any given combination of input and output speed can be calculated as follows:

$$\omega_{con} = \frac{p_{ppr}\omega_{ppr} - p_m\omega_m}{(p_{ppr} - p_m)} \qquad (2\text{-}32)$$

Using equations (2-31) and (2-32) flow of power through the device at any operating point can be evaluated. Apart from power splitting operation where input power is split between the mechanical and electrical branches, there are three special cases where the device behaves like a motor, a generator or a fixed ratio gear.

When pole piece rotor is stationary while the output rotor is rotating, speed of the control space harmonic becomes negative and electrical energy is consumed by the stator and is converted into output mechanical energy and the device behaves like an electric motor delivering mechanical power to the output shaft. Conversely, the device behaves like an electric generator when the output rotor is stationary since all input mechanical energy is converted into electrical energy. The line of zero control speed/stator frequency is the line where transition between electrical power generation and consumption occurs. When the dual rotor device operates at the line of zero control speed, all mechanical input power is transmitted to the output shaft, the stator windings are fed by DC current and the device effectively behaves like a passive magnetic gear with fixed gear ratio.

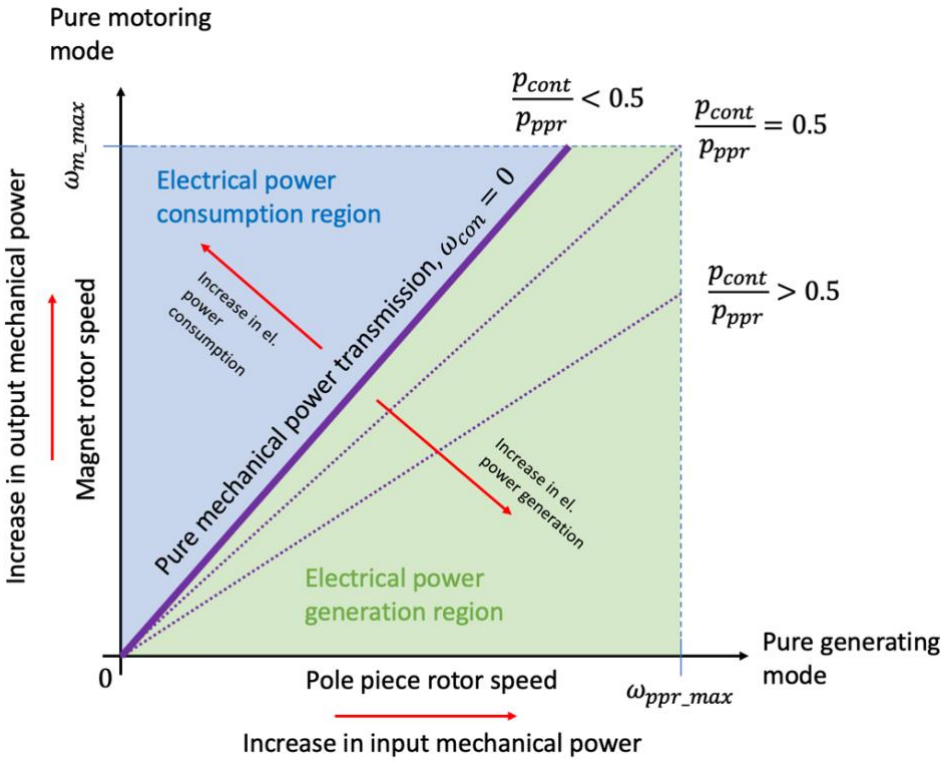

Fig. 2-24 Power flow map of the dual rotor device at constant input torque

Fig. 2-24 shows a two-dimensional map of all achievable combinations of input and output speed bounded by maximum allowable speed of each rotor. Each point on the map relates to a combination of input and output speed and it corresponds to a specific control space harmonic speed as per equation (2-32). The control space harmonic speed could be positive, negative or zero which in combination with unidirectional stator torque (assuming the torque applied to the pole piece rotor shaft by the ICE can have only one direction) divides the map into two regions according to direction of the electrical power flow. The line of zero stator frequency (and zero stator electrical power) is defined by the specific choice of number of pole pieces and magnet rotor poles. Three different lines of zero control speed (purple solid and dotted lines) for different ratios of pole piece and magnet rotor pole numbers are shown. It is apparent that choice of number of pole pieces and magnet rotor pole pairs affects the split of power between electrical and mechanical output for a given combination of input and output speed, hence the choice of configuration plays important role when designing the overall system with the dual rotor device.

2.8 Conclusion

In summary, this chapter discusses fundamental principles of magnetic gearing and their application in the dual rotor power split device. Theoretical analysis as well as FEA simulation indicate that interaction between permanent magnet magnetic field and an array of ferromagnetic pole pieces results in two dominant space harmonics in the outer air gap of the dual rotor device. Stator of the device is directly coupled to one of the space harmonics and controls flow of power through the device as well as speed ratio between input and output shaft.

Presence of two dominant space harmonics in the outer air gap has significant influence on stator winding selection. It is demonstrated on an example of dual rotor device with 9 pole pair magnet rotor and 16 pole pieces that a number of suitable windings, i.e. windings with no coupling to the parasitic space harmonic, is relatively limited. Selecting winding only on the basis of fundamental winding factor and its

multiples may result in EMF distortion and torque ripple. Winding factor calculation method based on harmonic analysis of winding function is used.

Additionally, presence of the parasitic space harmonic must be considered when connecting phase coils in parallel since difference in induced emfs between them will result in current circulation. Series connection with no parallel paths effectively eliminates potential current circulation, however, parallel connection is possible if symmetry between the parasitic harmonic and the stator winding exists.

It was shown that torques acting on all three principal components of the dual rotor device vary sinusoidally with internal load angle. Peak transmittable torque for a given electrical loading is reached when internal load angle equals $\pi/2$. Relationship between peak transmittable torque and electrical loading of the stator is influenced by non-linearity of the magnetic circuit and may limit overload capability of the device. Commutation of stator currents is controlled based on position of the control space harmonic which must be estimated from measured position of input and output shafts. Appropriate winding selection and correct commutation results in smooth torque transmission between shafts.

Speed of the control space harmonic, and consequently stator electrical frequency, controls the power flow through the device. The line of zero stator frequency divides the operating space into regions of electrical power consumption and generation. Operating the device along the line of zero stator frequency results in pure mechanical power transmission. Two extreme conditions are when the device behaves like an electrical motor of generator, i.e. it either purely converts electrical power into mechanical or vice versa.

Chapter 3 Configuration selection and electromagnetic design

3.1 Introduction

Reasons for electrification of automotive drivetrains together with the role of the magnetically geared dual rotor device in power split hybrid drivetrain was described in chapter 1 while principle of operation of the device was the focal point of chapter 2. This chapter discuses selection of a suitable configuration for a given application and presents methods for estimating the main dimensions of each principal component of the device with goal of maximizing transmittable torque density for the given space envelope defined by the target application.

The choice of configuration is limited by external factors imposed by the wider system in which the device is to be integrated as well as internal effects inherent to the device, such as unbalanced pull arising due to possible asymmetry between the components. Despite the fact that the proposed device has two rotating components, both input and output shaft, many of the techniques and methods used in conventional PM traction motor design could be used with slight modifications to account for magnetic gearing effects.

Similarities and differences in sizing of the magnetic circuit between the proposed device and conventional PM synchronous machines are discussed in detail and applied to design for the specific application. While the importance of mechanical and thermal considerations in design of all components is acknowledged, the Chapter is primarily focused on electromagnetic performance.

3.2 Application and initial design choices

As discussed in Chapter 1 and 2, primary application of the proposed device is in hybridisation of passenger or commercial vehicles. One of the main outcomes of the research presented in this thesis was to design, build and validate a full-scale proof of concept of the device which could be integrated into a power split hybrid drivetrain of a mid-sized passenger vehicle. In this type of application, the device will be directly attached to the engines bell housing on the power input side and to the MG2 on the power output side, replacing a mechanical planetary gear set and MG1. Schematic of this particular system arrangement can be seen in Fig. 3-1.

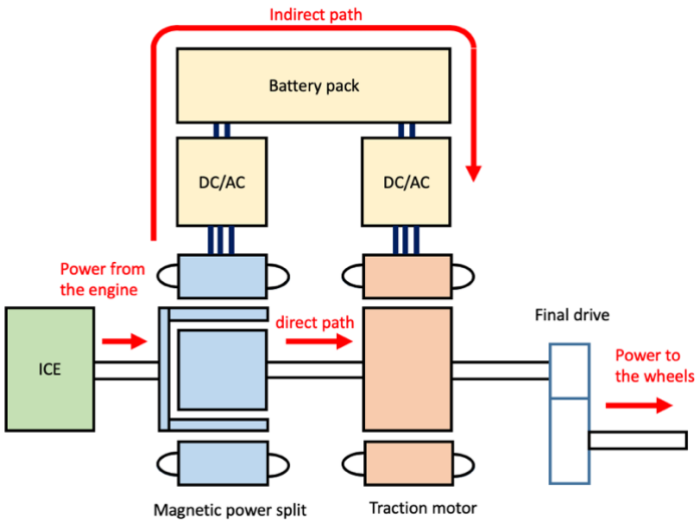

Fig. 3-1 Hybrid drivetrain with the dual rotor magnetic power split device

Although the prototype was only going to be designed for test bench validation and was not intended for integration with a real drivetrain system, elements of the real system were used to define realistic design targets and space envelope constraints for the prototype. The source of input power is gasoline internal combustion engine, performance parameters of which could be found in Tab. 3-1, which defines the torque rating of the device. The engine reaches its maximum power of 115kW at 6000rpm, however, in the target application the maximum speed was limited to 4000rpm and to output power of 75kW. The existing bell housing of the engine and the need for liquid cooling jacket restricts the available outer diameter for the stator lamination to 300mm. The axial length of the lamination stack is

restricted by the fact that the engine is mounted in transversal orientation and hence the ICE together with the power split device needs to fit within the available width of the engine bay. The packaging arrangement would be similar to that of the MG1 and planetary gearset in Toyota synergy drive. Maximum fundamental frequency of the stator was defined assuming standard state of the art automotive inverter with silicone-based power devices. In a real system both the power split device and MG2 (and possibly their inverters) would share the same liquid cooling circuit with 65^{0}C coolant temperature, having cooling jackets on the outer diameter of stators. Summary of design targets and constrains for the device can be seen in Tab. 3-2.

Tab. 3-1 Engine parameters

Fuel type	Gasoline
Combustion method	Atkinson cycle
Engine/drivetrain orientation	Transversal
Engine displacement (l)	2.0
Peak power (kW)	75
Peak torque (Nm)	180
Speed at peak power (rpm)	4000
Cooling type	Liquid

Tab. 3-2 Space envelope and design targets for the dual rotor device

Stator lamination outer diameter (mm)	300
Stack axial length (mm)	50
Peak input torque (Nm)	180
Max input speed (rpm)	4000
Max output speed (rpm)	4000
Cooling type	Liquid
Coolant temperature (°C)	65
Max fundamental frequency (Hz)	1200
DC link voltage (V)	650

Limitation of available slot and stator pole combinations for the dual rotor device was discussed in the second chapter and it was concluded that there are relatively

few viable options. However, some feasible options for both overlapping distributed and concentrated non-overlapping windings exist. Distributed windings tend to produce less MMF harmonics and, depending on coil pitch, could have higher winding factor. However, coil overhang length tends to be longer and such winding could be less efficient due to copper loss in the passive overhang portion of coils. Given the design target space envelope resulting in axially short machine, fractional slot concentrated winding with 0.5 slot per pole and phase was selected so as to achieve short overall axial length of the machine. Additionally, open slot stator was chosen as inserting coils pre-wound on bobbins into the stator slots is a technique commonly used in mass production of hybrid automotive traction motors.

Figures in the previous chapter show the dual rotor device with magnet rotor having surface mounted magnets. While this rotor configuration is feasible and some design implications of such choice will be briefly discussed, rotor with embedded magnets with V-shape arrangement was chosen for the prototype as the magnets are naturally retained by the lamination and don't need to be supported by retaining sleeve as in case of surface mounted magnets. In addition, embedded rotor construction is more common in mass manufactured automotive PM traction machines. In case of rotors with V shaped embedded magnets, additional goal of the rotor design could be to increase saliency, however, as it was pointed out in the previous chapter, saliency of the magnet rotor does not result in reluctance torque production by the dual rotor device, hence this consideration can be ignored. However, flux focusing of the V arrangement could be utilized to boost the rotor magnetic loading.

The dual rotor device has two air gaps, both of which were chosen to be 1mm and all three principal components will be made of laminated stack comprising of standard M270-35A electrical steel material. Neodymium-Iron-boron permanent magnets of N48SH grade, BH curves of which can be seen in Fig. 3-24, were chosen for the magnet rotor.

3.3 Configuration selection

3.3.1 Choice of intrinsic gear ratio

As it was explained in the section discussing the principle of operation, choice of magnet rotor poles and number of pole pieces defines the gear ratio of the dual rotor device and this is fixed for a given combination hence the term intrinsic gear ratio can be used. For a constant input power from the engine, devices with different intrinsic ratios will have different ratios of power going through the direct and the indirect power flow path, hence the choice of intrinsic ratio for the device is closely linked with the drivetrain system design, taking into account requirements on overall system efficiency (fuel consumption) and vehicle dynamics (acceleration targets, gradeability, top speed etc.). From the component point of view, intrinsic gear ratio defines where the line of zero stator fundamental frequency is on the operating speed map of the device, Fig. 3-2, and whether it is consuming or generating electrical power at a given combination of input and output rotor speed, Fig. 2-22. When the device is operated near the line of zero stator frequency, all the frequency dependent loss mechanisms, such as stator iron loss and AC copper loss, are minimized and the total loss is only dominated by DC copper loss, hence the region around the line of zero stator frequency represents the region with the lowest loss for the device at any given load. On the other hand, the highest fundamental frequency is reached in the corner points of the operating map. Both high and low fundamental frequency areas are visualized in Fig. 3-2 by means of colour shading where colour red represents high and colour green low value of frequency. It is apparent that operating the device in the region with the lowest loss could be beneficial for the overall system efficiency. Efficiency and all relevant loss mechanisms present in the device are discussed in detail in Chapter 5 but these top-level considerations are mentioned here in order to highlight what could drive the choice of optimal gear ratio.

While system level design and its influence on the device are outside of scope of this thesis, system level design of the hybrid drivetrain shown in Fig. 3-1. was performed under technology strategy board funded collaborative R&D project called MAGSPLIT where one of the partners, Romax technology, performed system optimisation and the results were fed into the design specification for the prototype

dual rotor device. As mentioned in Chapter 2, gear ratio of a magnetic gear can be defined in two different ways. The following discussion will use ratio of poles of the control space harmonic to number of pole pieces. The system analysis determined that the range of intrinsic gear ratios suitable for the target application is 0.4 – 0.45

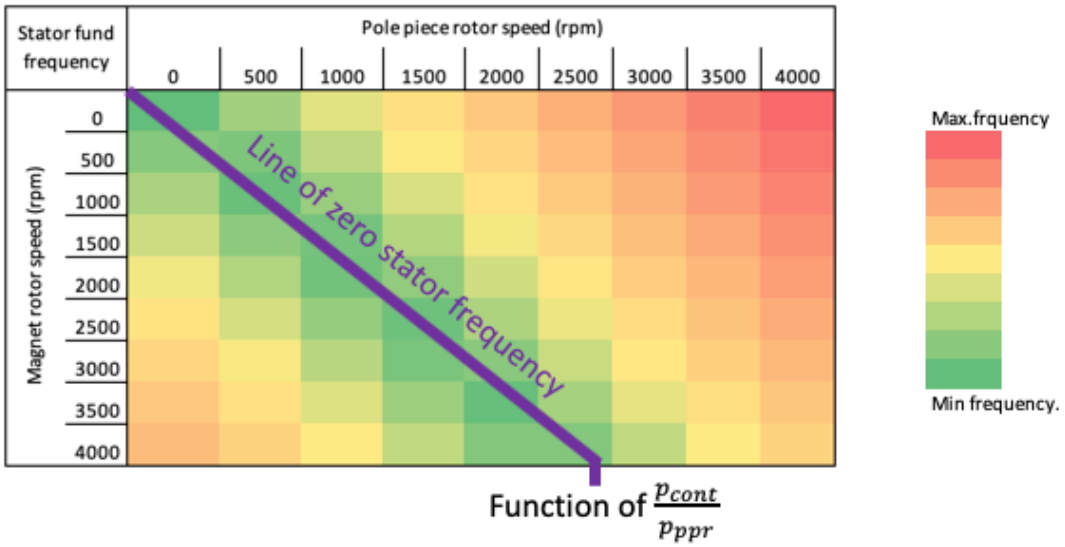

Fig. 3-2 Impact of intrinsic ratio selection on the position of line of zero stator frequency

3.3.2 Limitation by maximal stator frequency

As it was shown in the previous chapter, angular velocity of the useful space harmonic coupled to the stator winding is a function of speed of both rotors according to the theory explained in Chapter 2. Since commutation of the stator windings must be synchronised with speed of the useful control space harmonic, frequency limitation of the inverter supplying the windings must be taken into account. Generally, high stator frequencies are reached when the speed difference between the input and the output shaft is high, i.e. when one of the shafts is stationary while the other is rotating at maximum speed. Fundamental stator frequency is given by:

$$f_{stat} = \frac{\left(\omega_{ppr} \cdot p_{ppr} - \omega_{pm} \cdot p_{pm}\right)}{2 \cdot \pi} \qquad (3\text{-}1)$$

Based on the required intrinsic gear ratio, number of pole pieces is higher than the number of magnet rotor pole pairs and since maximum speed of both rotors is identical (Tab. 3-1) the highest stator frequency will be reached at maximum pole piece rotor speed and zero magnet rotor speed. Maximum stator frequency is therefore only function of number of pole pieces and maximal pole piece rotor speed.

$$f_{stat\_max} = \frac{\omega_{ppr\_max} \cdot p_{ppr}}{2 \cdot \pi} \qquad (3\text{-}2)$$

Given the limitation of 1200Hz and the maximum pole piece rotor speed of 4000rpm, it is apparent that the maximum allowable number of pole pieces is 16. All possible configurations satisfying the limitation of maximum fundamental frequency are summarized in Fig. 3-3 where each point in the graph represents a single discreet configuration. The dashed lines in the figure show the upper and lower boundary for the required intrinsic ratio.

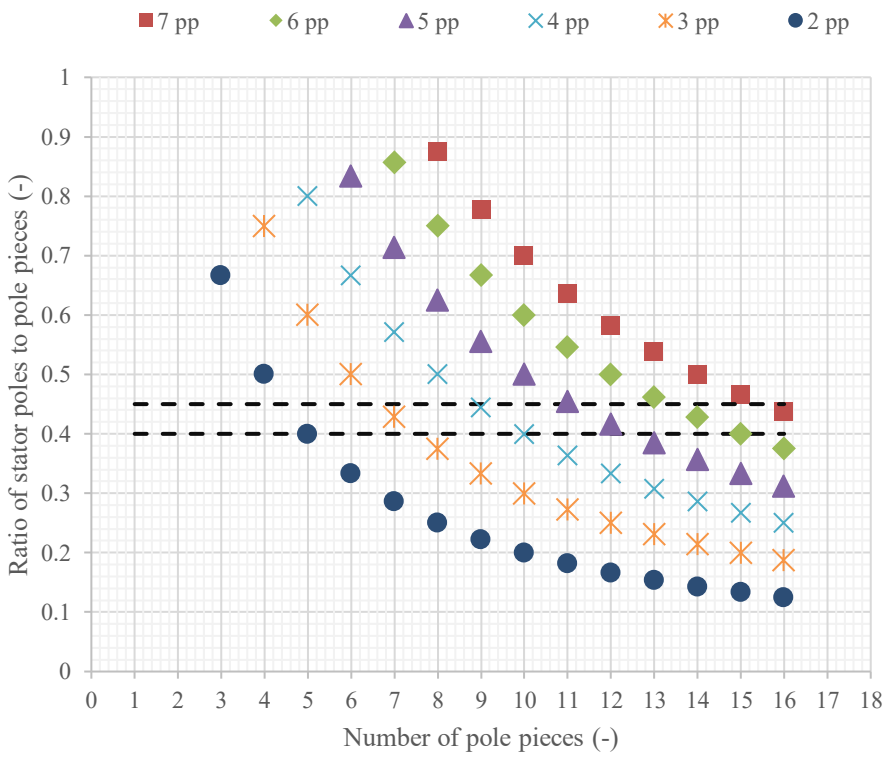

Fig. 3-3 Configurations satisfying the limit of maximal stator fundamental frequency and the boundaries of required intrinsic gearing ratio

3.3.3 Limitation by unbalanced magnetic pull

Magnetic fields present in air gaps of rotating electrical machines create both radial and circumferential forces. While the circumferential forces manifest themselves as useful torque, radial forces cancel out as long as magnetic symmetry within the machine exists and there are no winding faults. Magnetic asymmetry is often introduced by manufacturing imperfections such as static or dynamic rotor eccentricity, however, some machines with fractional slot windings are inherently asymmetrical even when the rotor is perfectly centred in the stator bore. In such machines, the resultant radial force (often called unbalanced magnetic pull) is not zero and acts as an extra load on the rotor bearings reducing their life span [62]. Example of an electrical machine with inherent unbalanced magnetic pull is a machine with 9 slot stator and 4 pole pair rotor where asymmetry between rotor poles and stator slots is apparent.

Similar problem could occur in magnetic gears, where asymmetry may exist between either of the magnet arrays and pole pieces. The authors in [31] comprehensively discuss the phenomenon of unbalanced pull in magnetic gears and propose method of determining whether a particular gear configuration will be prone to UMP. It is concluded that every magnetic gear will either manifest UMP or cogging torque, hence the authors suggest selecting configurations without UMP and reducing the cogging torque by means of rotor skewing. The method of determining possibility of UMP in a magnetic gear is based on evaluation of so-called symmetry factor which is given as a greatest common denominator between number of pole pairs of either of the magnet arrays and number of pole pieces. Configurations where the symmetry factor has value equal or larger than 2 do not generate UMP while symmetry factor of 1 indicates asymmetry. The method is, however, not limited to magnetic gears and can be used in any situation where symmetry between an array of magnetic poles and a salient structure with variable reluctance needs to be evaluated.

When analysing a PM motor, having one rotor magnetizing the air gap and a slotted stator, only one symmetry factor exists. There are two magnet arrays and one salient pole piece structure in a magnetic gear, hence two symmetry factors could be calculated. However, as pointed out in [31], both give the same value. In order to

determine symmetries between the three principle components of the dual rotor device, four symmetry factors can be defined since there are two dominant space harmonics and two salient structures (pole pieces, stator slots):

$$x_{s1} = \gcd(2p_{stat}, N_{slots}) \quad (3\text{-}3)$$

$$x_{s2} = \gcd(p_{ppr}, 2p_m) \quad (3\text{-}4)$$

$$x_{s3} = \gcd(2p_m, N_{slots}) \quad (3\text{-}5)$$

$$x_{s4} = \gcd(2p_{stat}, p_{ppr}) \quad (3\text{-}6)$$

The first symmetry factor, x_{s1}, evaluates the symmetry between the useful space harmonic in the outer air gap and the stator slots. As it was discussed in the previous chapter, distributed windings with integer number of slots per pole and phase and concentrated with 0.5 slots per pole and phase have high winding factor for the useful space harmonic and do not couple with the parasitic one. In addition, they are inherently symmetrical and do not produce UMP. If the stator slot selection is limited to these two types of windings, the x_{s1} can be ignored. Both x_{s2} and x_{s4} evaluate the symmetry of the gear element of the dual rotor device and give the same value. Symmetry between the parasitic harmonic (or the magnet rotor) and the stator slots is given by x_{s3}. It is apparent that out of the four symmetry factors which can be defined, one can be ignored due to winding choice and two give identical result hence only two, x_{s2} and x_{s3}, are essential to identify configurations with UMP.

It is worth mentioning at this point that local radial force density in the air gap of an electrical machine is a function of square of radial flux density as can be seen in the following equation:

$$f_r = \frac{B_r^2}{2 \cdot \mu_0} \quad (3\text{-}7)$$

Consequently, space harmonics in the outer air gap (Fig. 2-3), having much smaller amplitude than the harmonic in the inner air gap (Fig. 2-5), will create unbalanced force with smaller amplitude.

Tab. 3-3 Four configurations illustrating different symmetries

	Selected configurations			
	A	**B**	**C**	**D**
Stator pp, p_{stat}	7	5	6	7
Pole pieces, p_{ppr}	16	12	13	15
Magnet rotor pp, p_m	9	7	7	8
Stator slots, N_{slots}	21	15	18	21
Gear ratio	0.44	0.42	0.46	0.47
$x_{s1} = \gcd(2 \cdot p_{stat}, N_{slots})$	7	5	6	7
$x_{s2} = \gcd(p_{ppr}, 2 \cdot p_m) = x_{s4}$	2	2	1	1
$x_{s3} = \gcd(2 \cdot p_m, N_{slots})$	3	1	2	1
PPR force (N/m)	26	302	14656	11918
Mag. rotor force (N/m)	27	647	5916	4964

All possible dual rotor device configurations can be separated into four different categories on the basis of the two essential symmetry factors as can be seen in Tab. 2-1. The table contains four examples of configurations having different levels of symmetry and also values of resultant radial force per unit length acting on pole piece and magnet rotors obtained by FEA simulation. In the simulation, main dimensions and material properties were identical for all configurations and in line with the requirements defined at the beginning of the chapter. In configuration **A** all principal components are symmetrical and the device is completely free of UMP, however, it will likely exhibit cogging torque. In configuration **B**, asymmetry between magnet rotor (and its associated outer air gap space harmonic) and stator slots exists and consequently the resultant radial force is not zero. However, because amplitude of the parasitic space harmonic in the outer air gap is relatively small, the resultant UMP is small as well. While care must be paid to the UMP while designing bearings for the configuration **B**, it will unlikely cause any major problems. Both configuration **C** and **D** have asymmetry between the magnet rotor and the pole pieces creating considerable UMP. This is due to the fact that the magnet rotor creates flux density space harmonic in the inner air gap with large amplitude. Assuming 50 mm

stack length, unbalanced force acting on the pole piece rotor of configuration **C** exceeds 700N.

All configurations with 0.5 slots per pole and phase, having between 2 and 7 stator pole pairs and between 3 and 16 pole pieces are summarized in Fig. 3-4 according to how much unbalanced pull they are likely to produce. Green circles denote configurations free of UMP while configurations with orange/yellow square are expected to have manageable levels of UMP. Configurations marked by red triangle will likely have very high UMP and shall be avoided.

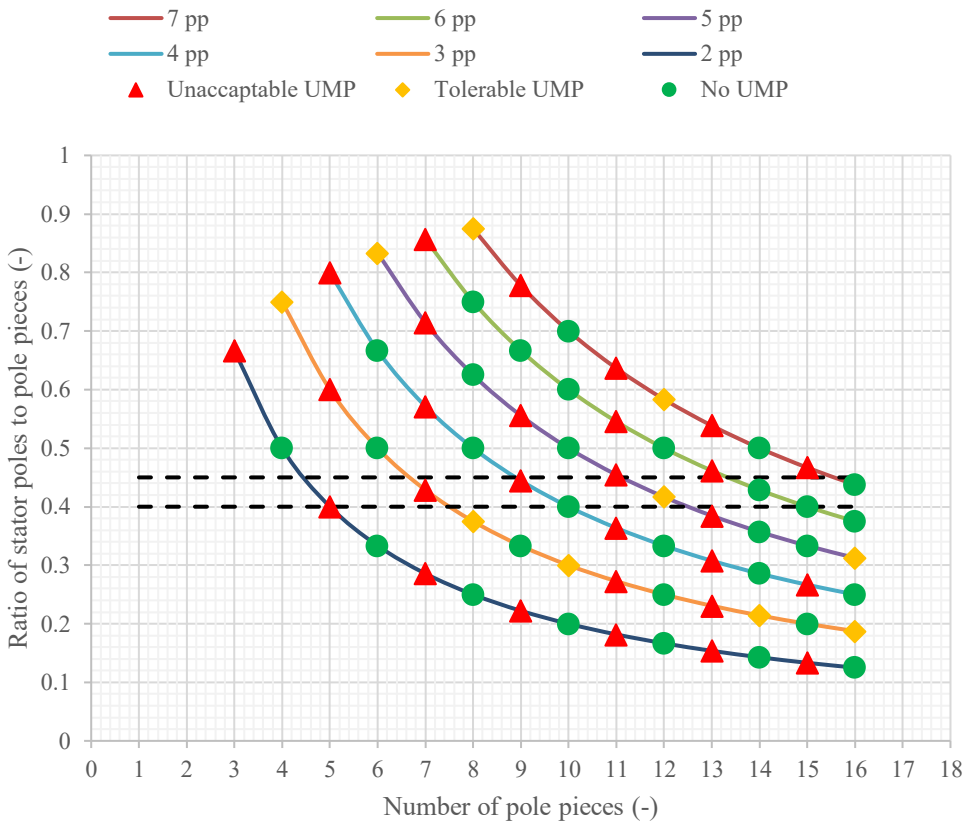

Fig. 3-4 Traffic light UMP scorring of configurations having fractional slot winding with 0.5 slot per pole and phase

It is important to mention that, in the figure, each triangle, dot or square is a discreet configuration, and some are joined by coloured lines in order to highlight that they have the same number of stator pole pairs. The lines should not be viewed as design continuum and it is not possible to pick a configuration with 11.5 pole pieces for instance.

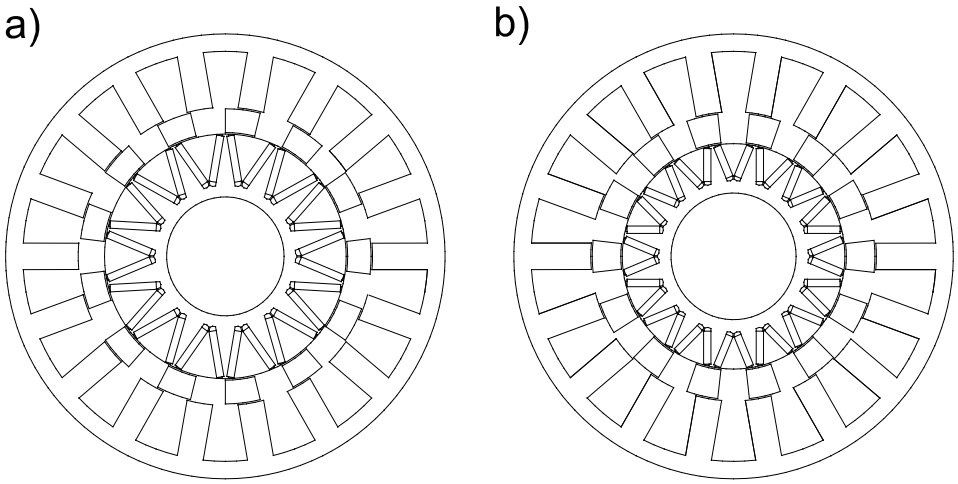

Fig. 3-5 Dual rotor device configurations with a) and without b) unbalanced magnetic pull

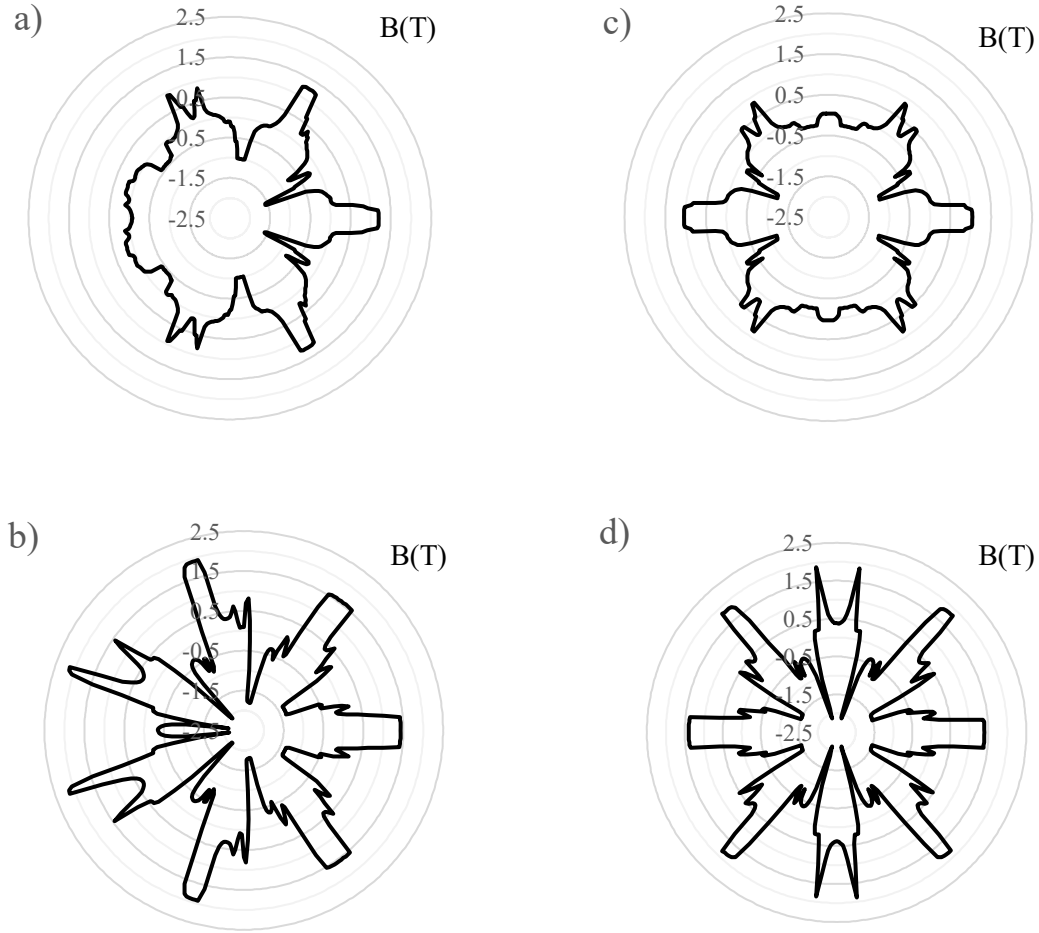

Fig. 3-6 Radial air gap flux density a) Inner air gap flux density of configuration from Fig.3-5 a) b) Outer air gap flux density of configuration from Fig.3-5 a) c) Inner air gap flux density of configuration from Fig.3-5 b) d) Outer air gap flux density of configuration from Fig.3-5 b)

It is apparent that configurations with even number of pole pieces are either completely free of UMP or have small amount of unbalanced force due to stator slotting. On the other hand, a choice of pole piece rotor will 3, 5, 7, 11 or 13 pole pieces with always result in very high UMP. Additionally, two dashed lines in the figure show the upper and lower limit of the required ratio of stator poles to pole pieces. It is apparent that there are only few configurations, with high number of stator pole pairs, within the boundaries of the required ratio.

To illustrate the asymmetry present in some configurations, flux density distribution in both air gaps of two different machines was calculated using FEA. Both machines have the same 6 pole pair stator with 18 slots while the first one has 7 pole pair magnet rotor and 13 pole pieces, Fig. 3-5 a), and the second one 8 pole pair magnet rotor and 14 pole pieces, Fig. 3-5 b). While the second machine is completely symmetrical, the first one has asymmetry between the magnet rotor and the pole pieces resulting in asymmetrical flux density distribution which is particularly obvious in the outer air gap, as can be seen in Fig. 3-6 b). Equation (3-7) can be directly used to evaluate the force density distribution and its integral will give the value of unbalanced force acting on each rotor.

Distributed windings, having integer number of slots per pole and phase, can be analysed using the same principles as described above and results of such analysis can be seen in Fig. 3-7. It is apparent that there is larger number of configurations free of UMP when integer slot stator is used. This is due to the fact that integer slot stators are always symmetrical with magnet rotors and consequently the symmetry factor x_{s3} is always larger than 1. Configuration **B** from Tab. 3-3 shows small level of UMP with fractional slot stator, however, the same machine with integer slot winding would be completely symmetrical. Generally, choosing even number of pole pieces guarantees machine without unbalanced force.

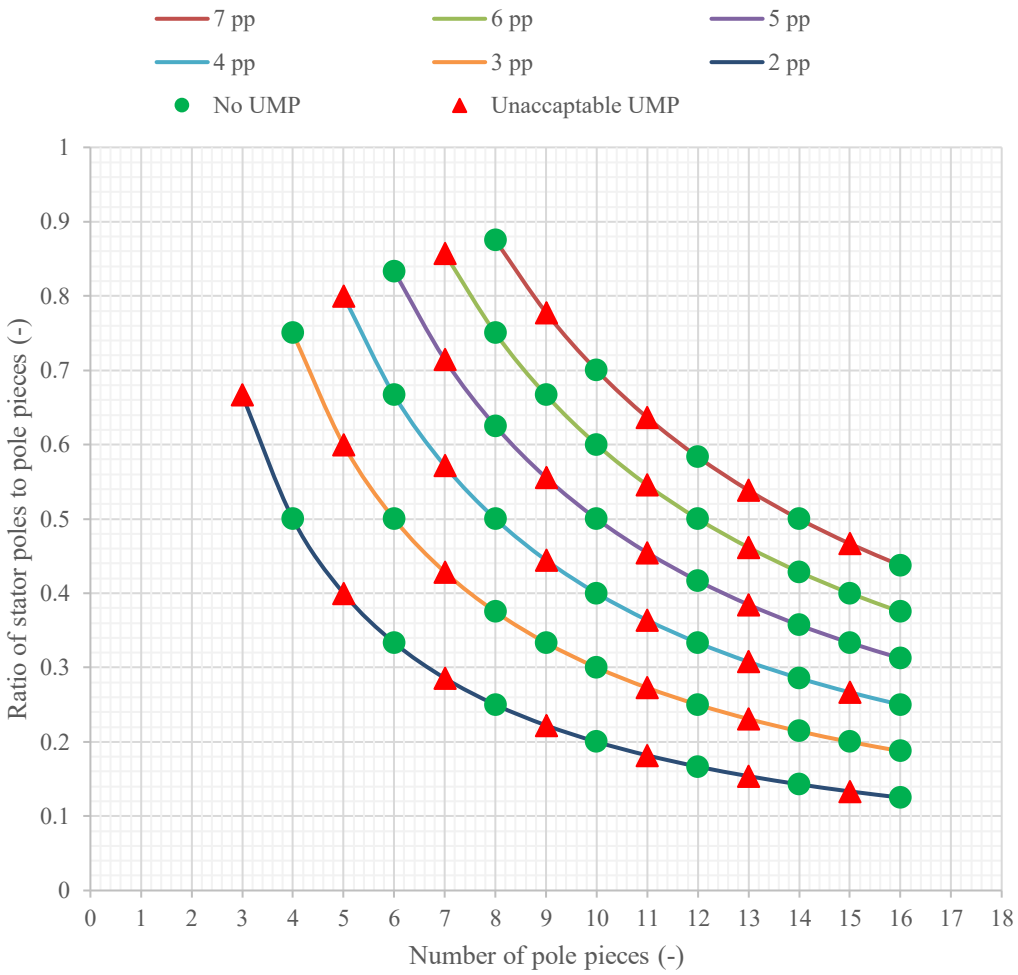

Fig. 3-7 Traffic light UMP scorring of configurations having distributed winding with 1 slot per pole and phase

It can be concluded that while configurations with high unbalanced magnetic pull can be constructed and would be functional, they would likely suffer from noise and the additional load imposed on bearings could lead to their premature failure. It is therefore important to identify such combinations and avoid them if possible.

3.3.4 Limitation by cogging torque

Another aspect which could pose a limit to what configurations are suitable for a particular application is cogging torque, i.e. no-load torque ripple created by the interaction between air gap flux density harmonics and magnetically salient structures of the magnetic circuit. As mentioned previously and pointed out in [31], cogging torque in magnetic gears is closely related to UMP and a magnetic gear will

either have UMP or cogging torque. The symmetry factors defined in the previous section can be used in order to assess whether a particular configuration is prone to produce high cogging torque, although the factors will not indicate an exact amplitude of the torque ripples.

Tab. 3-4 Four configurations with different symmetry factors and cogging torque amplitudes

Configuration	**A**	**B**	**C**	**D**
Stator pp, p_{stat}	7	4	6	6
Pole pieces, p_{ppr}	16	10	14	15
Magnet rotor pp, p_m	9	6	8	9
Stator slots, N_{slots}	21	12	18	18
Gear ratio	0.44	0.42	0.43	0.4
$x_{s1} = \gcd(2 \cdot p_{stat}, N_{slots})$	7	4	6	6
$x_{s2} = \gcd(p_{ppr}, 2 \cdot p_m) = x_{s4}$	2	2	2	3
$x_{s3} = \gcd(2 \cdot p_m, N_{slots})$	3	12	2	18
Peak PPR no load torque (Nm)	0.4	5.2	2.15	5.4
Peak mag. rotor no load torque (Nm)	0.35	13.35	1.75	12.8

If one of the symmetry factors equals 1 it means that an asymmetry within the device exists and this will lead to unbalanced pull. If all symmetry factors are equal or larger than 2 then the device will not suffer from unbalanced pull but will produce cogging torque. Generally, the larger the symmetry factors are the higher the amplitude of the cogging torque. Consequently, optimal configurations from both UMP and cogging torque point of view are the configurations where all symmetry factors are equal or close to 2.

Referring back to Fig. 3-4, it is apparent that there are four configurations which fall within the boundaries of required intrinsic gear ratio and which do not exhibit UMP. These for configurations are summarized in Tab. 3-4 together with their symmetry factors and peak values of cogging torque on both rotors obtained from FE simulation. In the simulation, main dimensions and material properties were identical for all configurations and in line with the requirements defined at the beginning of

the chapter. It is apparent that the two configurations with high symmetry factor between magnet rotor poles and stator slots exhibit significantly larger amplitude of cogging torque than the configurations with symmetry factors closer to 2. It is apparent that particularly configuration with 16 pole pieces, 9 magnet rotor poles and 21 slot stator produces almost negligible cogging torque despite the fact that no skewing was employed.

From a practical point of view, the proposed device is intended for integration with an internal combustion engine, a strong source of torsional vibration, and hence the torque ripple produced by the device may not be as important as other limiting factors described in the previous section.

3.4 Electromagnetic design of the dual rotor device

3.4.1 Initial sizing

Traditionally, initial sizing of electrical machines is based on sizing equations giving initial estimate of the rotor volume for a given torque requirement assuming typical values of magnetic and electrical loading [57]. The magnetic loading is a term related to the average achievable no-load air gap flux density created by the rotor magnets or field coils and tends to be limited by saturation of the magnetic circuit while the electrical loading is primarily constrained by the machine thermal management. Sizing of the dual rotor device is fundamentally equivalent to sizing of a typical synchronous machine with surface mounted magnets and traditional sizing equations could be used with few modifications to take into account the effects of magnetic gearing.

The simplest expression of electromagnetic torque acting on the rotor of an electrical machine is given by:

$$T = V_r \cdot 2 \cdot \sigma = 2 \cdot D_r \cdot L_{fe} \cdot A_{rms} \cdot B_{peak} \cdot \frac{2}{\pi} \quad (3\text{-}8)$$

where V_r is rotor volume, σ is air gap shear stress, D_r rotor outer diameter L_{fe} is rotor stack length, A_{rms} is rms value of linear current density (electrical loading) and B_{peak} is peak value of air gap magnetic flux density (average value of air gap flux density is defined as magnetic loading and is given by multiplication of $B_{peak}\ by\ 2/\pi$, assuming sinusoidal distribution of air gap flux density).

Typical values of fundamental air gap flux density created by rotors of PM synchronous machines utilizing rare earth magnets is around 1T [57], giving the magnetic loading of approximately 0.64T. A similar level of flux density in the inner air gap of the dual rotor device is achievable (Fig. 2-3). However, the stator does not directly interact with the field in the inner air gap and only couples to the product of interaction between the magnet rotor field and the pole piece rotor, i.e. the control space harmonic. For the purpose of sizing, the combination of the pole piece rotor and the magnet rotor could be replaced by an equivalent surface PM rotor having the same outer diameter as the pole piece rotor and producing an air gap flux density harmonic with equal number of pole pairs and amplitude of the useful asynchronous harmonic to which the stator couples. The theoretical amplitude of the asynchronous space harmonic can be obtained from equation (2-3) and is given by:

$$B_{cont} = B_m \cdot \frac{4}{\pi^2} \cdot k_{ppr\_c} \qquad (3\text{-}9)$$

where B_m is peak value of inner air gap flux density created by the magnet rotor and k_{ppr_c} is a factor which was added to the expression from equation (2-3) in order to express the non-ideal nature of a real physical pole piece rotor and combines several effects which tend to reduce the amplitude of the control harmonic. For instance, permeability of soft magnetic materials used to construct the pole pieces is not infinite and does not vary linearly with field strength. In addition, portion of the flux passing through the pole pieces in radial direction could leak in circumferential direction and therefore not enter the outer air gap. The factor can be seen as a measure of how effective the pole piece rotor is as a modulator or as a kind of goodness factor of a pole piece rotor design. The perfect pole piece rotor with no leakage and infinite permeability would have the pole piece factor equal to 1.

Assuming an ideal pole piece rotor ($k_{ppr\_c} = 1$) and 1T inner air gap peak flux density, the maximum theoretically peak value of the control space harmonic would be approximately 0.41T and maximal magnetic loading, i.e. the average value over half cycle of the control space harmonic, only 0.26T. Consequently, typical values of shear stress seen in conventional state of the art rare earth PM motors are not attainable by the proposed devise as the electrical loading of the stator would be too high, exceeding its electromagnetic and thermal limits.

Tab. 3-5 Magnetic and electrical loading of state of the art motor used in HEV and EV [63] [17]

Motor	**2010 Toyota Prius MG2**	**2010 Nissan Leaf**
Peak torque (Nm)	207	280
Rotor outer diameter (mm)	160	130
Active length (mm)	50	152
Rotor volume (m^3)	1.03E-03	2.02E-03
Peak shear stress (kPa)	100.8	69.4
Assumed magnetic loading (T)	0.637	0.637
Assumed peak electrical loading (kA/m)	158.24	108.95

Comparison of two state of the art traction motors currently used in hybrid and electric vehicles can be seen in Tab. 3-5. The table contains motor parameters typically used in sizing obtained from public domain reports published by Oak Ridge national laboratory [63] [17]. Both machines exhibit very high peak air gap shear stress and consequently high electrical loading. Since the stator of the dual rotor device in a hybrid power split drivetrain would typically use similar cooling systems as the two SoA EV/HEV traction motors, peak electrical loading of 100 kA/m is a reasonable value to use for a high-performance machine sizing.

Unlike a conventional electrical machine producing torque on a single shaft, the dual rotor device has two shafts and three values of torque. Product of the outer air gap magnetic loading and the stator electrical loading gives a value of outer air gap shear stress and can be used to calculate stator torque. However, when sizing the dual rotor device for a power split hybrid drivetrain, the peak engine torque would be known rather that the stator torque. Assuming the pole piece rotor is coupled to the engine, the stator torque is related to the pole piece rotor torque, i.e. engine output torque, by:

$$T_{stat} = T_{ppr} \cdot \frac{p_{stat}}{p_{ppr}} \qquad (3\text{-}10)$$

Substituting equations (3-9) and (3-10) into (3-8) leads to an equation which can be used to estimate the volume within the pole piece rotor outer diameter:

$$V_{ppr} = \frac{\pi}{2} \cdot D_{ppr}^2 \cdot L_{fe} = \frac{p_{stat}}{p_{ppr}} \cdot \frac{\pi^3 \cdot T_{ppr}}{8 \cdot A_{rms} \cdot B_m \cdot k_{ppr\_c}} \qquad (3\text{-}11)$$

where D_{ppr} is pole piece rotor outer diameter. Furthermore, overall active volume of the dual rotor device can be calculated for a given value of split ratio (ratio of pole piece rotor to stator outer diameter) and accuracy of the equation can be further improved by taking into account the magnetic circuit stacking factor and by introducing general stator leakage factor. Resulting equation can be rearranged so that the product of stator outer diameter and active stack length can be calculated:

$$D_{stat}^2 \cdot L_{fe} = \frac{p_{stat}}{p_{ppr}} \cdot \frac{\pi^3 \cdot T_{ppr} \cdot \lambda^2}{4 \cdot A_{rms} \cdot B_m \cdot k_{ppr\_c} \cdot k_\rho \cdot k_{fe}} \qquad (3\text{-}12)$$

where D_{stat} is stator outer diameter, k_{fe} is magnetic circuit stacking factor and k_ρ is general stator leakage factor. As discussed previously, the stator pole pair to pole piece ratio is largely driven by system level considerations and inherent limitation of the device while values of electrical and inner air gap magnetic loading can be assumed to be similar to conventional high-performance electrical machines.

Fig. 3-8 shows stator electrical loading and outer air gap shear stress as a function of pole piece rotor torque for a device with geometrical constraints and parameters given by Tab. 3-6. It is apparent that in order for the device to transmit 180 Nm engine torque, electrical loading of 90 kA/m is needed, and the resultant outer air gap shear stress only slightly exceeds 18 kPa.

Tab. 3-6 Dual rotor device parameters for sizing

Stator outer diameter D_{stat} (mm)	300
Active axial length L_{fe} (mm)	50
Stator pole pairs p_{stat} (-)	7
Number of pole pieces (-)	16
Inner air gap B_m (T)	1
Pole piece rotor factor k_{ppr_c} (-)	0.8
Stator leakage factor k_ρ (-)	0.95
Split ratio (-)	0.7
Stacking factor k_{fe} (-)	0.98

The equation (3-12) could be used at initial stages of the design process for approximate sizing based on estimated values of loadings and several constants. However, its accuracy is dependent on how accurate the constants are at representing the real machine. In addition, the sizing equation ignores non-linear behaviour of the magnetic circuit, i.e. the stator leakage factor is assumed to be constant irrespective of electrical loading, which in practice is not valid. The next few sections discus the specific design of all three principle components and how their geometry affects the constants in the sizing equation.

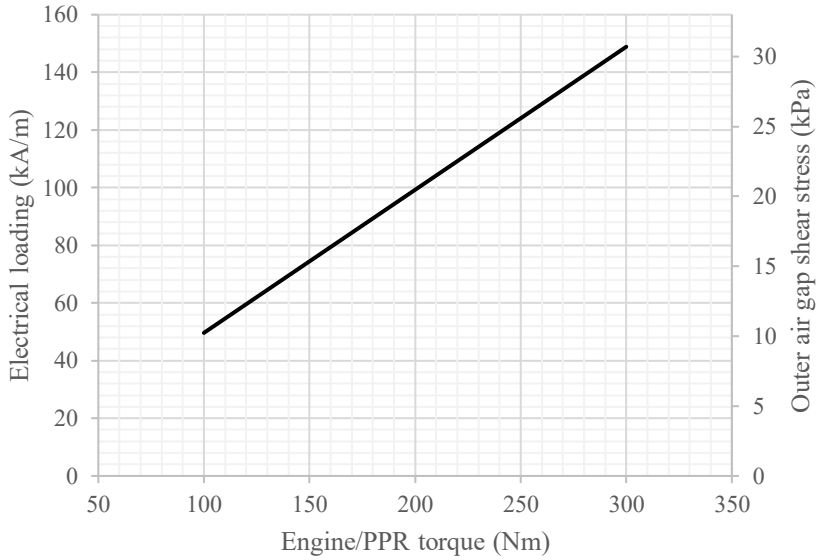

Fig. 3-8 Electrical loading and outer air gap shear stress as a function of pole piece rotor torque

3.4.2 Pole piece rotor design

The largest source of uncertainty in the general sizing equation introduced in the previous section is the factor k_{ppr_c} as it is a function of a number of geometrical as well as material parameters. Since the factor can be defined as a ratio between true amplitude of the outer air gap flux density and its maximum theoretical value, its estimation relies on accurate computation of field distribution in and around the pole pieces. The field distribution could be calculated analytically as comprehensively discussed in [64], however, the analytical methods generally ignore non-linearity of the soft magnetic materials and tend to be limited to relatively simple geometries of the magnetic circuit. For this reason, a finite element method will be used in detailed analysis of the pole piece rotor factor.

It is important to note that while the parasitic space harmonic can be ignored for the purpose of the machine sizing, it must be taken into account when sizing the stator as will be explained in greater detail in one the following section. Amplitude of the parasitic space harmonic can be computed similarly to the control harmonic:

$$B_{para} = B_m \cdot \frac{2}{\pi} \cdot k_{ppr\_p} \qquad (3\text{-}13)$$

where k_{ppr_p} is the pole piece rotor factor related to the parasitic space harmonic. Again, assuming perfect pole piece rotor and inner air gap peak flux density of 1T, maximum theoretical amplitude of the parasitic space harmonic in the outer air gap is 0.637 T, which is significantly higher than the theoretical amplitude of the control harmonic. Since the parasitic harmonic does not contribute to torque production but could contribute to excessive stator saturation, iron loss and torque ripple, the goal of the pole piece rotor design is not only to maximize k_{ppr_c} but also to minimize k_{ppr_p}. An ideal pole piece rotor would have $k_{ppr\_c} = 1$ and $k_{ppr\_p} = 0$, such design would have only one dominant harmonic in the outer air gap since the parasitic one would be completely eliminated.

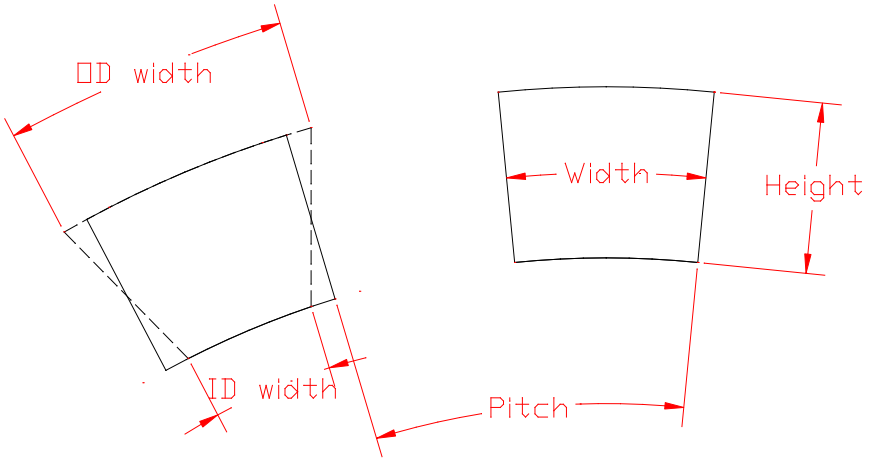

Fig. 3-9 Definition of pole piece dimensions

Fig. 3-9 shows the most basic geometry of two pole pieces and the definition of their geometrical parameters which were used in order to study their influence on the both pole piece rotor factors. Outer diameter of the pole pieces was fixed at 210mm and the inner air gap fundamental flux density was kept constant for all following analyses. In order to eliminate the influence of stator slotting, the stator in the following simulations was replaced by slotless steel cylinder.

Fig. 3-10 shows FE analysis results of a pole piece rotor with 16 pole pieces having 9 pole pair magnetic field at the inner diameter and creating 7 pole pair control and 9 pole pair parasitic harmonic. It can be seen that as ratio of pole piece circumferential width to radial height increases, k_{ppr_c} is only slightly affected while k_{ppr_p} declines sharply. When pole piece width ratio (i.e. ratio of pole piece width to pole piece pitch) is increased, k_{ppr_c} slightly increases while k_{ppr_p} remains almost constant as can be seen in Fig. 3-11. Altering bottom and top width of the pole pieces independently creates pole pieces with trapezoidal shape and an optimum ratio of top to bottom width exists, Fig. 3-12.

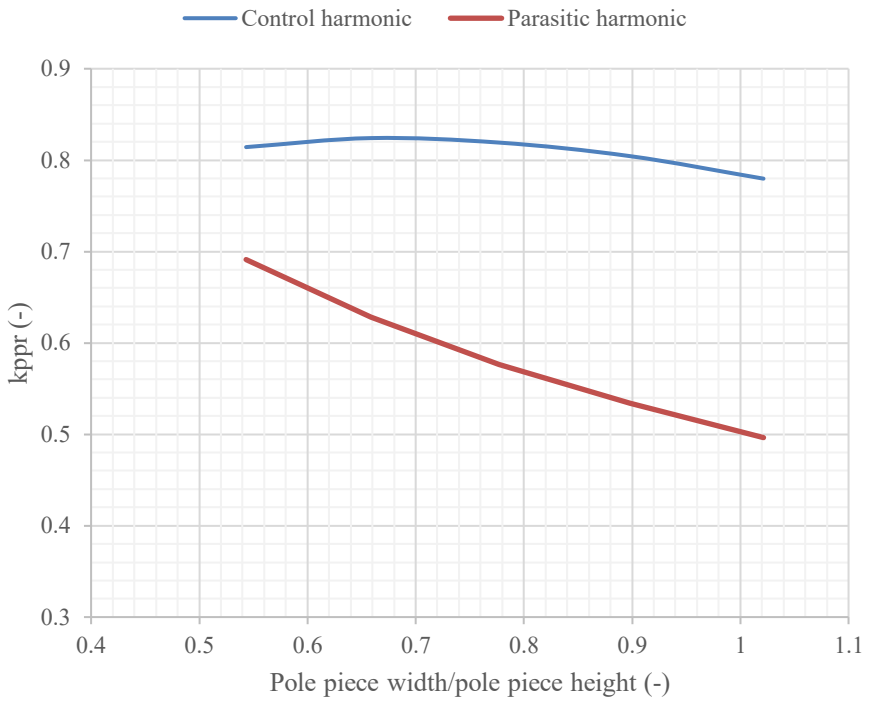

Fig. 3-10 Influence of pole piece width to height ratio on pole piece rotor factors

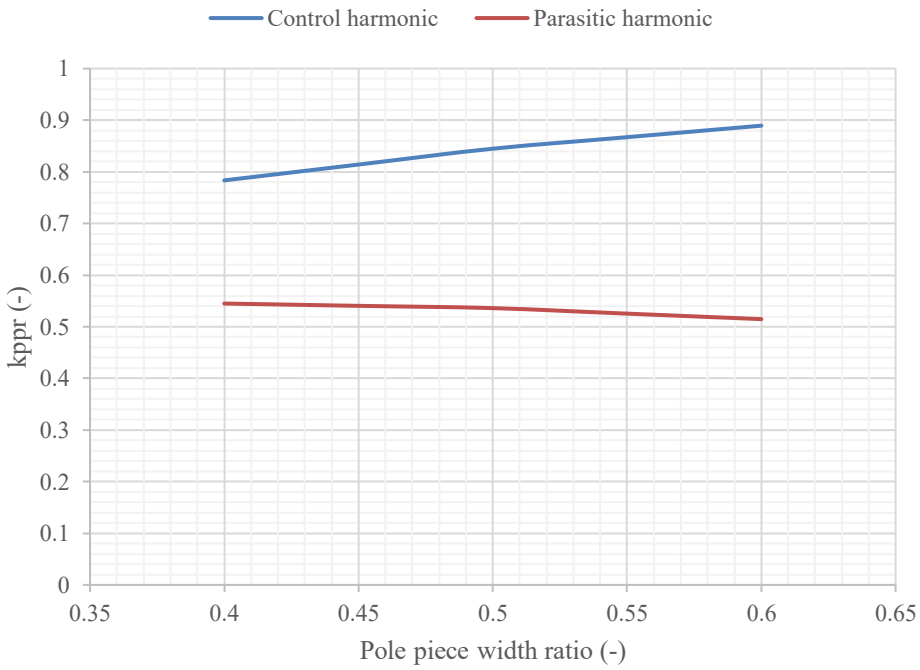

Fig. 3-11 Influence of pole piece width ratio on pole piece rotor factors

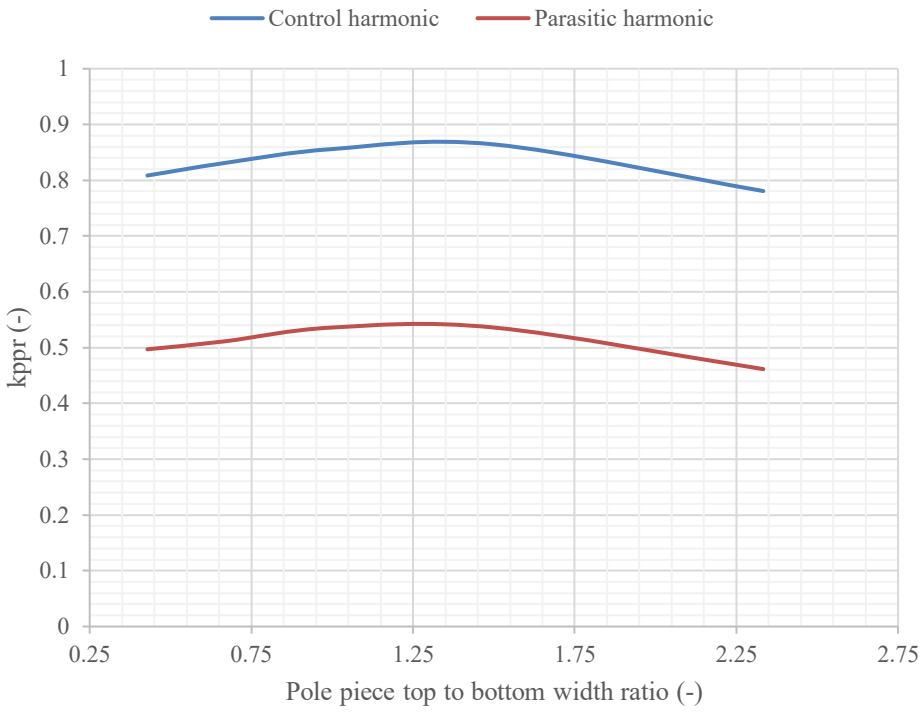

Fig. 3-12 Influence of pole piece top to bottom width ratio on pole piece rotor factors

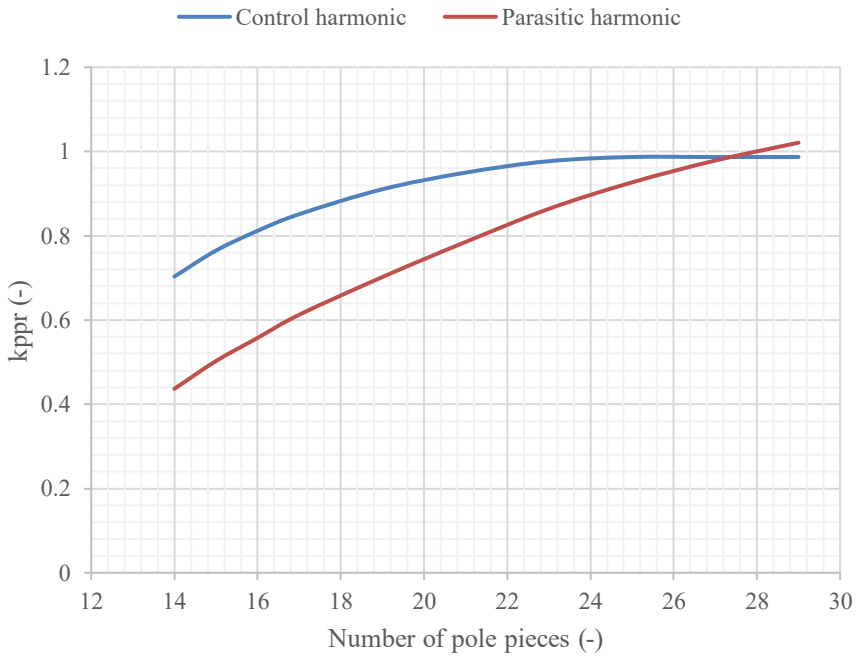

Fig. 3-13 Influence of combination of magnet rotor poles and pole pieces on pole piece rotor factors

All the aforementioned geometry modifications have an influence on the control harmonic pole piece factor, although the effect is relatively small. Variation of both factors with number of pole pieces for constant 9 magnet rotor pole pairs and constant ratio of pole piece width to height of 0.8 is shown in Fig. 3-13. It can be seen that as the number of pole pieces increases both factors start approaching 1. With 25 pole pieces, k_{ppr_c} reaches its maximum value of 0.99 while with 29 pole pieces k_{ppr_p} exceeds the value of 1. This can be attributed to the fact that as the number of pole pieces increases their circumferential width decreases and so does their radial height. Consequently, the distance between the inner and the outer air gap becomes smaller and larger portion of the inner air gap flux passes between the two air gaps through the gaps between pole pieces. It is apparent that increasing the number of pole pieces for a given number of magnet rotor poles, this alters the intrinsic gear ratio making the device unsuitable for a selected drivetrain hence these results are presented here only for the sake of completeness. It can be concluded that specific combination of pole pieces and magnet rotor poles has larger impact on both pole piece factors than geometry of individual pole pieces.

3.4.3 Stator sizing and split ratio selection

Having established the relationship between the input torque of the device and its active volume by means of a general sizing equation and quantifying the influence of pole piece rotor design on pole piece rotor factors, optimal sizing of the stator lamination can now be discussed. The sizing equation contains two variables related to stator lamination design, split ratio i.e. the ratio between outer air gap diameter and the stator lamination outer diameter, and the stator leakage factor which defines the proportion of overall stator flux involved in electromechanical energy conversion for a given number of stator slots is mainly affected by tooth and back iron dimensions. Optimal sizing of the stator laminations is primarily driven by its thermal and magnetic limitations, as is comprehensively discussed in [65], and its goal is typically maximization of torque density of a machine.

Thermal limitations refer to allowable temperature rise in the windings affecting insulation system selection and desired life span of the machine. Authors in [65] assert that there are global and local thermal limitations and an optimal design needs

to satisfy both. Additionally, non-linear properties of the lamination steel impose the magnetic limitation and need to be taken into account when sizing the stator teeth and back iron. Global thermal limit refers to maximal amount of loss which can be extracted from the machine by the cooling system while local limitations are imposed by selecting maximal allowable current density in the slot so as to prevent large thermal gradient in the copper bundle. Optimal design should achieve the highest torque density whilst satisfying both the maximal overall loss and maximal slot current density limits. Whilst the aforementioned publication relies on purely analytical methods for lamination sizing, FEA was used for the following analysis because of the complex flux distribution within the dual rotor device.

As mentioned at the beginning of the chapter, open slot stator was selected for the prototype with coils pre-wound on bobbins and then slid onto stator teeth. This manufacturing method can easily be automated in mass production setting; however, it imposes limit on achievable slot fill factor as the central portion of the slot cannot be fully filled with copper. Additional mid-tooth was added to the back iron in order to provide additional locating feature for the coil bobbins and also to aid heat extraction from the coils as can be seen in Fig. 3-14. Only the brown portions of slots in the figure are occupied by the coils and hence terms like copper area, slot current density and slot fill factor relate only to those areas. This type of lamination profile is used in all of the following analyses.

As the global thermal limit for stator sizing is based on the value of total copper loss, following equation could be used to quantify it:

$$P_{cu} = \rho_{cu} \cdot \left(L_{fe} + L_{ew}\right) \cdot J_{rms\,slot}^2 \cdot \frac{A_{cu}}{k_{cu}} \qquad (3\text{-}14)$$

where ρ_{cu} is copper resistivity, $J_{rms\,slot}$ is slot current density, A_{cu} is total stator copper area, k_{cu} is copper packing factor, L_{fe} is stack length and L_{ew} is end-winding length. All the following analyses assume that the copper packing factor is 0.5 and copper resistivity is adjusted to 100°C copper temperature.

The global thermal limit based purely on DC copper loss neglects AC loss mechanisms such as AC copper and iron losses and it is therefore more suitable for

low speed high torque machines where DC loss components dominate. The fundamental frequency of the dual rotor device could exceed 1000Hz at high differential rotor speeds and, therefore, it could be seen as a high frequency machine. However, the choice of intrinsic gear ratio and the drivetrain control strategy could be selected so that the machine spends most of the operating time close to the line of zero stator frequency where it behaves like a low speed high torque machine and benefits from higher efficiency. If, however, the device was designed for operation with predominantly high differential speeds between the rotors, then iron loss and AC copper loss would need to be taken into account during stator lamination sizing.

3.4.3.1 Selection of tooth width and back iron thickness

Assuming a fractional slot stator with 0.5 slots per pole and phase, back iron thickness is half of tooth width and can be calculated as follows:

$$b_t = \frac{t_w}{2} = \frac{2 \cdot \pi \cdot D_{stat} \cdot \lambda}{2 \cdot N_{slots}} \cdot \frac{B_{og}}{B_{fe\_max}} \quad (3\text{-}15)$$

where t_w is tooth width, B_{og} average air gap flux density, B_{fe_max} is maximal allowable no load tooth and back iron flux density and λ is split ratio defined as D_{rot}/D_{stat}. This equation can be used for initial sizing of stator teeth and back iron of any electrical machine with slotted stator (as long as they have 0.5 slot per pole and phase) since they only differ in the way how the average air gap flux density is calculated. However, as pointed out on Chapter 2, the air gap flux density has two strong harmonic components and sizing the lamination only for the useful control space harmonic, as in the case of conventional machines, would likely lead to saturation. The worst-case scenario for a stator tooth occurs when peak of both dominant space harmonics directly face the tooth. Fig. 3-14 shows no load flux density distribution in the stator of the proposed device and it is apparent that the tooth at precisely 3 o'clock position is perfectly aligned with magnet rotor pole and a pole piece and it has the highest flux density of all stator teeth. Consequently, all the stator teeth need to be sized for this condition as the saturation pattern will change with position of both rotors.

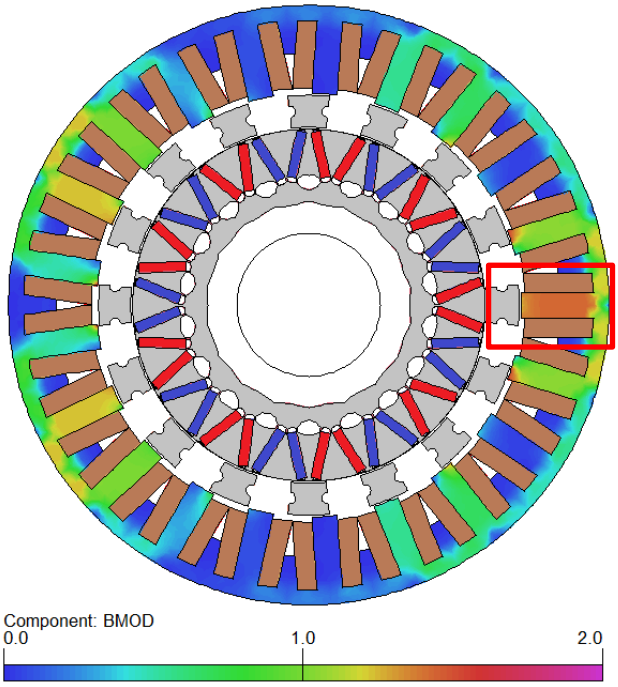

Fig. 3-14 No load flux density distribution in the stator of the device.

While, lamination sizing for maximal no-load flux density is commonly used, the choice of allowable flux density has an impact on on-load performance as could be seen in Fig. 3-15 where torque as a function of slot current density is plotted for three stator laminations sized for different allowable no-load flux densities. The choice of higher no-load flux density leads to smaller tooth width and larger slot area, which benefits the device at lower current densities where it produces more torque, however it becomes limited near the peak torque operation where the magnetic circuit becomes heavily saturated and overall the torque vs current characteristic is more non-linear. Pole piece rotor torque can also be plotted as a function of DC copper loss for the three different designs as can be seen in Fig. 3-16 It is apparent that the choice of low no-load tooth flux density leads to a design producing significantly larger torque per W of copper loss. Additionally, lower lamination flux density will reduce iron loss contribution to the overall loss of the machine.

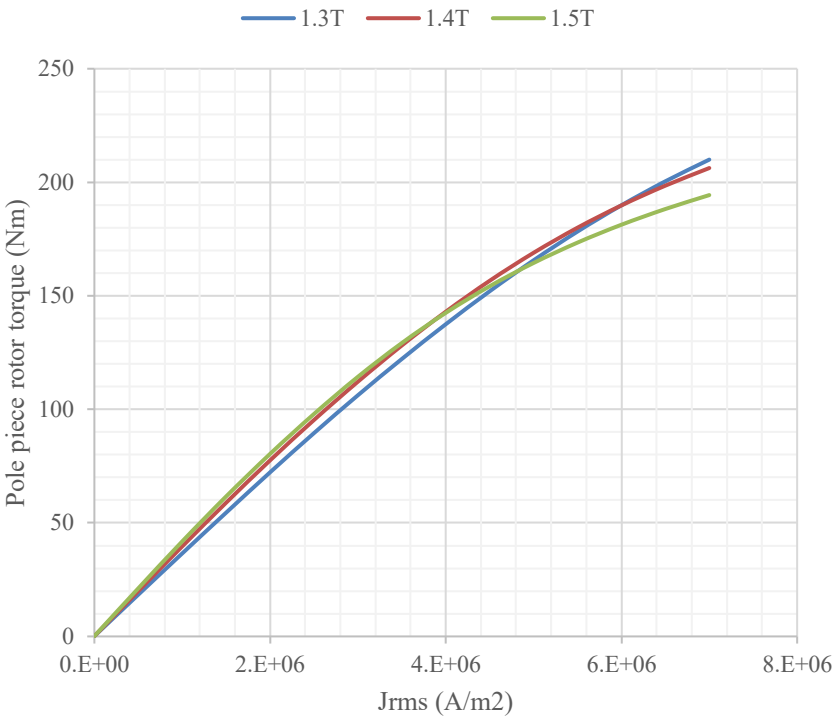

Fig. 3-15 Pole piece rotor torque as a function of slot current density for laminations sized for different no load flux densities

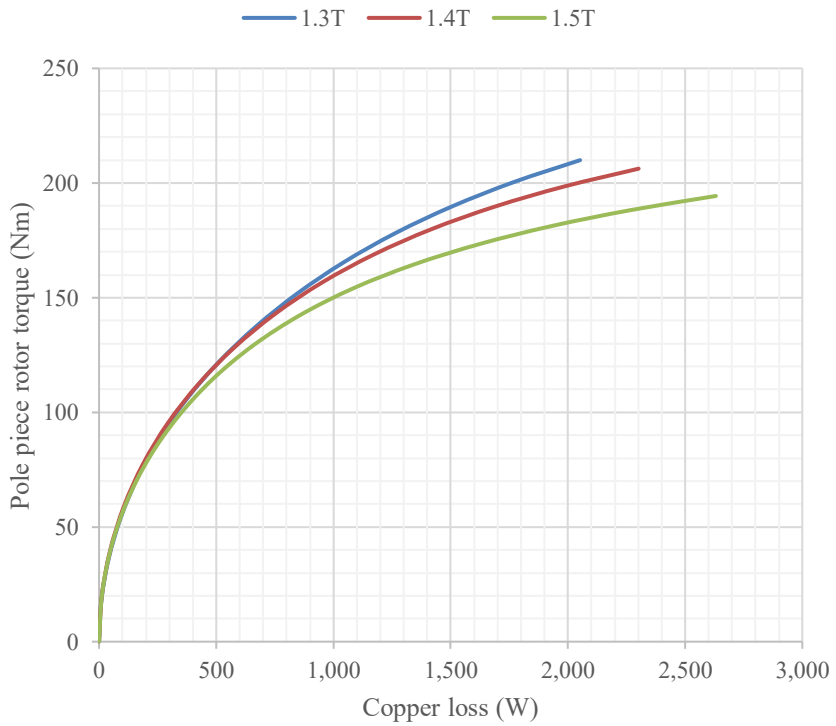

Fig. 3-16 Pole piece rotor torque as a function of DC copper loss for laminations sized for different no load flux densities

3.4.3.2 Choice of split ratio

As it was mentioned previously, choice of split ratio is closely linked with maximisation of torque density of the machine. Pole piece rotor torque as a function of split ratio was analysed separately for the global limit of 2kW of copper loss and for slot current density of 6.5A/mm2. It is apparent from Fig. 3-17 that the highest pole piece rotor torque, and consequently the highest torque density with the fixed active volume, is achieved at different split ratios depending on whether local or global thermal limitation is imposed. For the given lamination profile and outer air gap flux densities in the dual rotor device, constant slot current density is the more restricting limit resulting in smaller split ratio and lower torque density. With constant copper loss, higher torque density can be achieved but this results in high current density. For instance, with 0.8 split ratio, the required current density for 2kW of copper loss exceeds 7.7A/mm2. Furthermore, it can be seen in Fig. 3-18 and Fig. 3-19 that the choice of maximal current density or copper loss has relatively small impact on the value of optimal split ratio.

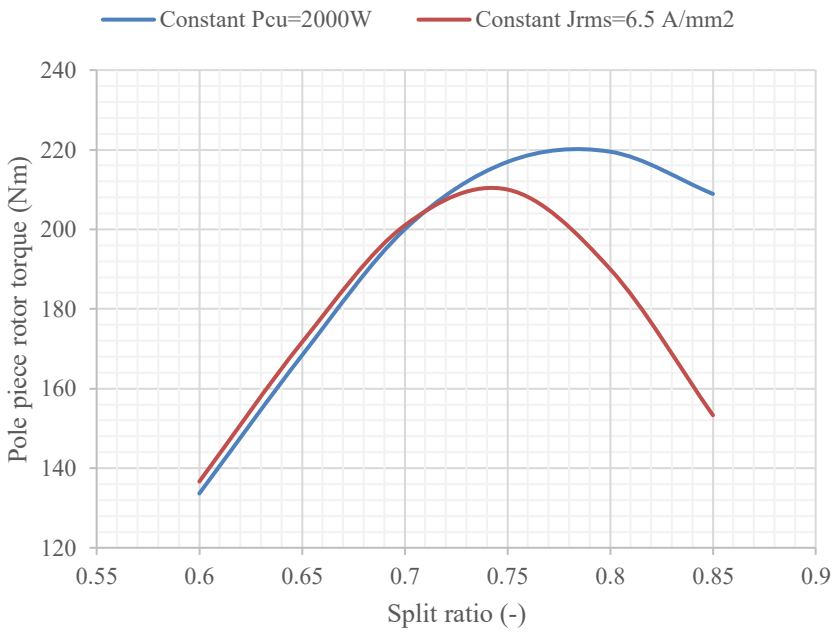

Fig. 3-17 Pole piece torque as a function of split ratio for constant slot current density and constant overall DC copper loss

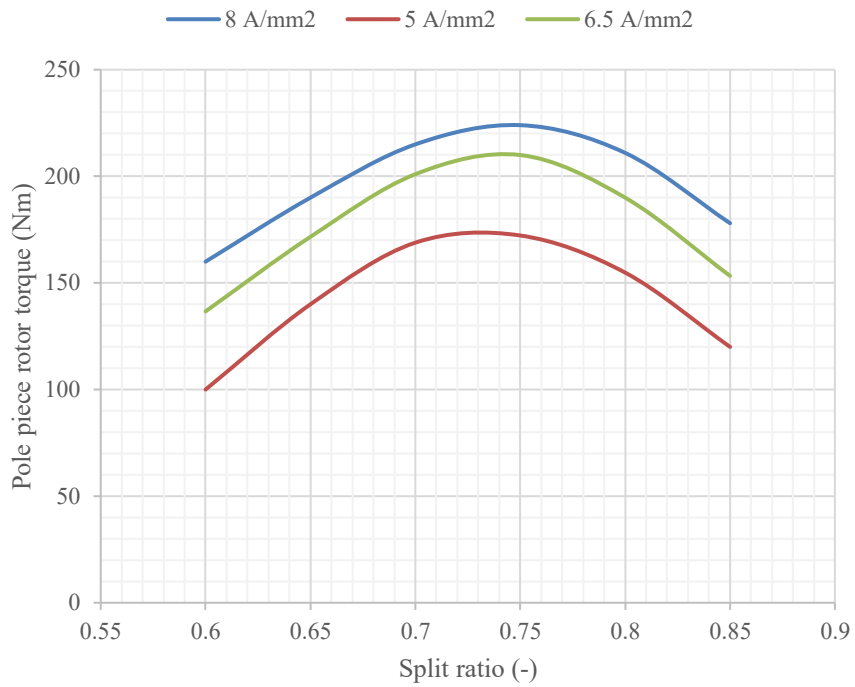

Fig. 3-18 Pole piece torque as a function of split ratio for different choices of constant slot current density

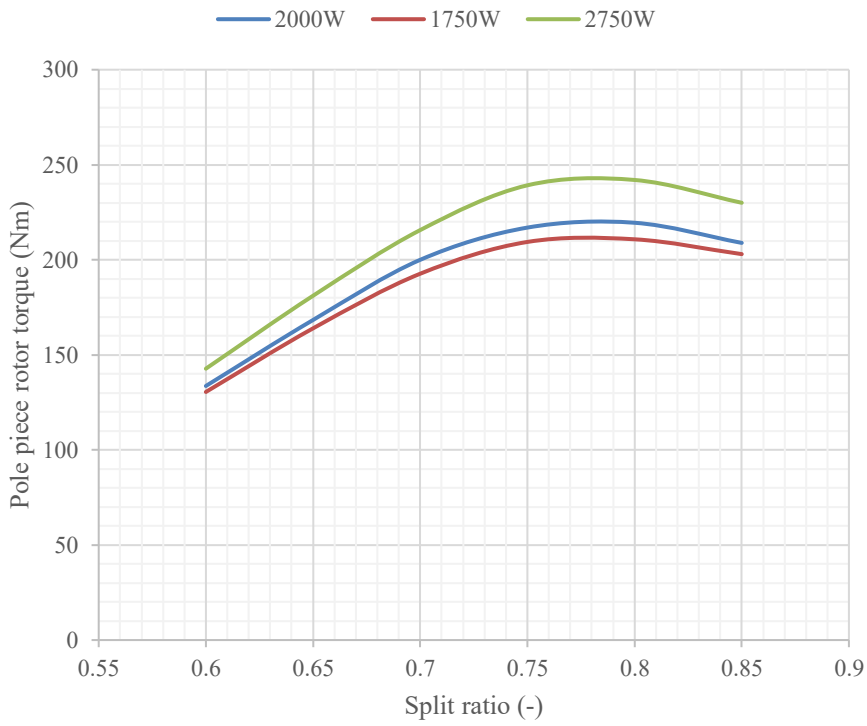

Fig. 3-19 Pole piece torque as a function of split ratio for different choices of constant DC copper loss

The sizing methods based on thermal limitations can be useful at the initial stages of the design process. However, detailed thermal modelling including all the features of a manufacturable design is essential in determination of real thermal performance and finetuning of the design.

It is also worth pointing out that with the increase in split ratio comes the increase in pole piece rotor outer diameter and this needs to be taken into account in structural design of the rotor since it increases centrifugal force acting on pole pieces. This may impose additional limit on split ration selection.

3.4.4 Magnet rotor design

The purpose of the magnet rotor in the dual rotor device is to generate inner air gap flux density of sufficient amplitude, which can then be modulated by the pole piece rotor, and to transmit a portion of the input power to the driven wheels of the vehicle. Goodness of a magnet rotor design can therefore be judged based on several criteria, such as magnet material utilisation, i.e. the amount of air gap flux generated by the rotor per unit magnet mass, and mechanical and electromagnetic robustness. From mechanical point of view, the rotor must maintain structural integrity when loaded by centrifugal and radial electromagnetic forces as well as to transfer peak output torque to the output shaft. Analysis of electromagnetic robustness is primarily concerned with possible demagnetisation of the rare earth magnets at elevated rotor temperatures and during electrical faults.

Referring back to the section 3.4.2 where calculation of pole piece rotor outer diameter and influence of the main geometrical parameters on its electromagnetic performance was presented, outer diameter of the magnet rotor can be calculated by the following equation:

$$D_m = D_{ppr} - 2\left(h_{ppr} + g_{in} + g_{out}\right) \quad (3\text{-}16)$$

where D_{ppr} is the pole piece rotor outer diameter, h_{ppr} is pole piece rotor radial height, g_{in} and g_{out} is radial length of inner and outer air gap respectively. The dual rotor device could be equipped with any standard magnet rotor topology commonly

used in conventional traction motors. Fig. 3-20 shows basic geometries and definition of geometrical parameters of the V shape embedded and surface mounted magnet rotors which will be used in the parametric analysis of both. As it was mentioned previously, embedded magnet rotor with V magnets was chosen for the prototype demonstrator and the surface mounted rotor will be only used as a point of reference for comparison.

It must be noted that in both cases, the structural robustness of rotors is of prime importance and does affect their electromagnetic performance. Surface mounted magnets are often glued to the back iron and further secured by retaining sleeves made of either carbo fibre or non-magnetic metallic materials such as stainless steel or Inconel. Thickness of the retaining sleeve influences the electromagnetic performance of the rotor inasmuch as it could increase the effective air gap between the rotor magnet surface and the inner diameter of the pole pieces. Similarly, the rotor lamination of an embedded rotor must be designed for it to be able to withstand centrifugal forces at higher rotational velocities. The structurally weakest part of an embedded rotor are the bridges atop and between magnet blocks which create a magnetic low reluctance path through which a significant portion of useful magnet flux can escape.

Detailed description of the structural design of the embedded rotor is outside of scope of this thesis. However, the bridges were analysed by means of structural FEA analysis and their thickness was kept to 0.7 mm which gave structurally sound design for wide range of rotor parameters. For the surface mounted rotor, thickness of a carbon fibre retention sleeve was assumed to be significantly smaller than 1mm and hence the electromagnetic air gap between the magnet outer diameter and the pole piece rotor was not increased.

In order to analyse achievable inner air gap flux density, magnet thickness and the V angle of magnets with constant magnet thickness (Fig. 3-25) was varied for the surface mounted and embedded rotor respectively. Variation of both of these parameters results in change in rotor magnet mass. Magnet rotor operating temperature was assumed to be 100°C. Fundamental component of inner air gap flux density as a function of magnet mass for both surface mounted and embedded magnet rotor is shown in Fig. 3-21.

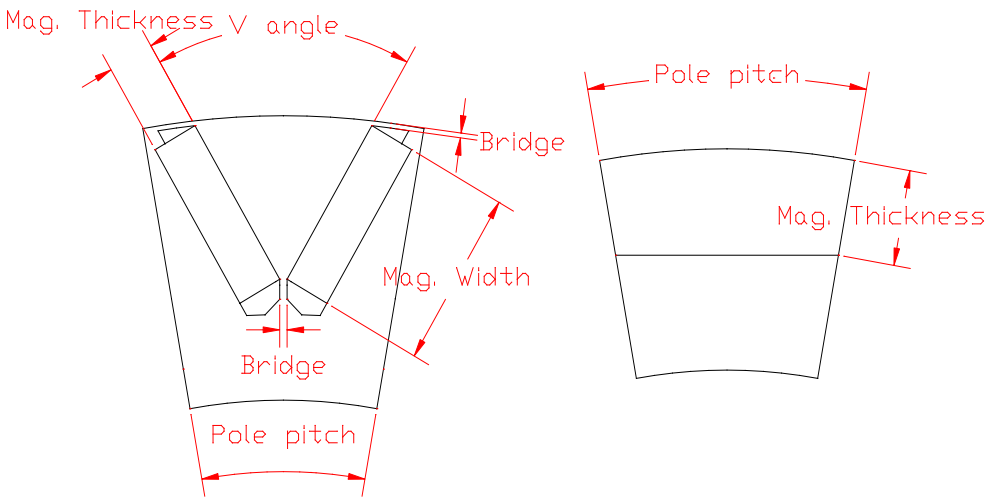

Fig. 3-20 Definition of geometric parameters of embedded and breadloaf surface mounted magnet rotors

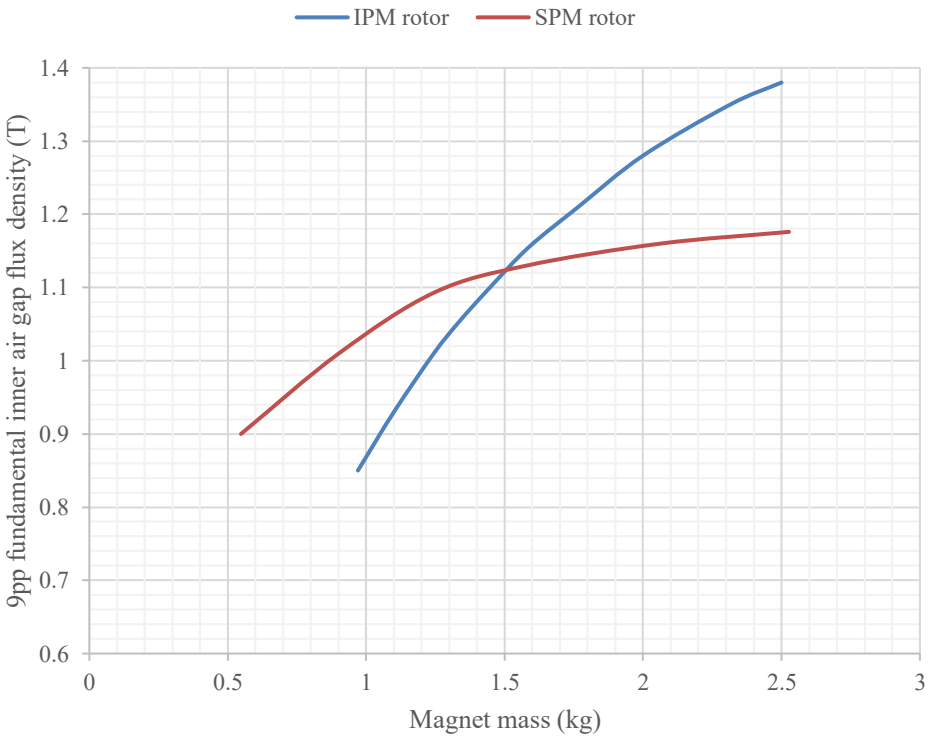

Fig. 3-21 Inner air gap flux density as a function of magnet mass for surface and V-shape embedded magnet rotor

It is apparent that in order to produce peak air gap flux density of 1T, surface mounted rotor needs approximately 0.3kg less magnets than the embedded one. However, when it is needed to increase the inner air gap flux density beyond approximately 1.15T, the embedded rotor begins to achieve higher active material utilisation (how much flux the rotor produces per unit of magnet mass) and air gap flux densities in excess of 1.3T could be achieved. This could be attributed to the flux focusing effect of the V-shape internal magnet rotor which allows the rotor steel flux density on the pole face to exceed remanent flux density of the magnets. Given the discussion in the previous section on how amplitude of the modulated useful harmonic in the outer air gap is relatively small, in comparison to SoA rare earth PM motors, and how it cannot be significantly increased by the pole piece rotor design, employing flux focused rotor is a viable way of increasing density of transmittable torque for a given machine volume.

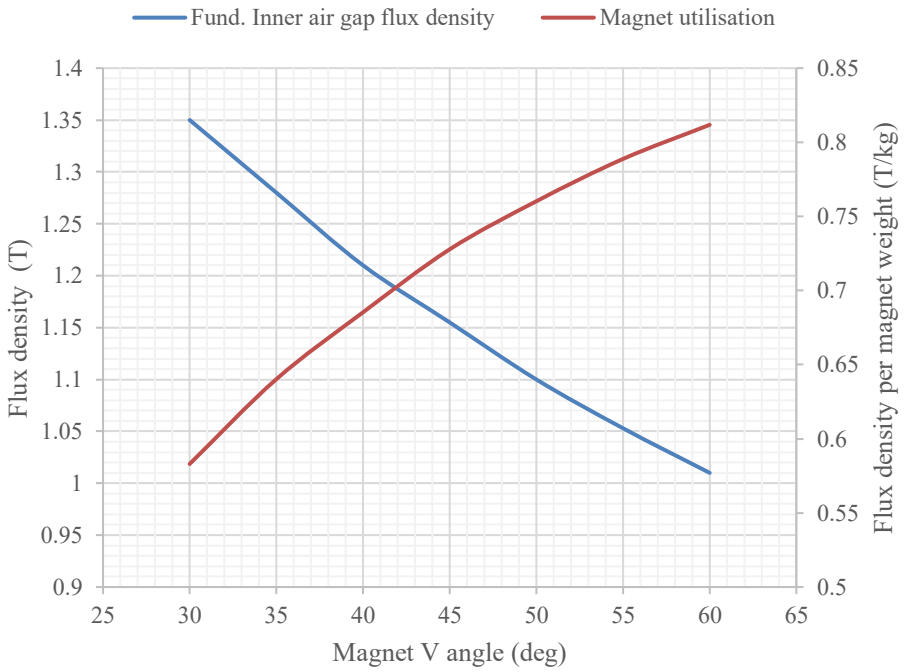

Fig. 3-22 Peak fundamental inner air gap flux density and magnet utilisation as a function of magnet V angle

While high inner air gap flux density could be achieved, the utilisation, i.e. the amount flux of per unit mass, of the magnets tends to decrease as the flux density

increases, as illustrated in Fig. 3-22 where inner air gap flux density and magnet utilisation as a function of the magnet V angle shown.

Another important aspect to consider when using permanent magnets as a source of excitation is their potential demagnetisation during normal operation and faults. This problem is present in all PM machines; however, it is exacerbated by the presence of the pole piece rotor. As the pole piece rotates at a relative speed with respect to the magnet rotor, the magnet rotor poles face the gap between individual pole pieces filled with air. When a rotor pole is perfectly aligned with the gap, the gap significantly increases the total reluctance of the flux path thus reducing flux density in the magnet and moving the operating point of the magnet closer to the knee point on its BH curve. Once the knee point is crossed, the magnet or its portion loses some of its remanence.

Family of BH curves of N48SH permanent magnet material for different temperatures is shown in Fig. 3-24. This particular material offers very high remanent flux density and its rated temperature is 150 degrees Celsius. However, it can be seen that at such high temperature, the knee point of the BH characteristic is at approximately 0.5T. Knee points for H, SH, UH and EH magnet grades at temperatures from 80°C to 180°C are summarized in Tab. 3-7. High temperature grades, such as EH and UH, offer superior resistance to demagnetisation at elevated temperatures, however, tend to be far more expensive due to higher dysprosium content. Additionally, magnets with a combination of higher remanent flux density and high temperature grade are not readily available or their usage tends to be limited to laboratory and special use.

The effect of pole piece position on magnet flux density is clearly illustrated in Fig. 3-23 where FE solution of field inside the permanent magnets of the embedded rotor is shown for two extreme relative positions of the pole piece rotor. The white areas in flux density plots are portions of the magnets which have flux density below 0.4T. It is apparent that when a pole is facing the gap between pole pieces, the flux density in the corners on the magnet surface facing the pole face drops significantly and these corners are at high risk of demagnetisation. Since this particular pole piece rotor position represents the worst-case scenario for magnet demagnetisation under normal operating conditions and since each pole experiences this unfavourable

position as the pole piece rotor rotates at relative speed with respect to the magnet rotor, it was used to perform demagnetisation analysis.

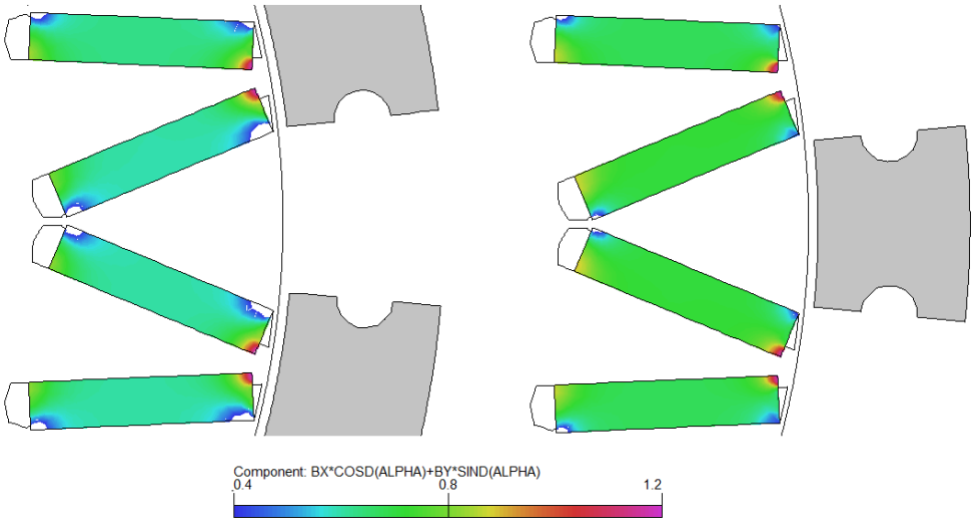

Fig. 3-23 Magnet flux density in the rotor magnets at two different pole piece positions

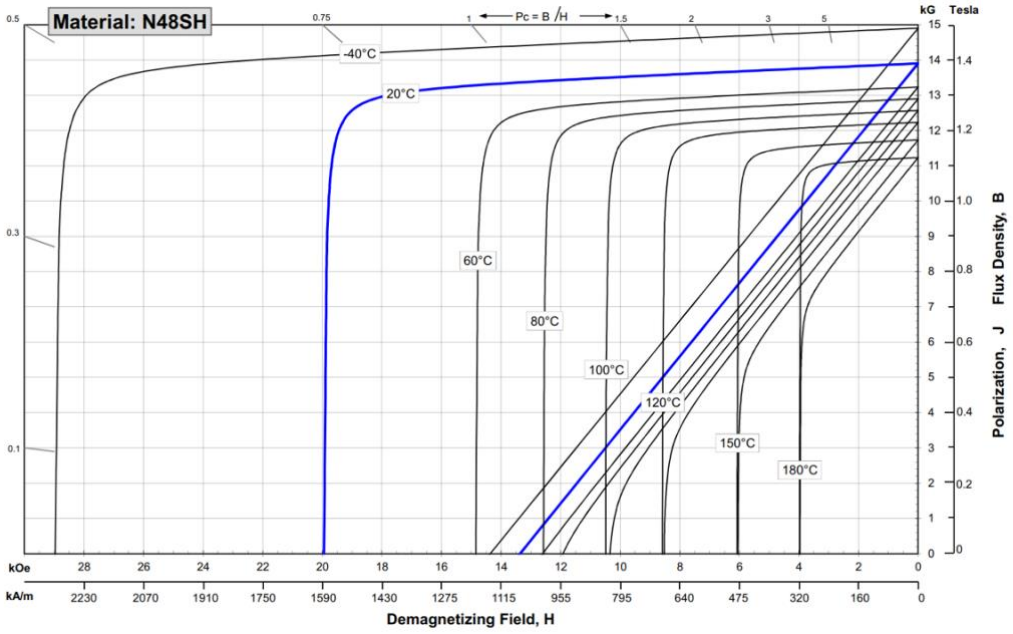

Fig. 3-24 Family of BH curves of N48SH magnet material at different temperatures [66]

Percentage of magnet volume with flux density lower than specified threshold was calculated for number of magnet V angles and the results can be seen in Fig.

3-26. It is apparent that sharper V angles not only lead to higher air gap flux density, lower magnet utilisation (as can be seen in Fig. 3-22) but also to higher percentage of magnet volume at risk of demagnetisation. This imposes limit on operating temperature of the magnet rotor or demands high temperature magnet grade. For instance, with 30 degree V angle and assuming that demagnetisation needs to be kept below 5% of the magnet volume, the rotor with N48H grade can only be operated up to 80°C while N48SH is safe up to 120°C. It must be noted that while the magnet grade can be selected such that the rotor could safely operate at temperatures higher than 150°C, elevated temperature leads to reduction of remanence of the magnets and reduction of air gap flux density produced by the rotor.

Tab. 3-7 Location of the knee point on BH curve of different magnet grades

Knee point [T]		Temp (°C)				
		80	100	120	150	180
Grade	48H	0.3	0.4	0.55	0.75	X
	48SH	0.05	0.15	0.3	0.5	0.7
	45UH	0	0	0.1	0.3	0.5
	42EH	0	0	0	0	0.15

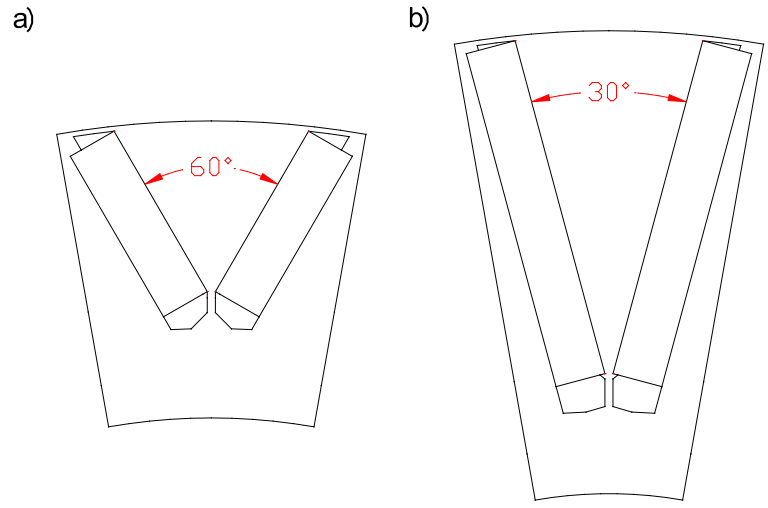

Fig. 3-25 Magnet rotor with constant 5mm magnet thickness and a) 60deg and b) 30deg magnet V angle

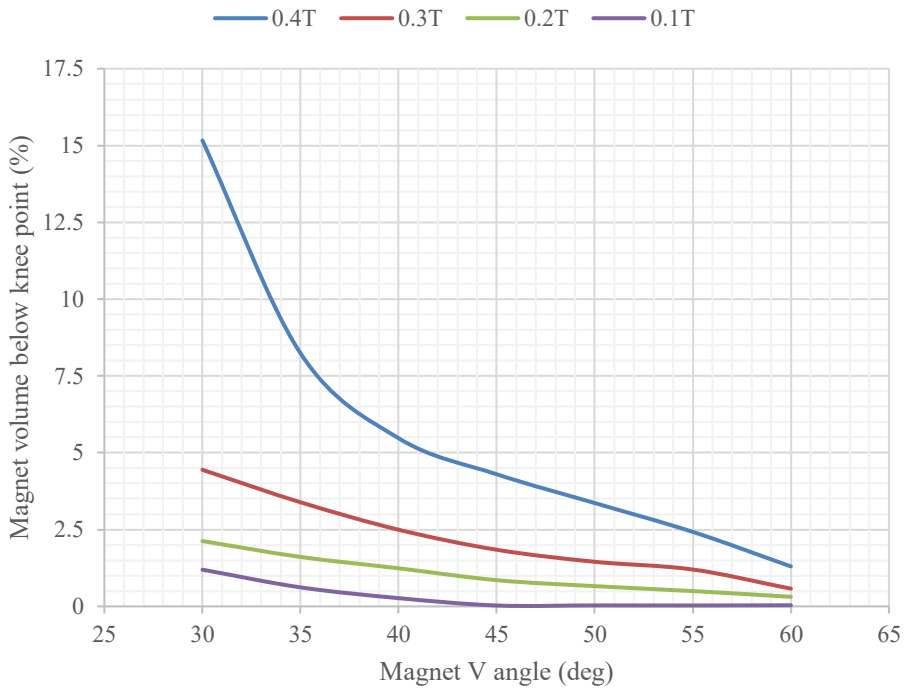

Fig. 3-26 Percentage of magnet volume at risk of demagnetization as a function of magnet V angle

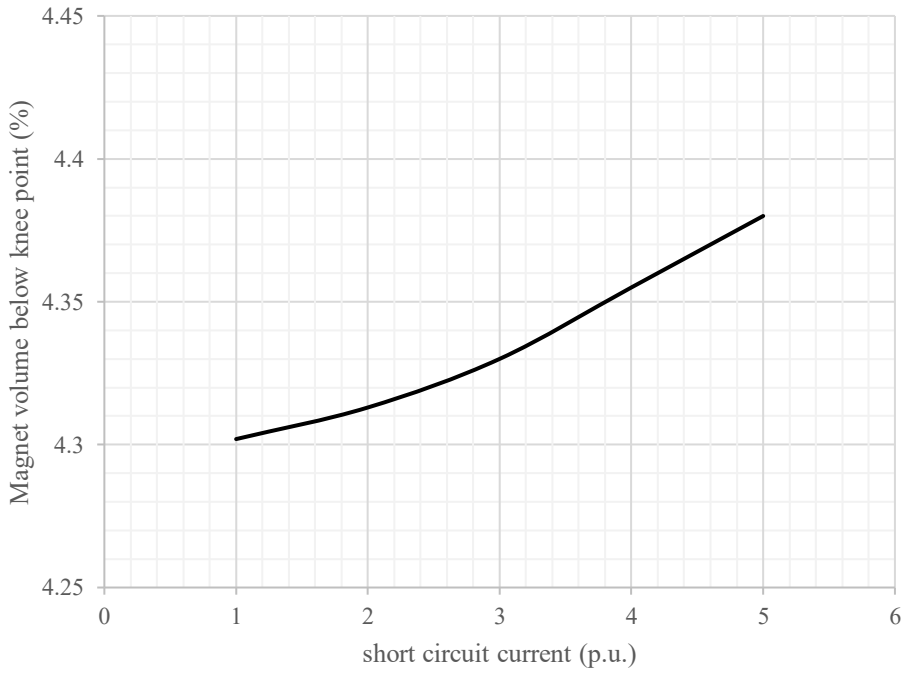

Fig. 3-27 Demagnetisation of magnets as a function of d-axis short circuit current

Apart from irreversible demagnetization which could occur at normal operation of the device, the rotor magnets in conventional machines could get damaged during sudden electrical faults. For instance, sudden three phase short circuit at the winding terminals leads to large direct axis current producing flux which opposes the magnet field. Fig. 3-27 shows demagnetisation of embedded magnet rotor with 45deg angle for multiples of negative rated D axis current. It is apparent that even high values of armature reaction current have negligible impact on magnet demagnetisation. This can be attributed to the fact that magnet rotor has different number of poles than the demagnetizing armature reaction field which can't oppose the magnets directly. Additionally, the magnet rotor is shielded by leakage flux paths of the pole piece rotor.

3.4.5 Magnetic circuit design summary

Based on the discussions in the previous sections, the dual rotor device was sized for further detailed analysis and prototyping. Tab. 3-8 summarizes the main parameters and dimensions of the design and the cross section of the magnetic circuit can be seen in Fig. 3-28. It is worth mentioning at this point that the research project described in this thesis aimed to deliver a functional technology demonstrator rather than a fully optimized design of the device and had a strict and constrained timing plan. During the design stage of the project, it was important to freeze some of the design dimensions relatively early so that prototype parts could be procured and delivered on time. In addition, it was important to manage risk and to avoid prototype failure during testing, therefore some design choices had to err on the conservative side of what seemed possible at the time.

For this reason, the design presented in this section shall not be seen as an optimum resulting from the analyses described in the previous sections. Some of the analysis work was done after the design for the prototype had been already frozen, aiming to explore how much further the design can be improved given the known constraints. The limitations described in the sections 3.3 and the magnetic circuit design principles in section 3.4 were initially explored using design of experiments techniques in an FEA software to achieve a feasible demonstrator design but were

later generalized such that they could be used to quickly assess feasibility of a particular design and to show where electromagnetic optimum might be.

Tab. 3-8 Summary of parameters of the selected configuration

Number of slots	21
Number of stator pole pairs	7
Number of pole pieces	16
Number of rotor pole pairs	9
Stator outer diameter (mm)	300
Axial length (mm)	50
Split ratio	0.7
Pole piece thickness (mm)	16
Inner and outer air gap (mm)	1
Pole piece rotor OD (mm)	208
Magnet rotor OD (mm)	174
Magnet mass (kg)	1.55
Stator steel mass (kg)	13.34
Estimated Copper mass (kg)	4.73
Magnet grade (-)	N48SH
Steel grade (-)	M270-35A

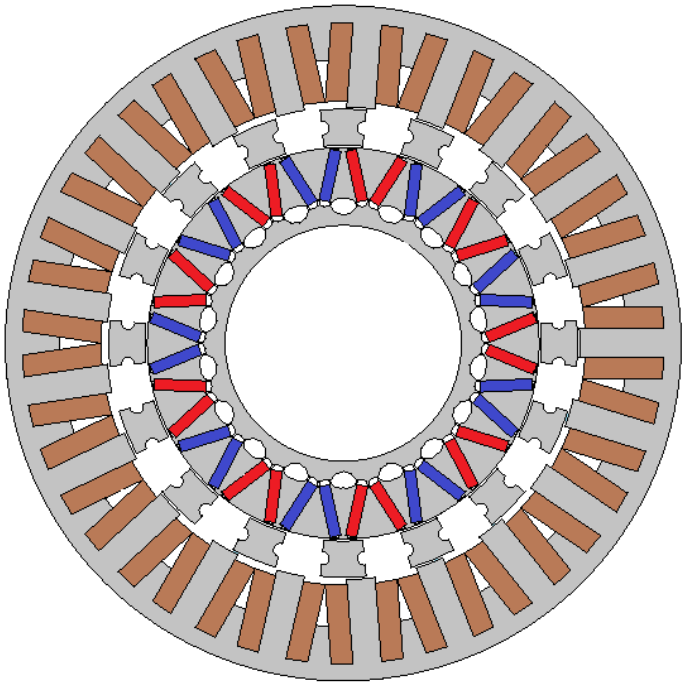

Fig. 3-28 2D cross section of the sized design for prototyping

For instance, the magnet rotor design described in section 3.4.4 shows the limits of what is possible to achieve in terms of air gap flux density for the given packaging space. However, a relatively conservative design with 45 degrees V angle and high temperature grade permanent magnets was selected for the demonstrator so that the risk of demagnetisation during design validation testing would be minimal. At that point, the rotor temperature rise was relatively poorly understood since thermal management of a machine with several rotors and complex modes of operation is a challenge. Similarly, it is possible to magnetically optimize the pole piece rotor, as described in section 3.4.2, however, approximately squared shaped pole pieces were initially selected since their mechanical retention within the pole piece rotor structure was still being developed. Finally, sub-optimal stator split ratio of 0.7 was selected despite the results of discussions in section 3.4.3.2, since larger value would increase outer diameters of both rotors and this would reduce their structural safety factors for the target input and output speeds. Some additional features which have not yet been discussed can be seen in the Fig. 3-28. For instance, the pole pieces have cut outs on the sides which will be used for their retention within the supporting structure of the pole piece rotor and also additional holes were added to the magnet rotor near the magnets in order to limit magnetic leakage and to improve magnet utilisation.

3.4.6 Selection of number of winding turns

Winding pattern selection was discussed in detail in Chapter 2 and fractional slot winding with 21 slots was selected for the prototype design since it offers relatively high winding factor for the control space harmonic, it does not couple with the magnet rotor harmonic and has short winding overhang reducing overall volume of the machine and copper loss. Once the winding pattern is selected, number of turns per phase and detail coils design must be performed.

The selection of number of turns per phase for a given winding pattern is closely linked with limitations of the inverter supplying the device, as is the case with any synchronous electrical machine [67]. Typically, output phase current is limited by the rated value which can be continuously supplied without the risk of overheating the inverter. Moreover, output phase voltage is a function of input DC link voltage and adopted switching strategy. Additionally, third limiting factor may be maximum

fundamental frequency of the output voltage although this will not be considered in the following discussion. The relationship between current and voltage limits of the inverter and stator quantities can be expressed using rotating dq reference frame:

$$\omega_{cont} \cdot \sqrt{\left(L \cdot I_q\right)^2 + (L \cdot I_d + \psi_{cont})^2} \leq U_{max} \quad (3\text{-}17)$$

$$\sqrt{I_d^2 + I_q^2} \leq I_{max} \quad (3\text{-}18)$$

where U_{max} and I_{max} are maximal output voltage and current of the inverter respectively. L is the winding inductance (assuming there is no saliency, i.e. $L_d = L_q$), I_d and I_q are d and q components of armature reaction current. It must be noted that the equation (3-17) neglects resistive voltage drop across the winding resistance. Furthermore, stator current is given by:

$$I = \sqrt{I_d^2 + I_q^2} = \frac{\sqrt{2} \cdot J_{slot} \cdot A_{slot} \cdot k_{cu}}{n_{turns}} \quad (3\text{-}19)$$

where J_{slot} is slot current density, A_{slot} is slot area, k_{cu} is slot packing factor and n_{turns} is a number of turns. Winding flux due to the control space harmonic can be computed directly from the 2D FEA magnetic vector potential distribution, as described in [68], Flux linked with a coil can be computed using the following equation:

$$\psi_{coil} = n_{turns} \cdot \phi_{coil} = n_{turns} \cdot L_{fe} \cdot \left(A_{avg\_go} - A_{avg\_retun}\right) \quad (3\text{-}20)$$

where ϕ_{coil} is the coil flux, A_{avg_go} and A_{avg_return} is average magnetic vector potential in go and return slot of the coil respectively. With known flux linkage, inductance can be computed simply by dividing the flux linkage by coil or winding current. Detailed procedure describing computation of phase inductances and their transformation into dq reference frame can be found in [68].

Torque-speed characteristic of a typical synchronous traction motor can be divided into two regions. The first region is between zero and base speed where the machine operates at constant torque and the inverter is able to supply voltage higher than that required by the machine. At the base speed, terminal voltage reaches the limitation of the inverter and the machine enters field weakening region where d axis component of the armature reaction current is used to supress field flux and to maintain constant terminal voltage. As the speed increases, more armature reaction current is needed to control the terminal voltage and, consequently, less current is available to produce torque and the machine operates with constant power.

Base speed, i.e. the speed where voltage required by the device matches the maximal available voltage of the inverter, can be calculated using the following equation:

$$\omega_{base} = \frac{U_{max}}{p_{cont} \cdot \sqrt{\left(L \cdot I_q\right)^2 + (\psi_{cont})^2}} \qquad (3\text{-}21)$$

Theoretically highest achievable speed is reached when q axis current is zero and armature reaction is purely employed to control terminal voltage.

$$\omega_{max} = \frac{U_{max}}{p_{cont} \cdot \left(L \cdot I_{d\_max} + \psi_{cont}\right)} \qquad (3\text{-}22)$$

As it was mentioned in one of the previous sections, maximal control space harmonic speed (or frequency) is reached when the magnet rotor is stationary, and the pole piece rotor is rotating at full speed. When the pole piece rotor is rotating at 4000rpm, the control space harmonic speed is approximately 9145rpm. The prototype machine is required to transmit full torque at this point and is not to be operated under field weakening. However, It is apparent from equation (3-22) that, apart from available current and voltage, maximal theoretical speed depends on inductance of the stator windings and flux linkage due to the control space harmonic. While fundamental component of no-load air gap flux density of state-of-the-art traction motors could reach 1T, peak flux density of the control space harmonic of the design in Fig. 3-28 is significantly smaller as can be seen in Fig. 3-29 where

amplitude of the control space harmonic is only slightly higher than 0.35T. Consequently, flux linkage due to the control space harmonic will be much smaller than flux linkage due to PMs in conventional machine and hence field weakening is possible even with relatively small amount of d axis current.

Assuming that the amplitude of DC link voltage is 650V and that the winding has 42 turns per phase, the corner point of the torque vs speed characteristic at 300Arms is at 10000rpm and 200Nm which represents 10% margin on top of what is required. Winding inductance as a function of load and flux linkage due to the control space harmonic is in Fig. 3-30 and Fig. 3-31 respectively. The torque speed characteristic generated using FEA model can be seen in Fig. 3-32. The torque speed characteristic is only plotted up to 20000rpm in order to show field weakening capability of the device, however, maximal speed is not shown in the graph as it can theoretically reach infinity, based on equation (3-22), because the armature reaction can completely suppress the relatively weak field created by the control space harmonic.

One negative aspect of the small no load flux linkage is that the device has relatively poor power factor, particularly at high load, as can be seen in Fig. 3-33. During Id=0 operation when only q axis component of the stator current exists and is aligned with the vector of EMF, power factor can be computed form the angle between the vector of EMF aligned with the q axis and the vector of total stator voltage (having both d and q axis components). Working directly with flux linkages obtained from FE solution, the power factor angle can also be calculated from arcus tangens of q axis flux linkage and flux linkage due to the control space harmonic as can be seen in phase diagram in Fig. 2-18.

Error! Reference source not found. and Fig. 3-35 show pole piece rotor torque as a function of phase current and internal load angle. It is apparent that the torque vs current curve is affected by non-linearity of the magnetic circuit and that the torque vs load angle characteristic shows negligible distortion from sinewave. Large slot openings and fractional slot windings in conventional PM machines often lead to considerable torque ripple unless rotor or stator skewing is employed. However, despite the fact that the proposed device has highly salient magnetic circuit and fractional slot winding, it manifests negligible amounts of on-load torque ripple on both the input and output shafts, as can be seen in Fig. 3-36 where torque of both

rotors vs pole piece rotor position is plotted. This is beneficial since skewing of any of the principle components would likely lead to reduction of transmittable torque. Additionally, skewing of the pole pieces would complicate the pole piece rotor construction and stator skewing would not be practical due to the chosen winding technology.

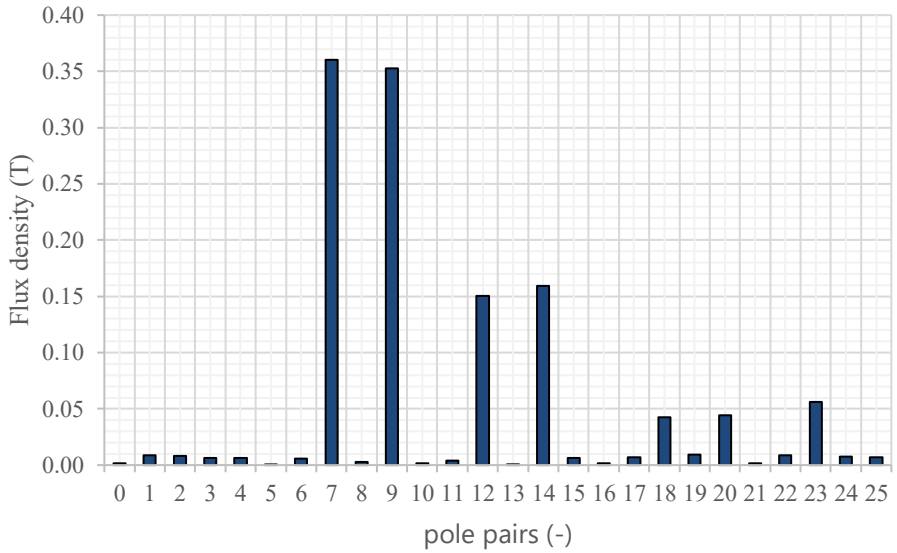

Fig. 3-29 No load outer air gap flux density spectrum of the prototype design

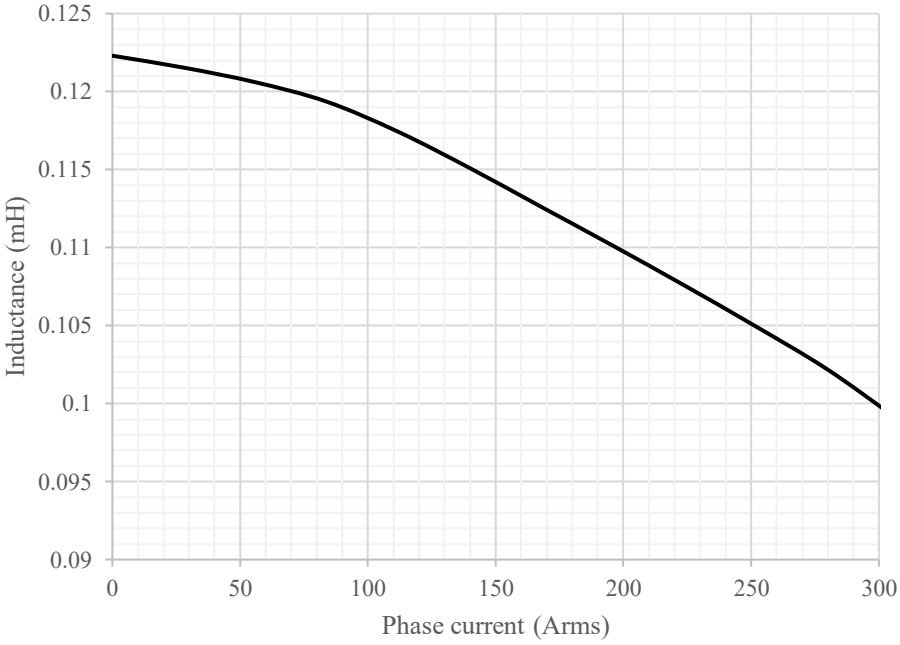

Fig. 3-30 Winding inductance as a function of phase current

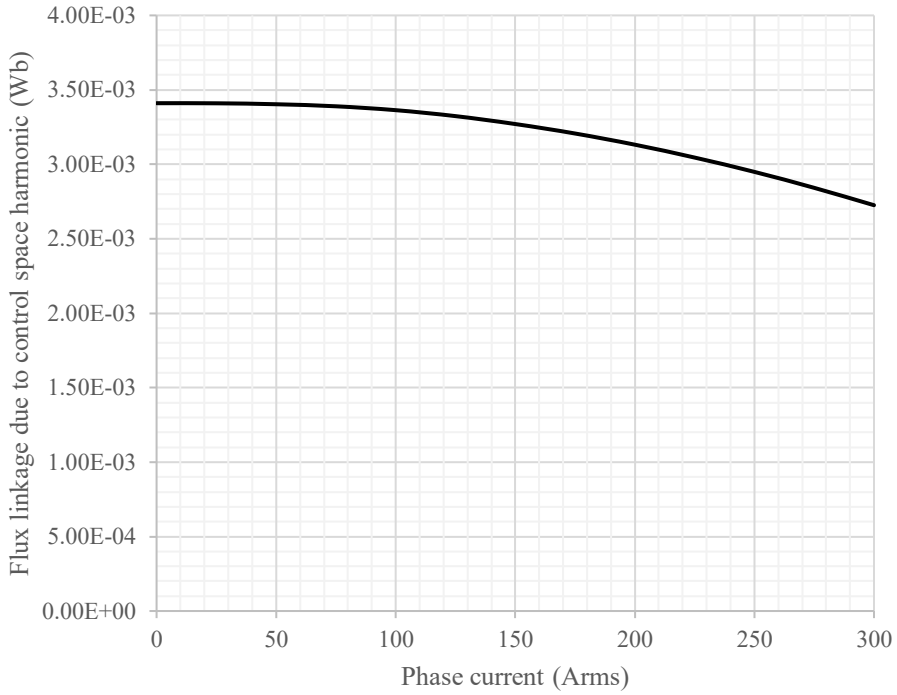

Fig. 3-31 Flux linkage due to the control space harmonic as function of phase current when Id=0

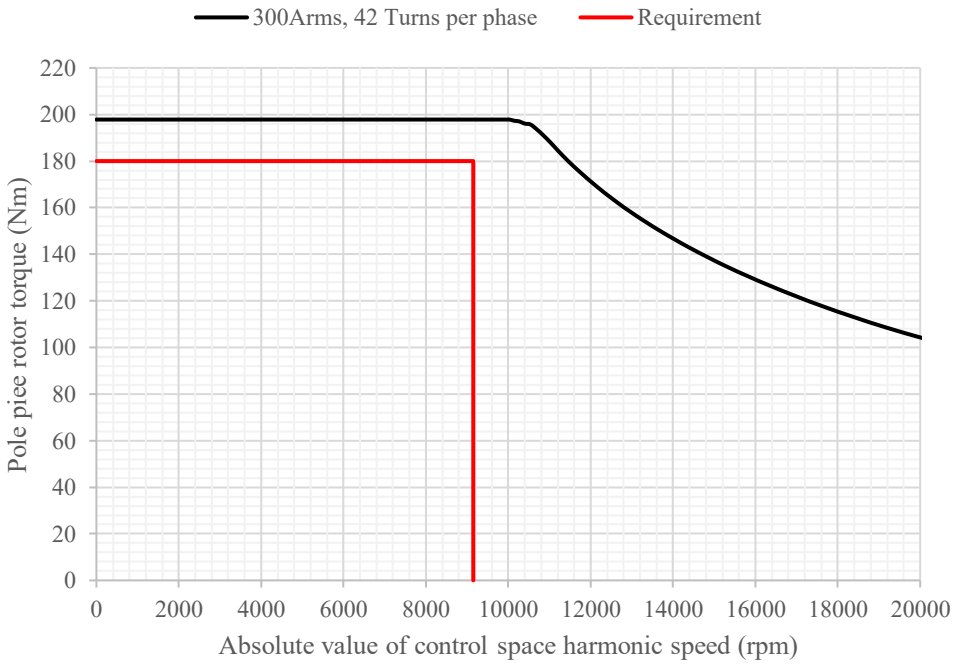

Fig. 3-32 Torque speed characteristic at constant 300Arms phase current

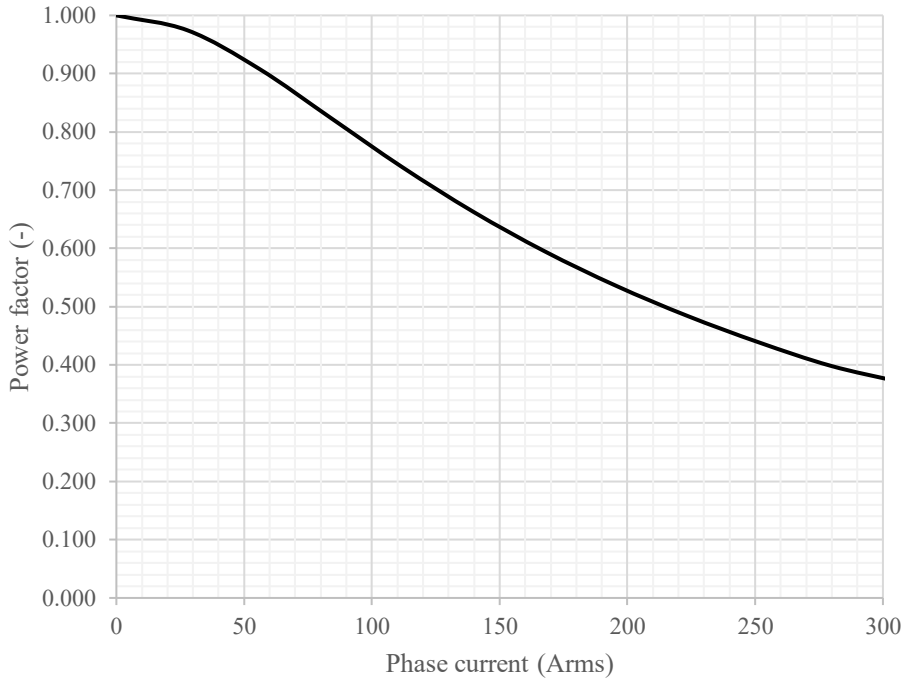

Fig. 3-33 Power factor as a function of phase current, Id=0 operation

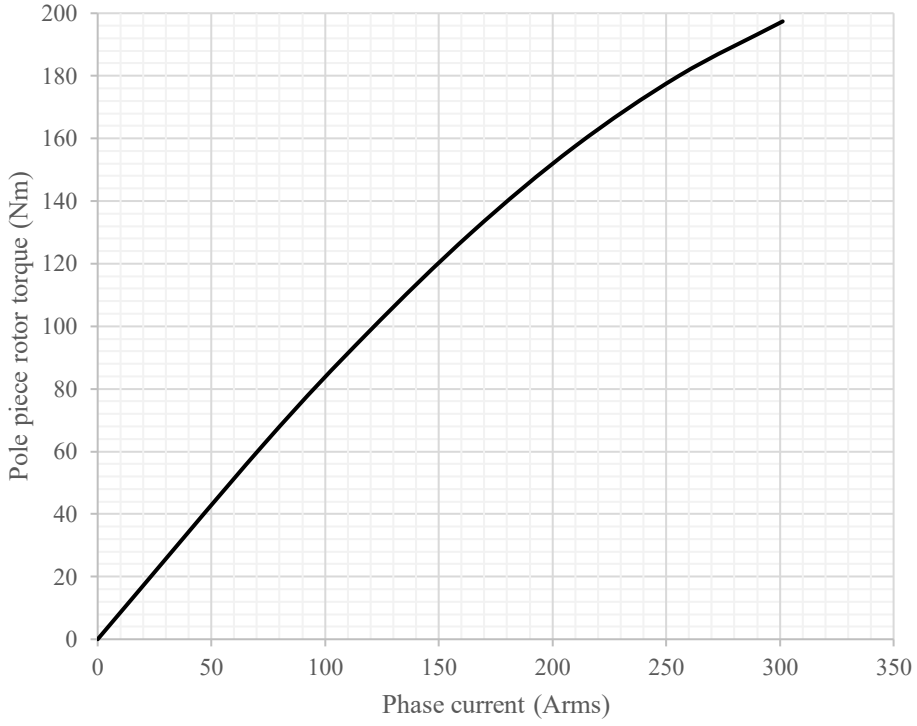

Fig. 3-34 pole piece rotor torque as a function of stator phase current at Id=0 operation

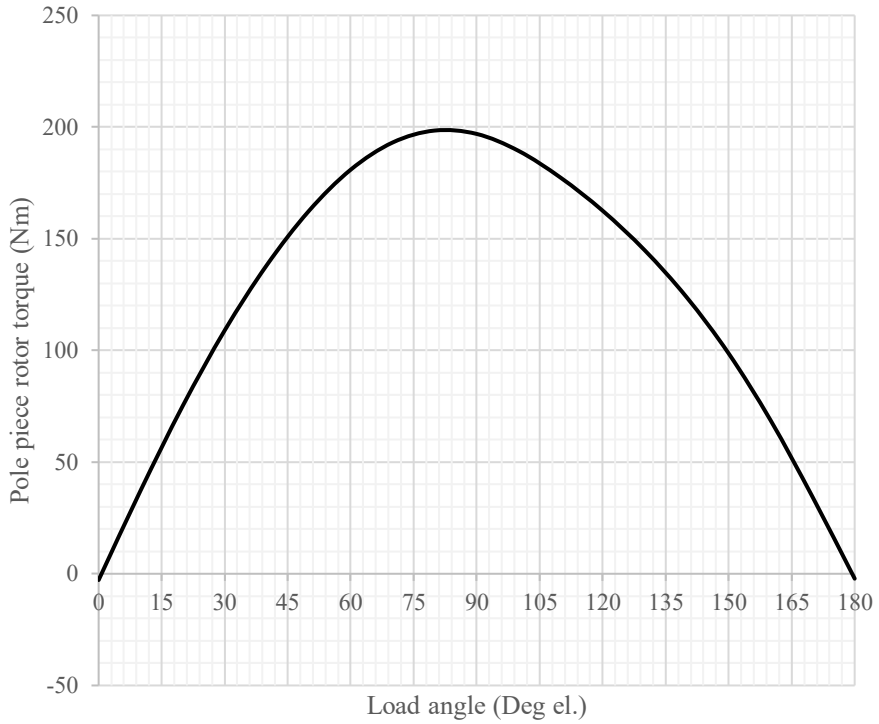

Fig. 3-35 Pole piece rotor torque as a function of internal load angle at 300Arms phase current

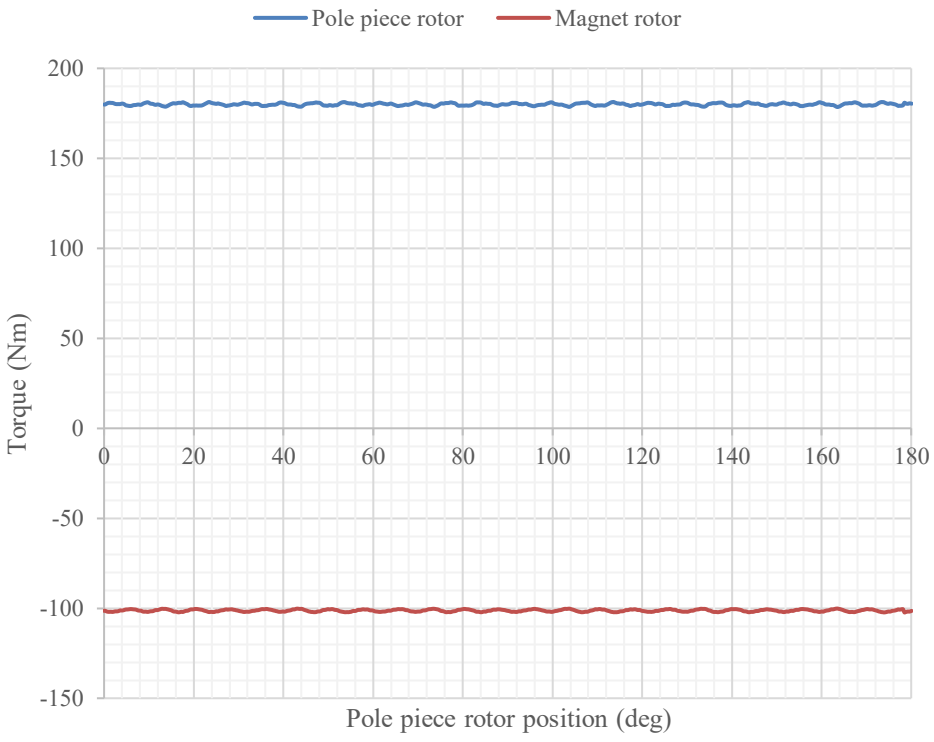

Fig. 3-36 Torque ripple on both rotors as a function of pole piece rotor position

3.5 Conclusion

In conclusion, this chapter focuses on ways of estimating the main dimensions of the dual rotor device for a specific design target. Configuration selection is largely driven by the overall system level design and required power flow. However, inherent magnetic asymmetries as well as constrains imposed by the inverter and stator windings further limit the number of suitable options. Despite this, it was shown that suitable configuration for the given application exists.

Sizing of the dual rotor device for a specific input torque is, in principle, similar to sizing of a surface mounted PM motor since the combination of the magnet rotor and the pole piece could be replaced by an equivalent SPM rotor. However, since the amplitude of the control harmonic is significantly smaller than that created by a state-of-the-art high-performance rotor, achievable shear stress is low even with high levels of stator electrical loading. While the parasitic space harmonic does not contribute to the torque production, it has to be considered for the stator lamination sizing and split ratio selection.

Goodness of a pole piece rotor design could be expressed by means of modulation factors for both the control as well as the parasitic space harmonics. Optimal design minimizes the parasitic whilst maximizing the control space harmonic. However, it is demonstrated that the influence of the pole piece shape on overall torque density of the machine is relatively minor.

It is demonstrated that embedded magnet rotor utilizing flux focusing topology is superior to an SPM rotor at creating high inner air gap flux density. However, designs achieving high air gap flux densities are prone to irreversible demagnetisation of the rotor magnets due to the large effective air gap created by the pole piece rotor and to magnet utilisation.

Finally, the sizing techniques described in this chapter were used to size the dual rotor device for the specific space envelope and torque rating and the lamination profile for all three principal components is shown. Despite the complex salient structure of the device, the sized design exhibits negligible on-load torque ripple even with no skewing.

Chapter 4 Effects of axial leakage

4.1 Introduction

Conventional radial field electrical machines, having only one stator and rotor separated by a relatively thin air gap, are often analysed by means of two-dimensional models where only tangential and radial components of the field are considered and influence of three-dimensional field fringing is ignored. Depending upon aspect ratio of the machine, i.e. ratio of axial length to outer diameter, air gap length and slot design, this leads to a relatively small error between measured and predicted EMF which in most cases could be neglected.

The same, two-dimensional, approach was adopted for initial sizing and basic design of the proposed dual rotor device in the previous chapters. However, the presence of the pole piece rotor between the stator and output rotor creates large effective air gap which, together with short axial length of the device, could lead to significant field fringing at the axial ends of the magnetic circuit.

The effect of axial field fringing on a magnetically geared device is two-fold. Firstly, it reduces the peak transmittable torque and introduces significant error between 2D predicted performance and a manufactured prototype. Secondly, the varying leakage fields could induce eddy currents in electrically conductive supporting structures of the device and in elements of the active magnetic circuit thereby reducing machine's efficiency and increasing electromagnetic drag torque.

Since achievable peak torque for a given volume (often expressed as torque density) is of paramount importance in automotive application and since restrictive packaging given by the target application, introduced in Chapter 3, led to axially short disc-like machine, the field fringing effects are studied in detail in the following chapter using three dimensional FEA.

4.2 Axial leakage in magnetically geared devices

The phenomenon of axial leakage in magnetic gears has been experimentally observed by number of researchers. One of the first observations of apparent difference between performance predicted by two dimensional models and measured on real prototype were mentioned in [24] where measured and predicted values of peak transmittable torque differed by as much as 30%. The authors offered two explanations, firstly mentioning the possibility of axial field fringing in relatively large effective air gap of the prototype and secondly torsional twisting of the pole piece structure at higher loads introducing unwanted skewing and hence reducing transmittable torque. However, neither of the two possibilities were researched any further.

End-effects in magnetic gears were extensively studied in [33] using three dimensional FEA. Authors explored the influence of leading design parameters on axial leakage and concluded that this phenomenon is inherent to magnetic gears and cannot be easily remedied. Performance predictions relying purely on 2D analysis will always lead to large errors. Additionally, influence of the structures supporting the pole pieces were studied and it was recommended to avoid using ferromagnetic materials in close proximity of the magnetic circuit. Practical investigation of end-effects was presented in [69] and implications on efficiency of magnetic gears of various constructions were discussed and experimentally analysed.

In all aforementioned publications, the pole pieces and the large effective air gap they create are mentioned as the major reasons for end-effects and axial leakage. The axial field in pole pieces was experimentally studied in a magnetically geared Pseudo Direct Drive (PDD) motor where pole pieces were instrumented by search coils and voltages induced by axial fields were measured [64]. Fig. 4-1 shows the instrumented pole piece rotor and also defines axial positions of the search coils. The resulting flux density measurement in Fig. 4-2 not only shows the amplitude of axial leakage field exceeding 0.3T in the pole pieces themselves but also shows near sinusoidal variation with pole piece rotor position having period equal to pole piece electrical cycle. In addition, search coils placed in different positions along the pole piece axial length show different amplitude of the axial flux density. The author

concludes that having pole piece laminations exposed to time varying stray field of such amplitude could lead to considerable stray loss and reduced efficiency, however, this is not quantitatively analysed.

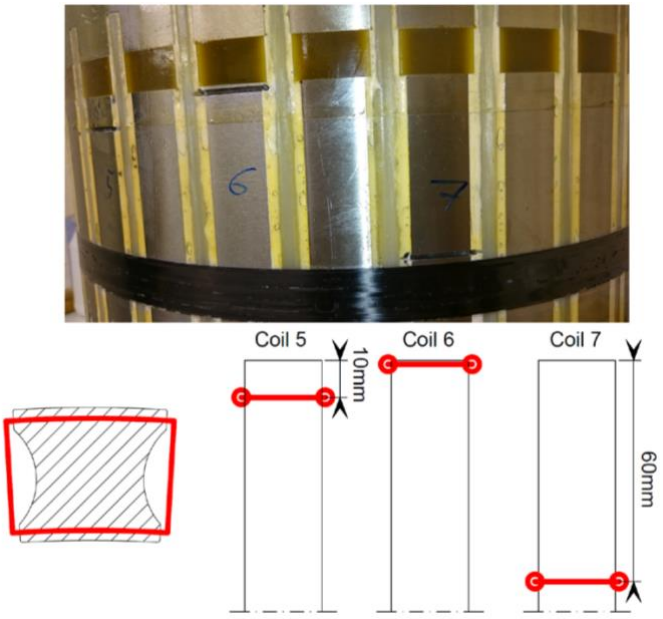

Fig. 4-1 Search coil positions on pole pieces [64]

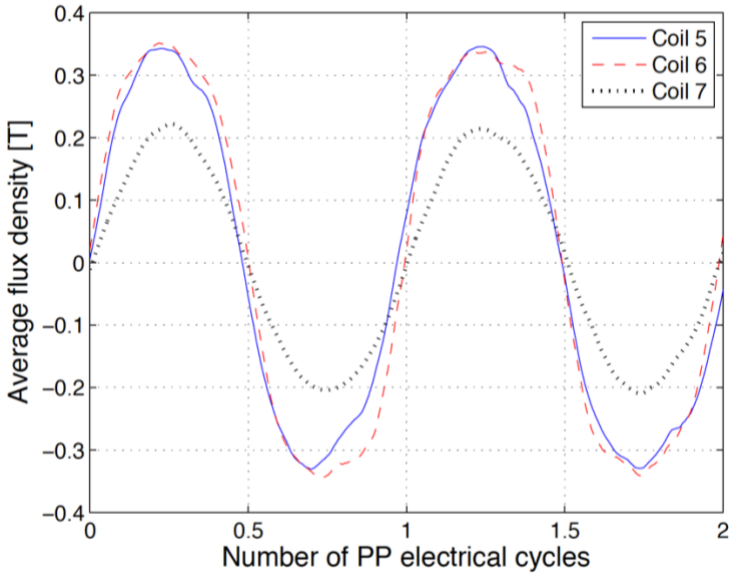

Fig. 4-2 Variation of axial flux density in a pole piece of a PDD machine measured by search coils [64]

4.3 Magnetic anisotropy of laminated stacks

Magnetic circuits of radial field electrical machines are composite structures most often constructed using stacks of laminations where the plane of lamination is perpendicular to the machine axis. Individual laminations within a stack are electrically insulated from each other by a thin layer of insulation coating. From a magnetic field analysis perspective, the insulation coating is not only electrical insulator but also an effective flux barrier since its permeability is close to that of air. Consequently, the insulation layers introduce a degree of anisotropy to the magnetic circuit since the equivalent permeability of a laminated stack becomes different in plane tangential and normal to the plane of lamination [70]. This significantly influences behaviour of electromagnetic devices employing laminated stack and having inherently three-dimensional flux paths but also becomes important when analysing devices where considerable amount of three-dimensional leakage is expected. The degree of anisotropy is often expressed by means of so-called stacking factor which is the percentage of total stack volume occupied by electrical steel. Stacking factor of a laminated stack with known lamination and coating thickness can be computed as follows:

$$k_{fe} = \frac{l_{fe}}{l_{fe} + 2 \cdot l_{insul}} = \frac{l_{fe}}{l_{stack}} \qquad (4\text{-}1)$$

where l_{fe} is lamination thickness and l_{insul} is insulating coating thickness. The equation (4-1) assumes that each side of the lamination is coated with the insulating coating of l_{insul} thickness. Typical coating thicknesses for 0.35mm thick lamination ranges from 1 to 6 μm per side resulting in stacking factors shown in Fig. 4-3.

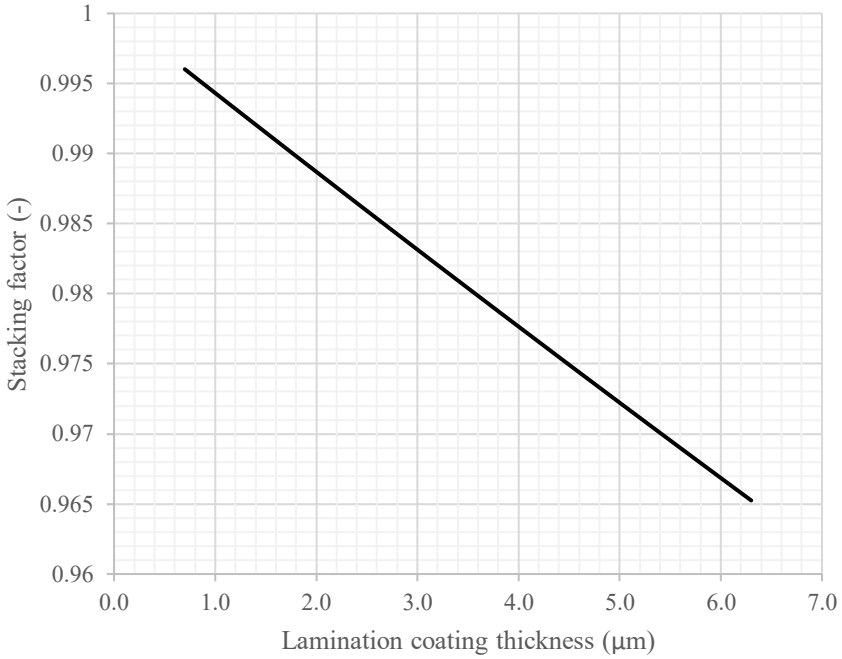

Fig. 4-3 Lamination stacking factor as a function of insulation coating thickness

When lamination stacking factor is known, equivalent permeabilities of stack can be computed using basic magnetic circuit theory. Definition of lamination stack dimensions can be seen in Fig. 4-4. In direction normal to the plane of lamination, flux density of the stack is assumed to be constant and total magnetomotive force is given by a sum of lamination and insulation components, as described by the following equations:

$$B_{stackn} = \mu_0 \cdot H_{insuln} = \mu_{fe} \cdot \mu_0 \cdot H_{fen} \quad (4\text{-}2)$$

$$l_{stack} \cdot H_{stackn} = l_{fe} \cdot H_{fen} + l_{insul} \cdot H_{insuln} \quad (4\text{-}3)$$

where B_{stackn} is normal component of flux density in the stack, H_{insuln} normal component of field strength in the insulation coating, μ_{fe} is lamination permeability, H_{fen} is a normal component of field strength in the lamination, l_{stack} is total stack length and H_{stackn} is normal component of stack field strength. In case of tangential field, total flux passing through the stack is given as a sum of component passing through the lamination and through the layer of insulation, Magneto-motive force is assumed to be the same in both materials:

$$\emptyset_{stackt} = \emptyset_{Fet} + \emptyset_{insult} = H_{stackt} \cdot l_{stackt} \cdot \left(\frac{1}{R_{fe}} + \frac{1}{R_{insul}}\right) \quad (4\text{-}4)$$

$$H_{stackt} = H_{fet} = H_{insult} \quad (4\text{-}5)$$

where $\emptyset_{stackt}$ is tangential flux through the stack, $\emptyset_{Fet}$ is tangential flux through the lamination, $\emptyset_{insult}$ is tangential flux through the insulation layer, H_{stackt} is tangential stack field strength, l_{stackt} is tangential length of the stack, R_{fe} is reluctance of the lamination in tangential direction, R_{insul} is reluctance of the insulation layer in tangential direction, H_{fet} is tangential lamination field strength and H_{insul} is tangential insulation layer field strength. Influence of stacking factor on equivalent permeability in tangential direction is not directly apparent from equations (4-4), (4-5), however, terms R_{fe} and R_{insul} are function of lamination and insulation normal cross sectional area respectively which could be expressed using lamination thickness l_{fe} and insulation thickens l_{insul}.

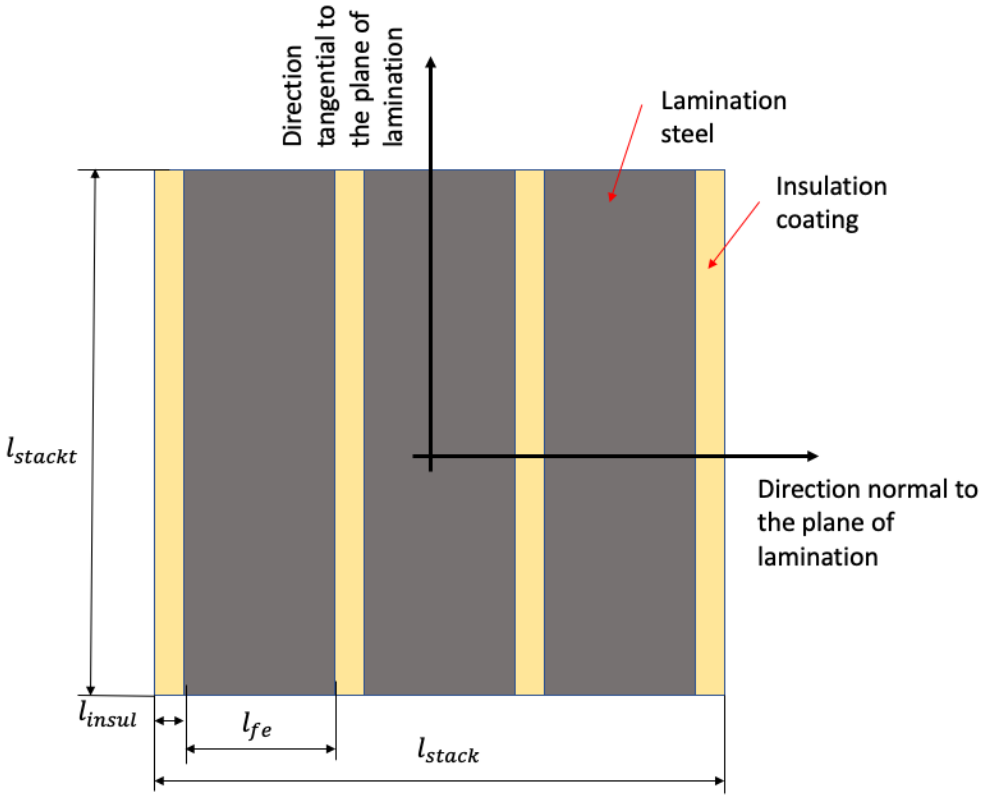

Fig. 4-4 Example of lamination stack with definition of dimensions

Combining equations (4-2), (4-3) and (4-4), (4-5) with the definition of stacking factor in equation (4-1) leads to following expressions for equivalent magnetic permeability of laminated stack in direction normal and tangential to the plane of lamination:

$$\mu_n = \frac{1}{\mu_0} \cdot \frac{B_{stack\_n}}{H_{stack\_n}} = \frac{\mu_{fe}}{(1 - k_{fe}) \cdot \mu_{fe} + k_{fe}} \quad (4\text{-}6)$$

$$\mu_t = \frac{1}{\mu_0} \cdot \frac{B_{stack\_t}}{H_{stack\_t}} = k_{fe} \cdot \mu_{fe} + (1 - k_{fe}) \quad (4\text{-}7)$$

Detailed derivation of both equations can be found in [71]. Using equations (4-6) and (4-7), equivalent BH curves for laminated stacks with known stacking factors can be calculated and expressed graphically as can be seen in Fig. 4-5, where both tangential and normal components were calculated assuming stacking factor of 0.96 (or 96%).

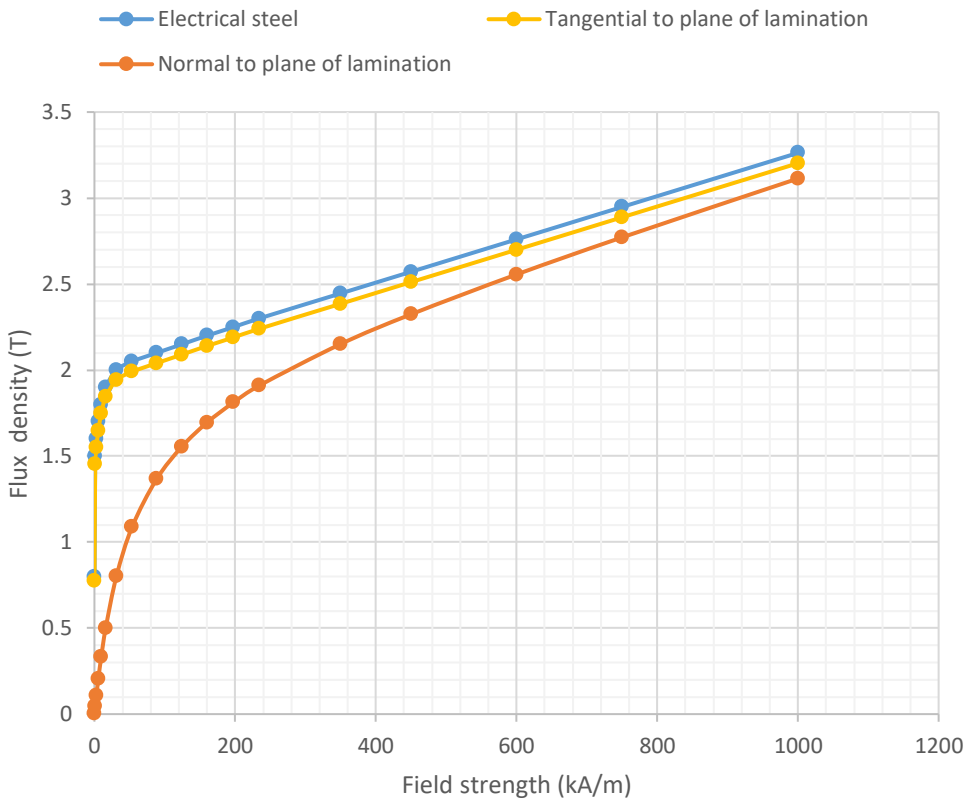

Fig. 4-5 BH curve of electrical steel and equivalent BH curves of laminated stack with stacking factor of 0.96

It is apparent that even though the layers of insulation occupy only a small portion of the overall stack volume, they significantly reduce normal component of equivalent permeability whilst having relatively minor influence on the tangential component. This means that the laminated circuit of a radial field machine, where plane of lamination is perpendicular to the rotor shaft, has significantly higher equivalent permeability in radial than in axial direction.

Sensitivity of equivalent BH curve to different stacking factors was examined in Fig. 4-6. It can be seen that the resultant equivalent BH curve differs dramatically from a pure electrical steel even when stacking factor is as high as 0.98. It is worth noting that the largest difference between solid and laminated steel could be observed at low and moderate levels of field strength since permeability of electrical steel starts to approach that of air once the material becomes saturated and the difference in permeability between laminations and insulations layers becomes less pronounced.

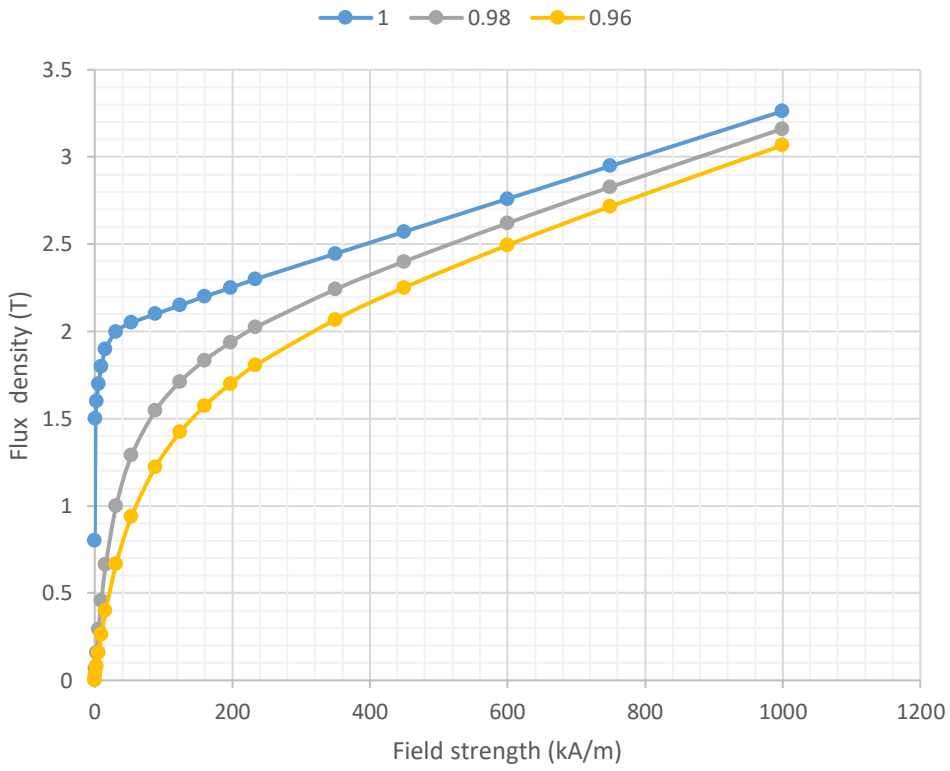

Fig. 4-6 Equivalent BH curves of laminated stack with different stacking factors

4.4 Influence of axial leakage on EMF and torque transmission

For the purpose of comparison with the 2D models of the proposed device, 3D FEA model, Fig. 4-7, was constructed in Opera 3D simulation software using the best simulation practice suggested by the software supplier. Volumes representing stator, pole piece and output rotor stacks were assigned equivalent magnetic material properties as described in the previous section to accurately determine the level of 3D field fringing. Stacking factor for all laminated components was assumed to be 0.98. Axis of the machine coincides with z-axis in the cartesian coordinate system and hence axial leakage field is the field component which has only z-axis component. High density of prismatic elements in the area around the pole piece rotor was used resulting in total of 6.7 million elements in the model. Since the proposed machine is inherently asymmetrical, cyclic symmetry around the z-axis cannot be used. Only one axial half of the device however, can be modelled by imposing tangential boundary condition on x-y plane in the middle. It is important to note that the 3D model only contains magnetically active components of the device and structural parts were assumed to be non-magnetic and non-conductive and hence were omitted. As was the case when modelling the device in 2D, temperature of the magnets was assumed to be 100°C

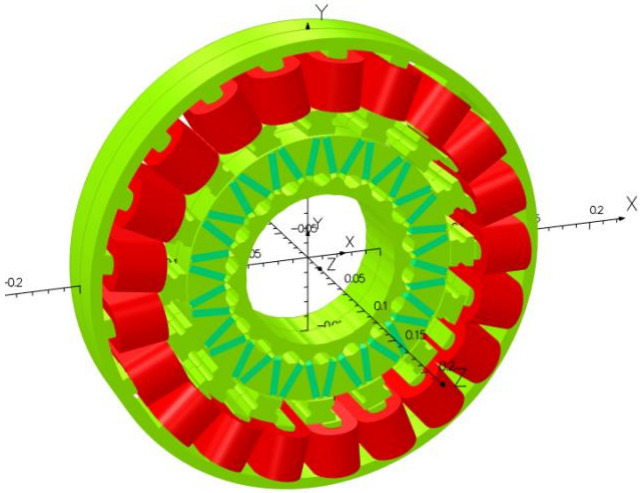

Fig. 4-7 3D model of the dual rotor device with Biot Savart conductors representing the winding

Time varying non-linear solver was used to evaluate EMF waveform. Both rotors were rotated at 2000rpm which, according to fundamental equations described in Chapter 2, results in stator electrical frequency of 233.33Hz and EMF period of 4.3ms. Fig. 4-8 shows resulting EMF waveforms from 2D and 3D simulation and it can be seen that whilst both waveforms have similar harmonic content, difference of approximately 9% in amplitude exists.

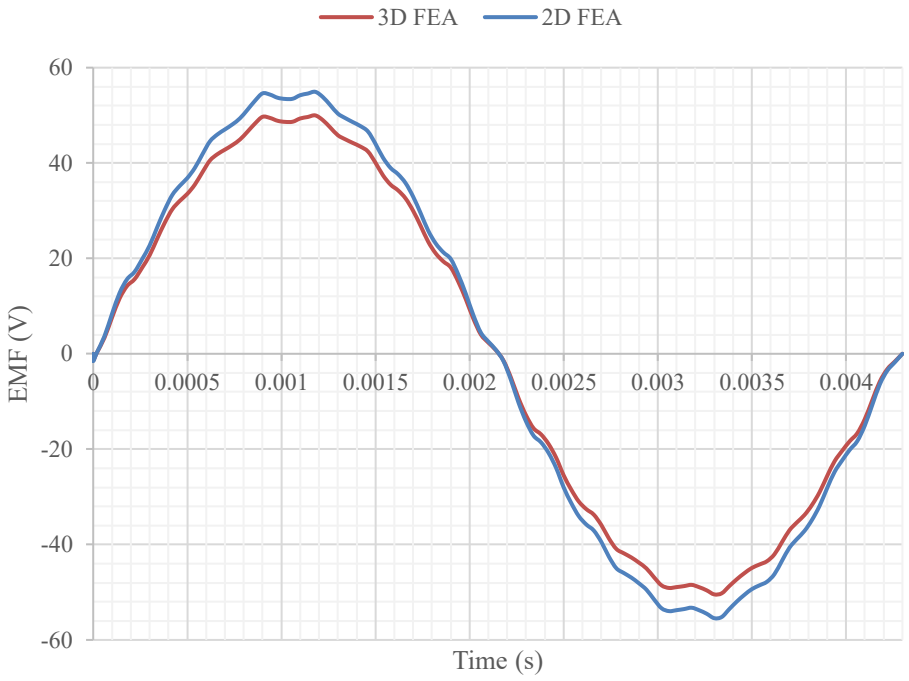

Fig. 4-8 EMF waveform obtained by 2D and 3D FE simulation

On-load performance was evaluated using magneto static simulation, where positions of both rotors were kept constant and stator electrical loading was varied whilst maintaining constant load angle of $\pi/2$ between the useful space harmonic and armature reaction field. Resulting pole piece rotor torque as a function of stator phase current for both the 3D and 2D model can be seen in Fig. 4-9. It is apparent that significant discrepancy between the two models exists and that the difference increases with stator current, suggesting that the axial leakage is a function of magnetic circuit saturation.

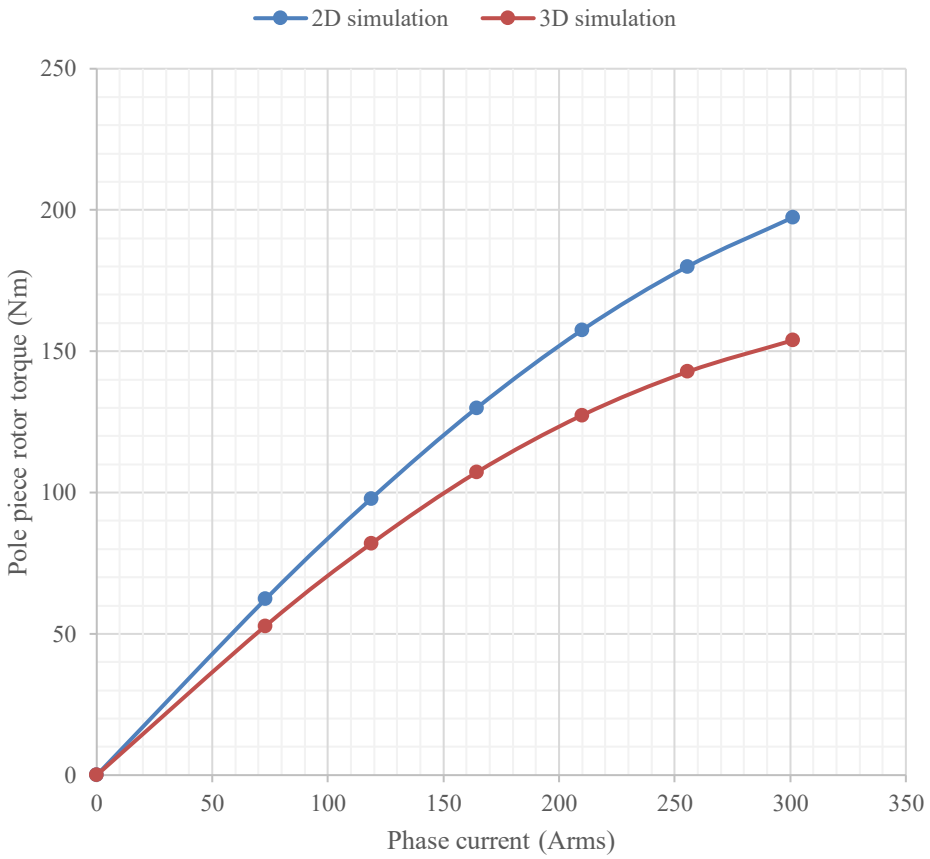

Fig. 4-9 Pole piece rotor torque as a function of phase current at constant load angle

The magnetic circuit of the device is primarily loaded by flux in radial and circumferential direction. As load and saturation of the magnetic circuit increases, reluctance of the flux path in radial and circumferential direction becomes larger, up to the point when axial flux path starts becoming the path of lower magnetic resistance. As a result, more of the useful radial flux starts leaking axially, thus reducing achievable torque for a given current. The 2D model does capture the effect of reluctance increase in radial and circumferential direction, hence the non-linearity of the 2D torque versus current curve, but unlike the 3D model, cannot capture the effects of axial leakage. Difference in percent between 2D and 3D estimated torque as a function of load can be seen in Fig. 4-10. At 300Arms, the difference reaches 30%, suggesting that the machine at this point operates at very low power factor and is heavily saturated.

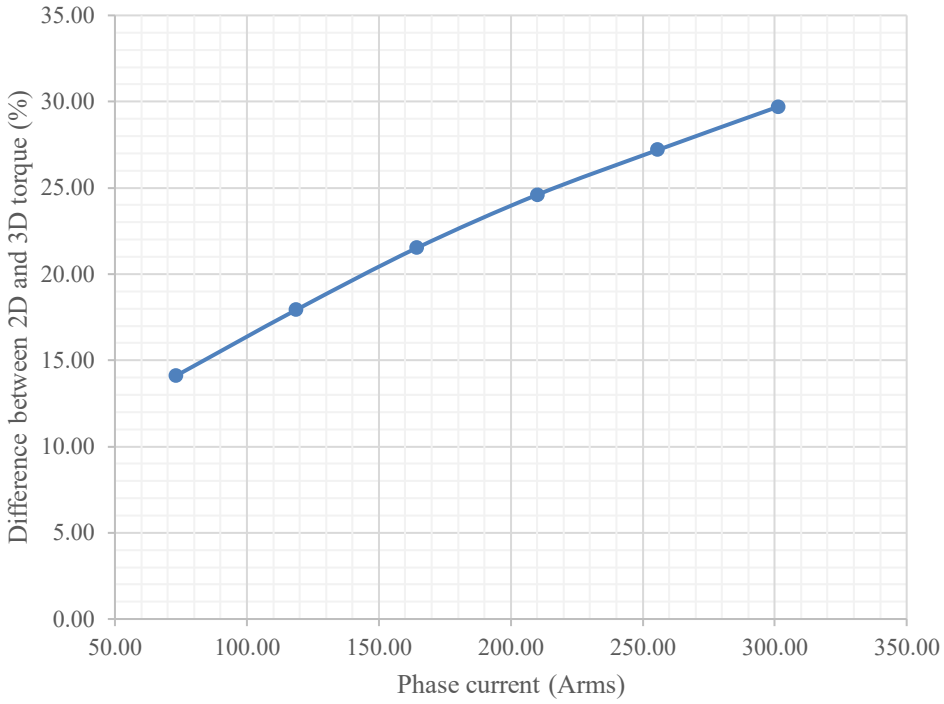

Fig. 4-10 Difference between 2D and 3D predicted torque as a function of phase current

4.5 Axial leakage field of the pole piece rotor

As mentioned previously, 3D effects in conventional radial field machines are often negligible due to radially small effective air gaps and favourable aspect ratios of gap diameter to its length. However, analysis shown in the previous section highlighted that 2D models cannot be relied upon for accurate performance prediction of the device and that considerable amount of axial leakage exists, Fig. 4-11. While both the stator and the output rotor of the dual rotor device are identical to that of a conventional IPM traction motor, it is the pole piece rotor and the resulting large effective air gap where the structure of the dual rotor device differs. Hence leakage field of the pole piece rotor needs to be examined in greater detail. Both static distribution, causing reduction of EMF, as well as dynamic variation, manifesting itself in form of stray loss, of the axial leakage field are of interest.

Assuming that the pole piece rotor shaft in the 3D model of the device coincides with the z axis, axial leakage constitutes of purely z axis component of the field in the model. Fig. 4-12 shows z axis component of flux density on the surface of pole

pieces in magneto static field solution when other components of the device were hidden so as not to obstruct view. It is apparent that in this static condition, each pole piece in the array experience different amplitude and orientation of the z axis field. In addition, it can be seen that the amplitude of z axis flux density can reach 0.4T near the axial edge of some pole pieces.

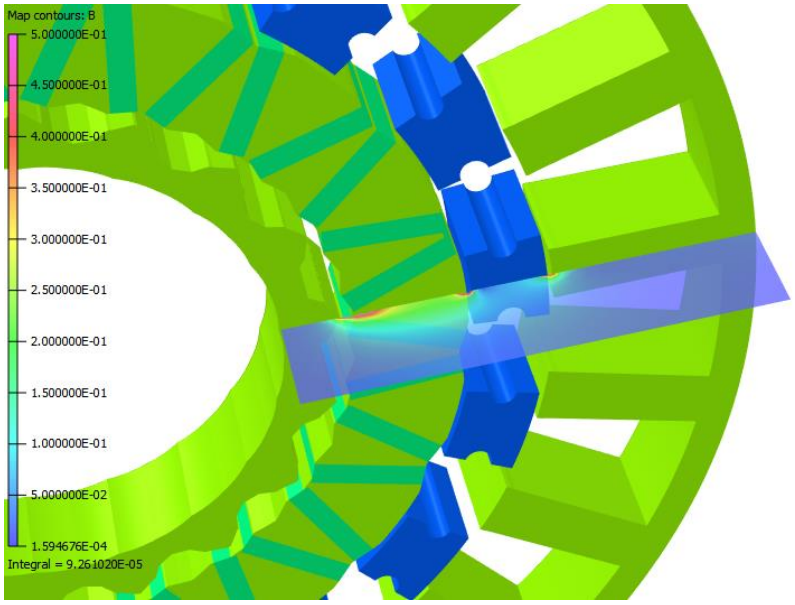

Fig. 4-11 Flux density distribution on a circumferential surface near the axial end of the magnetic circuit

In order to visualize the axial leakage field in a pole piece and examine its variation with pole piece position during normal operation of the device, the static model was solved at various pole piece rotor angular positions, keeping the output rotor position constant and synchronizing the armature reaction with the position of the 7 pole pair space harmonic. Axial flux density of the leakage field was calculated by averaging z axis flux density on cross sectional surfaces, according to the following equation:

$$B_{z\_Appr} = \frac{1}{A_{ppr}} \iint_{A_{ppr}} B_z(x,y) dA_{ppr} \qquad (4\text{-}8)$$

where A_{ppr} is axial surface area of the pole piece stack. Averaging flux density over the lamination surface neglects local variations of the leakage field a replaces surface distribution by a single number. However, the surface field distribution is relatively uniform (apart from the lamination edges) and the single average number can be easily evaluated for number of axial positions, starting from 0, which represents the axial centre of the machine, and ending at ±25mm, thus the leakage field as a function of axial position can be plotted using a simple 2D graph.

Fig. 4-13 shows axial field in a pole piece as it rotates through full 2π mechanical cycle, which constitutes 9 electrical cycles, at four axial positions. It is apparent that the flux density increases with distance from the pole piece axial centre and that the pole piece electrical frequency dominates the axial leakage variation as can be seen in Fig. 4-14 which shows harmonic analysis of the flux density waveform at 22.5mm axial position. Furthermore, axial flux density as a function of axial position can be seen in Fig. 4-15. It must be noted that these results were obtained from a magneto static model which ignores eddy currents induced by the variation of the axial field and the subsequent reaction field associated with them.

As mentioned previously, pole piece rotor leakage field was experimentally observed in [64] where search coils were placed in various positions along a pole piece of a pseudo direct drive machine and EMF induced by the leakage field was recorded as the pole piece rotor was rotated. Average value of leakage flux density was then calculated from measured flux and the known surface area encircled by the search coil. The experimentally obtained axial field variation shows larger amplitude and less distorted waveform which can be attributed to the different construction of both stator and the inner rotor of a PDD machine. In a PDD machine, the pole piece rotor is effectively sandwiched between two arrays of magnets, first mounted on the inner rotor back iron and the second on the stator, therefore the radial distance between pole piece, stator and inner rotor soft magnetic stacks is large. This could lead to higher amplitude of the axial leakage. On the other hand, influence of slot openings is diminished due to large effective air gaps leading to lower levels of distortion. Regardless of the difference between the dual rotor device and a PDD, the experiment clearly demonstrated that this phenomenon exists in magnetically geared devices.

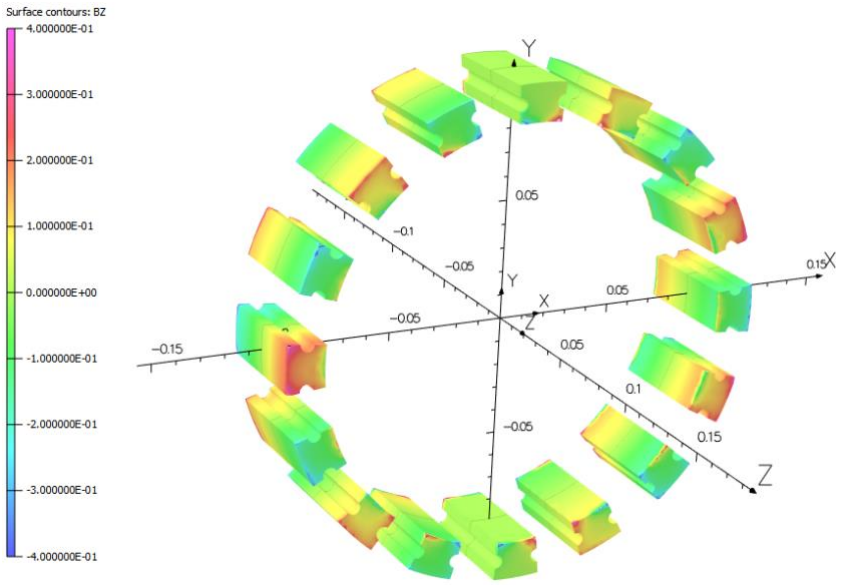

Fig. 4-12 Z axis component of flux density on the surface of pole pieces

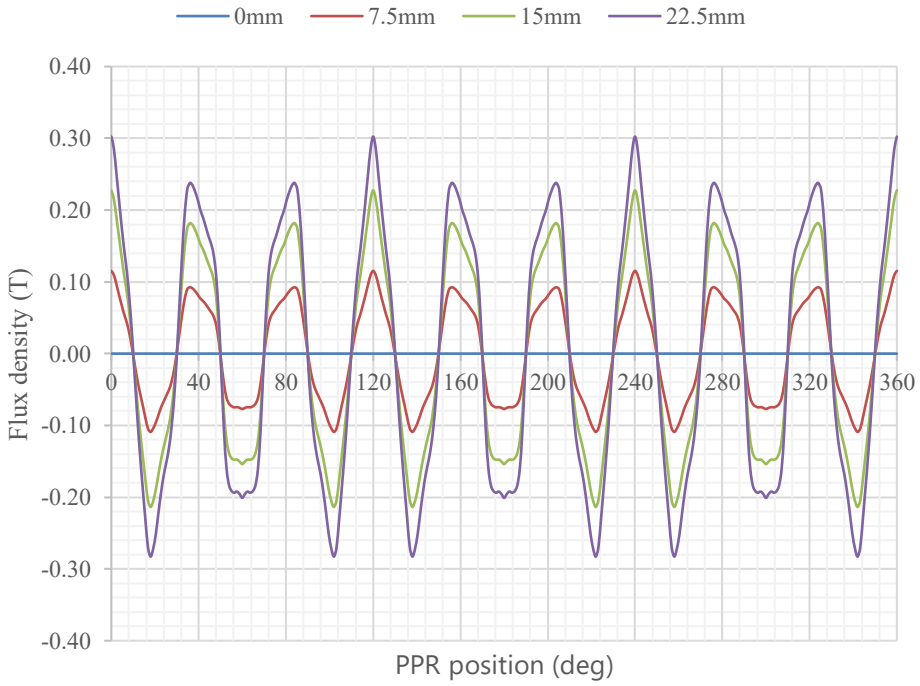

Fig. 4-13 Average axial flux density on a pole piece lamination surface as a function of pole piece rotor position for four axial positions

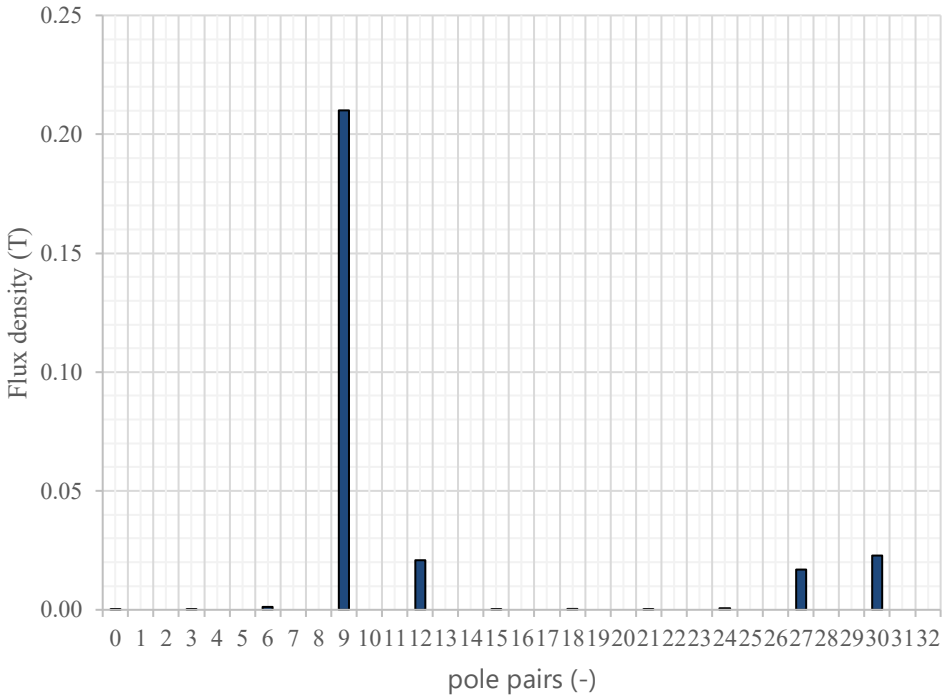

Fig. 4-14 Spectrum of z-axis flux density variation at 22.5mm axial position

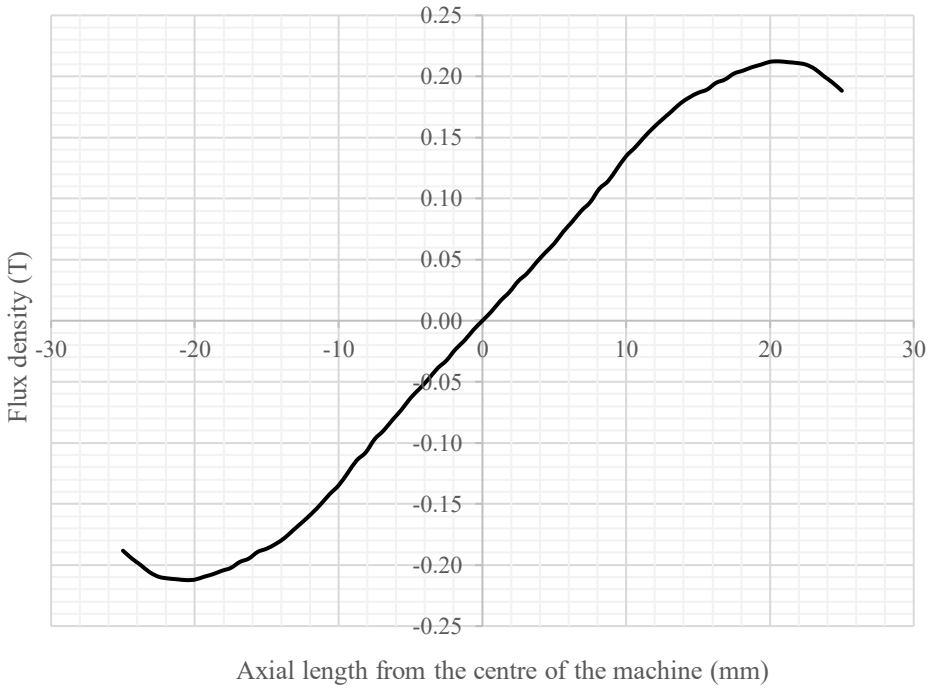

Fig. 4-15 Axial component of flux density vs axial length in a pole piece at 300Arms phase current

It is apparent from Fig. 4-15 that the leakage field varies along the pole piece length, peaking approximately 4mm from its end. Amplitude of the axial field at the edge of the pole piece stack is approximately 0.19T which suggests that structures

outside but in close proximity of the active volume of the device could be exposed to relatively strong time varying fields.

Equivalent average axial flux density experienced by the pole piece rotor could be calculated from its distribution using the following equation:

$$B_{z\_avg} = \frac{2}{L_{fe}} \int_0^{\frac{L_{fe}}{2}} B_z(z)\, dz \qquad (4\text{-}9)$$

where B_z is z axis flux density. While the equivalent average value of flux density ignores its distribution, it provides useful indication of magnitude of axial leakage for different pole piece rotor designs and levels of loading, making their direct comparison clearer. For instance, it can be seen in Fig. 4-16 how the equivalent average value of axial leakage increases as a function of stator current. There are two possible reasons for this. Firstly, armature reaction created by the increase in stator electrical loading naturally raises magnetisation of both air gaps and hence more flux is available to escape via axial leakage paths. Secondly, saturation of the electrical steel reduces its relative permeability and consequently radial flux faces higher reluctance of the magnetic circuit. Referring back to Fig. 4-16, it is apparent that at low levels of field strength, equivalent permeability of stator stack in axial and radial direction differs dramatically. However, once the material crosses the saturation knee point, the difference diminishes, and the stack becomes less effective in guiding the flux in radial direction and more of it escapes axially. When the phase current is zero, the axial leakage field only consist of the no load component created by the magnet rotor which, in case of the proposed design, dominates even when armature reaction is introduced.

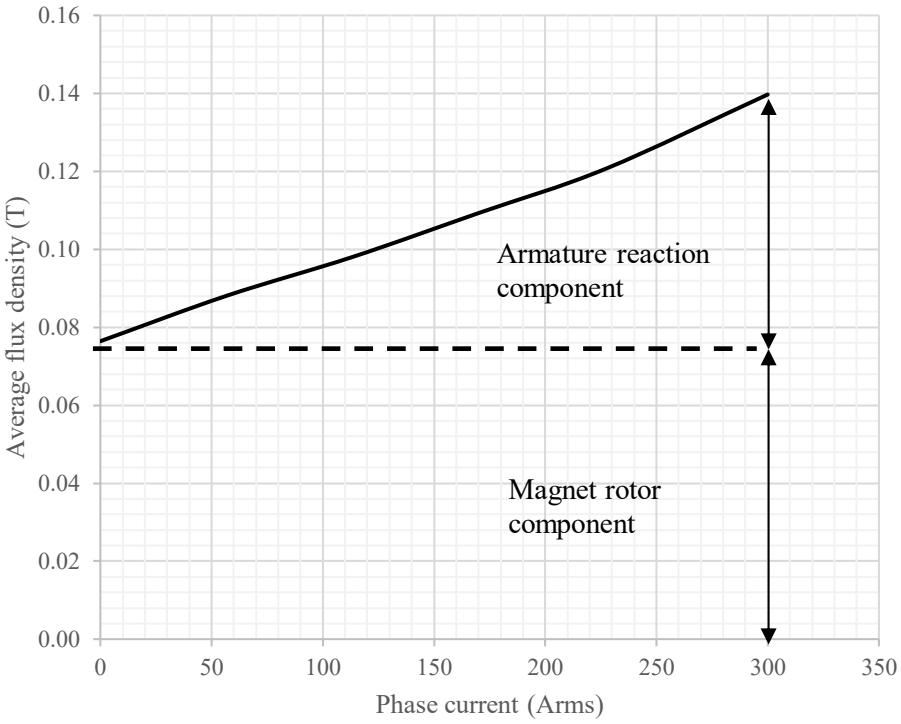

Fig. 4-16 Average value of axial component of flux density in a pole piece as a function of phase current

4.6 Methods of reducing axial leakage in pole pieces

Axial leakage is a parasitic effect which could have significant negative influence on performance of the device and hence it is apparent that its reduction is one of the main design goals. As mentioned before, the axial flux density experienced by each pole piece is time varying and oscillates at frequency depending on combination of input and output rotor speed. This means that, in theory, the stray field can be either suppressed by shielding or by increasing reluctance of the stray leakage path. Shielding coils made of highly conductive material could be wrapped around the pole pieces which would create their own reaction field acting against the stray field, however, this would inevitably result in ohmic loss in the shielding coils and additional heating of the rotor. The second, lossless, way of minimizing the leakage field is by selectively increasing reluctance of the magnetic circuit in the axial direction by introducing elements with low permeability into its construction. From

the cost-conscious automotive industry perspective, the second option seems more practical and hence it will be further analysed.

Influence of insulation layers on tangential and normal equivalent permeability of laminated stacks was discussed in one of the previous sections and it was concluded that axial permeability can be significantly reduced even at relatively high values of stacking factor. Each layer of insulation effectively behaves like a flux barrier for the axial field. In conventional machines, the aim is to achieve as high stacking factor as possible in order to fully utilize the space occupied by the magnetic circuit. However, the dual rotor device could benefit from reduced stacking factor, particularly for the pole piece rotor stacks. Artificially reduced stacking factor for the purpose of axial leakage minimisation can be viewed as an introduction of distributed flux barrier to the pole piece rotor construction. This could be achieved simply by increasing the thickness of the insulation layer on each lamination within the stack. While thickness of insulation layers could be gradually increased towards the axial ends of each stack, where axial leakage reaches its peak, this would complicate the stack assembly process and is unlikely to be adopted in practice.

One of the disadvantages of the distributed flux barrier is that it reduces stacking factor even in portion of the magnetic circuit where leakage field is relatively weak, i.e. close to the axial centre of the machine. This could be overcome by using high stacking factor stacks together with concentrated flux barriers positioned in areas of high axial flux density. From a magnetic point of view, the only requirement for the concentrated flux barrier is low permeability and hence air is the ideal material. However, other structural non-magnetic materials could be used for both suppressing the axial leakage and for improving structural strength of the pole piece rotor. For instance, continuous rings made of non-magnetic and electrically non-conductive glass fibre composite could form the barriers. Potential disadvantage of concentrated flux barriers is that pole piece stacks need to be split into multiple components which may make manufacture and assembly more complicated.

As a form of concentrated flux barrier can be seen the construction where axial length of the pole piece rotor is shorter than stator and output rotor stacks. Advantage of such construction is that it does not require splitting of pole piece rotor stacks into multiple components, the stacks are simply made shorter when the rotor is being

assembled. On the other hand, it requires the supporting structure of the pole pieces to enter the active volume of the device, in order to be in direct contact with the pole piece stacks, and therefore it is important to consider their magnetic and electrical properties so as not to introduce a source of eddy current loss.

Fig. 4-17 shows axial cross-sectional view of modified pole pieces as described in the previous paragraphs. Option a) is a standard pole piece with the same axial length as the output rotor and stator stacks, stacking factor of 0.98 and no flux barriers. This is the default construction against which other options will be compared. Option b) denotes a pole piece construction with artificially reduced stacking factor while c) is a pole piece with reduced axial length. Options d) to f) show different numbers of concentrated flux barriers incorporated into pole piece construction. In case of d) there are two 1.4mm long (length of four 0.35mm thick laminations) flux barriers located 8mm from either end of the pole piece. Design e) has four 1.4mm barriers in symmetrically positioned at 5 and 9mm from the pole pieces ends. Design f) has six 0.7mm barriers positioned at 4, 9 and 14mm away from pole piece ends. Whilst other pole piece designs with flux barriers are certainly possible, the three aforementioned designs were chosen as examples for further analysis.

Influence of flux barrier design on axial flux density can be seen in figures Fig. 4-18, Fig. 4-19 and Fig. 4-20. It is apparent that employing concentrated flux barriers in the area with the highest axial flux density leads to the most significant reduction of average axial field across the pole piece. However, this concept has relatively minor effect on the level of leakage at the end of the pole piece stack as the leakage field tends to concentrate there. Both pole pieces with reduced axial length and reduced stacking factor manifest lower values at the ends of the stack and more even distribution of the axial field. Comparison of different flux barrier configurations and their impact on axial field as well as peak transmittable torque at constant 300Arms phase current can be seen in Tab. 4-1. Again, equivalent average value of axial flux density along the pole piece lengths was used so that different designs can be compared on the basis of a single number rather than a complex field distribution.

While suppression of axial field by pole piece modification is effective, it comes at the cost of reduced transmittable torque since introduction of flux barriers into the pole piece rotor construction effectively reduces the active axial length of the device.

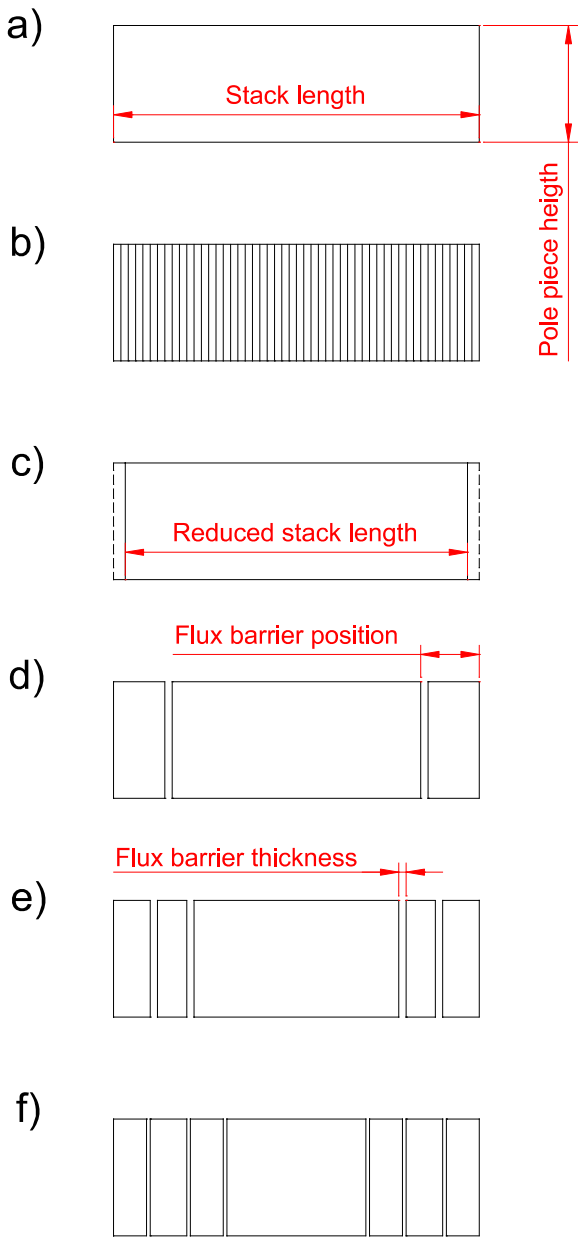

Fig. 4-17 Pole piece constructions aiding in minimizing axial leakage

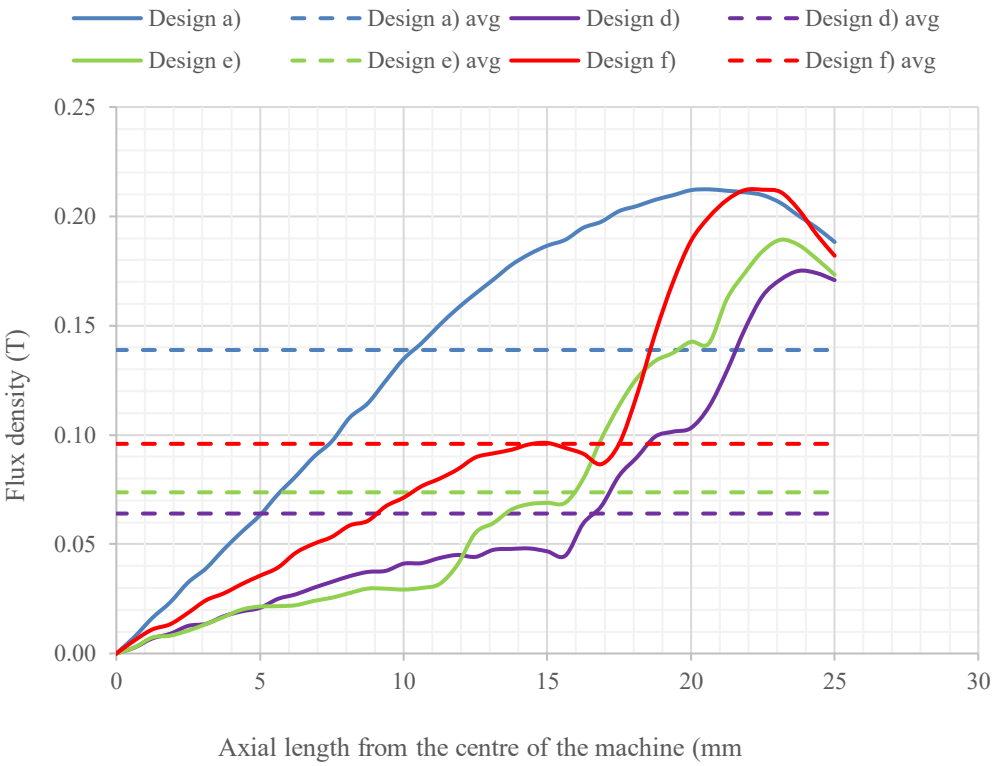

Fig. 4-18 Influence of concentrated flux barriers on axial leakage field for four PPR designs

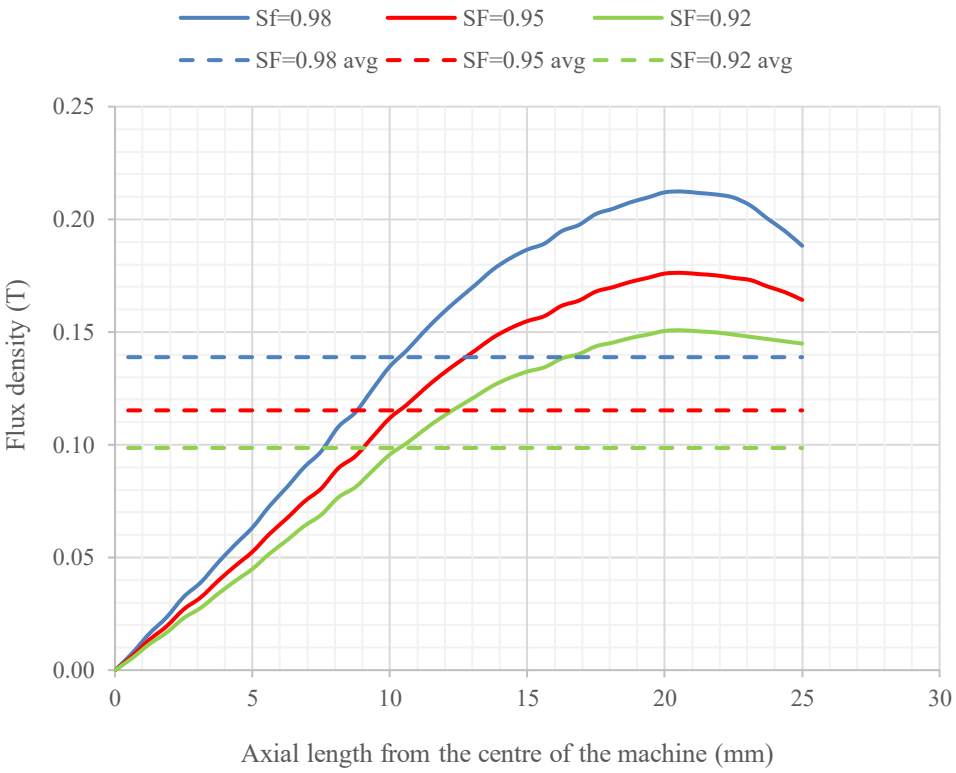

Fig. 4-19 Influence of stacking factor on axial leakage field

It is apparent from the table that the proposed modifications indeed reduce the transmittable torque, however, the reduction is relatively small compared to significantly lowered values of average axial field. For instance, pole piece rotor with 0.92 stacking factor reduces average axial field by approximately 30% but the difference in transmittable torque is only 1%. The construction with six distributed flux barriers seems to be the most efficient at supressing the leakage field, however, it also comes with the highest torque penalty of -4.5% compared to the unmodified pole piece rotor. The reduction of active length by the flux barriers is partially compensated for by the magnetic leakage reduction. For instance, 50mm long pole piece rotor having 0.98 stacking factor and six 0.7mm long flux barriers gives total active (or effective) pole piece length of approximately 44.9 mm equating to 8.4% reduction in active length. However, peak transmittable torque at 300Arms phase current is only reduced by 4.5% while average z axis flux density is decreased by 54%.

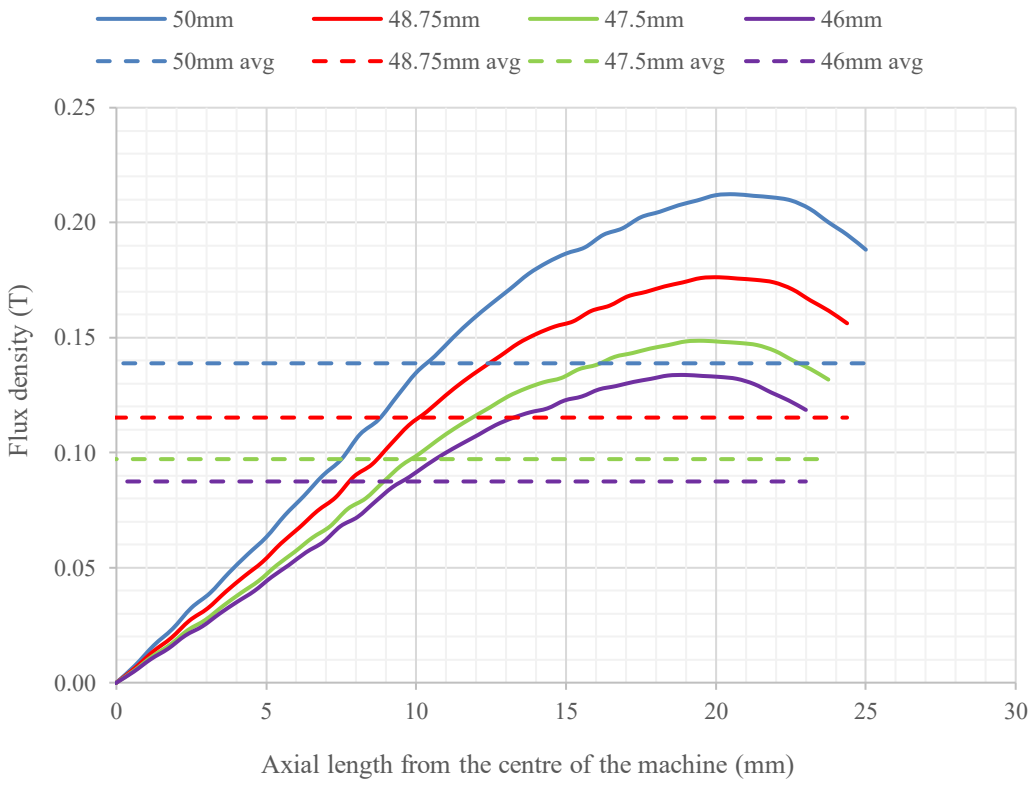

Fig. 4-20 Influence of pole piece shortening on axial leakage field

Tab. 4-1 Average axial flux density and pole piece rotor torque at 300Arms

PPR construction	Bz avg (T)	ΔBz avg (%)	PPR Torque (Nm)	ΔTorque (%)
Full, SF=0.98	0.139	0.0	155.6	0.0
Full, SF=0.95	0.116	-16.5	155.3	-0.2
Full, SF=0.92	0.098	-29.5	154.1	-1.0
Stack shortened by 1.25 mm	0.115	-17.3	155.1	-0.3
Stack shortened by 2.5 mm	0.097	-30.2	153.1	-1.6
Stack shortened by 4 mm	0.088	-36.7	150.9	-3.0
2 flux bariers (2x1.4mm)	0.096	-30.9	152.2	-2.2
4 flux barriers (4x1.4mm)	0.074	-46.8	150.6	-3.2
6 flux barriers (6x0.7mm)	0.064	-54.0	148.5	-4.5

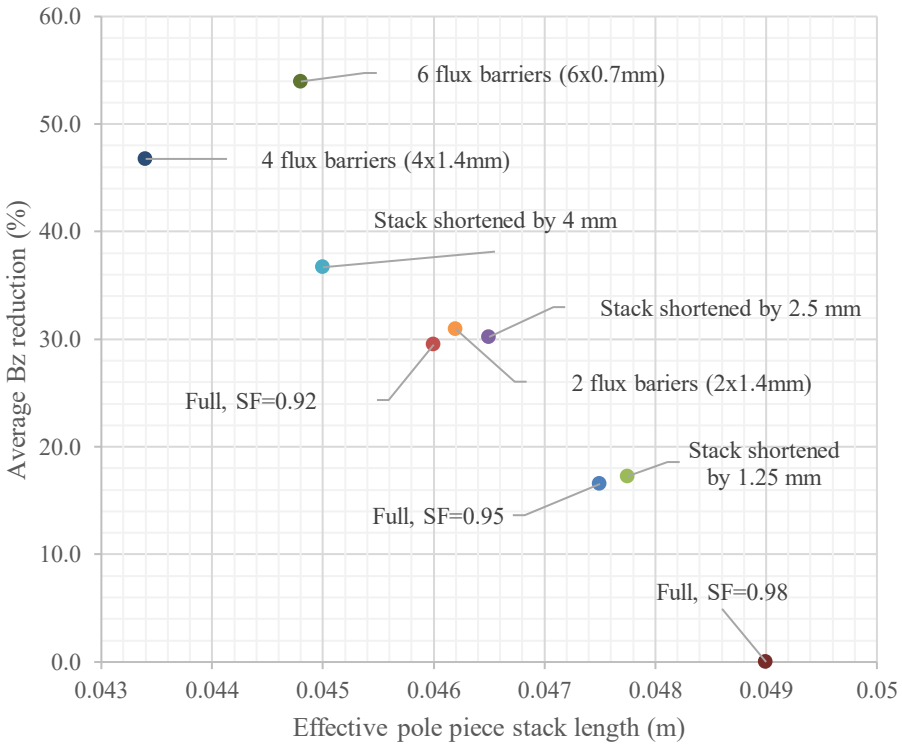

Fig. 4-21 Average axial flux density reduction as a function of effective pole piece stack length

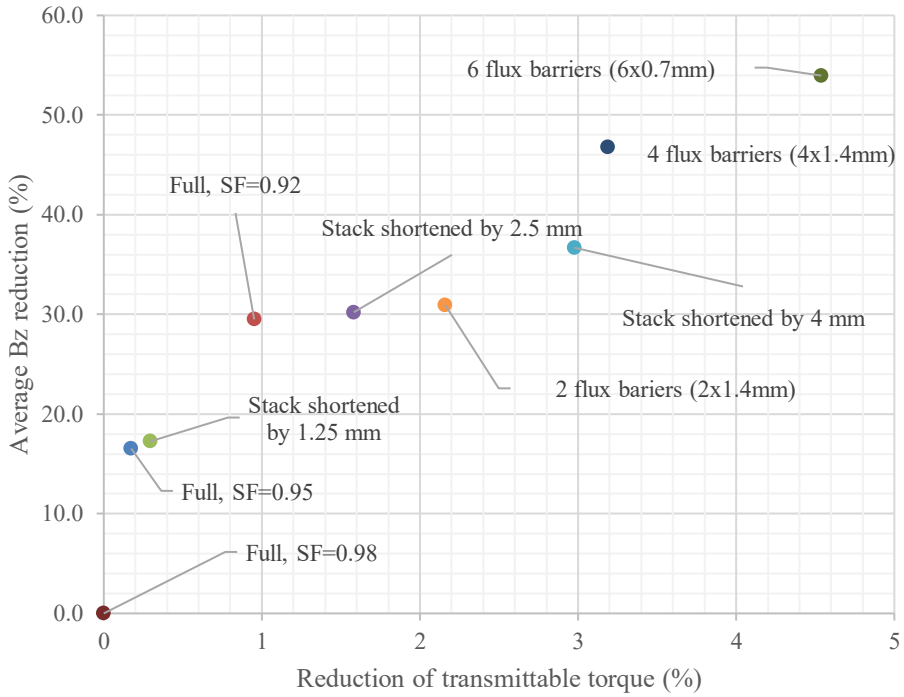

Fig. 4-22 Average axial flux density reduction as a function of reduction of transmittable torque

All above mentioned methods of reducing equivalent axial permeability of the pole piece stack achieve the goal by reducing effective stack length, i.e. length of the stack purely occupied by steel. Relationship between effective stack length and reduction of axial field is examined in Fig. 4-21. It can be seen that correlation between effective stack length and leakage field exists, however, leakage field amplitude is not purely a function of effective stack length. For instance, it can be seen that pole piece rotor designs with 0.92 stacking factor, two 1.4mm long flux barriers and 2.5mm stack reduction have similar effective stack lengths as well similar reduction of the leakage field density. However, the design with six 0.7mm flux barriers is more effective at reducing leakage than the design with four 1.4mm barriers even though its effective stack is longer. Similarly, Fig. 4-22 shows correlation between reduction in the leakage field and reduction in transmittable torque for all designs and while. Optimal design is the one which results in maximal reduction in leakage field and minimal reduction (or even increase) of transmittable torque.

4.7 Axial leakage field of stator and output rotor

Axial leakage field in the pole piece rotor and its suppression was discussed in detail in the previous sections. It is, however, worth noting at this point that the phenomenon of axial leakage is not limited to the pole piece rotor structure. The other two principal components of the machine are subject to it as well with the same negative consequences.

In case of pole pieces, axial flux density is relatively uniformly distributed across the lamination surface and while averaging it does neglect local variations of the field, the average value is still a useful indicator of the overall axial field and allows for visualisation of field distribution along a pole piece. Axial leakage field of the stator, however, exhibits large variation with most of the axial field being concentrated in the tooth tip region near the axial ends of the stack, as can be seen in Fig. 4-23 where its distribution is plotted for a situation where the machine was operated at 300Arms phase current. According to the model, axial field at the edge of the tooth tip could exceed 0.4T.

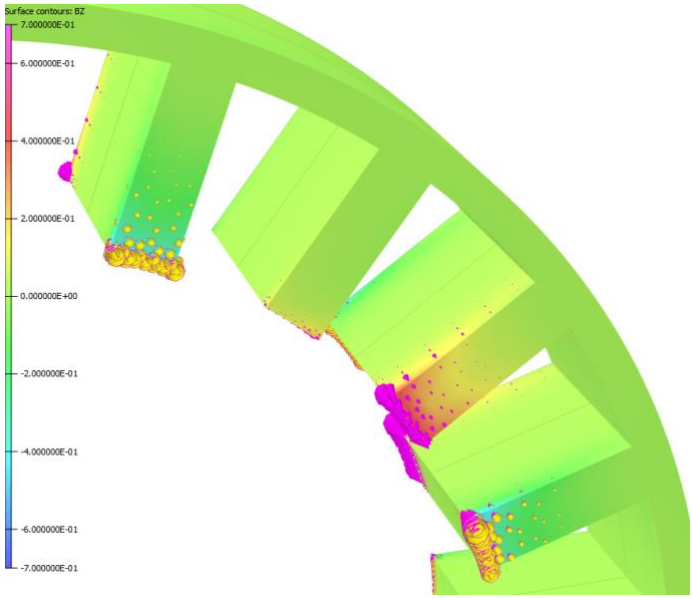

Fig. 4-23 Stator axial flux density distribution at the surface of the stator on load

Similarly, Fig. 4-24 shows axial flux density distribution on the surface of the magnet rotor. While the amplitude is significantly higher than in the case of the stator and the pole piece rotor, the axial field is likely to be dominated by DC component with only small variation caused by pole piece and stator relative motion.

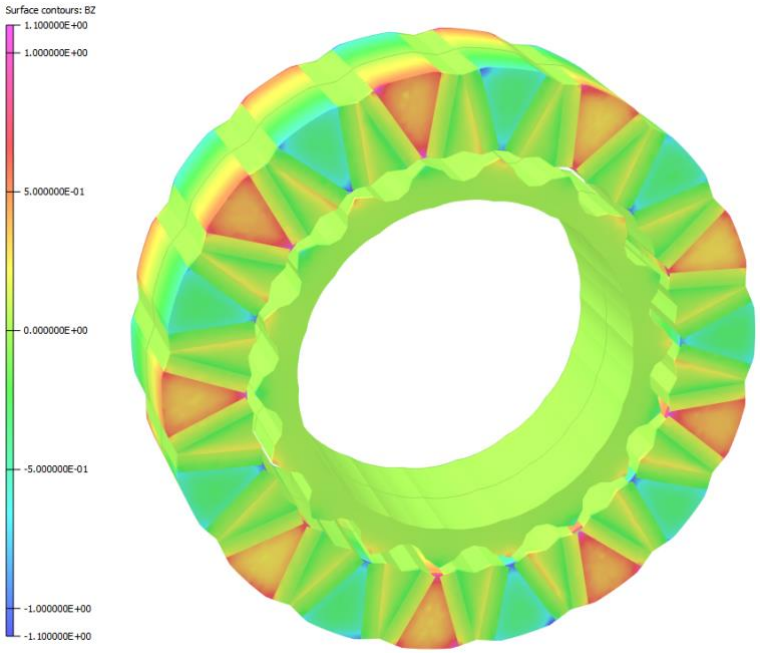

Fig. 4-24 Axial field distribution on the surface of the output rotor

From the practical standpoint, the methods of axial field reduction in pole piece rotor introduced in the previous section are equally applicable to other principal components of the device. Inclusion of distributed or concentrated flux barriers could reduce the leakage at the cost of effective stack length. While loss of useful flux due to leakage in all principle components is generally unwanted (unless high leakage inductance is a design goal) it is the field's time variation and consequent eddy current power loss, which can be more problematic. Eddy current stray losses will be discussed in detail in the following chapter.

4.8 Conclusion

Axial leakage forms a significant part of the overall leakage field of the proposed device and it has considerable impact on both EMF and static transmittable torque. Pole piece rotor and the subsequent high effective air gap of the device was

identified as the primary cause of the high axial leakage. It was demonstrated in simulation that large discrepancy between EMF and transmittable torque at constant electrical loading predicted by 2D and 3D FE analysis exists.

It was shown that axial leakage could be significantly reduced by means of reducing equivalent permeability of the pole piece stack in axial direction and few construction methods for achieving this were presented. However, even though the axial leakage field could be reduced, this does not lead to increase in transmittable torque for a given stator electrical loading as the reduction of axial permeability effectively removes active material, needed for the primary radial field, from the pole pieces making the effective stack length shorter. The reduction of torque is within 5% of the peak torque and thus relatively small compared to reduction of axial field which can exceed 40%.

Even though the reduction of axial leakage field does not seem to lead to increase in transmittable torque (or torque density) of the device, its reduction is still an important design goal since its time variation during dynamic operation of the device could lead to considerable stray eddy current power loss. Impact of stray fields on efficiency of the device will be discussed in the next chapter.

Chapter 5 Electromagnetic efficiency

5.1 Introduction

Loss calculation is an important part of electric machine design as it feeds into thermal analysis and also makes it possible to perform system level efficiency assessment which in case of hybrid drivetrains translates to estimates of fuel consumption. Based on the discussions in Chapter 3, a device with 7 stator poles, 16 pole pieces and 9 pole pair magnet rotor was sized for the specified space envelope and required rating. Having defined dimensions of each of the principal components and analysed the effects of axial leakage on torque transmission, loss analysis of the proposed device could now be performed.

In case of conventional electrical machines, efficiency or overall loss is often visualized in a form of a map having two axes, one representing rotor speed and the other shaft torque. Evaluation of efficiency of the dual rotor device is more complex due to the fact that the device has two shafts able to rotate at different speeds and also transmitted torque can vary with stator electrical loading. Each operating point of the device is therefore defined by three independent variables and hence efficiency (or loss) need to be expressed in a form of a three-dimensional cube with two speed axes and one torque axis. Purpose of the following discussions is to identify all relevant loss mechanisms and investigate their dependency on the aforementioned three variables in order to quantify overall efficiency of the proposed device.

The discussions in this chapter are limited to losses of purely electromagnetic nature and mechanical losses, such as those due to bearing friction or aerodynamic drag are not considered. In addition, the machine is assumed to be supplied by source of sinusoidal currents without any harmonic distortion. Influence of voltage pulse width modulation on the device is, therefore, neglected.

5.2 Winding losses

Winding losses, more commonly referred to as copper losses, tend to be one of the dominant loss mechanisms present in all electrical machines equipped with windings carrying electrical current and the dual rotor device, having conventional windings embedded in the slots of the stator, is no exception. Accurate estimation of copper loss is crucial at the design stage as winding insulation is one of the most thermally sensitive components of an electrical machine with significant impact on its lifespan.

5.2.1 Winding loss mechanisms

Generally speaking, total winding loss in electrical machines could be divided into four categories [72] [73]:

1. Joules losses (DC copper loss =$3 \cdot R_{phase} \cdot I_{ph}^2$)
2. Losses due to current circulation between parallel strands (redistribution of current within wire bundle)
3. Losses due to current circulation between parallel coils
4. Losses due to current redistribution within conductors

The first category, Joules losses, is the most common one and it refers to loss created by the flow of current through a resistive conductor. Out of the all loss mechanisms, Joules loss is the only one which does not depend on frequency and is purely function of current loading of the winding. Losses due to circulation between either parallel strands or parallel coils occur when difference in induced EMF between parallel connected elements of the winding exists. For instance, leakage field crossing the slot tends to be non-uniform and hence two parallel strands belonging to the same turn can be exposed to different amplitude of the leakage field as they cannot physically occupy the same space. Similarly, parasitic flux harmonics could lead to difference in emf among parallel connected coils belonging to the same phase. Both of these aforementioned loss mechanisms could be eliminated by design and are not always present in all winding designs. Circulation between parallel strands could be eliminated by strand transposition while series connections of phase coils eliminates the possibility of current circulation between them. However, both solutions are not always possible or desirable. Lastly skin and proximity effect losses

refer to power loss caused by eddy current flow induced in conductors by field generated by the conductors themselves or by neighbouring conductors.

5.2.2 Cross slot leakage of the dual rotor device

The term cross slot flux leakage is the portion of stator flux which rather than entering the air gap closes the loop around the coils by crossing the slot. While it is present in all electrical machines, presence of the pole piece rotor structure and the resultant large effective air gap exacerbate its amplitude and increases AC winding loss.

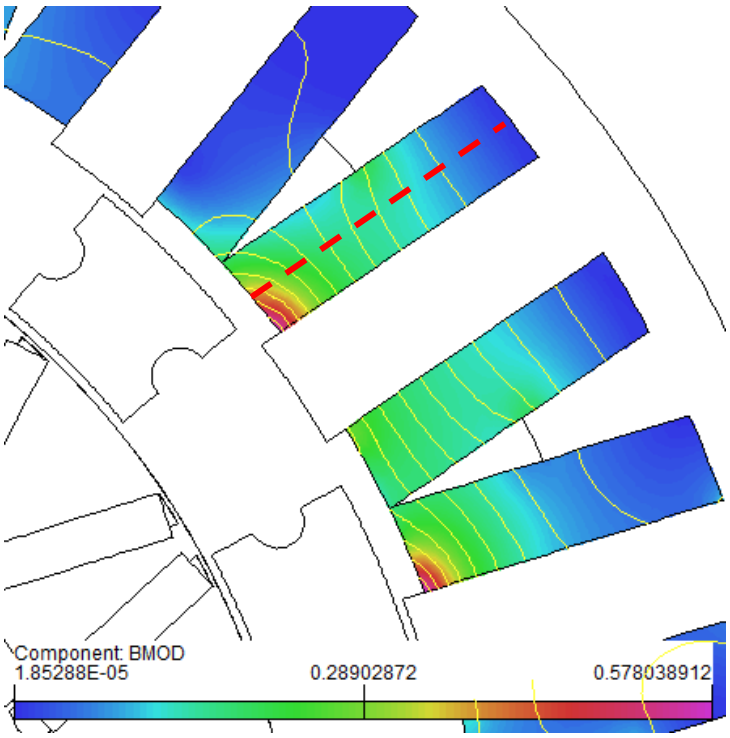

Fig. 5-1 Slot flux density distribution at 300Arms

Fig. 5-1 shows flux density distribution in the slots at 300Arms phase current and it is apparent that with this extreme level of electrical loading, the flux density can exceed 0.4T, particularly in the area near tooth tips. In order to highlight influence of the pole piece rotor on the leakage field, the device was simulated with pole piece rotor replaced by a solid cylinder.

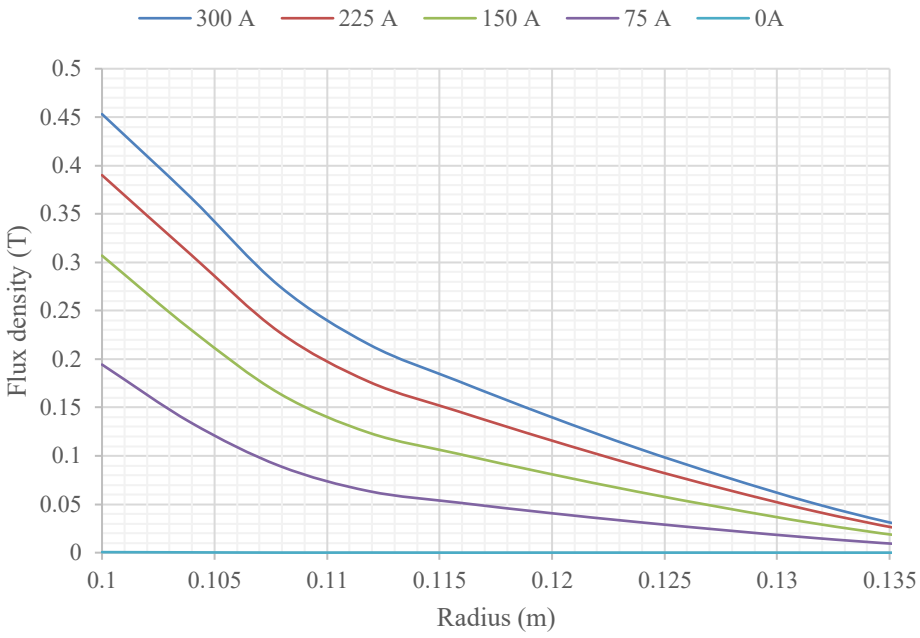

Fig. 5-2 Slot flux density at different levels of electrical loading

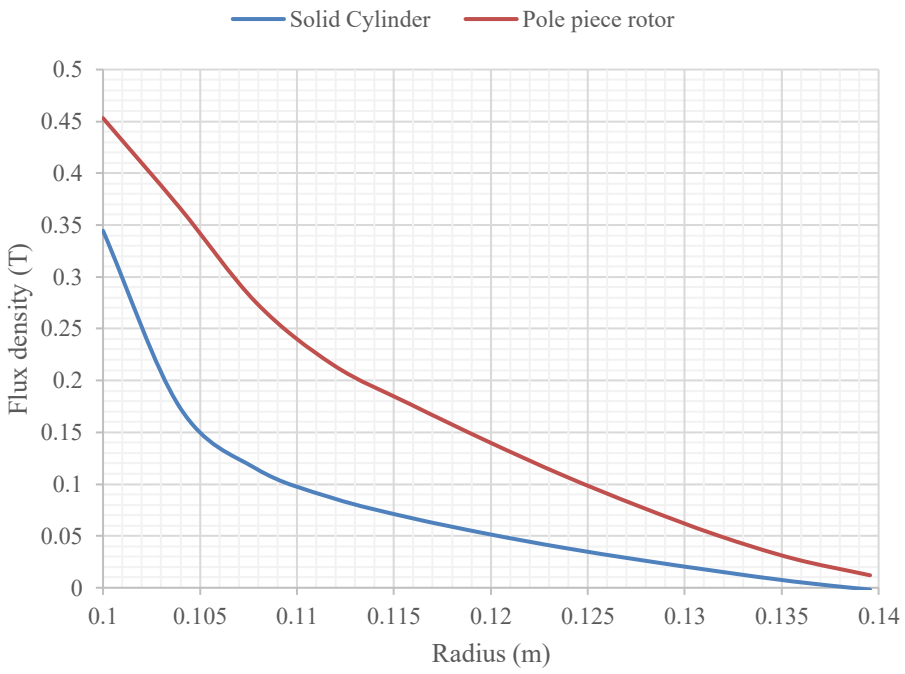

Fig. 5-3 Cross slot leakage at 300A with and without pole piece rotor

The resultant slot flux density along the red dashed line in Fig. 5-1 for model with normal pole piece rotor and the cylinder can be seen in Fig. 5-3. It is apparent that flux leakage has considerably higher amplitude with the pole piece rotor. In

addition, leakage flux density as a function of phase current for normal construction with the pole piece rotor can be seen in Fig. 5-2. It is apparent that that leakage flux density increases with load and is particularly high in the first third of the slot radial length near the outer air gap. It is apparent that the large effective air gap created by the pole piece rotor has strong influence on amplitude of the cross-slot leakage.

5.2.3 Coil design

Based on calculations presented in Chapter 3, 42 turns per phase were selected for the proposed device. In addition, it was shown in Chapter 2 that series connection of phase coils is preferred due to presence of the parasitic space harmonic in the outer air gap which induces unequal emf in coils belonging to the same phase. Since each phase has 7 coils, series connection leads to 6 turns per coil. Given the slot shape and the desire for high slot packing factor, series of trial winds were performed with 1mm diameter magnet wire coated with grade 2 enamel which was wound around a winding fixture (Fig. 5-4 b), mechanically compressed, impregnated and cured. Based on the trial winds, it was determined that the maximum practical slot packing factor was 58%, which in case of series connected winding results in relatively high number of strands per turn. While series connection is preferred, the parallel option will be analysed in the following section to examine advantages and drawbacks of each solution. Parameters of both series and parallel connected coils are summarised in Tab. 5-1.

Tab. 5-1 Series and parallel winding parameters

Winding connection	Series	Parallel
Turns per coil	6	42
Coils per phase	7	7
Strands per turn	42	6
Strand diameter (mm)	1	1
Slot packing factor (%)	58	58
Phases	3	3
Stack length (mm)	50	50

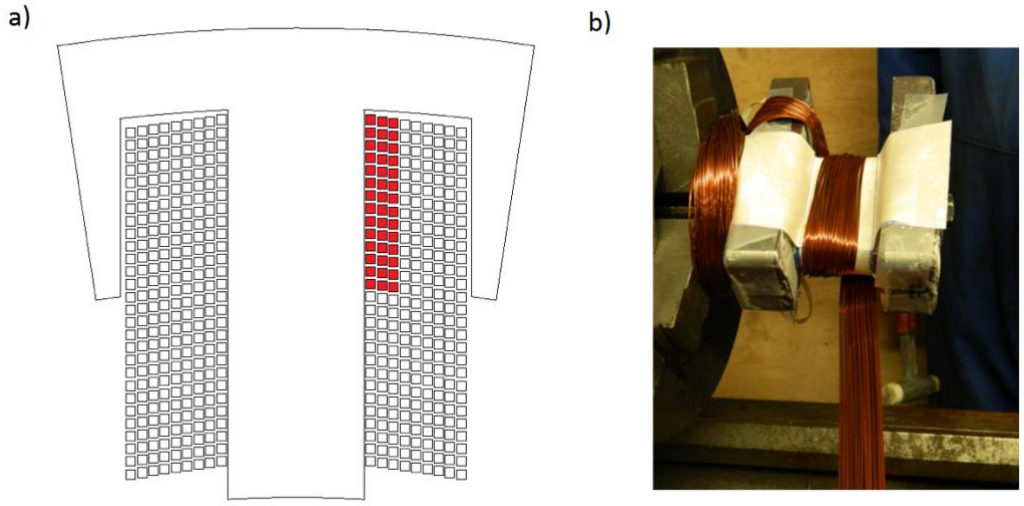

Fig. 5-4 a) FEA model geometry of a coil with high packing factor b) Prototype coil being wound by hand

5.2.4 Method of analysis

While DC copper loss could easily be calculated based on estimated resistance of the winding and current, calculating AC loss components is inherently more complex as it depends on magnetic field distribution within the slot and position of individual conductors as well as their connection. Authors in [72] and [73] discuss analytical, FEA and hybrid FEA/analytical methods of AC winding loss calculation, however, they ultimately conclude that the only commonly accepted approach which takes into account all winding loss mechanisms is to use 2D FEA model of the analysed device where coils are modelled as bundles of individual wires and their connection is done via external electrical circuit coupled to the FEA model. Time stepped simulation then could be performed, and overall copper loss is calculated by averaging instantaneous copper loss obtained by integration of copper current density distribution and known resistivity. Although the most comprehensive, the FEA transient method is computationally intense as it requires dense mesh in the slot area.

The same method was used for AC copper loss analysis of the proposed device. In the transient FEA model, each conductor was modelled as a conductive eddy current filament coupled to the external circuit. Resistance of the winding overhang was taken into account via external circuit elements and inductance of the overhang is neglected as it was expected to be negligible in concentrated coils with short

overhang. Individual strands in the coils have circular cross section with 1mm wire diameter, however the coils were compressed so as to achieve high copper packing factor. During the compression, conductors were deformed making it difficult to model their exact geometry. Hence in the FEA model, equivalent square conductors with the same cross-sectional area were used as can be seen in Fig. 5-4 a). Since each coil is random wound by hand, the exact position of each individual conductors belonging to a turn is not known, therefore the strand distribution as highlighted by red colour in Fig. 5-4 a), is an assumption and shows one turn of the series connected coils consisting of 42 parallel strands. All other turns have the same pattern of 3 by 14 conductor. In case of the parallel connected phase coils, each coil has 42 turns with 6 strands per turn and strands were arranged in 3 by 2 pattern. In addition, it was assumed that the temperature of the copper is constant (100°C) and evenly distributed within the bundle.

5.2.5 Influence of coil design and winding connection on copper loss

Using the full transient FEA model based on the method described in section 5.2.4 various conductor connections were analysed in order to assess their drawbacks and benefits. Assuming constant number of conductors in a slot, constant total copper cross section and identical conductor positions, three winding connections were analysed. Firstly, series connection with the number and position as per Fig. 5-4 a) was analysed when the pole piece rotor was rotated at 3000rpm creating fundamental frequency of 900Hz. Resultant instantaneous copper loss in one the coils can be seen in Fig. 5-5, total winding copper loss as a function of phase current is plotted in Fig. 5-6 and distribution of current density within conductors of a coil in Fig. 5-7 a). It is apparent that that total copper loss in series connected winding with no transposition at high frequency and high electrical loading becomes nearly 4 times larger than DC copper loss. The extremely high copper loss can be attributed to the combination of large number of strands per turn and high cross slot leakage which creates large difference in strand EMFs and consequent current circulation between them. It is apparent from the current density distribution in Fig. 5-7 a) that strands located near the bottom and top of each turn carry particularly high current which could lead to localised overheating and insulation failure.

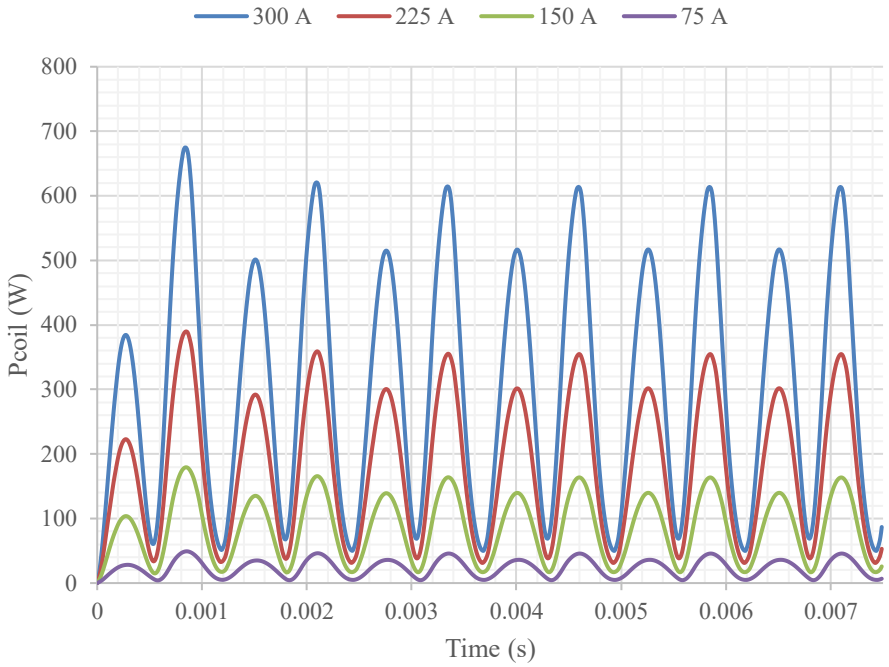

Fig. 5-5 Instantaneous copper loss in one the coils of series connected winding for different phase currents

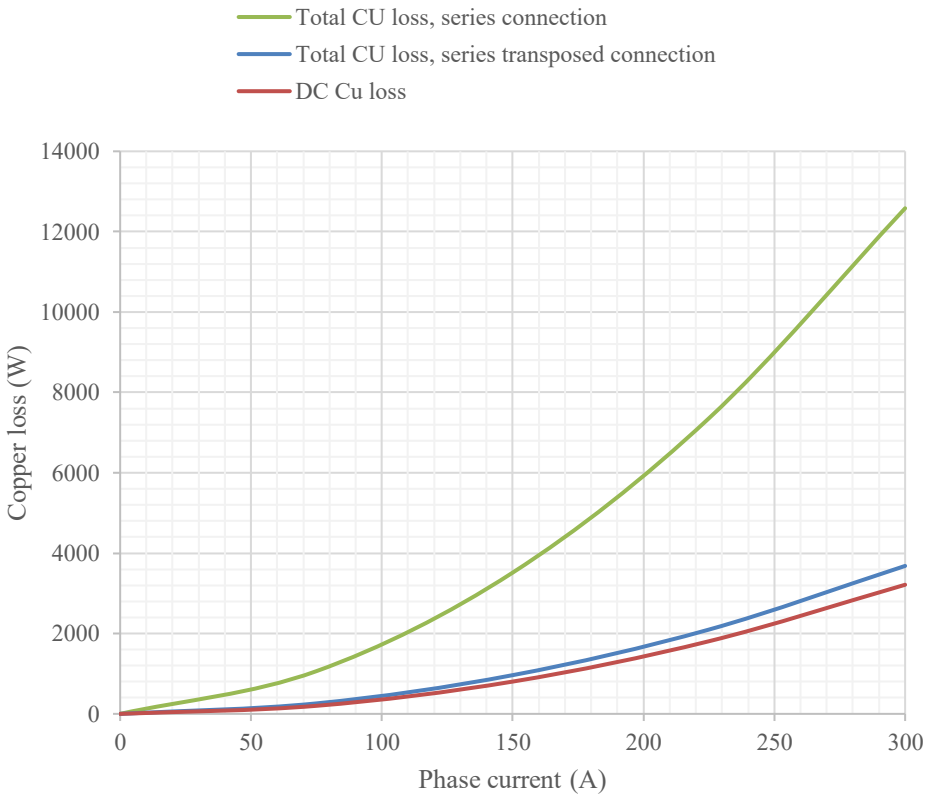

Fig. 5-6 Comparison of copper loss as a function of phase current at constant 900Hz fundamental stator frequency

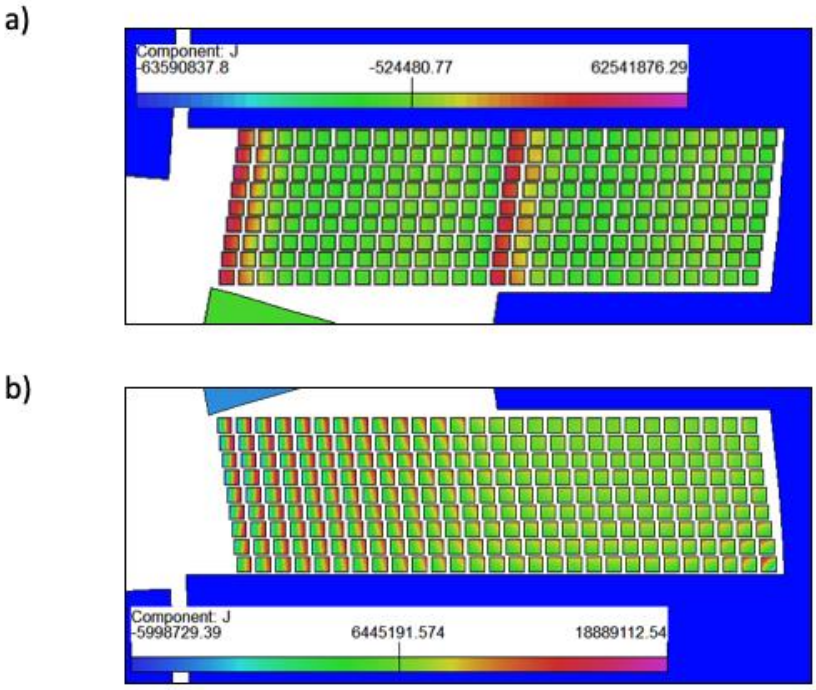

Fig. 5-7 Current density distribution in one coil side at 300Arms phase current for a) series connection without transposition b) series connection with perfect transposition

Transposition is a known technique used to limit current circulation by continuously varying conductor position through the axial extent of the slot so that average position of each conductor within the slot is the same. In ideal case, each conductor is exposed to the same leakage field and hence no EMF difference between them exists. Ideal transposition could be modelled by connecting all parallel conductors in series and adjusting input current so that the total turn current is the same as in case of non-transposed coil. In series connected winding with transposed coils, only DC and eddy current copper loss exist. It is apparent from Fig. 5-6 that transposition dramatically reduces AC copper loss and that AC eddy current loss is relatively small in comparison to DC copper loss. From practical point of view, conductor transposition tends to result in reduced slot fill factor and consequent increase in DC coil resistance and copper loss, however this effect was ignored in the presented analyses. In addition, continuously transposed coils are more difficult to manufacture unless the coils are wound using LITZ cable which tends to increase cost of the winding.

While it was concluded in the Chapter 2 that parallel connection of phase coils will inevitably lead to current circulation among them, this option was further investigated as parallel connection of phase coils makes it possible to increase the number of turns in each slot and, consequently, reduce the number of parallel wires in each turn. Compared to the series connection, parallel connected winding will exhibit all four winding loss mechanisms, however impact of strand current circulation will be reduced. Fig. 5-8 shows comparison of ideal coil current waveform and real waveforms caused by current circulation when the magnet rotor was rotating at 4000rpm and it is apparent that real coil currents oscillate around the ideal sine wave. The current distortion is caused by the magnet rotor space harmonic and hence is only present when the rotor is rotating. While the focus of this chapter is primarily on losses, it must be noted that the circulating currents are likely to affect transient performance of the device, since the parallel connected winding effectively behaves like a damper cage of an induction machine with slip frequency equal to electrical frequency of the magnet rotor.

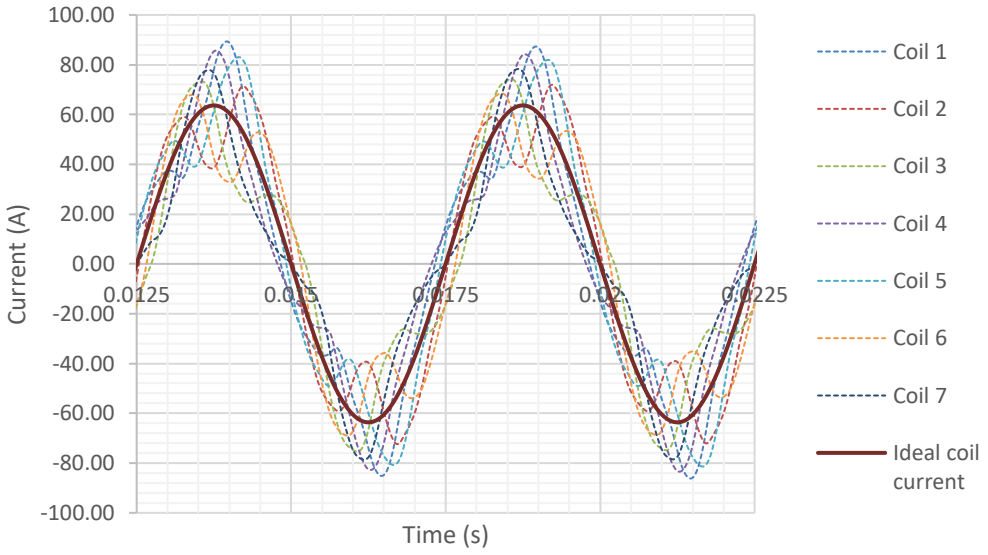

Fig. 5-8 Currents in individual coils of parallel connected winding when magnet rotor was rotating at 4000rpm

In order to compare all three winding connections, three characteristic operating points were analysed. The first operating point is such that the stator frequency is at its maximum while frequency of the magnet space harmonic is zero. In the second case, magnet rotor is rotating at maximal speed and pole piece rotor is stationary.

The third characteristic operating point is when the stator frequency is zero while both rotors are rotating. Resulting copper loss for all three winding connections for the three operating points is shown in Fig. 5-9, Fig. 5-10 and Fig. 5-11 respectively.

For the analysis of the first operating point, pole piece was rotating at 4000rpm with magnet rotor at stand still resulting in 1067Hz fundamental stator frequency. Combination of high fundamental frequency, high electrical loading and large number of wires in hand creates extremely high loss due to circulation between parallel strands in series connected winding. Total copper loss of parallel connected winding is significantly lower at this operating point due to the much smaller number of parallel strands and their close position within the slot. Since the magnet rotor speed is zero at this operating point, the loss due to circulation between parallel coils is zero. As expected, series connection with ideal transposition eliminates circulation between strands and coils and it makes the winding the most efficient.

The second operating point represent the situation when the magnet rotor is revolving at 4000rpm while the pole piece rotor is at stand still. This results in a 600Hz stator fundamental frequency but also 600Hz magnet rotor frequency. While the loss due to circulation between parallel strands is smaller in both series and parallel winding due to reduced frequency, the parallel winding is still more efficient, despite the fact that there is additional loss due to circulation between parallel coils.

Tab. 5-2 Winding loss mechanisms in different winding configurations

	Series connection	Series transposed	Parallel
DC copper loss	X	X	X
Current circulation between parallel strands	X		X
Current circulation between parallel coils			X
Eddy current loss	X	X	X

In the last operating point both the magnet rotor and the pole piece rotor are rotating at 4000rpm and 2250rpm respectively which results in zero stator fundamental frequency. This is the only operating point where all AC loss

mechanisms which are function of stator frequency are zero and also the only point where the parallel connected winding has a disadvantage compared to the series connection without transposition.

It is apparent from the analysis results that the choice of winding connection could be largely driven by the duty cycle of the device. If the overall system is designed and controlled such that the device operates mostly at low differential speed with low stator frequency, it might be advantageous to employ series connected winding without transposition. If, however, operating with large differential speeds for prolonged periods of time is necessary than high AC copper loss may be the limiting factor and parallel connection might be better suited. In addition, it was shown that AC copper loss strongly depends on electrical loading of the stator, but the device is unlikely to operate at high loads for long periods of time in a typical passenger vehicle. Series connection with conductor transposition is the most efficient solution (assuming transposition has no impact on slot packing factor) across the operating range, however, this might also be the most expensive solution due to more complex coil manufacture. Tab. 5-2 shows which of the four winding loss mechanisms are present in each winding connection option.

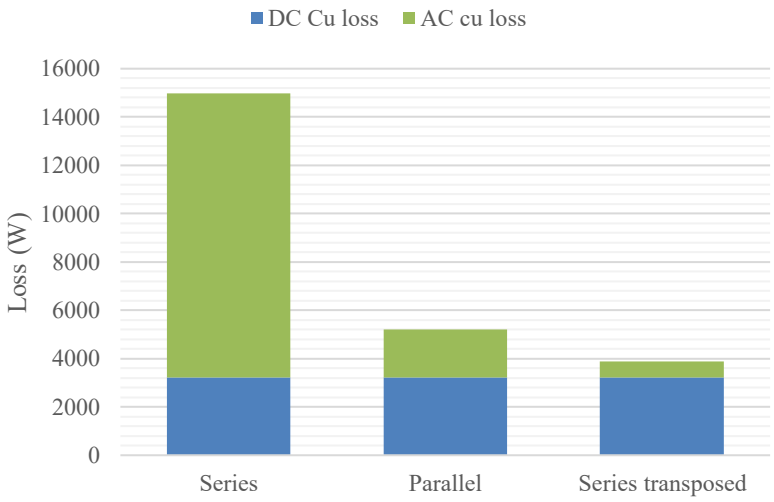

Fig. 5-9 AC and DC copper loss, 4000rpm pole piece rotor speed and 0rpm magnet rotor speed operating point

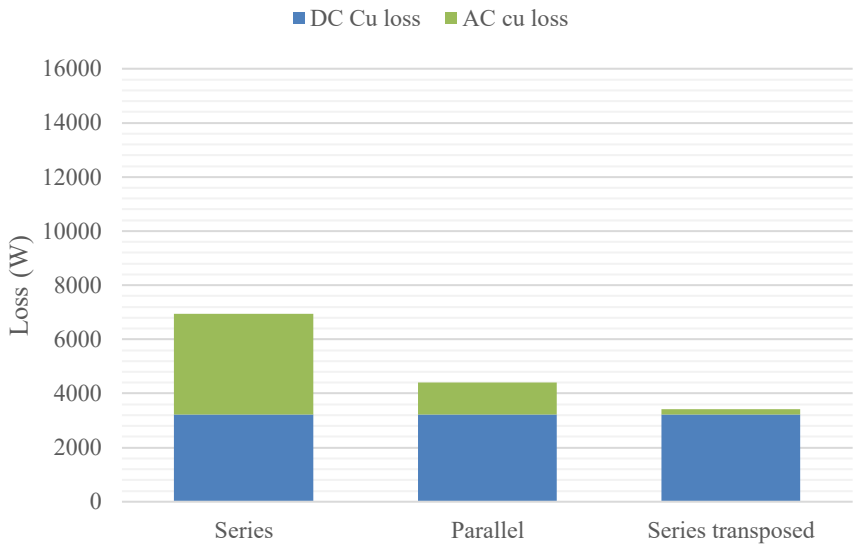

Fig. 5-10 AC and DC copper loss for 300Arms, 0rpm pole piece rotor speed and 4000rpm magnet rotor speed operating point

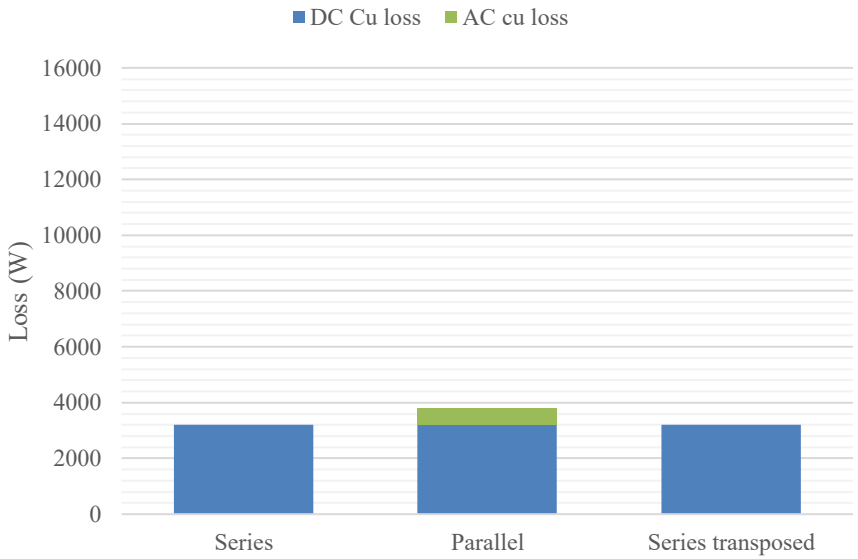

Fig. 5-11 AC and DC copper loss, stator frequency = 0Hz, 4000rpm pole piece rotor speed and 2250rpm magnet rotor speed operating point

5.3 Iron losses

Together with copper loss in the windings, iron loss induced by variation of flux density in the magnetic circuit is one of the two most prominent loss mechanisms in electrical machines, therefore its analysis is of prime importance. Magnetic circuit of

the dual rotor device consists of three principal components which are all subject to varying magnetic fields. Unlike in conventional electrical machines, stator of the dual rotor device is exposed to two dominant space harmonics hence contribution of both of them to the overall loss must be understood. Although volume of electrical steel used for pole pieces is comparatively smaller than that employed in the stator, it is exposed to relatively high flux densities and at some operating points, high frequencies. Additionally, heat generated in the pole pieces may be difficult to remove since they are surrounded by air gaps in radial direction and, depending upon its construction, thermally poorly conductive materials. Flux in the magnet rotor is mostly unidirectional due to the constant field provided by the permanent magnets, however relative motion of the highly salient pole piece rotor with respect to the magnet rotor is likely to cause variation of flux density near the rotor surface and consequently rotor heating. While the level of rotor loss can be expected to be much lower than in the stator, it is generated in close proximity of thermally sensitive magnets.

The following sections describe the method used for iron loss analysis and discuss practical implications to the device design and operation. The focus is on aspects of iron loss analysis which are unique to the proposed device.

5.3.1 Iron loss model and method of analysis

Iron losses in magnetic circuits of electrical machines are predominantly analysed by means of models based on the well-known Bertotti equation whereby total iron loss is decomposed into three separate components, each describing different physical loss mechanism [74]. Overall iron loss per unit volume is given by:

$$P_{fe} = k_e \cdot B_p^2 \cdot f^2 + k_h \cdot B_p^\alpha \cdot f + k_{exc} \cdot B_p^{1.5} \cdot f^{1.5} \qquad (5\text{-}1)$$

where k_h, k_e, k_{exc} and α are coefficients associated with the three iron loss mechanisms called hysteresis, eddy current or classical and excess or anomalous. The model assumes sinusoidal variation of flux density hence B_p and f are peak flux density and frequency of variation respectively. The loss coefficients are grade specific and are often obtained by curve fitting of measured data on samples of

electrical steel using Epstein test, with exception of eddy current loss coefficient, which can be calculated using following equation:

$$k_e = \frac{\sigma \cdot \pi^2 \cdot d^2}{12} \qquad (5\text{-}2)$$

where σ is steel conductivity and d is lamination thickness. Authors in both [51] and [52] assert that the iron loss coefficients are function of both flux density and frequency and propose alternative models where both dependencies are taken into account. Additionally, practical methods of determining the loss coefficients are discussed. Apart from dependency on flux density and frequency, the loss coefficients also vary between different batches of the same material grade and processing of the steel (such as punching and welding) further increases uncertainty with regards to the correct value of loss coefficients for modelling.

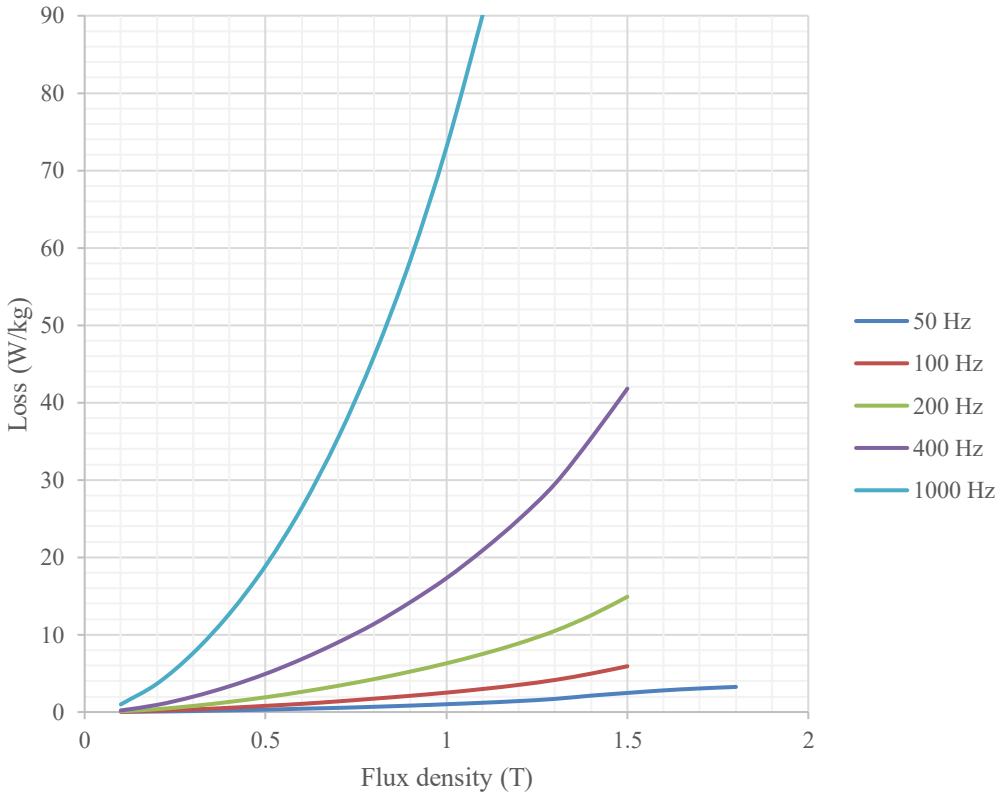

Fig. 5-12 Loss curves for M270-35A electrical steel

Tab. 5-3 Iron loss coefficients

	M270-35A
K_e	50e-6
K_h	11.745e-3
K_{exc}	0.447e-3
α	1.992

Since precise characterisation of electrical steel was outside of scope of the research presented in this thesis and relatively limited amount of data was available for the selected steel (M270-35A), model described by equation (5-1) with constant loss coefficients was used. Fig. 5-12 shows specific loss curves of M270-35A electrical steel for range of flux densities and frequencies published by the steel manufacturer. The loss curves were used to derive the loss coefficients shown in Tab. 5-3 by means of least squares curve fitting of the published data.

In order to determine iron loss in a magnetic circuit using the model described by equation (5-1), peak flux density and corresponding frequency of variation in different parts of the circuit must be known. Since various parts of the magnetic circuit are exposed to different levels of magnetisation, the circuit needs to be discretized into smaller volumes where peak flux density is constant. For instance, stator tooth will likely experience the same level of peak magnetisation throughout its volume whereas the tooth tip region may need to be further subdivided into smaller regions. Advantageously, FE based models can be used as they naturally discretize the analysed geometry into elementary volumes. Due to this high level of discretisation, iron loss can be computed in each element and the model offers insight into where iron loss 'hot spots' may occur and is less prone to errors due to averaging peak flux densities over larger volumes.

Flux density waveforms in elements of FE mesh can be obtained by either solving series of magnetostatics models with varying rotor positions or time transient model representing steady state operation of the machine. In both cases, it is essential to capture at least one full electrical period of flux density variation with enough data points. This becomes particularly important in case of the dual rotor device, where

certain parts of the magnetic circuit are exposed to multiple dominant harmonics and determination of period and required number of data points can be challenging.

Based on the flux density waveforms obtained from the FE model, iron loss can be calculated either in time or frequency domain. Both approaches are described in detail in [75] where authors suggest that the frequency domain calculation underestimates iron loss compared to the time domain method. However, this is due to the fact that only fundamental component of flux density variation was considered in the frequency domain analysis and contribution of higher order harmonics were neglected. Otherwise, both methods are fundamentally equivalent. In frequency domain, the flux density waveforms of each element are decomposed into harmonic components by means of Fourier analysis and contributions of each component to the overall iron loss is calculated using equation (5-1). The frequency domain method was selected for iron loss analysis of the dual rotor device specifically because it makes it possible to separate contribution of multiple dominant harmonics to the total iron loss.

5.3.2 Stator iron loss

As mentioned before, the stator of the dual rotor device is exposed to two dominant space harmonics, both having different number of pole pairs and angular velocities. Fig. 5-13 and Fig. 5-14 show variation of average tooth flux density with time at no load for two different operating points. In the first figure, pole piece rotor is rotating at 3000rpm while the magnet rotor at 2000rpm, resulting in 500Hz control frequency. It is apparent that flux density variation is not purely sinusoidal and contains contribution from both air gap space harmonics. Flux density waveform depicted in the second figure contains sinusoidal variation of flux density with large DC offset. In this case, the control space harmonic was stationary, creating constant flux density in the tooth. Pole piece rotor was rotating at 2250rpm while magnet rotor at 4000rpm.

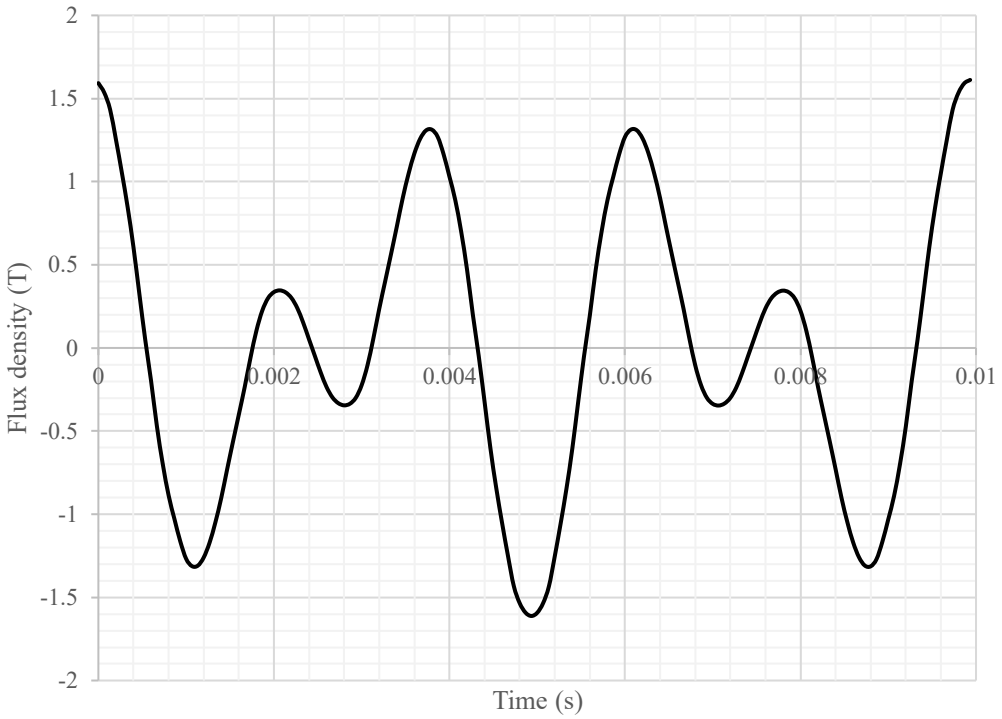

Fig. 5-13 Tooth flux density at no load, 3000rpm pole piece rotor speed, 2000rpm magnet rotor speed

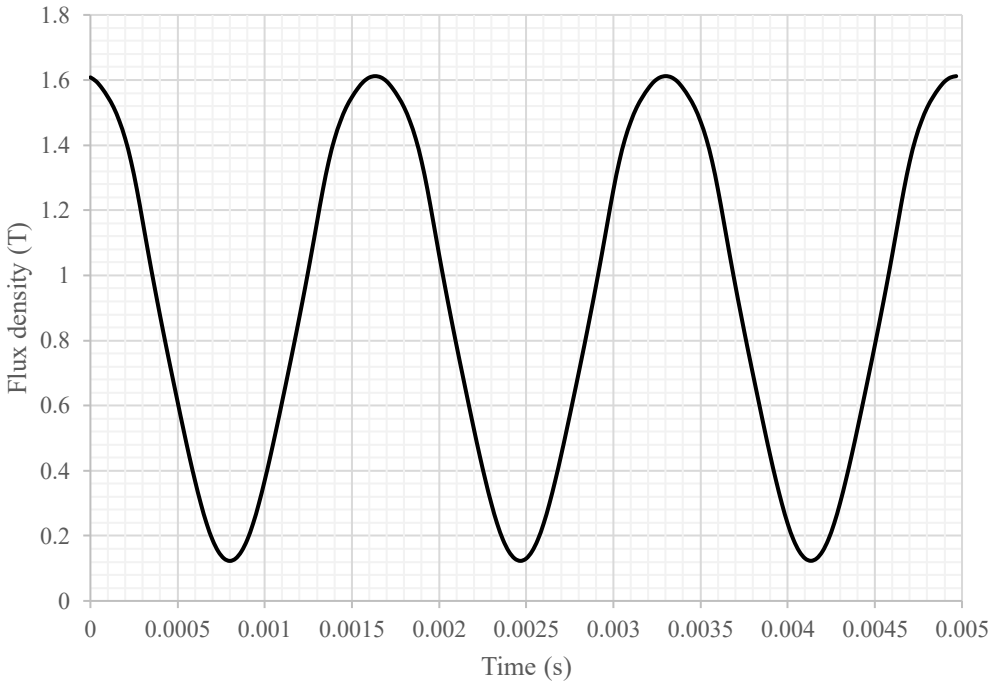

Fig. 5-14 Tooth flux density at no load, 2250rpm pole piece rotor speed, 4000rpm magnet rotor speed

As it was described in the previous section, both time and frequency domain methods of iron loss calculation rely on knowledge of fundamental frequency at which flux density in the steel varies. Frequency of the control rotor harmonic for a specific operating point can be calculated as follows:

$$f_{cont} = \frac{p_{ppr}\omega_{ppr} - p_m\omega_m}{(p_{ppr} - p_m) \cdot 2 \cdot \pi} \quad (5\text{-}3)$$

While control frequency depends on angular velocity of both pole piece and magnet rotor, magnet rotor frequency is pure function of magnet rotor speed and is given by:

$$f_m = \frac{\omega_m \cdot p_m}{2 \cdot \pi} \quad (5\text{-}4)$$

Frequency domain analysis of flux density variation in the steel gives amplitude of flux density for fundamental frequency and its integer multiples. However, as it is apparent from equation (5-3) and (5-4), control and magnet rotor frequency are not always multiples of each other. Frequency of control and magnet rotor space harmonics are evaluated in Tab. 5-4. At certain operating points, such as 1500rpm pole piece rotor and 2000rpm magnet rotor speed, magnet rotor frequency of 300Hz becomes integer multiple of the control frequency 100Hz. In this particular case, transient FEA was solved for period T=0.01s which contains one full electrical cycle of the control space harmonic and three cycles of the magnet rotor harmonic. Consequently, amplitude spectrum of the stator flux density distribution will show high amplitude at first and third harmonic. Contribution to the overall iron loss by each harmonic can then be separated and evaluated at range of frequencies.

Fig. 5-15, Fig. 5-16 and Fig. 5-17 show amplitude of flux density in elements of stator mesh due to magnet rotor space harmonic, control harmonic at no load and control harmonic at 300Arms phase current respectively. It is apparent that both harmonics create flux density distribution with the highest amplitude in the stator teeth where most of the stator iron loss will be concentrated. At 300Arms, the portion

of tooth body adjacent to the back iron experiences particularly high flux densities. Although, both air gap space harmonics have similar amplitude at no load, flux density due to the control harmonic is higher, particularly in the back-iron region of the stator. This can be attributed to the fact that 21 tooth stator has much higher symmetry factor (3.3.3) with the 7 pole pair control harmonic than with the 9 pole pair magnet rotor and hence less of the magnet rotor flux closes the magnetic flux loop through the back iron as the overall reluctance of the flux path for the 9 pole pair harmonic is higher.

Tab. 5-4 Control and magnet rotor frequency for different input and output seeds

f_{cont} (Hz)	Pole piece rotor speed (rpm)									f_m (Hz)
Magnet rotor speed (rpm)	0	500	1000	1500	2000	2500	3000	3500	4000	
0	0	133	267	400	533	667	800	933	1067	0
500	75	58	192	325	458	592	725	858	992	75
1000	150	17	117	250	383	517	650	783	917	150
1500	225	92	42	175	308	442	575	708	842	225
2000	300	167	33	100	233	367	500	633	767	300
2500	375	242	108	25	158	292	425	558	692	375
3000	450	317	183	50	83	217	350	483	617	450
3500	525	392	258	125	8	142	275	408	542	525
4000	600	467	333	200	67	67	200	333	467	600

Stator iron loss due to the magnet rotor harmonic as a function of magnet rotor frequency at no load can be seen in Fig. 5-18. While it can be generally assumed that loss due to the magnet rotor space harmonic is independent of electrical loading of the stator (because the selected winding does not directly interact with it), saturation of the stator magnetic circuit and consequent increase in reluctance of the flux path caused by stator winding will have an effect. Fig. 5-19 shows iron loss due to the magnet rotor space harmonic as a function of stator phase current at constant magnet rotor frequency of 500Hz. It is apparent that as the stator electrical loading increases, loss due to the magnet rotor harmonic declines.

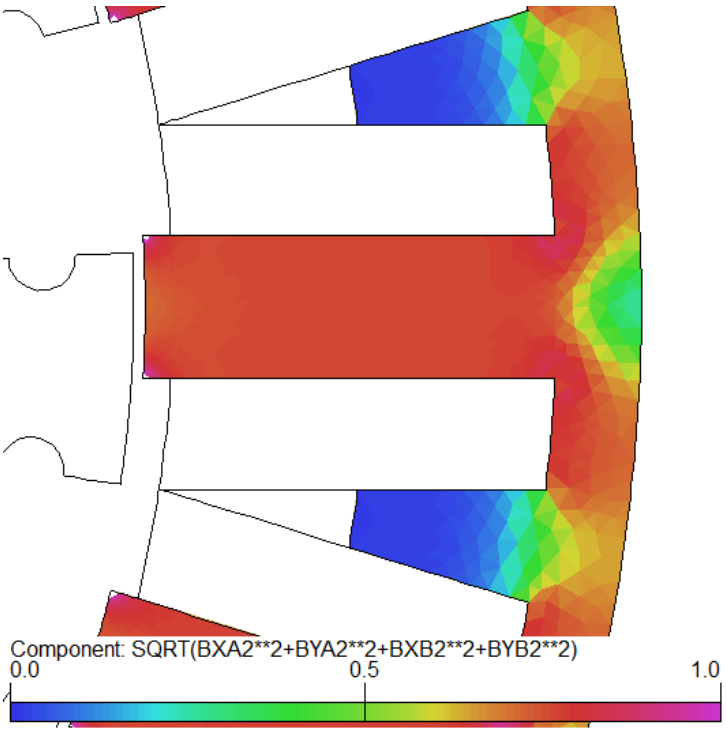

Fig. 5-15 Amplitude of flux density due to control space harmonic in elements of stator magnetic circuit at no load

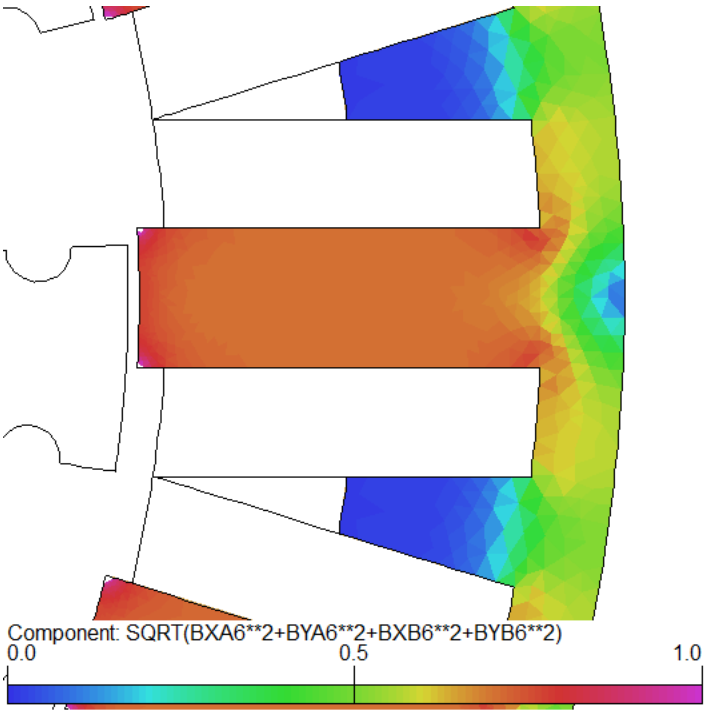

Fig. 5-16 Amplitude of flux density due to magnet rotor in elements of stator magnetic circuit at no load

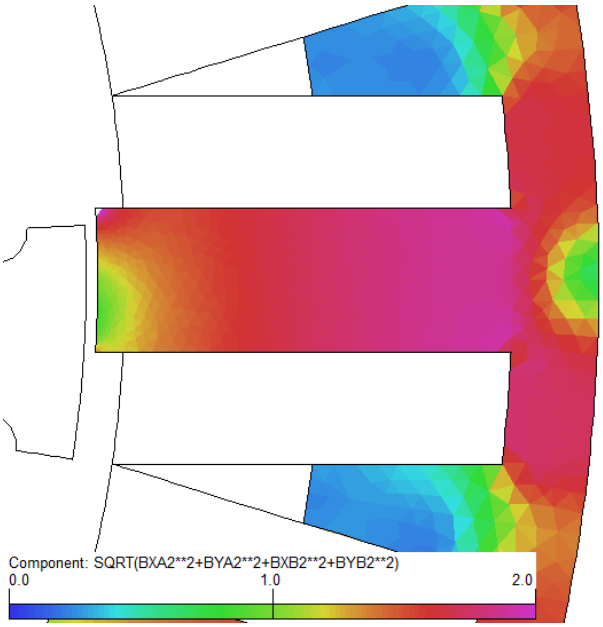

Fig. 5-17 Amplitude of flux density due to control space harmonic in elements of stator magnetic circuit at rated load

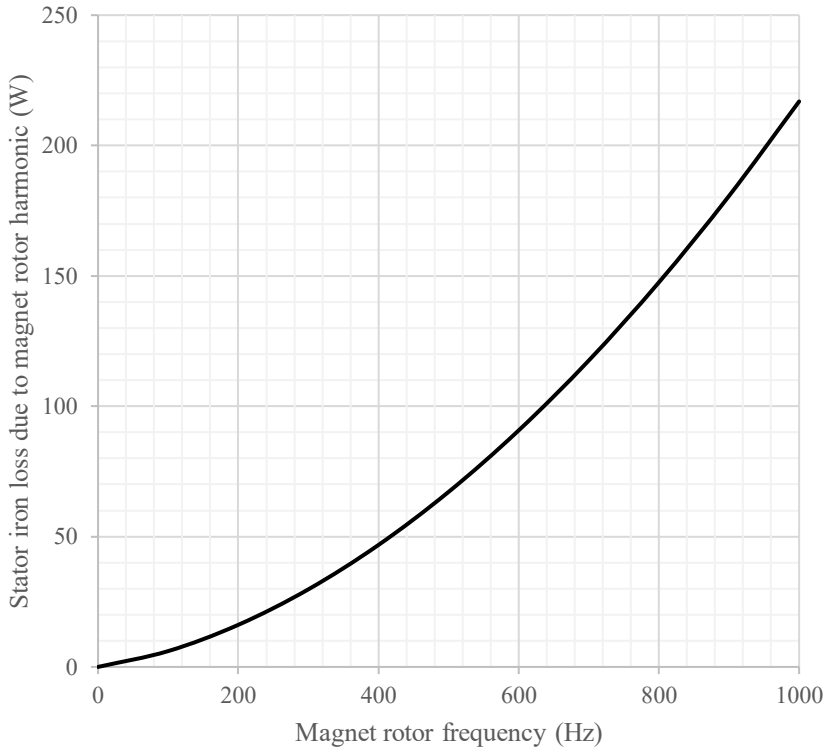

Fig. 5-18 No load stator iron loss due to magnet rotor space harmonic

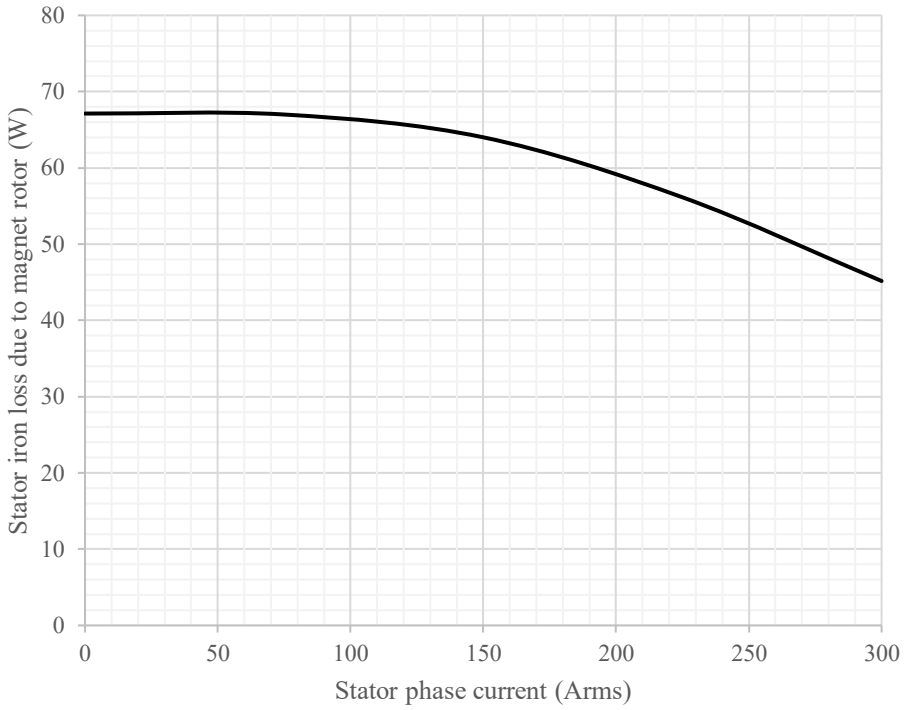

Fig. 5-19 Iron loss due to magnet rotor space harmonic at different electrical loads and constant magnet rotor speed of 4000rpm

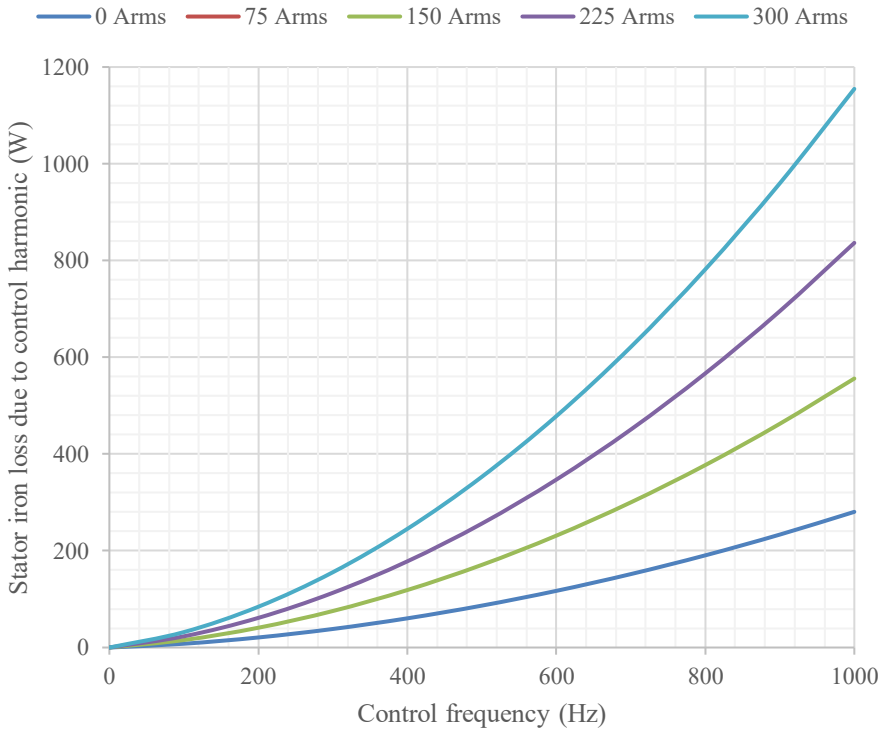

Fig. 5-20 Stator iron loss due to control space harmonic at different electrical loads

Fig. 5-20 shows iron loss due to the control harmonic and armature reaction as a function of electrical loading and control frequency. It is apparent that while contribution of the magnet rotor harmonic is not insignificant, loss due to the control harmonic and armature reaction is dominant even at low levels of electrical loading.

5.3.3 Pole piece rotor iron loss

Frequency of flux density variation in pole pieces of the dual rotor device is a function of relative speed between the two rotors and is given by following equation:

$$f_{pp} = \frac{|\omega_{ppr} - \omega_m|}{2 \cdot \pi} \cdot p_m \qquad (5\text{-}5)$$

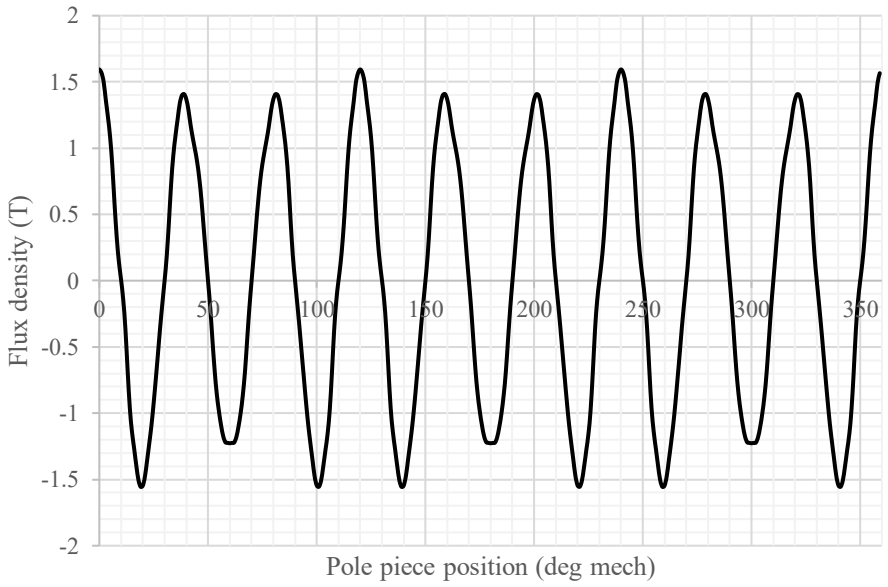

Fig. 5-21 Radial flux density in the centre of a pole piece vs its angular position

Fig. 5-21 shows flux density in the centre of one of the pole pieces as it rotates through one full mechanical rotation of the pole piece rotor when the magnet rotor was stationary and Fig. 5-22 harmonic spectrum of the flux density waveform. It is apparent that the waveform contains dominant 9 pole pair harmonic and that contribution of other harmonics is insignificant.

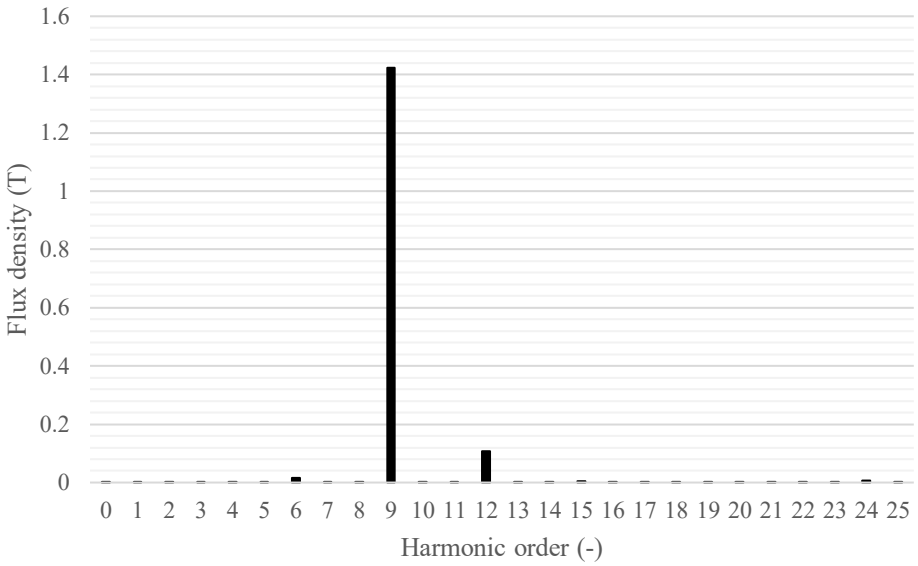

Fig. 5-22 Harmonic spectrum of pole piece radial flux density shown in Fig. 5-21

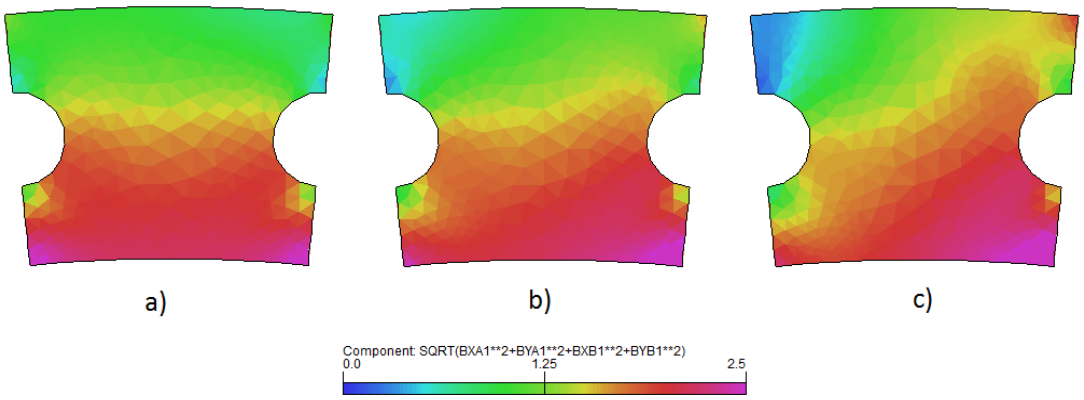

Fig. 5-23 Amplitude of flux density variation in elements of pole piece mesh at a) no load, b) 50% load and c) 100% load

Fig. 5-23 shows peak flux density in elements of the pole piece mesh at frequency given by equation (5-5) and three different levels of electrical loading while Fig. 5-24 contains curves of total iron loss in all pole pieces as a function of differential speed between the magnet and pole piece rotor. It is apparent that electrical loading of the stator influences distribution of peak flux density in the pole pieces, however, its influence on pole piece rotor iron loss is negligible. Magnetisation of the pole pieces is dominated by the flux due to the magnet rotor and

majority of the iron loss is concentrated in the half adjacent to the magnet rotor, particularly in the corners where peak flux density exceeds 2T. The corners are the areas of the highest iron loss density and also areas where iron loss model based on equation (5-1) with constant loss coefficients is likely to produce the highest calculation error.

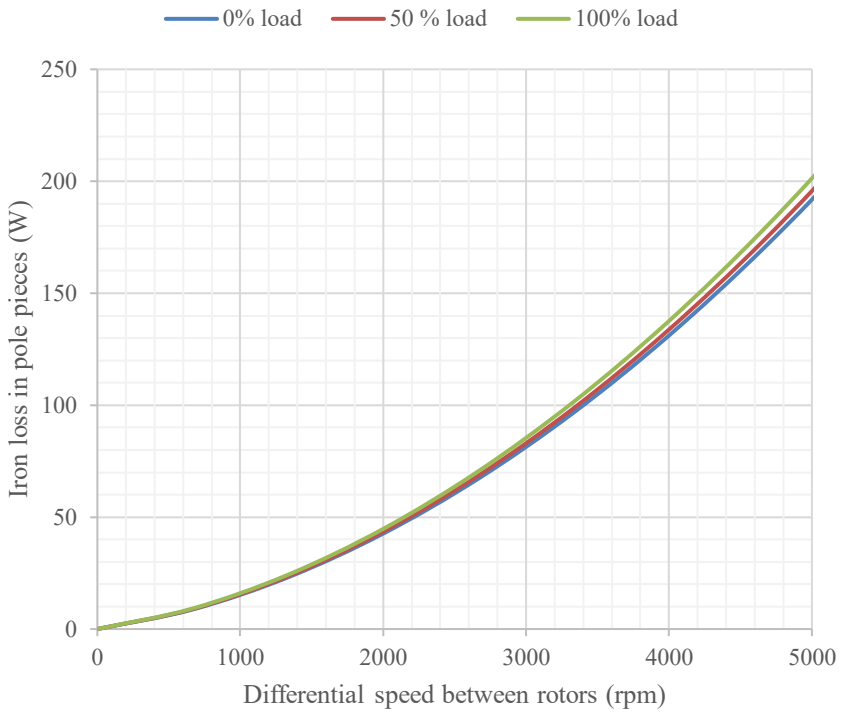

Fig. 5-24 Pole piece rotor iron loss as a function of differential speed at three levels of stator loading

5.3.4 Magnet rotor iron loss

In theory, rotor iron losses of a synchronous machine should be zero as the rotor rotates in synchronisms with the armature reaction field. In practice, effects such as permeance variations introduced by, for instance, stator slotting or armature reaction MMF harmonics cause fluctuation of flux density near the rotor surface and consequently rotor heating by iron loss. In case of the dual rotor device, similar phenomenon can be observed due to relative motion between the highly salient pole piece rotor structure and the magnet rotor and also due to the fact that the armature

reaction field is rotating at different speed than the magnet rotor. Pole piece and armature reaction (fundamental component only) passing frequency relative to the poles of the magnet rotor have the same value at any given combination of input and output speed and can be calculated as follows:

$$f_{fe\_mag} = \frac{|\omega_{ppr} - \omega_m|}{2 \cdot \pi} \cdot p_{ppr} = \frac{|\omega_{cont} - \omega_m|}{2 \cdot \pi} \cdot p_{cont} \qquad (5\text{-}6)$$

Since both passing frequencies are the same, their individual contributions cannot be separated by means of harmonic analysis. Additionally, passing frequency between the magnet rotor and the stator slots could be defined:

$$f_{fe\_slots} = \frac{|\omega_m|}{2 \cdot \pi} \cdot N_{slots} \qquad (5\text{-}7)$$

However, the contribution to overall magnet rotor iron loss by permeance variation due to stator slotting is assumed to be small, as the rotor is separated from the stator by large effective air gap, and hence will be ignored in the following analysis.

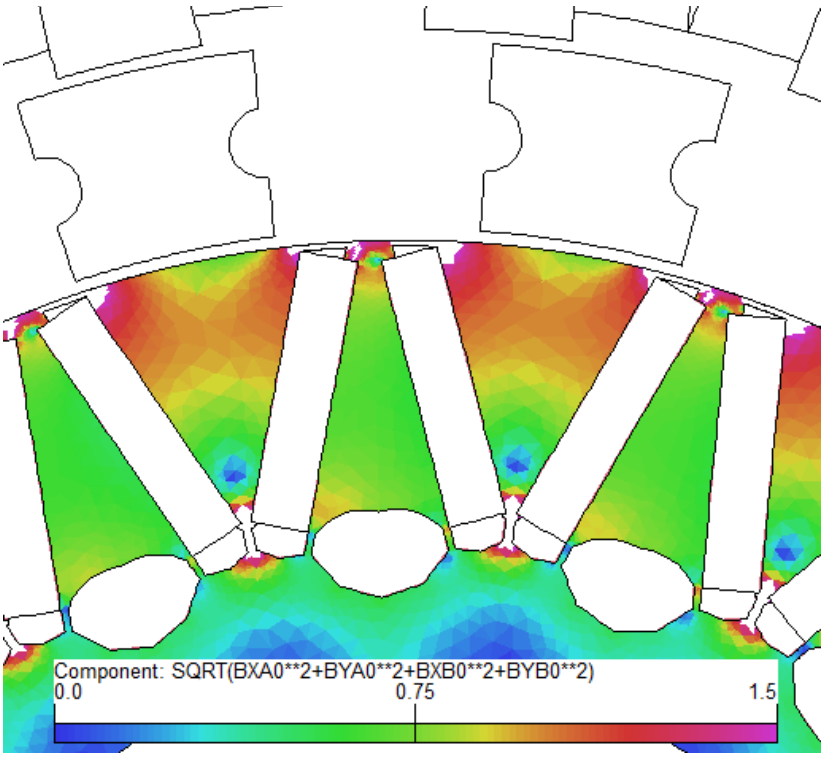

Fig. 5-25 Amplitude of DC flux density component in elements of magnet rotor magnetic circuit

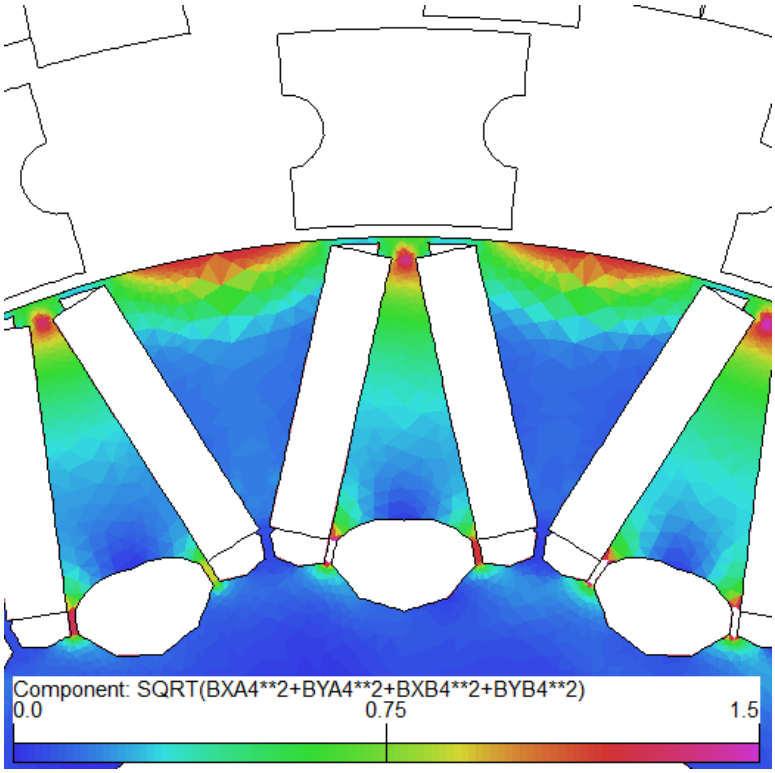

Fig. 5-26 Amplitude of flux density due to relative motion of pole piece rotor in elements of magnet rotor magnetic circuit

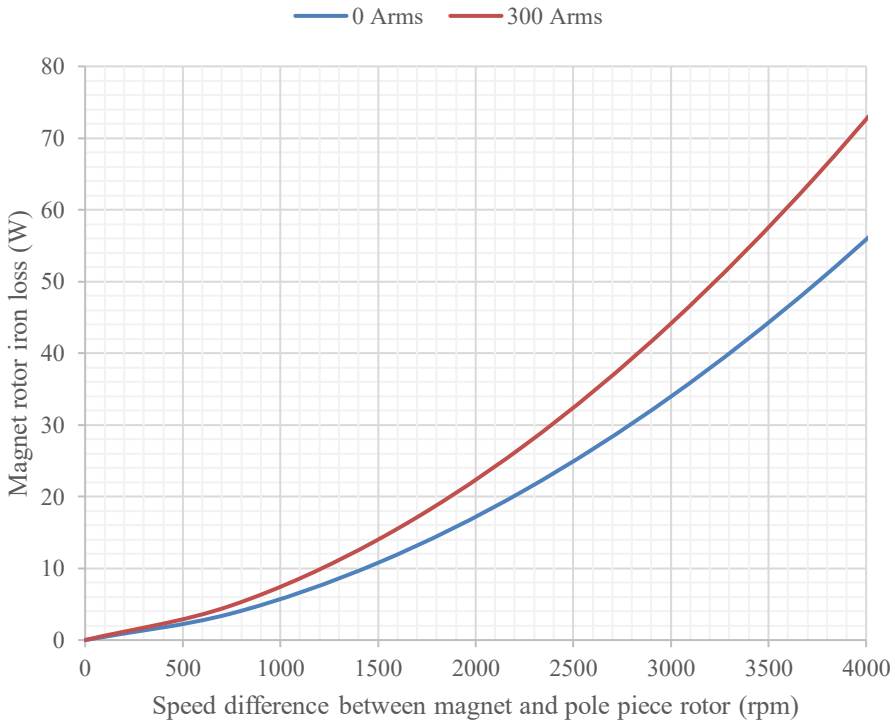

Fig. 5-27 Magnet rotor iron loss versus differential speed between magnet and pole piece rotor

Using the same approach as in case of stator and pole piece rotor iron loss analysis, pole piece rotor was rotated so that the time stepped field solution would contain several full periods calculated from frequency obtained by equation (5-6). Peak flux density variation in the elements of stator steel at the passing frequency can be seen in Fig. 5-26 and it is apparent that the variation with the largest amplitude is near the rotor surface. As it was mentioned previously, flux density in the magnet rotor is dominated by strong DC component, amplitude of which can be seen in **Error! Reference source not found.**.

Total magnet rotor iron loss as a function of differential speed at no and full load can be seen in Fig. 5-27. It is apparent that the magnet rotor iron loss is a function of load as well as differential speed, however, the difference in loss between the two extreme load points is relatively small. This means that the magnet rotor iron loss is dominated by the no-load component created by relative motion of the pole piece rotor and contribution of the control space harmonic is considerably smaller. It must be noted, however, that these results contain only loss due to the fundamental component, having frequency given by (5-6), and all other harmonic components are ignored. This means that the loss values in Fig. 5-27 are likely to be underestimated.

While iron loss in the magnet rotor is considerably smaller than in the stator and pole piece rotor, it is concentrated in relatively small volume and in close proximity of temperature sensitive rare earth permanent magnets. In addition, the generated heat could be difficult to remove unless the rotor is actively cooled.

5.3.5 Summary of results and discussion

Overall iron loss of the dual rotor device has four components and is a function of three variables, namely stator current, pole piece and magnet rotor speeds. Total iron loss can be described by the following model:

$$P_{fe} = P_{sc}(\omega_c, \omega_m, I_{ph}) + P_{sm}(\omega_m, I_{ph}) + P_{ppr}(\omega_c, \omega_m, I_{ph}) + P_m(\omega_c, \omega_m, I_{ph}) \quad (5\text{-}8)$$

where P_{sc} is stator loss due to control space harmonic, P_{sm} is stator loss due to magnet rotor space harmonic, P_{ppr} is pole piece rotor loss and P_m is magnet rotor iron loss due to relative motion of magnet and pole piece rotor. It must be noted that the equation (5-8) assumes that the device is operated at Id=0 control strategy with no field weakening and therefore all loss components are only function of current magnitude. If field weakening operation was to be taken into account, then all loss components would depend on both I_d and I_q (or I_{ph} and phase advance angle). Since the iron loss is defined by at least three parameters, in can be visualized either as a three-dimensional cube or as map if one of the variables is kept constant.

Evaluation of overall iron loss of the dual rotor device at different combinations of input and output speed at constant 0 and 300Arms can be seen in Tab. 5-5 and Tab. 5-6 respectively. The operating point with the highest iron loss is when pole piece rotor is rotating at high speed while magnet rotor is stationary. This operating condition represents the situation when all of the engine output power is converted into electrical energy. The area of lowest iron loss coincides with the line of zero control harmonic speed (and consequently zero stator frequency). It can be seen that, apart from the point where both rotors are stationary, total iron loss of the device is never zero even when stator frequency equals zero. Some loss components become zero at zero rotor differential speed (magnet rotor iron loss caused by pole piece motion) while some at zero control space harmonic speed (stator iron loss due to control space harmonic and armature reaction), however these two conditions never occur at the same time. It is apparent that the line of the highest efficiency moves towards the line of zero control harmonic speed as the load increase. This means that the stator loss due to the control harmonic and the armature reaction dominates the overall iron loss of the device at load. The two loss maps presented in Tab. 5-5 and Tab. 5-6 were presented in order to highlight this.

The iron loss analysis and the presented results show the general trends and behaviour of iron losses in the proposed device, however, their accuracy could be compromised by number of influences. For instance, amplitude of flux density variations in both the stator and pole piece rotor could reach 2T where the material is deeply saturated. This combined with the fact that fundamental frequencies can

exceed 1kHz requires the lamination material to be characterized in wide range of conditions.

Tab. 5-5 Total iron loss at 0Arms phase current

Total iron loss (W)	Pole piece rotor speed (rpm)								
Magnet rotor speed (rpm)	0	500	1000	1500	2000	2500	3000	3500	4000
0	0	22	55	101	159	229	311	404	510
500	18	5	30	67	116	177	250	335	433
1000	45	11	11	39	79	132	197	273	362
1500	79	31	12	18	50	94	150	218	298
2000	122	58	25	18	25	62	109	169	240
2500	172	92	50	25	25	37	76	127	189
3000	230	132	82	43	30	34	49	91	145
3500	296	179	121	75	41	36	44	63	108
4000	370	233	166	111	68	46	45	55	78

Zero rotor differential speed

Zero control harmonic speed

Tab. 5-6 Total iron loss at 300Arms phase current

Total iron loss (W)	Pole piece rotor speed (rpm)								
Magnet rotor speed (rpm)	0	500	1000	1500	2000	2500	3000	3500	4000
0	0	59	156	289	459	667	912	1194	1514
500	37	18	91	202	349	534	756	1015	1311
1000	89	14	42	129	254	416	615	851	1124
1500	158	55	22	72	174	313	488	701	952
2000	243	111	34	44	108	224	377	567	795
2500	344	182	81	31	72	151	281	448	652
3000	461	267	144	58	51	107	200	344	525
3500	594	368	221	113	45	78	148	255	413
4000	744	484	314	182	87	64	111	195	316

Zero rotor differential speed

Zero control harmonic speed

However, loss curves or material constants covering the whole range of flux densities and frequencies are not readily available from the steel manufacturers. In addition, the points of high saturation are close to the lamination edges which are subject to mechanical stress during manufacturing. Mechanical stress is known to alter material properties of electrical steel. Influence of manufacturing is often expressed in a form of so called "build factor" which groups all negative effects associated with steel processing into one multiplier. In all aforementioned analyses the build factor was assumed to be 1 (i.e. the steel processing was assumed to have no negative effect on material properties). Furthermore, harmonic analysis of elemental flux densities was primarily used to identify fundamentals of dominant components and higher harmonic components with smaller amplitudes were ignored. As it was pointed out in both Chapter 2 and 3, spectrum of flux densities in both air gaps is rich in space harmonics which could further increase overall iron loss.

5.4 Magnet losses

5.4.1 Reason for magnet loss

Neodymium-iron-boron rare earth permanent magnets selected for the prototype of the proposed device contain iron and are known to be electrically conductive, hence any time variation of the operating on their BH curve will inevitably lead to flow of eddy currents within the magnet bodies and consequent ohmic power loss. In conventional traction motors, the most common source of operating point variation are the magnetic circuit reluctance variation introduced by stator slotting and MMF harmonics created by stator windings which are particularly important source of magnet loss in case of motors with fractional slot windings [76].

The most widely employed way of reducing the magnet loss is segmentation and electrical insulation of individual segments from each other which is in principle equivalent to segmentation of soft magnetic parts of the magnetic circuit (laminations). Unlike the parts made of steel laminations, the amplitude of flux density variation in magnets is relatively small hence even relatively coarse segmentation of magnets leads to significant reduction of magnet loss. For instance, in the 2010 Nissan Leaf motor the stator stack is 150 mm long and is divided into

more than 400 laminations, while the rotor magnets have only 18 axial segments [63].

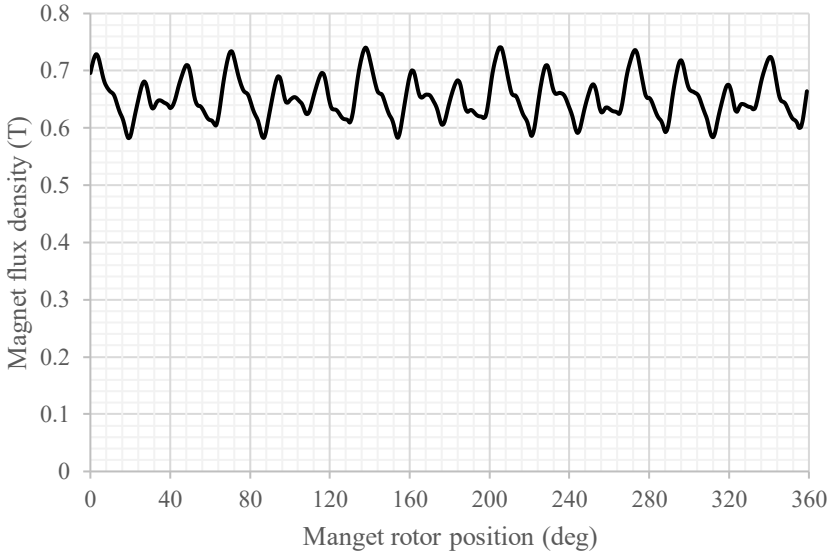

Fig. 5-28 Average magnet flux density vs magnet rotor position

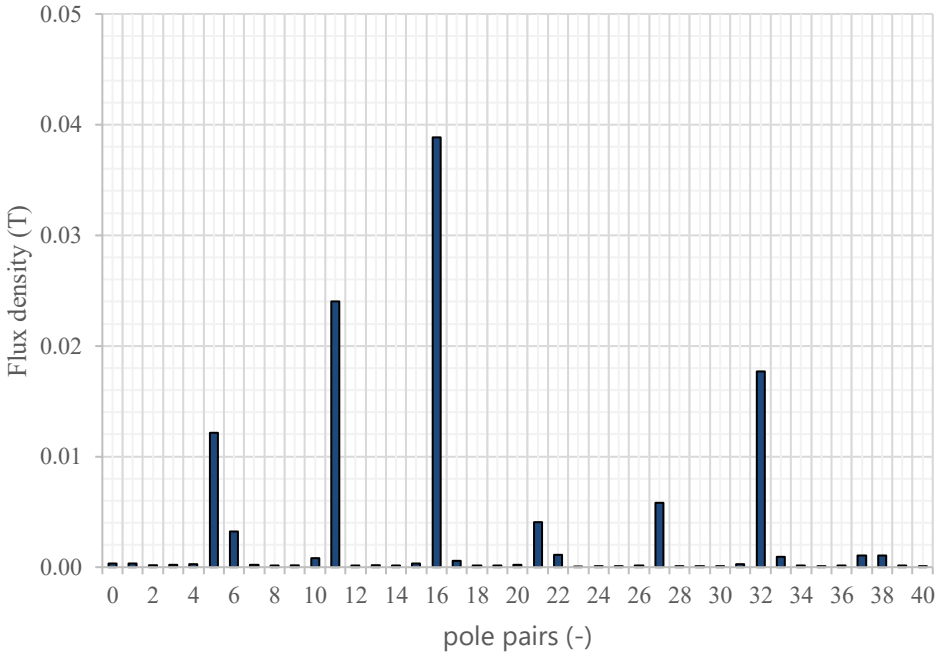

Fig. 5-29 Spectrum of magnet flux density variation with magnet rotor position

The mechanisms by which the magnet loss is induced, and the way of minimizing it is identical in case of the dual rotor device. However, the reluctance variation

could be introduced by both the relative motion of the stator and the pole piece rotor relative to the magnet rotor. Effectively, the magnet rotor is exposed to so called slotting harmonics of two salient structures and therefore two slot passing frequencies can be defined. In addition, the very principle on which the dual rotor device is based, i.e. modulation of magnetic field by pole pieces, creates asynchronous harmonics which further complicate magnet loss analysis.

Average flux density of one of the rotor magnets as a function of magnet rotor angular position for one full revolution when the pole piece rotor was kept stationary at the windings were fed by 300Arms phase current can be seen in Fig. 5-28 and its corresponding spectrum with DC component (0_{th} harmonic) removed in Fig. 5-29. The DC component was removed from the graph since its amplitude it's significantly larger than amplitudes of the other harmonic components and its presence would make the graph less clear. When the magnet rotor is rotating, relative speed between it and both the stator and the pole piece rotor exists. In the spectrum in Fig. 5-29, both 16_{th} harmonic associated with 16 pole pieces and 21_{st} harmonic corresponding to 21 stator slots are present, however the 16_{th} harmonic clearly dominates.

5.4.2 Method of analysis

The common way of modelling magnet loss in electrical machines is to utilize either 2D or 3D time stepping FE model where volumes representing the magnets are conductive (with typical conductivity of NdFeB magnets being 667000 S/m [66]). Rotor motion leads to eddy currents being induced in the magnets and power loss can be easily computed by integrating product of current density distribution and known conductivity [76]. Time stepping 3D models with the complete geometry of the analysed device offer high accuracy of loss prediction, however, solving the model is computationally intense. Using 2D FE model could save considerable amount of solving time but is inherently less accurate since it only considers flow of eddy currents in axial direction of the machine. Various analytical models have been developed for buried magnet rotors, [77] for instance. However, much like the 2D FEA, the proposed methods neglect three dimensional effects, and in addition greatly simplify the analysed geometry (effect of stator slotting is often ignored, and only very basic rotor geometry is considered). Combination of relatively complex

geometry and short axial length of the proposed device makes analytical modelling of magnet loss challenging.

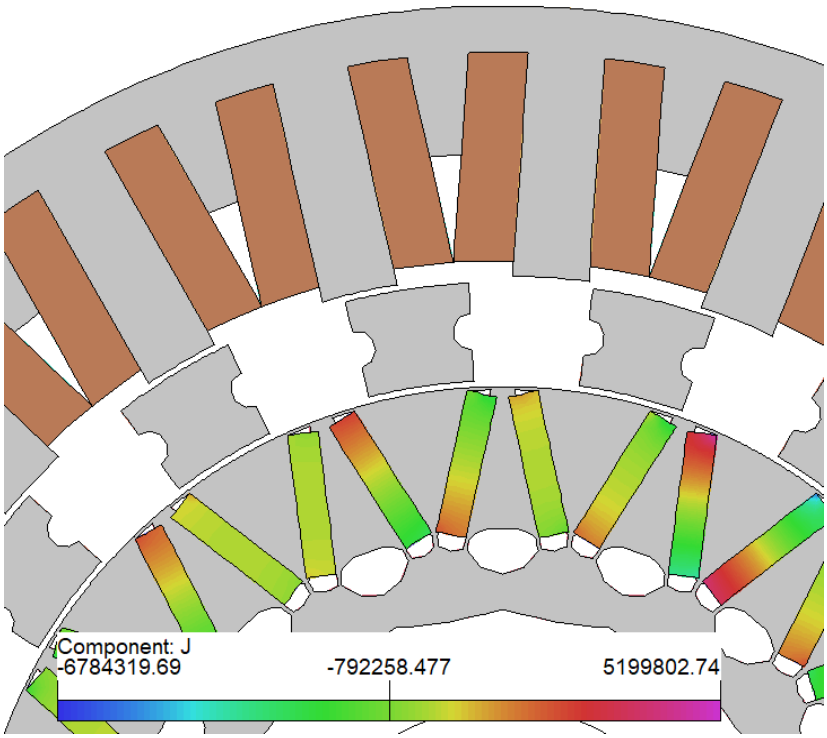

Fig. 5-30 Current density distribution in rotor magnets in 2D FEA model

The purpose of the analysis presented in this section is not only to try to accurately predict the magnet loss but also to understand its behaviour at various operating points. For this reason, the 2D model was initially used to perform large number of analyses to map loss as a function of both rotor speeds and stator loading and it was assumed that while amplitude of loss obtained by 2D and 3D simulation would differ but the trends would be the same. 3D simulation was later employed for more accurate prediction and for analysis of effectiveness of axial magnet segmentation.

It is worth pointing out that when performing analysis using 2D FE model of the machine, it must be ensured that integral of current density in each magnet at any given time step is always zero; the current is forming a loop within the magnet body. For instance, in Opera simulation software each magnet is treated as a bulk eddy current conductor which is coupled to a resistor with near infinite resistance. Current

density distribution in the 2D model with correct boundary condition can be seen in Fig. 5-30.

5.4.3 No load magnet loss behaviour

In order to investigate influence of rotor speeds on magnet loss, the 2D FEA model was used to calculate a map of magnet loss. The results are summarized in Tab. 5-7. Three characteristic loss curves, Fig. 5-31, can be obtained from the full magnet loss map represented by lines in the loss map. The diagonal line represents a situation when both rotors are rotating at the same speed in the same direction, hence there is no relative motion between. There is, however, a relative motion between the magnet rotor and the stator which may cause magnet operating point fluctuations and consequent loss. Additionally, air gap harmonics due to pole piece modulation have non-zero speed. It is apparent from the graph that the diagonal line represents the line of the lowest magnet loss. However, the only point where the magnet loss is zero is when both rotors are stationary and as long as one of the rotors is moving, the magnet loss is present.

Tab. 5-7 No load magnet loss map

Magnet loss (W)		Pole piece rotor speed (rpm)				
		0	1000	2000	3000	4000
Magnet rotor speed (rpm)	0	0.00	42.79	138.43	297.80	502.08
	1000	33.38	7.39	52.75	155.00	324.85
	2000	116.04	37.50	24.32	77.50	199.45
	3000	248.01	120.00	53.75	52.17	117.65
	4000	429.22	250.00	140.12	100.00	87.72

Horizontal and diagonal could be drawn in the map intersecting the point where speed of one of the rotors is zero. In both of these cases the relative speed between the two rotors is constant. However, the relative speed between the magnet rotor and the stator is different resulting in different values of loss. The highest magnet loss occurs when only the pole piece rotor is rotating despite the fact that the relative speed between the magnet rotor and the stator is zero. This could be attributed to the fact that the asynchronous space harmonic created by the pole piece modulation is rotating at higher speed when only the pole piece rotor is moving.

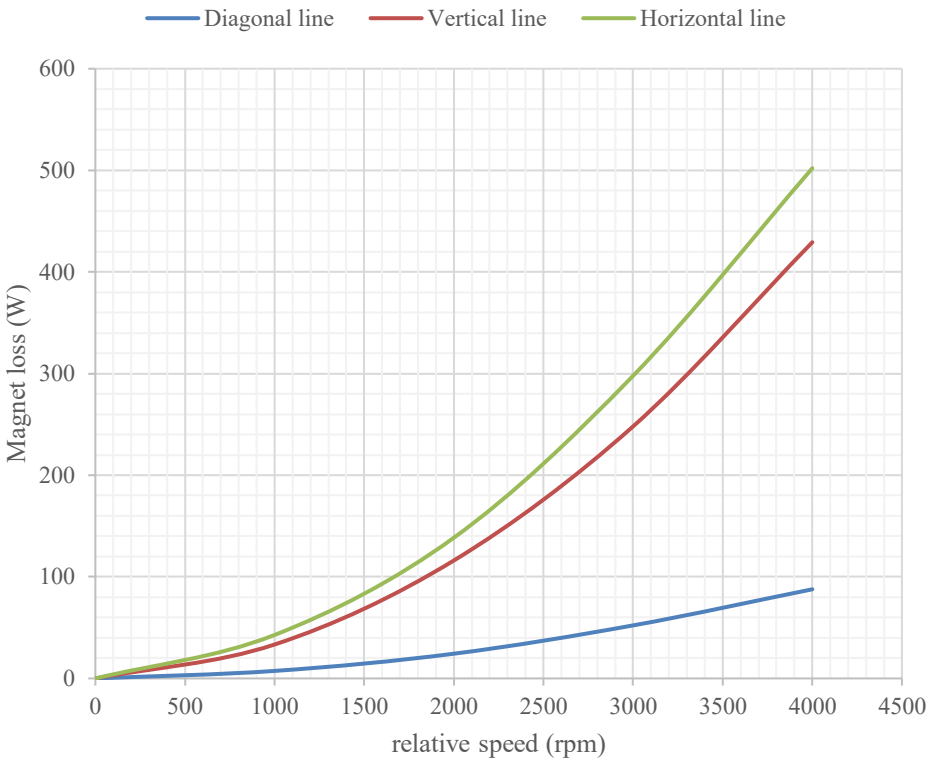

Fig. 5-31 Three characteristic magnet loss curves

5.4.4 Influence of stator loading on magnet loss

Stator loading manifests itself by air gap MMF harmonics and even though the magnet rotor is separated from the stator by the pole piece rotor structure and does not operate on the same fundamental frequency, the fractional slot winding with 0.5 slot per pole and phase chosen for the device is known to create more MMF harmonics than typical overlapping integral slot winding and hence its influence of magnet loss must be considered.

The extreme operating point, where only the pole piece rotor is rotating at 4000rpm, from the loss map, Tab. 5-7, was chosen study influence of stator loading on magnet loss. Stator current loading was varied from 0 to 300Arms and the steady state magnet loss was calculated for each point. The results can be seen in Fig. 5-32. It is apparent that total magnet loss more than doubles at full load compared to the no load scenario. Additionally, the relationship between loss and electrical loading of the stator is close to quadratic.

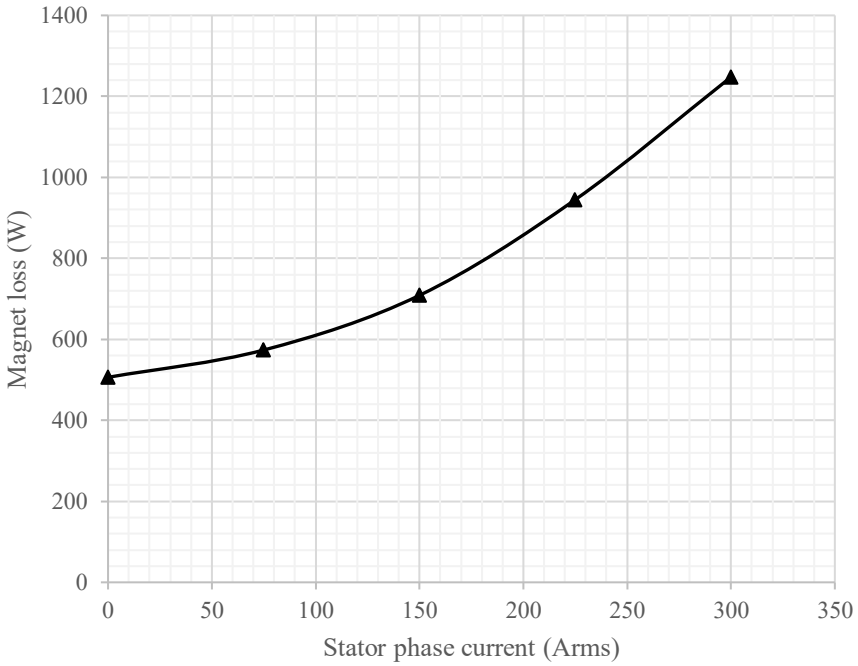

Fig. 5-32 magnet loss at 4000rpm pole piece rotor speed

5.4.5 Influence of magnet segmentation on magnet loss

As it was mentioned previously, magnet loss could be minimized by means of magnet segmentation which breaks the eddy current loops in magnet bodies. Up to this point, 2D time stepping FE model was used for loss computation which is, however, fundamentally unsuitable for segmentation analysis since it assumes that the axial (z axis) length of the magnet block is infinite. In case of Full 3D model of the device, the magnet blocks can be subdivided into segments and insulated from each other by either a layer non-conductive material (realistic representation of real world insulating coating) or assigned electrically insulating boundary condition on the interfaces between individual segments.

Again, the extreme operating point when the pole piece rotor is rotating at 4000rpm was chosen to study influence of magnet segmentation on power loss. Fig. 5-33 shows total magnet loss for different magnet segmentation lengths as well as the result from the 2D model. It is apparent from the graph that if the magnets were constructed as a single solid block, the total loss at 4000rpm pole piece rotor speed would exceed 900W and the loss would be concentrated in the relatively small

volume of the magnets with complicated heat rejection path. While reduced efficiency at such operating speed may be acceptable, the excessive heating of the magnets would likely lead to their demagnetisation. Dividing the 50mm long magnet block into 32 axial segments reduces the total loss to only approximately 50W, however this is relatively fine level of segmentation compared to conventional automotive traction motors. The relatively large difference between the 2D and 3D model can be attributed to the short axial length of the device since the error is a function of machine's aspect ratio, i.e. the longer the machine is the closer the current density distribution within the magnet body is to the ideal infinitely long magnet block with only z axis components of current density.

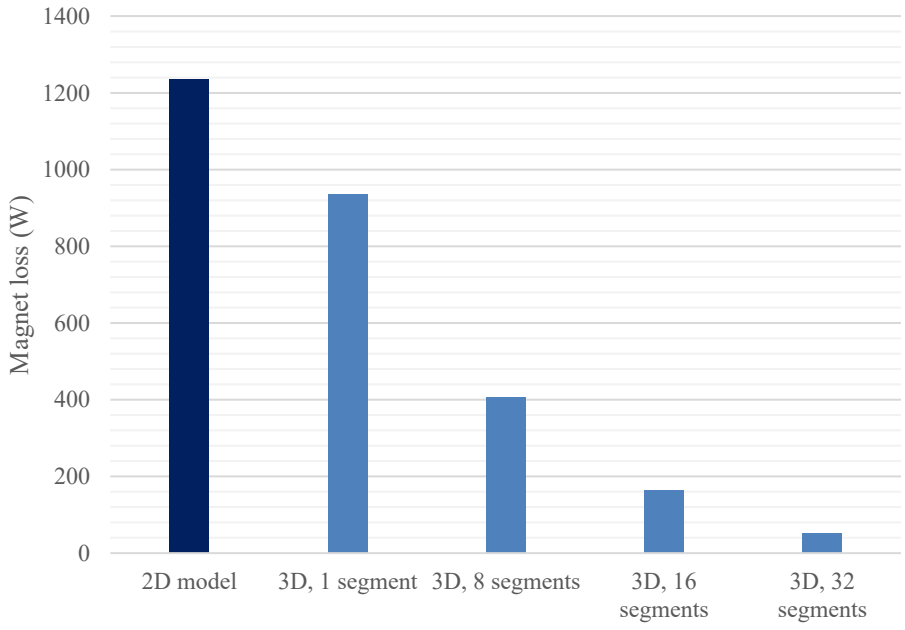

Fig. 5-33 Total magnet loss for different magnet segment lenghts at full load and 4000rpm pole piece rotor speed

From the practical point of view, it is worth noting that magnet segmentation doesn't come without a cost, particularly when fine segmentation is needed. The need for layer of insulation between magnet segments effectively reduces utilisation of the available magnet volume the same way the insulation between laminations does. Additionally, segmenting the magnets and then bonding them back together could increase manufacturing costs. Optimal level of magnet segmentation depends

on thermal management of the rotor, temperature rating of the magnets and whether the device needs sustain high differential speeds continuously or only for short periods of time.

5.5 Stray losses due to the axial leakage field

Axial leakage, discussed in Chapter 4, not only leads to reduction of EMF and torque for a given electrical loading but could also lead to additional stray loss not accounted for during initial design based on two-dimensional modelling. Although amplitude of the axial component of the pole piece rotor field is small in comparison to the radial field, it is penetrating the laminations in direction in which they are ineffective at minimizing eddy currents induced by the field. Purpose of the following sections is to explore methods by which this stray loss component could be quantified and to discuss its impact on the device.

5.5.1 Method of analysis

A pole piece stack in the proposed device consists of number of thin laminations, each of which is exposed to radial, circumferential and axial magnetic field. Calculation of the eddy current component of overall iron loss of laminated stacks was discussed in section 5.3, although the focus was only on loss induced by tangential and radial fields. It was shown that eddy current loss generally depends on square of frequency, flux density and on specific properties of the steel expressed by the constant k_{eddy} which can be calculated analytically from steel material properties and lamination thickness. Similar formulation for eddy current loss as in (5-1), could be used for calculation of loss induced by the axial fields since the nature of the phenomenon is the same. Amplitude of the flux density distribution along the pole piece length and frequency of its variation is known from the 3D FE analysis of the device shown in Chapter 4. However, the analytical expression for eddy current loss constant k_{eddy} used for loss calculation in thin sheets of steel is not valid in this case since the geometrical assumptions made when deriving it do not apply to the actual axial shape of pole pieces.

Unlike the aforementioned thin laminations, a pole piece has got an axially square shape with approximately the same radial length and circumferential width. Outer and inner diameter of the pole piece lamination are curved so as to maintain constant air gap between it and the other two principal components of the device. In its simplest form, sides of pole pieces are straight, however, additional features could be added to the pole piece lamination profile to aid its mechanical retention, Fig. 3-28. It is apparent that deriving an analytical formulation for eddy current losses in such complex shape would be difficult and hence an FE model was used to estimate eddy current loss in a single pole piece lamination as a function of axial flux density and frequency. Eddy current loss due to axial field in a single lamination can be expressed as follows:

$$P_{stray\_eddy} = k_{lam\_eddy} \cdot B_z^2 \cdot f_{ppr}^2 \qquad (5\text{-}9)$$

where k_{lam_eddy} is lamination eddy current loss constant. The FE model used to determine value of k_{lam_eddy} consist of a single pole piece lamination (Fig. 5-34) surrounded by air background region and exposed to an externally applied uniform field, creating the required flux density in the lamination with sinusoidal variation at predefined frequency. The external field has only the component perpendicular to the plain of lamination (aligned with z-axis in the model) effectively emulating the axial field in the machine as described by the following set of equations:

$$\begin{aligned} H_{x\_lam} &= 0 \\ H_{y\_lam} &= 0 \\ H_{z\_lam} &= \frac{B_{z\_lam}}{\mu_0 \cdot \mu_{lam}} \end{aligned} \qquad (5\text{-}10)$$

where B_{z_lam} is the lamination axial flux density and μ_{lam} is lamination permeability. In order to solve the model, linear time harmonic solver could be used as there is only sinusoidal variation of the applied field and flux axial flux densities are well below the saturation point of the steel. Boundary conditions applied to extremities of the background region are such that the field is tangential to x-z and y-z planes and normal to x-y plane.

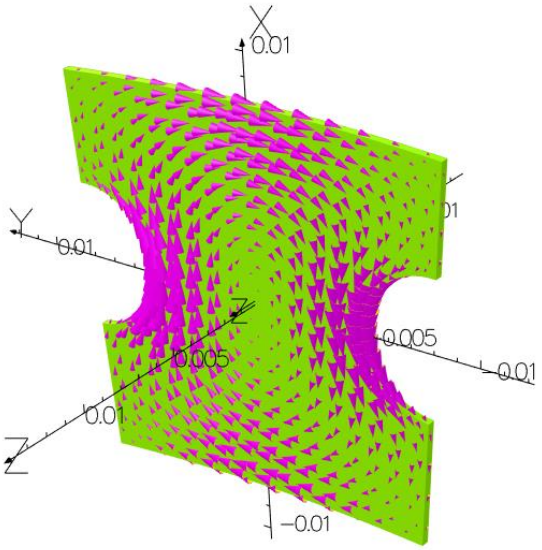

Fig. 5-34 Pole piece lamination model with eddy current vectors induced by varying z axis field

Tab. 5-8 Pole piece lamination loss map

Lamination loss (W)		Flux density (T)									
		0.025	0.05	0.075	0.1	0.125	0.15	0.175	0.2	0.215	0.25
Frequency (Hz)	100	0.000	0.000	0.001	0.002	0.003	0.004	0.006	0.008	0.009	0.012
	150	0.000	0.001	0.002	0.004	0.007	0.010	0.013	0.017	0.020	0.027
	200	0.000	0.002	0.004	0.008	0.012	0.017	0.023	0.031	0.035	0.048
	250	0.001	0.003	0.007	0.012	0.019	0.027	0.037	0.048	0.055	0.075
	300	0.001	0.004	0.010	0.017	0.027	0.039	0.053	0.069	0.080	0.108
	350	0.001	0.006	0.013	0.023	0.037	0.053	0.072	0.094	0.108	0.146
	400	0.002	0.008	0.017	0.031	0.048	0.069	0.094	0.122	0.141	0.191
	450	0.002	0.010	0.022	0.039	0.060	0.087	0.119	0.155	0.179	0.242
	500	0.003	0.012	0.027	0.048	0.075	0.108	0.146	0.191	0.221	0.299
	550	0.004	0.014	0.033	0.058	0.090	0.130	0.177	0.231	0.267	0.361
	600	0.004	0.017	0.039	0.069	0.108	0.155	0.211	0.275	0.318	0.430

Compared to the real world situation, the proposed method is making certain assumptions which could compromise its accuracy. Firstly, the single lamination model applies the external field uniformly. However, in a real machine the axial field distribution is not perfectly uniform across the whole lamination area. Secondly, the single lamination model neglects presence of other laminations in the stack and how reaction fields created by eddy currents in them could affect axial field distribution.

While only fundamental component of flux density variation will be considered the method makes it possible to include higher harmonic components. Eddy current loss is calculated based on induced current density and known conductivity of the lamination material. Results obtained from the model for the pole piece lamination as depicted in Fig. 5-34 is shown in Tab. 5-8. The values in the table could be curve fitted and the eddy current constant k_{lam_eddy} for the specific pole piece shape can be estimated.

Once the value of eddy current loss constant for the specific pole piece lamination shape is known, eddy current loss distribution along the pole piece length can be calculated. In a 50mm long pole piece with 0.98 stacking factor, there are one hundred and forty 0.35mm thick laminations. Using the known axial flux density distribution along the pole piece length (Fig. 4-15) and frequency, loss in each lamination within the stack can be calculated using equation (5-9). Total pole piece rotor loss can be obtained simply by summing losses in individual laminations of a pole piece and multiplying the result by number of pole pieces:

$$P_{stray\_ppr} = p_{ppr} \cdot \sum_{n=1}^{n_{lam}} P_{stray\_eddy}\,(n) \qquad (5\text{-}11)$$

where n_{lam} is number of pole piece laminations.

5.5.2 Analysis results

Using the previously described method, total stray loss of all pole piece rotor designs shown in Fig. 4-17 having axial stray field distribution as per Fig. 4-18, Fig. 4-19 and Fig. 4-20 was analysed. Fig. 5-35 shows stray loss density along the length of pole piece from the centre to the end and it is apparent that majority of the loss is concentrated in the last third of each pole piece stack. Integral of loss density distribution gives the total loss which, for 50mm long pole piece rotor having 0.95 steel fill factor, can be seen in Fig. 5-36 for three values of stator electrical loading. It is apparent that at 300 Arms, the stray loss exceeds 350W which is considerably higher than iron loss of 137W calculated in section 5.3.3. Both sources of loss together create relatively high loss density in the small volume of pole piece rotor steel. Additionally, the stray loss is both speed and load dependant and could be

separated into two components, firstly stray loss induced by the magnet rotor field and secondly stray loss induced by armature reaction field. At low levels of stator electrical loading, the magnet rotor induced component dominates but as the load increases and the machine becomes saturated larger portion of the overall loss is caused by the armature reaction field.

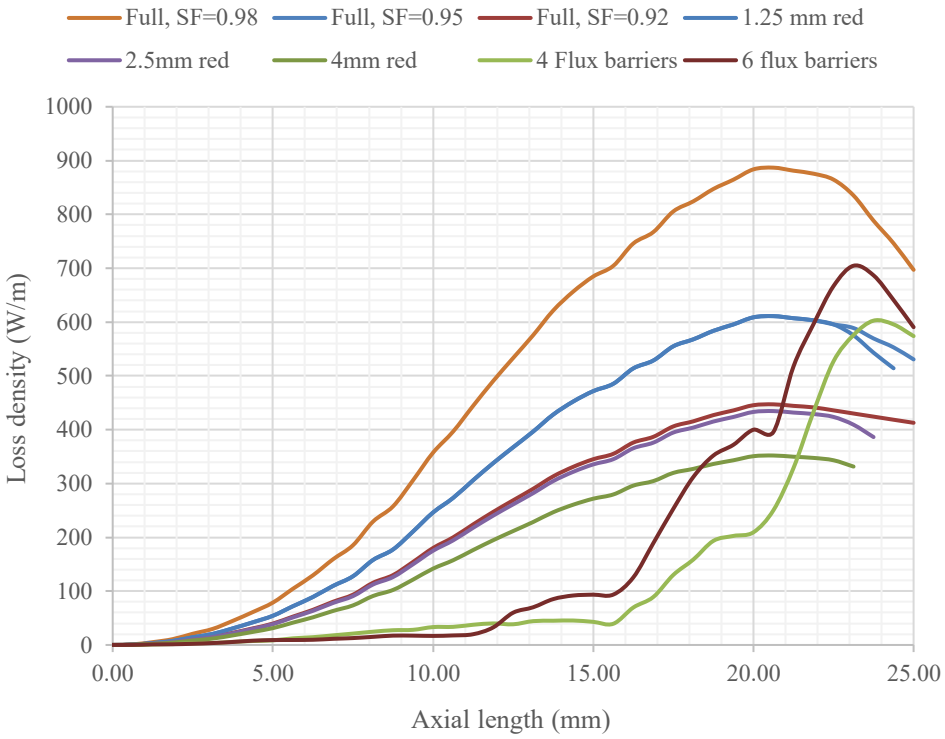

Fig. 5-35 Loss density due to the axial field as a function of pole piece axial length

Comparison of per unit pole piece rotor torque and stray loss for different pole piece designs can be seen in Fig. 5-37. Per unit notation was used in order to clearly differentiation the benefits and drawbacks of designs in comparison with the baseline 50mm rotor with 0.98 steel fill factor. It is apparent that significant reduction in stray loss can be achieved with only small reduction of transmittable torque. Fig. 5-38shows per unit pole piece rotor loss as a function of per unit pole piece steel volume. Again, the 50mm rotor was used as a baseline having 1per unit steel volume. Any modifications to the pole piece (reduction of stacking factor, introduction of concentrated flux barriers etc.) result in reduction of total per unit steel volume. It is apparent from the graph that there is a strong correlation between steel volume and total stray loss. While some methods of axial leakage reduction are more efficient

than others, it can be concluded that overall reduction of pole piece steel volume is more important than the exact method of achieving it.

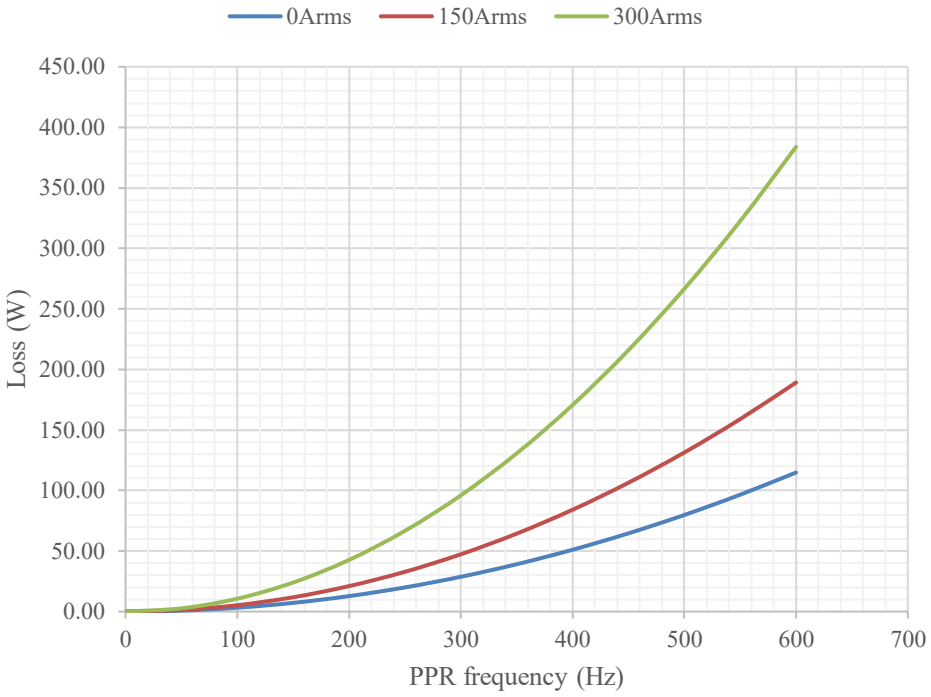

Fig. 5-36 Total pole piece rotor eddy current stray loss as a function of load and frequency for 50mm pole piece rotor with 0.98 steel packing factor

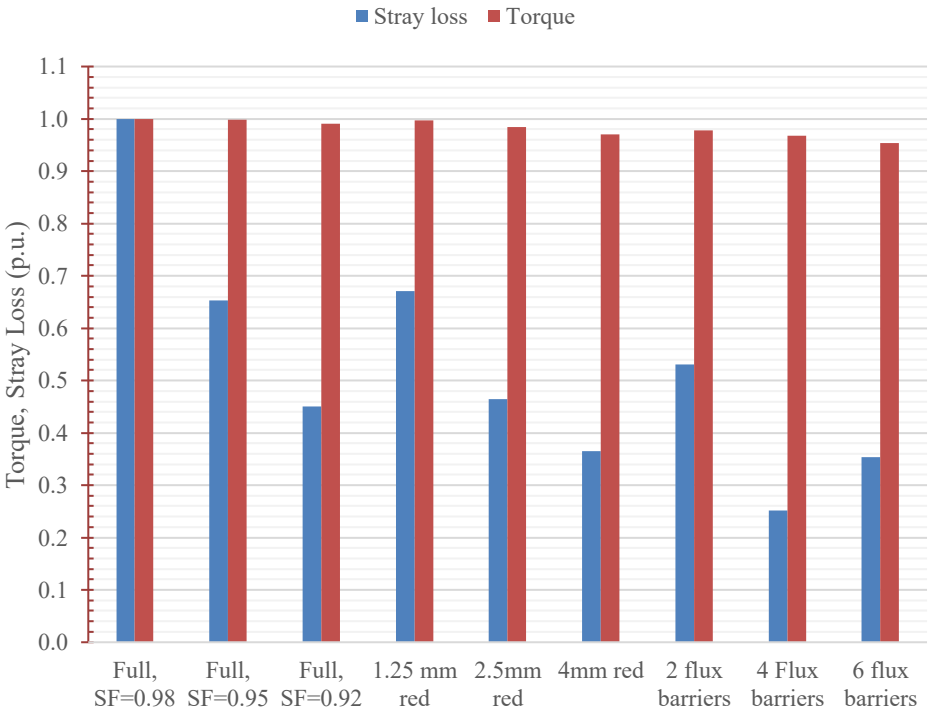

Fig. 5-37 Comparison of per unit loss and torque for different PPR

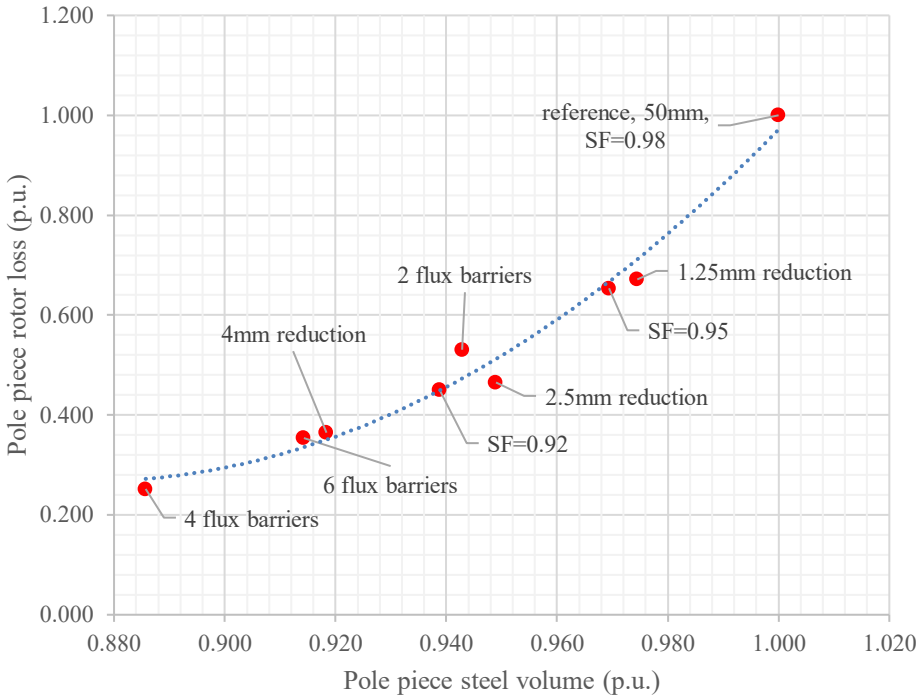

Fig. 5-38 Pole piece rotor stray loss against pole piece steel volume

Tab. 5-9 Pole piece rotor stray loss map at 300A rms phase current

PPR stray loss (W)		Pole piece rotor speed (rpm)								
		0	500	1000	1500	2000	2500	3000	3500	4000
Magnet rotor speed (rpm)	0	0.0	6.0	24.0	54.0	96.0	149.9	215.9	293.9	383.8
	500	6.0	0.0	6.0	24.0	54.0	96.0	149.9	215.9	293.9
	1000	24.0	6.0	0.0	6.0	24.0	54.0	96.0	149.9	215.9
	1500	54.0	24.0	6.0	0.0	6.0	24.0	54.0	96.0	149.9
	2000	96.0	54.0	24.0	6.0	0.0	6.0	24.0	54.0	96.0
	2500	149.9	96.0	54.0	24.0	6.0	0.0	6.0	24.0	54.0
	3000	215.9	149.9	96.0	54.0	24.0	6.0	0.0	6.0	24.0
	3500	293.9	215.9	149.9	96.0	54.0	24.0	6.0	0.0	6.0
	4000	383.8	293.9	215.9	149.9	96.0	54.0	24.0	6.0	0.0

Fig. 5-38 shows per unit pole piece rotor loss as a function of per unit pole piece steel volume. Again, the 50mm rotor was used as a baseline having 1per unit steel

volume. Any modifications to the pole piece (reduction of stacking factor, introduction of concentrated flux barriers etc.) result in reduction of total per unit steel volume. It is apparent from the graph that there is a strong correlation between steel volume and total stray loss. While some methods of axial leakage reduction are more efficient than others, it can be concluded that overall reduction of pole piece steel volume is more important than the exact method of achieving it.

Pole piece rotor stray loss at 300Arms phase current as a function of pole piece rotor and output rotor speed for the baseline design is shown in Tab. 5-9. It is apparent that the stray loss is zero along the diagonal line which equates to zero differential speed between the two rotors. When the differential speed becomes zero, the axial leakage still exists but it does not induce eddy current loss in the pole pieces since there is no variation with time. The line of zero differential speed does not coincide with the line of zero stator frequency, although they are not far from each other. Purely generating or motoring mode of the device will generate the highest value of axial flux induced stray loss.

5.5.3 Validation by dynamic model

As mentioned before, the method of stray loss calculation presented in the previous sections makes number of simplifying assumptions which could compromise its accuracy. Validation of the model by experiment would be complicated since separation of different loss mechanisms from total measured loss would be challenging, potentially impossible. Due to this, alternative calculation method was developed utilising transient time stepping solver and 3D model of the entire device with anisotropic material conductivity. The aim of the following analysis is comparison of both methods. Baseline 50mm long pole piece rotor with 0.98 steel fill factor will be used for the following analyses.

As explained in Chapter 4, laminated stacks in 3D FEA are represented by volumes with equivalent anisotropic permeability to take into account the non-magnetic layers of insulation between individual laminations. Similarly, the influence of the insulating layers on electrical properties of the stack could be modelled using anisotropic conductivity described as follows:

$$\sigma_{tangential} = 1.95e6\ Sm^{-1}$$
$$\sigma_{radial} = 1.95e6\ Sm^{-1} \quad (5\text{-}12)$$
$$\sigma_{axial} = 0\ Sm^{-1}$$

This form of anisotropic conductivity only allows the eddy currents to flow in the plane tangential to the plane of lamination and prevents them from flowing in the direction of the machines axis, effectively emulating a laminated stack with infinitesimally thin insulation layers providing perfect electrical insulation.

In the ideal case, the fully dynamic 3D time stepping model needs to fulfil the following requirements:

1. Ability to rotate the two rotors independently
2. Need for anisotropic and non-linear permeability of laminated stacks
3. Need for anisotropic conductivity of laminated stacks
4. Winding model synchronized with the useful control space harmonic
5. Mesh fine enough to accurately capture eddy current distribution in the magnetic circuit

While most commercial FEA packages could handle such model, it is apparent that solving such model for number of time steps could be computationally intense and time consuming. In addition, the size of the model cannot by reduced using cyclic symmetry since the proposed device is not symmetrical, although only one axial half can be modelled. While material anisotropy and mesh quality are paramount to stray loss modelling, material properties could be assumed to be linear since amplitude of the axial leakage is much smaller than the saturation point of M270-35A electrical steel. When comparing the axial field profile at full load obtained by linear and non-linear FEA, Fig. 5-39, it is apparent that the non-linear model has slightly higher amplitude of the axial field and more even distribution of the stray field along the pole piece length. However, both curves are quite similar and when solving transient time-stepping models it is advantageous to use linear materials as they dramatically reduce solution time.

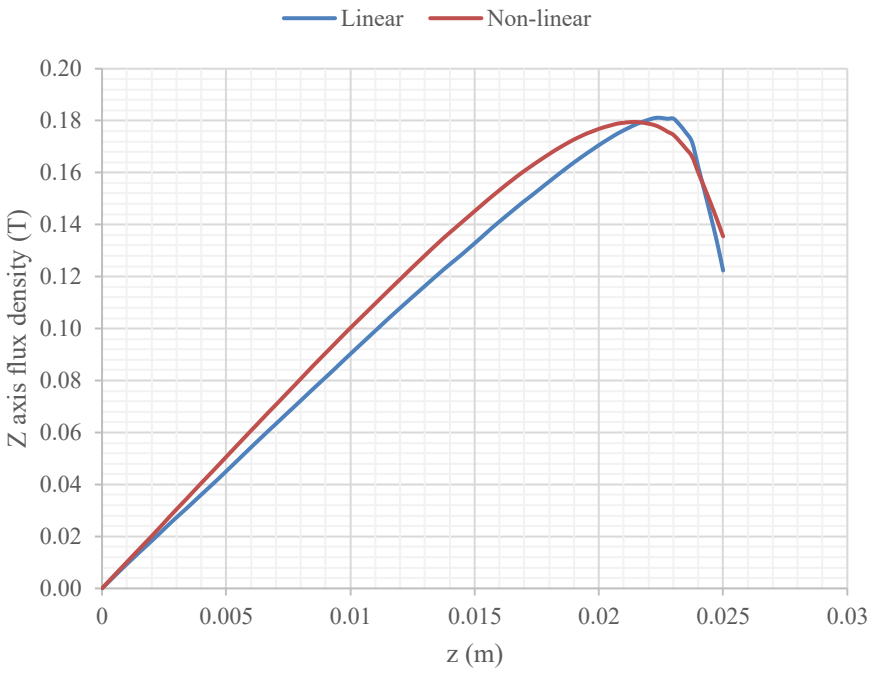

Fig. 5-39 Comparison of pole piece rotor z-axis flux density obtained from linear and non-linear 3D FE model

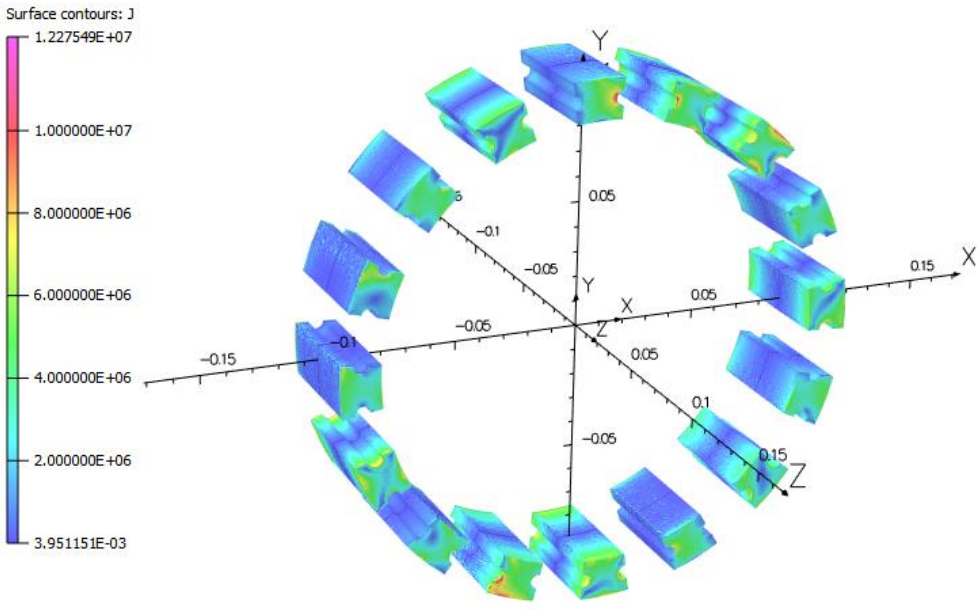

Fig. 5-40 Current density distribution in the pole pieces dynamic model with anisotropic conductivity

It is worth noting that using linear materials poses a problem for realistic modelling of rotors with embedded magnets since the bridges at the sides of the magnets can carry infinite amount of flux without going into saturation. This can be, however, overcome by assigning material properties of air to the bridges so that they behave as if they were heavily saturated by the leakage flux. This approach was used in all models with linear material properties.

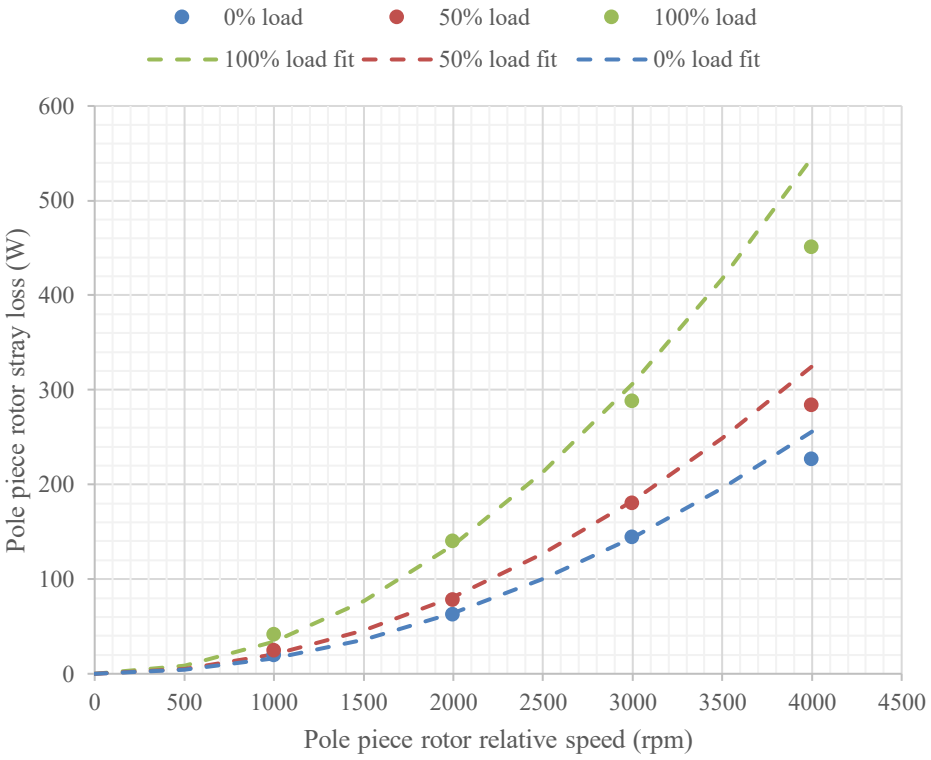

Fig. 5-41 Pole piece stray loss as a function of pole piece relative speed

Fig. 5-40 shows current density distribution in pole pieces at one particular time step when the pole piece rotor was rotated at 4000rpm while the stator phase current was 300Arms. It is apparent that the eddy current density is highest near the axial edges of the pole pieces, as expected based on axial field distribution. Instantaneous stray loss can be calculated by integrating the product of square of current density and the known resistivity of the laminated steel. Fig. 5-41 shows total pole piece rotor stray loss at different loads and pole piece rotor relative speeds. Single data points are values obtained from the FE model while the dashed lines represent a curve fit of the data points assuming that the stray loss is a function of square of pole piece rotor relative speed and is purely resistance limited. It is apparent from the

relative position of the calculated data points and the fitted curves that the stray loss is not purely resistance limited particularly at high values of relative speed where the reaction field in individual laminations is not negligible.

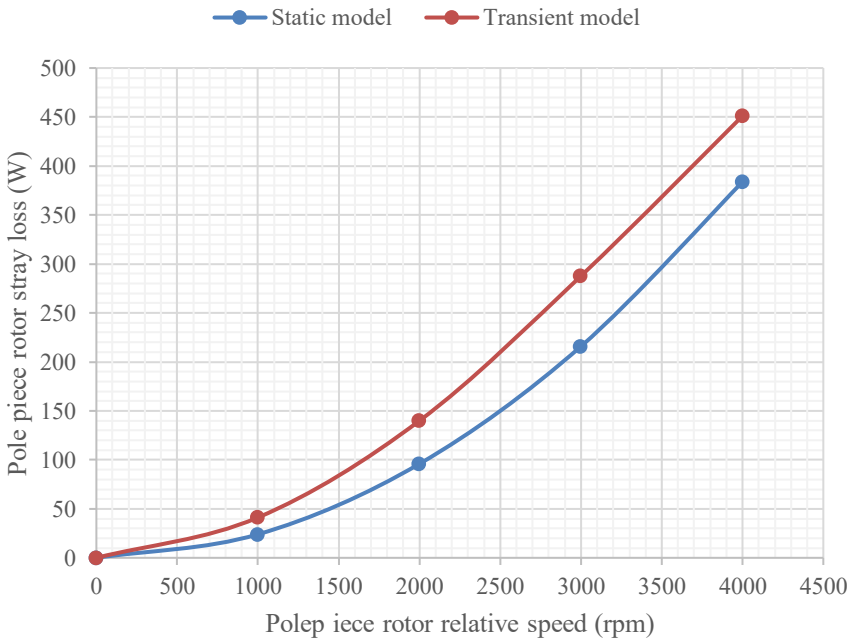

Fig. 5-42 Comparison of stray loss obtained by static and transient model at full load

When comparing loss values obtained by the two calculation methods, Fig. 5-42, it is apparent that losses predicted by the transient time stepping model are approximately 15% higher at full load and 4000rpm relative speed. This can be attributed to the fact that the static model assumes sinusoidal variation of the stray field at fundamental pole piece rotor frequency and also assumes constant average axial field distribution in each lamination while the result obtained by the transient model inherently takes into account higher harmonics as well as uneven distribution of axial flux density. It is also worth pointing out that the difference between the two methods reduces with increase in relative speed due to the fact that the static model ignores reaction fields created by eddy currents in the laminations. However, the static model can provide a good estimate of the stray losses in the pole pieces due to the axial field component, particularly at the early design stages.

5.5.3.1 Stray loss in other active components

While the focus of the previous sections was primarily on the stray field and consequent stray losses in the pole piece rotor, the other two active components of the machine are equally prone to axial field induced losses. The static loss modelling technique based on averaging axial flux density over the pole piece cross sectional area is impractical for stator and magnet rotor as the variation across the surface is much larger than in the pole pieces. However, the dynamic model with anisotropic conductivity developed for pole piece rotor modelling could be used to analyse magnet rotor and stator loss.

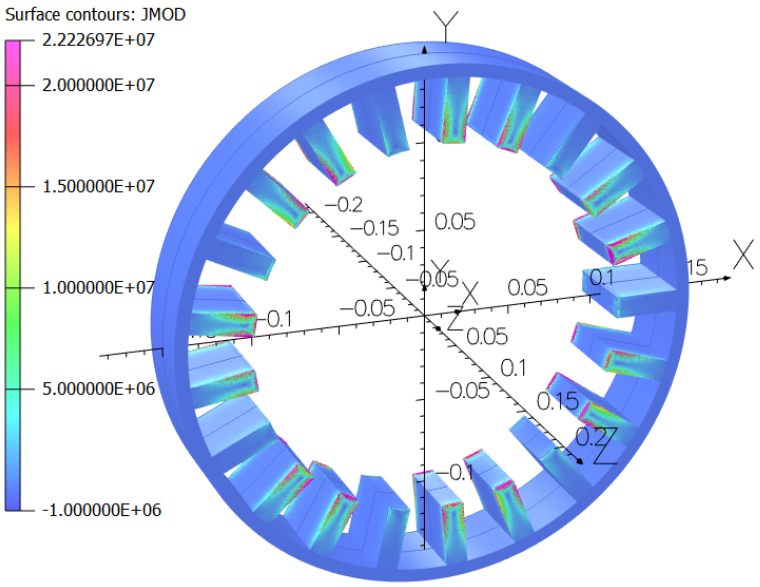

Fig. 5-43 Eddy current distribution in stator teeth at 300 Arms phase current and 1067 Hz fundamental frequency (coils and rotors hidden from view)

As was the case with the pole piece rotor, both stator and output rotor need to be meshed with large number of elements in order to capture the eddy current distribution accurately. Hence analysing stray loss in all three principal components of the device at the same time becomes computationally intense. Fig. 5-43 and Fig. 5-44 show eddy current distribution on the surface of stator and magnet rotor respectively. It is apparent that in the case of the stator, the eddy currents are concentrated near the very edge of the stator stack and particularly in the portion of teeth near the stator bore which means that the leakage field is strongest near the air gap. The magnet rotor axial stray field is primarily dominated by strong DC

component created by the rotor magnets, however, the salient pole piece rotor structure creates variation in magnet operating point and consequent variation in axial field oscillating at pole piece passing frequency related to relative speed of magnet rotor and the pole piece rotor.

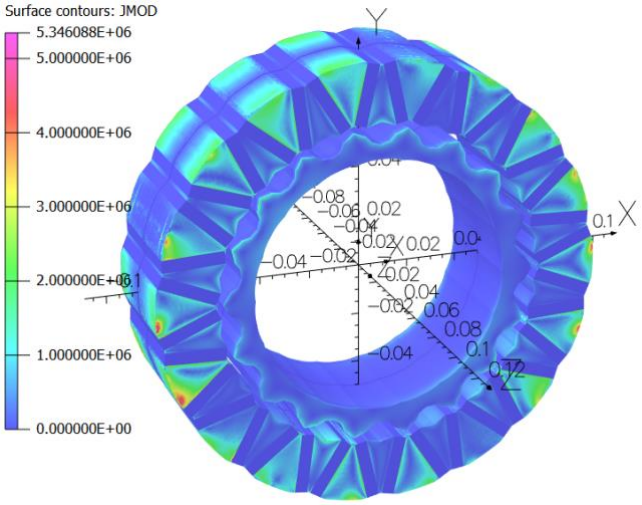

Fig. 5-44 Eddy current distribution in output rotor stack

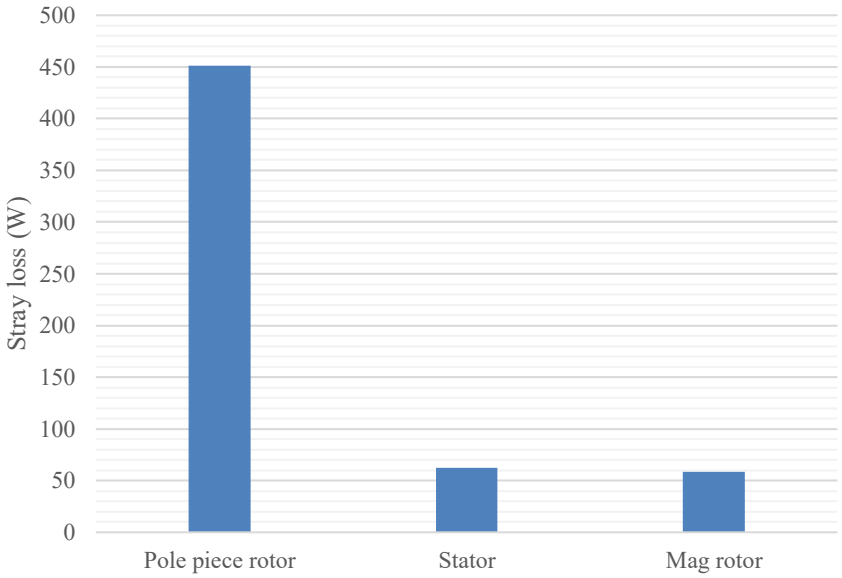

Fig. 5-45 Comparison of axial stray loss in the three principal components of the dual rotor device at 300Arms and 4000rpm differential speed

Comparison between total stray loss in all three principal components of the device at 300Arms phase current when pole piece rotor was rotated at 4000rpm and magnet rotor held stationary can be seen in Fig. 5-45 and it is apparent that the pole piece rotor stray loss accounts for approximately 80% of overall axial field induced stray loss in the device. It is worth pointing out that while the stator stray loss will have impact on overall efficiency of the device, the extra loss can be easily thermally managed since it is generated in the stator steel which is in direct contact with the liquid cooling jacket. On the other hand, even a small amount of additional loss in the magnet rotor can be problematic as it is generated in close proximity of the temperature sensitive magnets. While pole piece rotor steel is thermally insensitive, the combination of small volume of pole pieces and relatively high combined iron and stray loss creates considerable loss density at high differential speeds. Temperature rise in the pole piece will have negligible effect on magnetic performance, it could however, influence structural robustness of the rotor depending on specific design of the supporting structures and their thermal sensitivity.

5.5.4 Practical implications of stray loss

It was shown in the previous sections that stray loss induced by axial leakage field could have considerable impact on efficiency as well as thermal management of the proposed device. Modifications proposed in Chapter 4 were shown to reduce stray loss considerably at the cost of slight reduction in transmittable torque. However, stray loss is a function of rotor differential speed and hence becomes only problematic when the device is required to operate at the extreme differential speed points for prolonged period of time. Moreover, reduced transmittable torque needs to be compensated by increase in stator electrical loading which will increase both DC and AC components of copper loss. It is therefore necessary to consider all effects together with operating limits of the system to decide whether modifications of pole pieces are beneficial from both efficiency and thermal point of view.

As an alternative to reducing equivalent permeability of the pole piece laminated stacks in axial direction, pole pieces can be made of granular soft magnetic composites which have isotropic magnetic properties (the same permeability in all directions) and would be effective at breaking eddy current loops induced by the

leakage field. However, high axial permeability is a disadvantage since it promotes axial leakage and permeability of soft magnetic core tends to be lower than that of a laminated one which could have negative effect on torque transmission. Another option is further radial and/or circumferential segmentation of the pole piece laminations although this could compromise structural rigidity of the pole piece rotor.

It is important to note that both presented methods of stray loss analysis are difficult to validate by experiment as stray losses are generally hard to separate from other loss mechanisms since effects of the stray leakage field in a real machine cannot be effectively isolated from influence of the main field. A way of experimentally quantifying how pole piece rotor design affects stray loss would be to build several prototypes which would fit with the same stator and magnet rotor and measure the difference in overall loss. Such experimental work is outside the scope of this thesis and could be performed as a part of the future work. The methods and the analyses should be viewed as attempts to understand the axial stray loss phenomenon in the dual rotor device rather than tools for accurate loss prediction.

5.6 Total loss model of the dual rotor device

It is apparent from the previous discussions of loss mechanisms present in the proposed device that two-dimensional map of efficiency or loss is not sufficient to graphically represent its performance. Most loss mechanisms are function of both rotor speeds and also of stator electrical loading, hence three-dimensional loss/efficiency cube must be used. The overview of all electromagnetic loss mechanisms can be seen in Tab. 5-10. As it is apparent from the list of loss mechanisms, the loss model only takes into account losses of electromagnetic nature. Frictional losses in the bearings and aerodynamic drag are assumed to be negligible.

Tab. 5-10 Electromagnetic loss mechanisms present in the dual rotor device

Loss mechanisms	**Function of**
DC copper loss	I_{ph}
AC copper loss	$I_{ph}, \omega_{ppr}, \omega_m$
Stator iron loss	$I_{ph}, \omega_{ppr}, \omega_m$
Magnet rotor iron loss	ω_{ppr}, ω_m
Pole piece rotor iron loss	$I_{ph}, \omega_{ppr}, \omega_m$
Pole piece rotor stray loss	$I_{ph}, \omega_{ppr}, \omega_m$
Magnet rotor stray loss	ω_{ppr}, ω_m
Stator stray loss	$I_{ph}, \omega_{ppr}, \omega_m$
Magnet loss	$I_{ph}, \omega_{ppr}, \omega_m$

5.7 Predicted efficiency of the prototype machine

Using the analysis methods introduced in this chapter, total loss and efficiency of the prototype machine was predicted. Several design choices were made which have an effect on efficiency. Firstly, series connection of phase coils was used, and the coils were wound using transposed LITZ cable. Continuous transposition in LITZ cable together with small diameter of each strand within the bundle ensures that AC components of copper loss are minimal. DC phase resistance of the winding wound with LITZ cable was estimated at 9mΩ at 20°C and 12mΩ at 100°C. Out of all four copper loss mechanisms, only DC copper loss will be considered in the loss mapping as circulation between parallel coils is eliminated by series connection and eddy current loss together with circulation between parallel strands is assumed to be minimized to negligible value by the LITZ cable. Secondly, the rotor magnets were segment axially with 2.5mm segment length to minimize rotor losses.

Predicted total loss for 75, 150 and 300 Arms phase current can be seen in Tab. 5-11, Tab. 5-13 and Tab. 5-15 respectively and efficiency in Tab. 5-12, Tab. 5-14 and Tab. 5-16 respectively. Efficiency of the device can be computed using the following equation:

$$\eta = \frac{P_{in} - P_{loss}}{P_{in}} = \frac{\left(P_{ppr} + P_{stat}\right) - P_{loss}}{\left(P_{ppr} + P_{stat}\right)} \quad (5\text{-}13)$$

where P_{in} is total input power, P_{loss} is total power loss, P_{ppr} is pole piece rotor power calculated as a product of pole piece rotor speed and torque, P_{stat} is stator power calculated either from stator reaction torque and control space harmonic speed. It is important to note that stator power can be negative or positive depending on specific combination of input and output rotor speed and hence the stator could be operating in motoring or generating mode as described in Chapter 2. Temperature of 100°C was assumed for components of the device hence the copper resistivity and remanent magnet flux density were adjusted accordingly.

Tab. 5-11 Total loss map at 75Arms, 50Nm input torque, 100°C temperature

Total loss (kW)	Input speed (rpm)								
Output speed (rpm)	0	500	1000	1500	2000	2500	3000	3500	4000
0	0.20	0.26	0.33	0.43	0.55	0.69	0.85	1.03	1.23
500	0.24	0.22	0.28	0.36	0.46	0.58	0.72	0.88	1.07
1000	0.30	0.23	0.24	0.30	0.38	0.49	0.61	0.75	0.92
1500	0.38	0.29	0.25	0.27	0.33	0.41	0.52	0.64	0.79
2000	0.48	0.37	0.28	0.27	0.29	0.36	0.44	0.55	0.68
2500	0.59	0.46	0.36	0.29	0.29	0.32	0.39	0.48	0.59
3000	0.72	0.58	0.45	0.35	0.31	0.32	0.35	0.42	0.51
3500	0.87	0.71	0.57	0.45	0.35	0.34	0.35	0.38	0.46
4000	1.04	0.86	0.70	0.56	0.44	0.38	0.37	0.39	0.42

Tab. 5-12 Efficiency map at 75Arms, 50Nm input torque, 100°C temperature

Efficiency (-)	Input speed (rpm)								
Output speed (rpm)	0	500	1000	1500	2000	2500	3000	3500	4000
0		0.909	0.939	0.947	0.949	0.949	0.948	0.946	0.943
500	0.855	0.921	0.948	0.956	0.957	0.957	0.955	0.953	0.951
1000	0.905	0.925	0.955	0.962	0.964	0.963	0.962	0.960	0.957
1500	0.919	0.937	0.954	0.967	0.969	0.969	0.967	0.965	0.963
2000	0.924	0.940	0.953	0.966	0.972	0.973	0.972	0.970	0.968
2500	0.925	0.940	0.953	0.964	0.972	0.976	0.975	0.974	0.972
3000	0.923	0.938	0.950	0.961	0.970	0.976	0.978	0.977	0.976
3500	0.921	0.935	0.947	0.958	0.967	0.974	0.978	0.979	0.978
4000	0.918	0.931	0.943	0.954	0.963	0.971	0.976	0.979	0.980

Tab. 5-13 Total loss map at 150Arms, 100Nm input torque, 100°C temperature

Total loss (kW)	Input speed (rpm)								
Output speed (rpm)	0	500	1000	1500	2000	2500	3000	3500	4000
0	0.81	0.87	0.95	1.06	1.20	1.37	1.56	1.77	2.02
500	0.85	0.83	0.89	0.98	1.10	1.24	1.41	1.60	1.83
1000	0.92	0.84	0.85	0.92	1.01	1.13	1.28	1.46	1.66
1500	1.00	0.90	0.85	0.88	0.95	1.05	1.17	1.33	1.51
2000	1.10	0.98	0.89	0.88	0.91	0.98	1.09	1.22	1.38
2500	1.22	1.08	0.97	0.90	0.91	0.94	1.02	1.13	1.27
3000	1.37	1.21	1.07	0.96	0.92	0.94	0.98	1.06	1.18
3500	1.53	1.35	1.19	1.06	0.96	0.95	0.97	1.01	1.11
4000	1.71	1.51	1.33	1.18	1.06	0.99	0.99	1.01	1.06

Tab. 5-14 Efficiency map at 150Arms, 100Nm input torque, 100°C temperature

Efficiency (-)	Input speed (rpm)								
Output speed (rpm)	0	500	1000	1500	2000	2500	3000	3500	4000
0		0.858	0.917	0.937	0.946	0.950	0.953	0.954	0.954
500	0.776	0.863	0.922	0.941	0.950	0.955	0.957	0.958	0.958
1000	0.866	0.875	0.925	0.945	0.954	0.958	0.961	0.962	0.962
1500	0.899	0.907	0.925	0.947	0.957	0.961	0.964	0.965	0.965
2000	0.915	0.923	0.930	0.947	0.959	0.964	0.967	0.968	0.968
2500	0.923	0.931	0.938	0.946	0.959	0.965	0.969	0.970	0.971
3000	0.928	0.936	0.943	0.948	0.958	0.965	0.970	0.972	0.973
3500	0.931	0.939	0.945	0.951	0.956	0.965	0.970	0.973	0.974
4000	0.932	0.940	0.946	0.952	0.957	0.964	0.970	0.973	0.975

Tab. 5-15 Total loss map at 300Arms, 150Nm input torque, 100°C temperature

Total loss (kW)	Input speed (rpm)								
Output speed (rpm)	0	500	1000	1500	2000	2500	3000	3500	4000
0	3.24	3.31	3.44	3.63	3.87	4.17	4.53	4.94	5.41
500	3.29	3.26	3.35	3.49	3.70	3.95	4.27	4.64	5.07
1000	3.37	3.27	3.29	3.39	3.55	3.77	4.04	4.37	4.76
1500	3.49	3.35	3.29	3.33	3.44	3.62	3.85	4.14	4.48
2000	3.65	3.46	3.34	3.32	3.37	3.50	3.69	3.94	4.24
2500	3.84	3.61	3.44	3.34	3.35	3.42	3.57	3.78	4.04
3000	4.06	3.79	3.58	3.43	3.37	3.40	3.48	3.65	3.87
3500	4.32	4.01	3.76	3.56	3.43	3.41	3.45	3.55	3.73
4000	4.61	4.26	3.96	3.73	3.55	3.46	3.46	3.51	3.63

Tab. 5-16 Efficiency map at 300Arms, 150Nm input torque, 100°C temperature

Efficiency (-)	Input speed (rpm)								
Output speed (rpm)	0	500	1000	1500	2000	2500	3000	3500	4000
0		0.703	0.820	0.867	0.890	0.904	0.912	0.918	0.921
500	0.573	0.707	0.824	0.871	0.895	0.909	0.917	0.922	0.925
1000	0.724	0.730	0.827	0.874	0.898	0.912	0.921	0.926	0.930
1500	0.791	0.798	0.827	0.876	0.901	0.916	0.924	0.930	0.933
2000	0.829	0.836	0.841	0.877	0.903	0.918	0.927	0.933	0.937
2500	0.852	0.860	0.865	0.876	0.904	0.920	0.930	0.936	0.940
3000	0.867	0.875	0.881	0.885	0.903	0.920	0.931	0.938	0.942
3500	0.878	0.885	0.892	0.897	0.902	0.920	0.932	0.939	0.944
4000	0.885	0.892	0.899	0.905	0.909	0.919	0.932	0.940	0.945

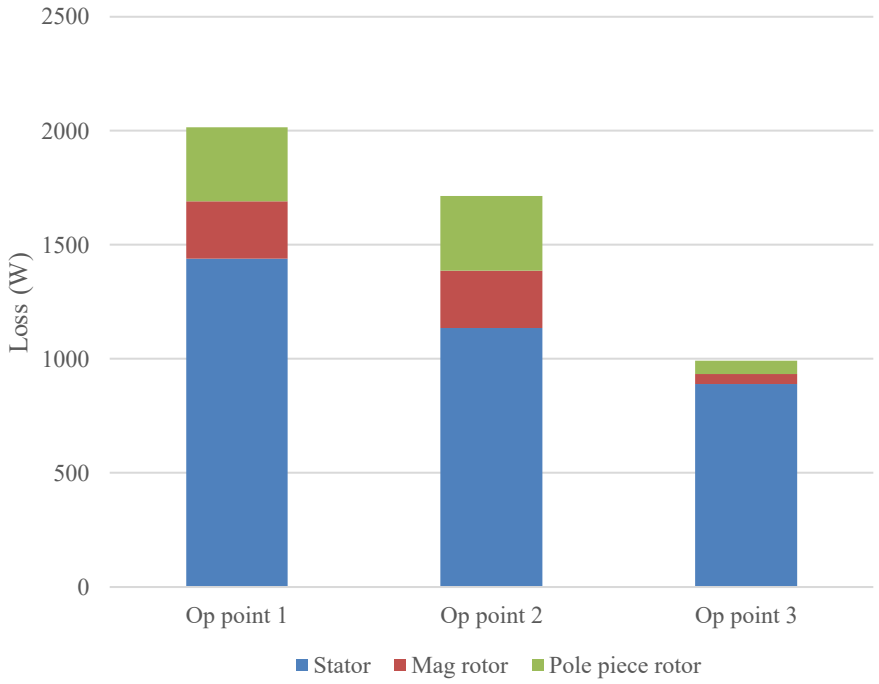

Fig. 5-46 Loss breakdown between components of the device at 3 operating points and 150Arms, 100°C temperature

It is apparent from the predicted loss maps that the area of lowest loss occurs near the between the line of zero stator frequency and the line of zero differential speed which is to be expected based on discussions of individual loss mechanisms. The highest value of total loss occurs when pole piece rotor rotates at 4000rpm while the magnet rotor is stationary, this is the point when maximum input mechanical power

is converted into output electrical power. For both values of phase current, the highest efficiency occurs at 4000rpm pole piece and magnet rotor speed. It is apparent from the efficiency maps that the highest efficiency doesn't coincide with the area of the lowest loss. This is due to the fact that maximum power flow through the device occurs when the pole piece rotor is rotating at 4000rpm and even though the total loss is high at this point, the overall efficiency is higher than at lower pole piece rotor speeds.

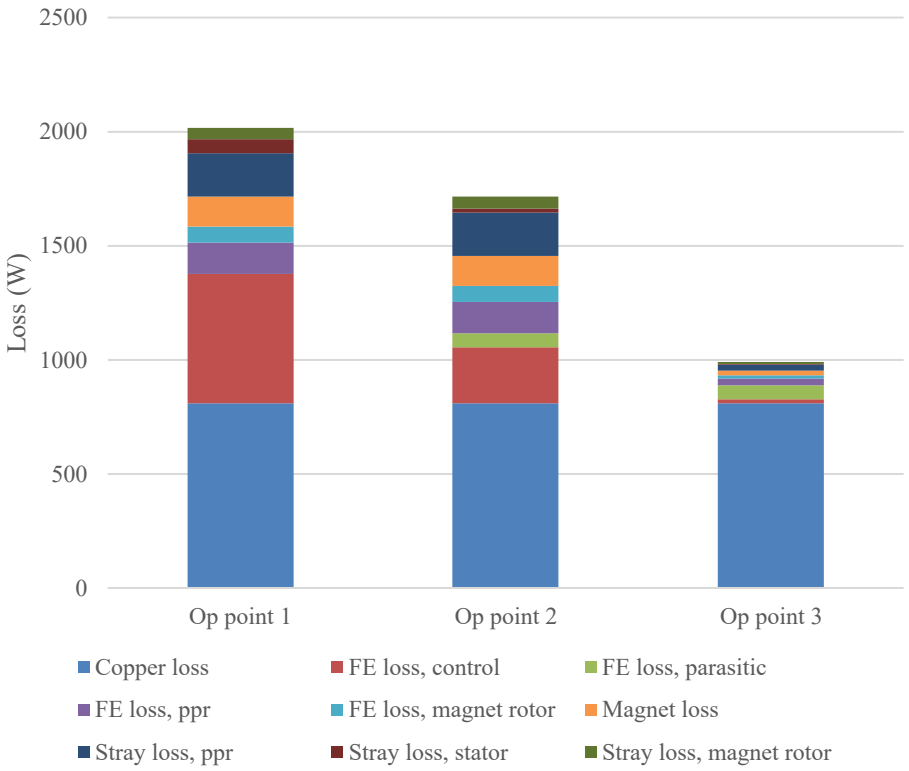

Fig. 5-47 loss breakdown at 3 operating points and 150Arms, 100°C temperature

Contribution of each principal component to the total loss of the device at three different operating points can be seen in Fig. 5-46. Operating points 1 and 2 represent corner points on the map when pole piece rotor or magnet rotor is rotating at 4000rpm respectively while the other rotor is stationary. Operating point 3 is when the pole piece rotor is rotating at 2500rpm while magnet rotor at 4000rpm. This point is in between the lines of zero stator frequency and zero rotor differential speed. Constant phase current of 150Arms with 100Nm pole piece rotor torque was kept for all three operating points. Additionally, contribution of each loss mechanism to the overall loss at the three operating points is shown in Fig. 5-47. It is apparent that

stator contributes the most to the total loss of the device with the main loss mechanism being copper loss. At points with high stator frequencies, however, combined iron, magnet and stray losses are larger than copper loss.

While operation at zero stator frequency is possible and results in the highest efficiency of the device, it could lead to uneven distribution of copper loss among stator phases. However, during a normal operation of the hybrid drivetrain, the device is unlikely to operate at zero stator frequency for significant amount of time. Additionally, the drivetrain of the vehicle can be controlled in such a way that even temperature rise in all three phases is achieved.

5.8 Conclusion

Loss mechanisms present in the proposed device were identified, discussed and quantified for the range of input and output speeds and input torque. Loss analysis of the proposed device is more complex and computationally intense when compared to conventional traction motors due to the presence of multiple space harmonics in the airgaps, two rotating components and also to strong axial leakage field.

Iron loss analysis of the device is unique since the stator is exposed to two strong flux density space harmonics which rotate at frequencies independent from each other, which makes it impossible to define common period for time or frequency domain analysis of iron loss at most operating points. However, it was shown that the iron loss component related to the control space harmonic is dominant even at no load.

While magnet and copper loss are common loss mechanisms present in PM traction motors, presence of the pole piece rotor between the stator and magnet rotor was shown to exacerbate both of them. Salient structure of the pole piece rotor causes large operating point fluctuations in the magnets and also increases effective air gap between the rotors and the stator giving rise to strong cross slot leakage field, which could lead to considerable AC copper loss. However, both AC copper and magnet loss could be minimized by design.

Apart from apparent reduction of transmittable torque, axial leakage also manifests itself in a form of additional eddy current stray loss. Two FE based methods of stray loss calculations were presented. It was shown that stray loss could become a significant part of the machines overall loss, particularly at high differential speeds between the two rotors. Although focus was primarily on the pole piece rotor, it was shown that stray loss is present in stator and magnet rotor as well.

It can be concluded that the device can achieve high theoretical peak electromagnetic efficiency of nearly 98%, despite its inherent constructional complexities.

Chapter 6 Experimental validation

6.1 Introduction

In order to validate the analysis methods and design principles described in the previous chapters, a full-scale prototype of the proposed machine was built and tested on a test rig simulating a real-world operation of the machine in a power split hybrid drivetrain. Focus of the testing was to demonstrate the principal functionality of the device, its performance, control and efficiency over the specified operating range.

Assembly of the prototype, construction of test rig and the testing itself was performed at Magnomatics Ltd. using facilities dedicated to development of magnetically geared electrical machines and transmission systems. Control of the testing rig and data acquisition was done using proprietary lab view based software.

Among the performance indicators of interest are all those associated with conventional electrical machines such as EMF generated at winding terminals and torque on both shafts as a function of phase current. Additionally, control of power flow between the mechanical shafts and electrical terminals represents core functionality of the device which needed to be validated. As pointed out in Chapter 5, losses of the device and their modelling are more complex than in case of conventional electrical machines as the additional shaft adds another dimension to most loss mechanisms. As efficiency is a function of both rotor speeds and stator phase current, two-dimensional loss/efficiency map does not capture the entire operating range of the device and a three-dimensional loss/efficiency cube has to be measured.

6.2 Construction of the prototype machine

The prototype of the proposed machine was built as per Tab. 3-8 and Fig. 3-28 shown in section 3.4.5. Individual components of the device were made by sub-contractors based on provided specifications and the final assembly was performed by technicians at Magnomatics Ltd facilities. The disassembled prototype can be seen in Fig. 6-1 where wound stator and magnet rotor (PMR) is shown inside an aluminium housing with integrated liquid cooling jacket. Interference fit between the stator stack and the housing was employed to ensure optimal heat transfer. Coils were pre-wound using Litz cable, compressed, trickle impregnated and inserted into slots. 0.33mm thick Nomex paper slot liner provides the insulation between coils and the stator stack. As mentioned before, the magnetic circuit of all three principal components of the dual rotor device was made of laminated electrical steel of M270-35A grade.

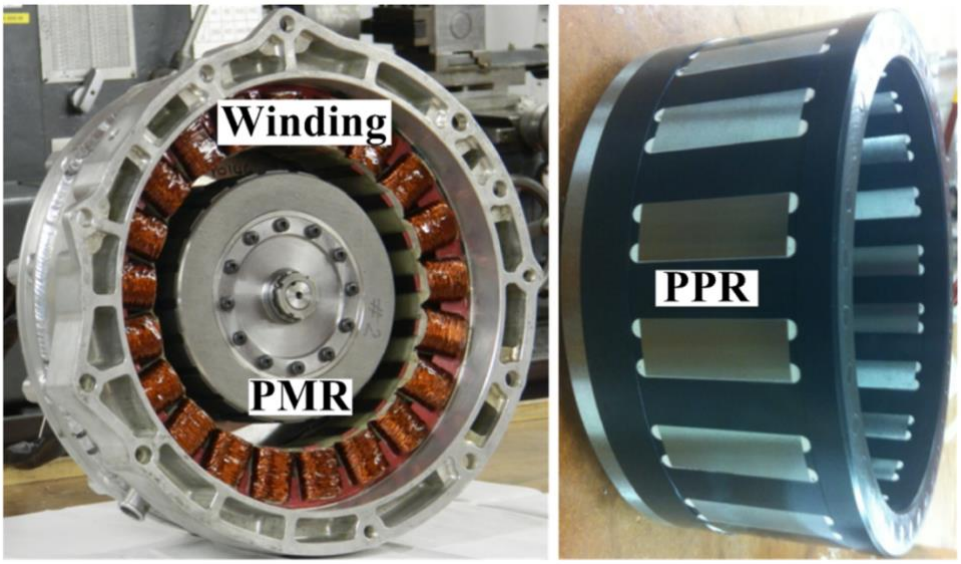

Fig. 6-1 Prototype of the proposed device with removed pole piece rotor (PPR) and highlighted stator winding and the magnet rotor (PMR)

Ensuring structural integrity of the pole piece rotor under centrifugal as well as electromagnetic loads is particularly challenging since materials used for its supporting structure must be non-magnetic, so as not to compromise the ability of the pole pieces to modulate the magnetic fields, as well as non-conductive to prevent formation of eddy currents. For this reason, PEEK engineering plastic which is

known for its strength and temperature resistance was used to support pole pieces. 50mm long pole piece stacks are purely supported by the plastic and do not come into contact with other metallic parts. The plastic supporting structure was equipped with threaded inserts and attached to a mild steel plate which facilitated torque transfer from the input shaft.

An important part of the research presented in this thesis was the study of influence of axial leakage on performance of the proposed device. The entire Chapter 4 was dedicated to analysis of the phenomenon and how it can be mitigated by design. However, for the prototype device, none of the proposed pole piece rotor modifications were adopted for several reasons. Firstly, the phenomenon was initially experimentally observed on another magnetically geared machine developed by Magnomatics which had much higher power rating and physical size. Because of the machine's size and construction, it was relatively easy to study the influence of the phenomenon on it which manifested itself as a drag torque during no-load operation and which could not have been attributed to any other known loss mechanism. FEA analysis, performed later, confirmed presence of substantial axial leakage. However, during the time when the axial leakage was studied on the larger machine, the pole piece rotor design for the prototype of the dual rotor device was already being manufactured. Secondly, while the pole piece rotor lamination stack modifications, such as introduction of concentrated or distributed flux barriers, could minimize axial leakage, they could also affect structural integrity of the pole piece rotor and increase risk of mechanical failure during testing. Since the prototype was the first of its kind, it was decided to use the simplest construction possible and eliminate as many potential failure modes as possible.

6.3 Test rig setup and instrumentation

Fig. 6-3 shows the prototype mounted on the test rig, whilst Fig. 6-2 shows schematic layout of the test rig used for the performance evaluation. The dynamometer consists of two Leroy-Somer induction machines, the green machines in Fig. 6-3 , first one providing input torque to the pole piece rotor and the second one acting as a mechanical load coupled to the output rotor. Both the two induction

machines and the prototype machine were supplied by Control Techniques SPM1404 industrial drives and are controlled via Modbus communication protocol.

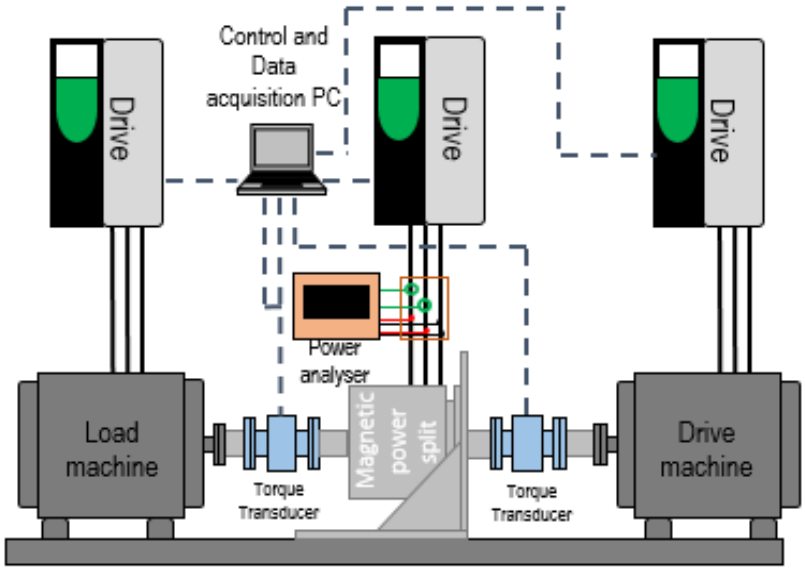

Fig. 6-2 Schematic layout of the test rig

Torque on both shafts was measured by Kistler 4520A torque transducers with measuring range up to 200Nm and ±10V output signal connected to DAQ. Temperature of the prototype machine was monitored by K-type thermocouples embedded in the concentrated coils and connected to TCO-08 data logger. Power flow in or out of the stator windings by Newtons 4th power analyser. The entire test rig setup was controlled by a PC with proprietary National Instruments LabView based control and data acquisition software, developed my Magnomatics ltd., controlling the drives as well as collecting and processing the measured data. Input and output shaft of the power split device are equipped with position sensors so that position of the asynchronous harmonic can be estimated, and the industrial drive connected to the device can be synchronised with it. With this setup, any combination of input and output speed and load could be tested, and the performance evaluated.

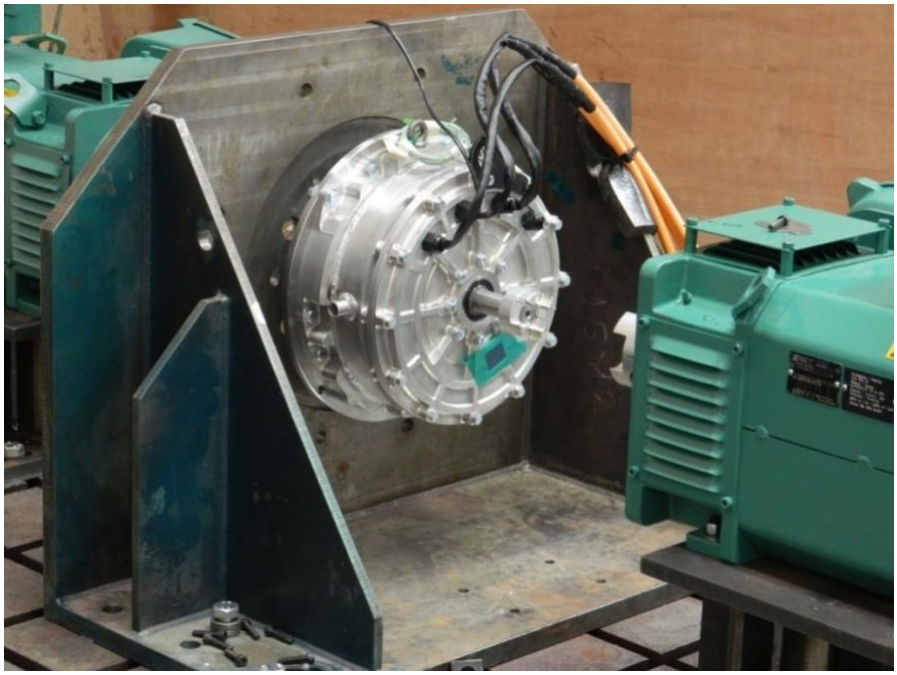

Fig. 6-3 Prototype of the dual rotor device on the test rig

6.4 Test results

6.4.1 EMF test

For the purpose of EMF measurement, both rotors were rotated at 2000rpm which resulted in control space harmonic speed of 2000rpm, as per equation (2-15), and electrical frequency of 233.33Hz. Electrical frequency of the parasitic space harmonics associated with the magnet rotor was 300Hz at this operating point. Comparison of the measured and predicted line to line EMF waveform can be seen in Fig. 6-4. The device was kept at room temperature prior to the test. It is apparent that there is a good agreement between measured EMF waveform and predicted by 3D FEA. Although the predicted waveform shows slightly higher harmonic distortion than the measured one, in both cases the distortion is negligible. The measured waveform has a period of approximately 4.29ms which agrees with the predicted space harmonic frequency. Additionally, there is no distortion which could be attributed to the parasitic space harmonic which suggests appropriately selected winding as per the discussions in section 2.5.2 of Chapter 2.

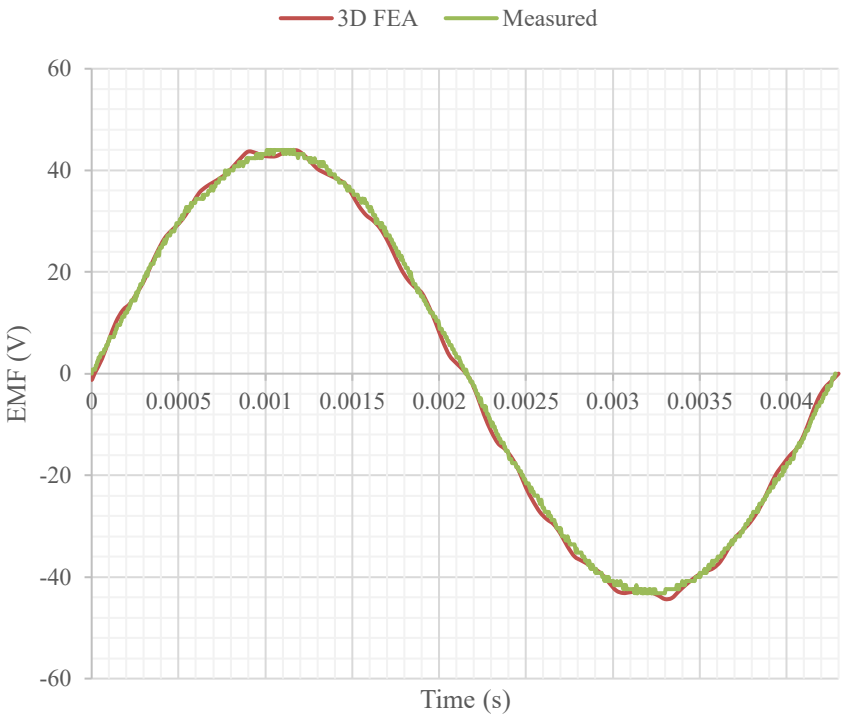

Fig. 6-4 Predicted and measured EMF at 2000rpm input and output speed

6.4.2 Torque transmission

As a part of the on-load testing, torque transmission, i.e. torque on input and output shaft, as a function of stator phase current with Id=0 control strategy was measured. The resulting load characteristic can be seen in Fig. 6-5. All load points in the graph were measured in quick succession so that the change in temperature would not affect the experiment. The measurement was performed on cold machine at room temperature with 40ºC stator coolant temperature. It can be seen that the load characteristic shows significant non-linearity, particularly at high values of stator current. The ratio of output to input torque calculated from the measured torques is approximately 1.76 whereas predicted value is 1.77 (calculated as a ratio of pole pieces to rotor pole pairs).

Comparison of measured and predicted pole piece rotor torque can be seen in Fig. 6-6. As pointed in Chapter 4, large discrepancy between 2D and 3D FE simulation exists, however there is a good agreement between the 3D simulation and the measured results.

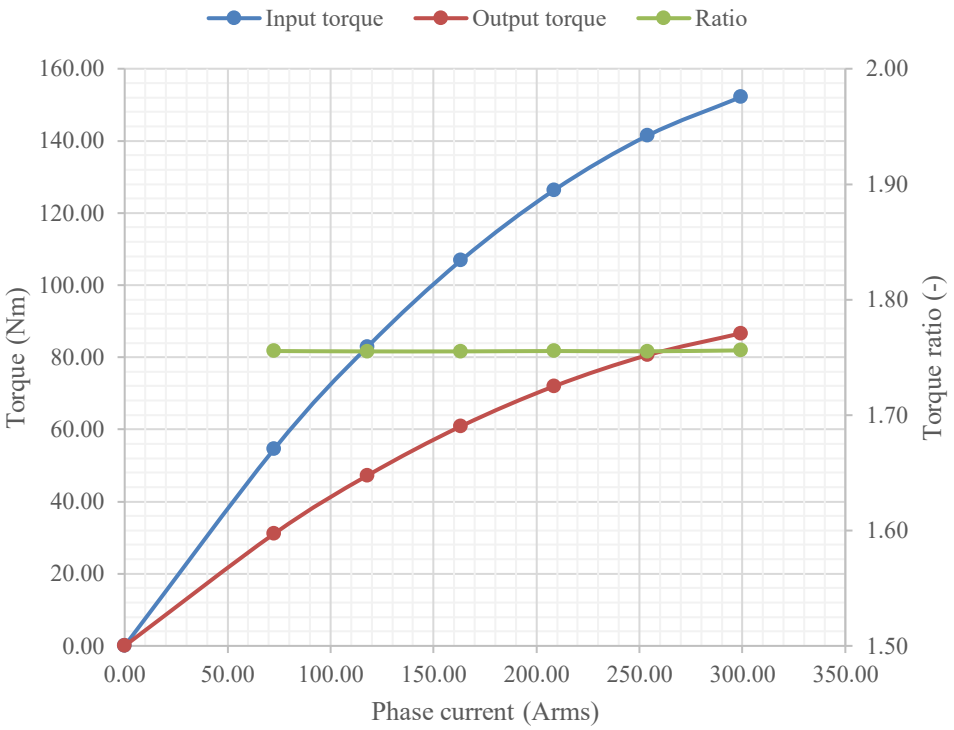

Fig. 6-5 Measured torque on both shafts as a function of stator phase current

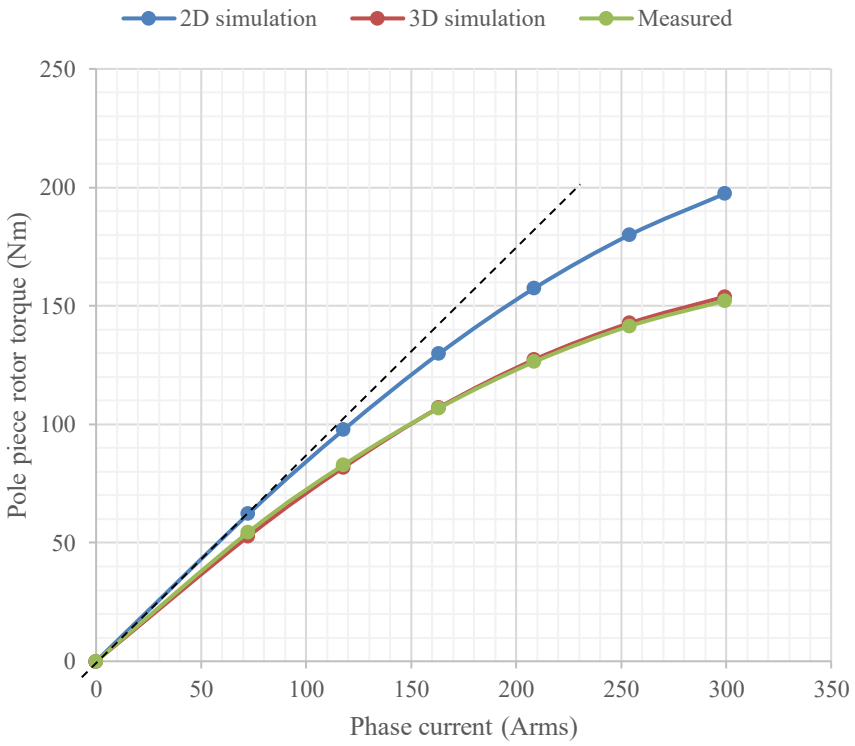

Fig. 6-6 Predicted and measured torque as a function of phase current

In order for the 2D to react 150Nm input torque, only 200Arms phase current is needed while the tested prototype requires nearly 300Arms. It must be noted that the simulation was performed assuming 40°C magnet temperature, real temperature of the magnets during testing were not known, however, prior to the test the machine was kept at room temperature.

6.4.3 Power flow control

As explained in Chapter 2, one of the key functions of the dual rotor device is to control the flow of power from the engine and distribute it between direct and indirect path to the wheels of the vehicle. Series of test with constant input or output power were performed in order to demonstrate the aforementioned functionality.

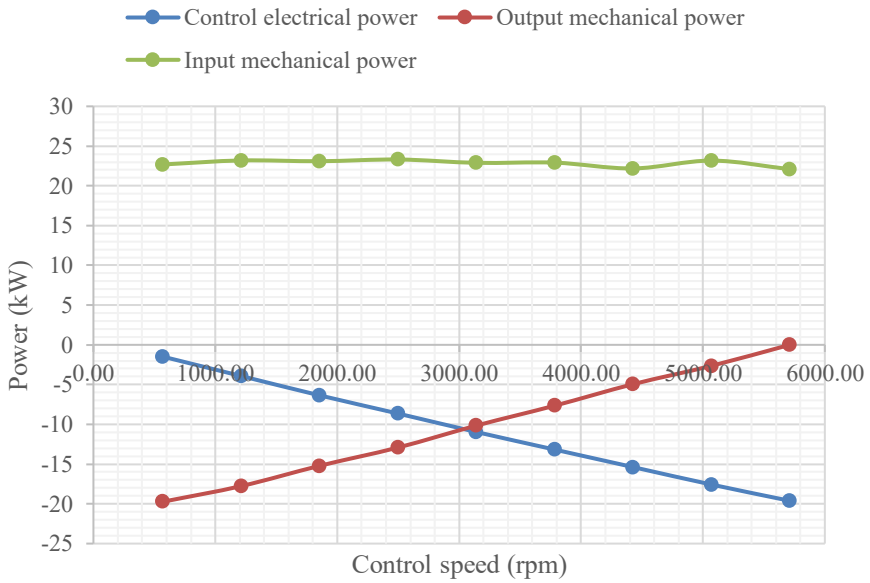

Fig. 6-7 Measured input, output and control power vs control speed at constant 2500rpm input speed and with 150Arms phase current

Fig. 6-7 shows variation of the output mechanical and control electrical power with control speed at constant input speed and torque. It can be seen that the input mechanical power is split between mechanical and electrical outputs with the split ratio controlled by the control speed. Positive value of power indicates flow of power into the device while negative values describe power drawn out of the device. The

difference between total input and output power is the total power loss converted into heat inside the machine.

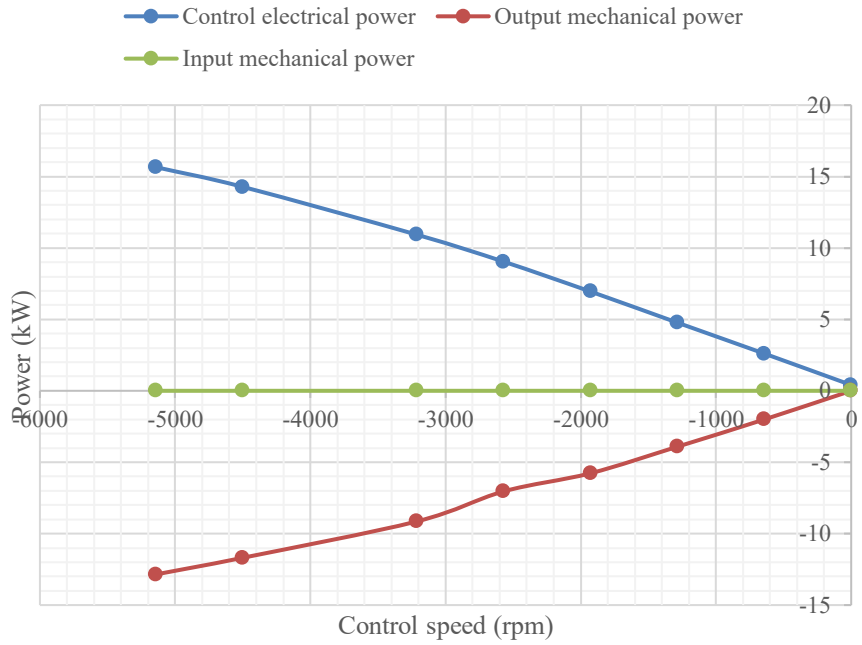

Fig. 6-8 Measured input, output and control power vs control speed at constant 0rpm input speed and with 150Arms phase current

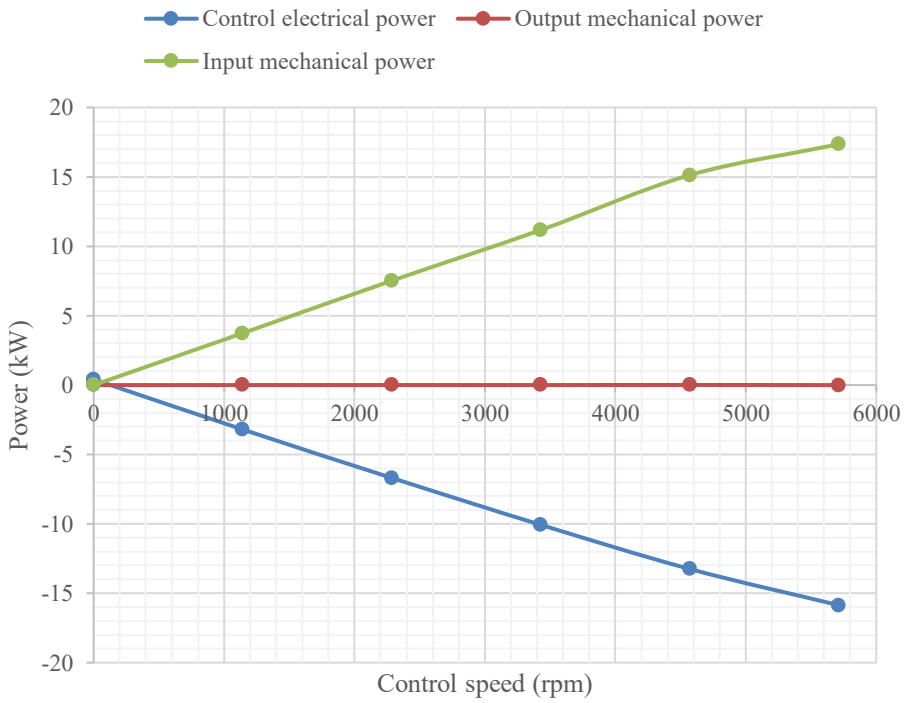

Fig. 6-9 Measured input, output and control power vs control speed at constant 0rpm output speed and with 150Arms phase current

Fig. 6-8 and Fig. 6-9 show operation of the device as pure motor and generator respectively. In motor mode, the pole piece rotor is stationary and hence no power from the engine flows into the device. Electrical power drawn from the batteries by the stator is directly converted into mechanical power delivered to the wheels. In pure generation mode, the output rotor and the wheels are kept stationary while the pole piece rotor is rotating, therefore all the mechanical power delivered by the engine is converted into electrical power to charge batteries. It is important to note that when one of the rotors is stationary there is no mechanical power being delivered to the load or consumed by the device, however, there still is torque on the shaft.

6.4.4 Efficiency/loss maps

In order to validate loss modelling from Chapter 5 and to assess performance of the prototype efficiency and power loss were measured at different levels of stator current loading and for range of input and output speeds. Fig. 6-10, Fig. 6-11, Fig. 6-12 and Fig. 6-13 show measured efficiency (left hand side, numbers represent ratio of output to input power) and loss maps (right hand side, numbers represent Watts of loss) at 50, 100, 200 and 300Arms phase current. Terms “drive machine” and “load machine” in the graphs indicate the induction machines used on the test rig to act as an engine and wheel load respectively. The white area with missing information in the graph shows where the industrial drive used to control the device reached its limitation of frequency and hence the measurement could not have been performed. At the beginning of the test, the machine was cold and thermally stable with coolant inlet temperature of 40°C and ambient temperature of 20°C. All the operating points were measured in quick succession so as to limit the machine temperature variation. Temperature of phase windings at the beginning of the test was 40°C but rose up to maximum of 55°C during the test. Temperature of both rotors were not measured during the test. All quantities needed for the loss and efficiency mapping were automatically recorded from the test rig instrumentation by the LabView based data acquisition system and then later post processed by dedicated Matlab script which makes it possible to generate efficiency and loss maps shown in the aforementioned figures.

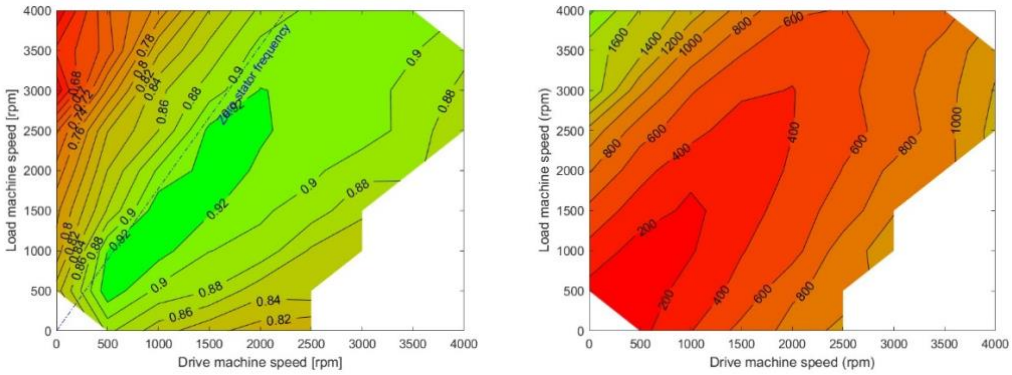

Fig. 6-10 Measrued efficiency and loss map at 50Arms phase current

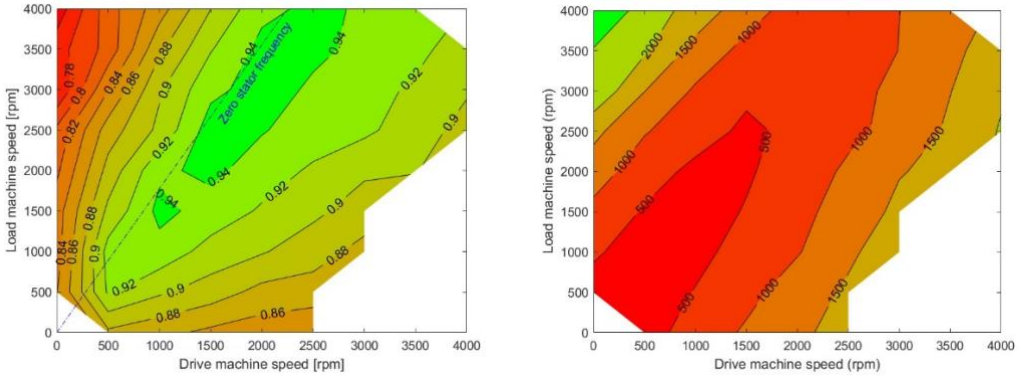

Fig. 6-11 Measrued efficiency and loss map at 100Arms phase current

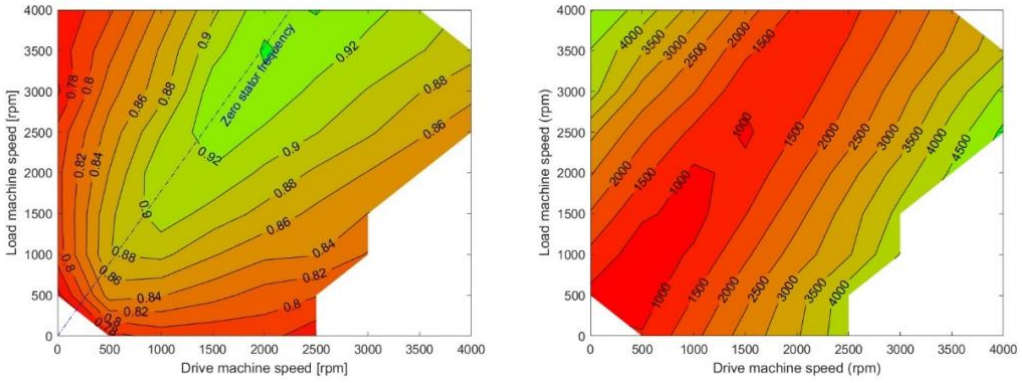

Fig. 6-12 Measrued efficiency and loss map at 200Arms phase current

It is apparent from the measured results that there is a strong correlation between stator frequency and loss/efficiency. The area of the highest efficiency and the lowest loss at low phase current lies close to the line of zero stator frequency and as the loaded increases becomes almost perfectly aligned with it. This suggests that the loss

mechanism which are function of stator frequency are dominant. Additionally, it is apparent that at all levels of electrical loading, that frequency dependent component of the overall loss is significantly larger than the DC copper loss. For instance, the lowest contour of loss in the 300Ams loss map is 2000W which at low stator frequency and low differential speed consists of almost pure DC copper loss, however, the overall loss in the corner point when the output rotor is rotating at 4000rpm exceeds 7000W and hence the AC loss component of the overall loss in the corner point is more than twice the pure DC copper loss.

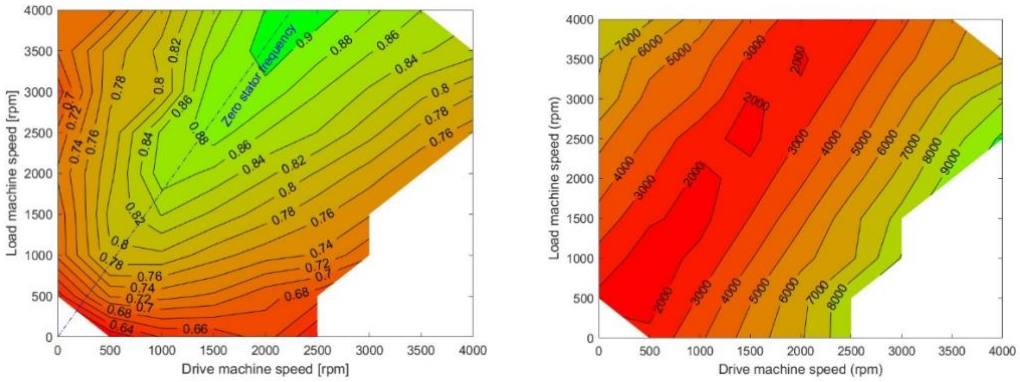

Fig. 6-13 Measrued efficiency and loss map at 300Arms phase current

The general trends and behaviour of losses agree with the discussions presented in Chapter 5, however, the loss mechanisms associated with stator frequency are considerably larger and dominate the overall loss of the prototype. Difference between predicted and measured loss in percentage, assuming winding temperature of 50°C, can be seen in Tab. 6-1,Tab. 6-2 and Tab. 6-3 for stator phase current of 100, 200 and 300Arms respectively. Positive percentage means that the measured loss is larger than predicted. It is apparent that the difference is lowest along the line of zero stator frequency and peaks in the corner regions of the map where high differential rotor speed occurs. Additionally, it can be observed that the difference in predicted and measured loss along the line of zero differential speed reduces as stator current load increases. For instance, at 2000rpm input and 4000 output speed and 100Arms phase current, the difference is 38.5% while at 300Arms it is only 8.1%. It is apparent that at high current loads, DC copper loss becomes dominant and loss mechanisms associated with rotor differential speed become less significant.

Tab. 6-1 Difference between predicted and measured total loss at 100Arms phase current

Loss difference (%)	Input speed (rpm) 0	500	1000	1500	2000	2500	3000	3500	4000
Output speed (rpm) 0		7.8	45.9	56.5	57.6	58.1			
500	-1.0	-3.4	39.7	53.0	61.0	60.9			
1000	40.7	-3.9	22.2	50.9	56.2	62.9	63.8		
1500	51.5	27.0	2.9	43.0	58.0	62.2	65.7		
2000	58.6	43.6	15.3	30.8	55.4	63.5	67.2	64.3	
2500	61.6	51.6	44.4	18.6	46.7	60.0	62.9	67.5	69.3
3000	62.1	59.3	47.0	34.5	35.9	56.8	65.6	69.1	71.5
3500	63.2	64.0	54.4	42.8	33.4	48.7	61.3	68.6	73.2
4000	64.1	62.7	59.2	50.9	38.5	44.4	58.9	62.7	

Tab. 6-2 Difference between predicted and measured total loss at 200Arms phase current

Loss difference (%)	Input speed (rpm) 0	500	1000	1500	2000	2500	3000	3500	4000
Output speed (rpm) 0		22.3	47.3	59.8	64.3	68.1			
500	-4.3	0.1	38.1	57.2	61.8	70.6			
1000	31.0	1.1	17.7	50.0	61.9	66.2	71.0		
1500	47.4	13.8	0.8	38.5	53.2	66.7	71.0		
2000	55.6	37.3	-3.0	21.2	50.7	63.9	70.1	72.7	
2500	60.0	48.6	27.1	-3.2	38.9	56.9	66.5	76.1	74.6
3000	63.3	56.0	45.9	10.2	19.1	50.7	63.7	70.7	73.8
3500	65.2	61.2	52.6	32.4	5.4	37.9	57.8	66.4	70.8
4000	65.4	64.1	58.6	45.8	21.6	23.4	50.0	63.5	

Tab. 6-3 Difference between predicted and measured total loss at 300Arms phase current

Loss difference (%)	Input speed (rpm) 0	500	1000	1500	2000	2500	3000	3500	4000
Output speed (rpm) 0		13.0	45.3	58.3	63.3	67.9			
500	-2.6	-0.6	35.4	56.3	64.7	70.8			
1000	21.4	-1.3	14.0	47.8	61.3	64.5	70.3		
1500	41.4	6.1	-0.9	35.1	55.8	65.9	70.2		
2000	48.6	30.7	-3.0	15.8	46.7	61.4	68.2	72.6	
2500	53.2	41.5	4.7	0.4	34.1	54.1	65.6	71.8	73.7
3000	60.4	47.1	41.3	5.1	9.2	46.4	61.2	69.3	71.7
3500	58.3	50.9	45.9	21.1	4.2	31.1	54.7	63.2	65.0
4000	55.2	59.2	52.3	37.1	8.1	7.0	43.2	62.0	

The apparent difference between measured and predicted loss can be attributed to number of things. For instance, the ideal loss model of the stator laminations was used for iron loss prediction. However, it is generally accepted that the properties of electrical steel degrade as it goes through the manufacturing process and is subject to mechanical stress and heat during lamination cutting, compression, welding, and pressing into the housing. Number of publications have been dedicated to modelling and experimental measurement of these phenomena, [78] for instance. Such effects were not considered during the theoretical analysis. Additionally, the iron loss analysis was primarily focused on the fundamental components of flux density variation in each component. However, it was shown that magnetic field spectra of both air gaps are rich in harmonic components which could cause additional iron loss unaccounted for in the analysis presented in Chapter 5. Furthermore, only magnetically active components were taken into account in the loss analysis and all structural components were considered non-magnetic and non-conductive. However, components such as stator housing and end caps were made of aluminium and possibility of stray leakage fields inducing eddy currents in them exists.

The concentrated coils were wound using LITZ cable and this was assumed to minimize AC copper loss to negligible level. When modelling the transposed winding, perfect transposition of conductors throughout the axial length of each slot was assumed, i.e. average position of each conductor in the slot was assumed to be the same. However, imperfect transposition could lead to frequency dependent increase in copper loss. Strong sensitivity of the proposed device to cross slot leakage and subsequent AC copper loss was noted in Chapter 5.

As mentioned before, mechanical losses such as those due to friction in bearings and aerodynamic drag were not considered during loss modelling, however, those are unlikely to generate significant amount of loss particularly at relatively moderate rotor speeds. Bearings were inspected during the assembly of the prototype and no significant drag torque was noticed.

Despite the larger than predicted AC loss component, it can be concluded that the prototype machine can achieve peak efficiency in excess of 94%.

6.5 Conclusion

Full scale prototype of the proposed device was built, and its operation was validated on the dedicated test rig simulating a real-world operation of a power split hybrid drivetrain. A set of experiments were performed in order to validate theoretical assumptions and predictions described throughout the thesis.

Good agreement between predicted and measured EMF was obtained during testing suggesting correctly selected winding with no measurable distortion due to the presence of the parasitic space harmonic. The measured EMF waveform is near perfect sine wave. In addition, control of power flow through the device was demonstrated by varying control speed and monitoring of electrical and mechanical power in and out of the device. Both measured and predicted torque versus phase current curves show considerable non-linearity but there is negligible difference between them. It has been confirmed that in case of both EMF and torque, it is essential to use 3D FEA models for performance prediction.

While general trends and behaviour of power loss in the device agrees with theoretical assumptions, its actual value is considerably larger, in particular at high differential rotor speeds. The cause of this discrepancy is not currently known and will have to be a subject of future research, although number of possible causes have been discussed.

Overall it can be concluded that functionality of the prototype has been validated and its operation agrees with theoretical predictions presented in this thesis. While considerable discrepancy exists between predicted and measured loss at high rotor differential speeds, the prototype could achieve efficiency exceeding 94%.

Chapter 7 Conclusion

7.1 Introduction

As the global automotive industry enters the era of electrification driven by stringent legislation related to emission limits on green house and noxious gasses, development of novel devices for efficient electromechanical energy conversion is at the forefront of academic as well as industrial research. The device presented in this thesis, aimed at hybridization of passenger vehicles drivetrain, is an example of technology which could become a key enabler in the transition from mainly internal combustion engines of today to pure electric drivetrain of the future.

As it is apparent from the discussions in Chapter 1 and 2 describing automotive application and the principle of operation, the proposed device aims to simplify and enhance performance of the so-called power split hybrid drivetrain which is the most prevalent full hybrid drivetrain on the passenger vehicle market. The backbone of any conventional power split drivetrain is mechanical planetary gear set coupled to two electrical machines and their corresponding controllers. Despite the high level of structural and functional integration achieved by state-of-the-art power split drivetrains, they are still relatively complex with large number of parts. It was shown that concentric magnetic gear is functionally a magnetic equivalent of the mechanical planetary gear set which could be integrated with a permanent magnet synchronous machine in order to realize an integrated magnetic power split device replacing the mechanical gear and one of the machines in conventional power-split drivetrain.

The device proposed in this thesis takes the integration of the magnetic gear into an electric machine a step further by removing one of the rotors of the aforementioned three-rotor power split device and directly interfacing a synchronous machine stator with the magnet and pole piece rotor of the magnetic gear. Such level of integration reduces complexity of the device and could make it more viable for high volume automotive production, however, it does introduce number of design challenges, many of which were addressed in the thesis.

The following sections conclude and summarize the main findings of the research work presented in this thesis to the emerging field of magnetically geared electrical machines for automotive applications and propose topics for further research.

7.2 Choice of configuration

It was demonstrated that spectra of flux density in air gaps of concentric magnetic gears are rich in harmonics with high amplitudes relative to the working fundamental space harmonic. Consequently, the direct interface between the magnetic gear element and the stator of the synchronous machines constrains the number of feasible configurations and the design of both parts of the device, as was demonstrated in Chapter 3.

It was shown that there are number of aspects to consider when selecting a configuration of the proposed device. Firstly, the choice of number of pole pieces, rotor and stator poles directly influence the intrinsic gearing of the device which together with input torque and speed ranges of both shafts define the power flow through the device and in the wider system. Hence, the overall drivetrain architecture and the configuration of the power split device are inseparably interlinked. What is best for a single component may not be the best for the system and vice versa.

Secondly, even when the desired intrinsic gearing of the device is known, it was shown that not all combinations of poles and pole pieces are feasible, as a number of electromagnetic limitations exist. Since speed of the control space harmonic linked with the stator is a function of both rotor speeds and since it reaches its maximum when the differential speed between the two rotors is high, number of stator poles must be selected such that the stator fundamental electrical frequency is within limits of available automotive controllers. Additionally, the choice of winding pattern for a given number of poles is further limited by the presence of dominant parasitic space harmonic associated with the magnet rotor. It was demonstrated, that in order for the winding pattern to be suitable for the device, it needs to have high winding factor (ideally equal to 1) for the useful space harmonic whilst having zero winding factor for the parasitic space harmonic. It was shown that this requirement is met by windings with integer number of slots per pole and phase and fractional slot

windings with 0.5 slots per pole and phase. Both of these winding patterns are commonly used in industry with the fractional slot option being particularly suitable for machines with short axial length due to its compact winding overhang.

Finally, it was shown that magnetic imbalance between the three principal components of the device results in large unbalanced pull and a method of down selecting configurations which do not suffer from this was presented. The asymmetry between pole pieces and the magnet rotor was identified as the most significant source of unbalanced magnetic pull, and while magnetic symmetry is beneficial from UMP point of view, it tends to increase cogging torque. However, it was demonstrated that it is possible to select configuration with negligible UMP and cogging.

7.3 Design principles

Magnetic circuit of the proposed device is fundamentally more complex than that of a conventional electric machine, however, it was shown that the fundamental design principles could be used with slight adaptions to account for the effects of magnetic gearing. For the purpose of initial sizing, the gear element could be seen as a surface mounted PM motor providing magnetic loading for the stator. Similarly to conventional motors, achievable magnetic loading of the SPM rotor and electrical loading of the stator dictates the size of the device or its transmittable torque rating. It was demonstrated that the value of magnetic loading of the equivalent SPM rotor does not reach the same level as in state-of-the-art PM traction motors despite using high-performance rare-earth magnets in the gear element.

Sizing of stator teeth and back iron is governed by allowable flux density and saturation limits of the lamination material as is the case in conventional machines. However, presence of the parasitic space harmonic must be considered despite the fact that it does not link with the stator winding because it could still cause excessive saturation of stator core. The way steel saturation together with either global or local thermal limitations of the stator define its key dimensions was discussed, although the discussions were limited to fractional open slot stator with 0.5 slot per pole and phase topologies.

Design of the gear element has two major goals. Firstly, the magnet rotor needs to be designed such that it is magnetically robust, i.e. does not exceed acceptable levels of magnet demagnetization during normal operation and fault conditions, and that it creates sufficiently high magnetic loading in the innermost air gap of the device. The role of the pole pieces in the gear element is to modulate the field created by the magnet rotor and it was shown that even in case of ideal modulation the amplitude of the useful modulated space harmonic in the outer air gap is relatively small. Additionally, the modulation process does not eliminate the space harmonic associated with the magnet rotor which in the outer air gap is considered parasitic. Second design goal, therefore, is to optimize the pole piece shape so that it maximizes amplitude of the useful space harmonic while minimizing the parasitic one. Both design goals are purely electromagnetic, however, structural robustness of both rotating components is equally important and could limit the magnetic optimisation. However, structural design was outside of scope of this thesis.

Initial sizing and design of conventional radial field machines mostly relies on simplified two-dimensional models as the influence of field fringing at the end of the stack is negligible. However, it was demonstrated that in the case of the proposed device with short axial lengths and large effective air gap, significant discrepancy between 2D and 3D models exist. The difference can be observed in EMF generated at winding terminals as well as in torque acting on both shafts. The effect is further exacerbated by electrical loading of the stator as the error between the 2D and 3D modelling increases with load. The pole piece rotor structure and its considerable axial leakage field was identified as the main source of the discrepancy. In addition, it was demonstrated that by lowering equivalent permeability of the laminated stack in axial direction, the axial leakage could be reduced. This, however, does not result in increase in transmittable torque as the proposed methods reduce effective active length of the pole pieces.

7.4 Efficiency

While the loss mechanisms present in the proposed device are not unique to it and commonly accepted methods of analysis could be used, the fact that the device has two independent rotating components makes the analysis more challenging. Each

operating point of the device can be fully defined by either input or output torque and speed of both shafts. Apart from DC copper loss, all other loss mechanisms described in the Chapter 5 are function of all three variables and hence to fully describe loss or efficiency of the device, three-dimensional loss/efficiency cube is needed.

Among the loss mechanisms commonly found in all electrical machines are iron losses which tend to be highest in the stator. Since the stator of the proposed device is exposed to multiple dominant harmonics, frequency domain method of iron loss calculation was used since it allows to separate individual contribution of harmonic components to the overall stator iron loss. Although iron loss due to the control space harmonics dominates, it was shown that the contribution from the parasitic one is considerable. The same method was used for analysis of pole piece and magnet rotor loss. Even though iron losses in rotors are smaller than in stator, they lack the direct heat transfer path to the cooling jacket and, in case of the magnet rotor, are generated in close proximity of the temperature sensitive magnets. Iron loss in the magnet rotor is primarily induced by relative motion of the salient structure of the pole piece rotor which also causes variation of the working point of magnets and subsequent flow of eddy currents in the magnets themselves. It was shown that in order to limit the magnet eddy current loss, it is necessary to use relatively fine segmentation.

Apart from achievable slot fill factor primarily affecting DC copper loss, several other factors have significant influence on winding loss in the proposed device. The combination of fundamental stator frequency exceeding 1 kHz, large effective air gap promoting cross slot leakage and high peak electrical loading (needed to compensate for relatively low magnetic loading generated by the gear element) all promote AC winding losses. High frequency in combination with series connected phase coils results in small number of coil turns with large number of parallel strands which need to be transposed to prevent considerable current redistribution among them. On the other hand, parallel connection is problematic due to presence of the parasitic space harmonic which induces EMFs with different phase shifts in individual coil within a phase and causes current circulation. It was concluded that, from the loss point of view, the optimal solution is to connect phase coils in series

and wind the using transposed LITZ cable. However, this solution may be too expensive for high volume automotive production.

As mentioned in the previous section, the device suffers from high level of axial leakage which causes reduction of EMF and transmittable torque. As a secondary effect, variation of the axial leakage field was shown to induce eddy currents flowing in plane normal to the direction of lamination of the magnetic circuit. Pole piece rotor was identified as the component were most of the stray loss is generated. Two different methods were proposed to estimate the additional stray loss, one based on static FEA analysis of the leakage field distribution followed by time harmonic calculation of eddy current loss in single lamination sheet and the second based on time stepping FEA solution where the magnetic circuit material has anisotropic conductivity which only allows flow of eddy current in radial and circumferential direction. The second method was also used to demonstrate that while most of the stray loss is indeed generated in the pole pieces, it is present in all principle components of the device.

As mentioned before, most of the loss mechanism depend on both rotor speeds and transmitted torque. At constant torque, dependency of loss on both rotor speeds could be plotted in a form of 2D map. It was shown that the lowest loss is achieved at low differential rotor speeds, particularly along the line of zero stator frequency, and hence it is beneficial when the drivetrain could be operated so that the difference between input and output rotor speeds is small. The position of the line of zero stator frequency on the loss map depends on choice of intrinsic gear ratio which, as mentioned before, is strongly influence by the overall system architecture.

7.5 Experimental validation

Full scale prototype of the proposed device was built and tested on a test rig emulating power split hybrid drivetrain. The experimental testing proves the key functionality and principles described in the theoretical chapters and confirms suitability of the device for control of power flow in a power-split hybrid drivetrain. In addition, good agreement between the measured and predicted EMF and torque as a function of phase current curves was achieved. Although it must be noted that the

measurement only agrees with results obtained from 3D FEA and the aforementioned discrepancy between 2D FEA and the experimental data exists.

Efficiency and total loss of the prototype were measured for range of input and output speeds and transmitted torque. The general behaviour of loss agrees with predictions, however, large discrepancy between values of measured and predicted loss were observed, particularly at high differential rotor speeds. Number of possible reasons for this were discussed in Chapter 6, although the real cause is not currently fully understood. Although the measured efficiency is considerably lower than predicted, its peak value does exceed 94%.

7.6 Areas for future research

While a number of important topics related to design and operation have been covered in this thesis, the novelty of the proposed device and relative lack of publications on the topic leave a plethora of opportunities for academic as well as industrial research. Following paragraphs give several examples of research problems which the author views as important for better understanding of the device and its application.

Loss analysis was discussed in detail in Chapter 5, however, large discrepancy between measured and predicted loss at high differential speed was observed during experimental validation which suggests that either the proposed methods were not accurate enough or some other important loss mechanism was overlooked. While the total loss could be easily measured, its separation into individual components is challenging and hence it is not currently understood where the additional loss was generated. Accurate prediction of losses is key area for further research as efficiency of the device as well as its thermal stability is of prime importance in automotive application.

Structural limitations were taken into account during mechanical design of the prototype; however, they were not studied in detail and discussion of pole piece design was only focused on electromagnetic performance. Multi-physical optimisation of the pole piece rotor structure in particular could be an important topic for future research as the pole pieces are subject not only to centrifugal forces but

also to varying forces of magnetic nature. While the primary concern for the pole piece rotor design is its structural robustness, understanding of dynamic behaviour and noise the structure could emit would have to be considered in order for the device to meet automotive requirements for noise and vibration.

In its target application, the proposed device will be operated within a wider system which will strongly influence the fundamental design choices on component level. Importance of system level considerations was mentioned several times in this thesis, however, no approach for overall drivetrain sizing and optimisation which would include magnetic power split device was presented. It would be of great benefit if a method of synthesizing optimal magnetic power split architecture and rating for the target vehicle drive cycle was developed. The approach would need to take into account electromagnetic as well as transient thermal performance of the proposed device.

In addition, since the proposed device aims to replace conventional mechanical power split devices, either experimental or analytical comparison between static and dynamic performance of the two options would indicate whether the concept has a future in the industry. Such research could (and perhaps should) even include other competing hybrid drivetrain architectures such as parallel and series. Of course, analytical comparison would require detailed and accurate understanding of efficiency of both solutions as mentioned before. Furthermore, cost of manufacture and ownership would have to be considered.

In the experimental setup described in Chapter 6, the stator armature reaction was controlled based on position of the useful space harmonic which was estimated from positions of the two physical rotors. The need for two independent position sensors to operate the device adds cost and could be a potential source of unreliability. It would be beneficial to reduce the number of required position sensors or to develop a method of sensor less control.

References

[1] P. Roper, "6 Trends Driving Vehicle Electrification in 2018," available at: https://www.greentechmedia.com/articles/read/how-vehicle-electrification-will-evolve in-2018#gs.x6j3pt, February 19, 2018.

[2] "European Roadmap:Electrification of Road Transport," *European Road Transport Research Advisory Council*, p. 48. , Belgium, 2017.

[3] W. Nes, "Magna Powertrain eDrive System: One stop shop for Hybrid and Electric Vehicles," in *Drivetrain Forum 2016*, Untergruppenbach, 2016.

[4] "Climate Change 2014 Synthesis Report Summary for Policymakers," *The Intergovernmental Panel on Climate Change,* available at: https://www.ipcc.ch/site/assets/uploads/2018/02/AR5_SYR_FINAL_SPM.pdf

[5] "Road transport: Reducing CO2 Emissions from Vehicles," *European Commission*, available at: https://ec.europa.eu/clima/policies/transport/vehicles_en

[6] "Global Temperature Trends,", *NASA*, available at: https://climate.nasa.gov/vital-signs/global-temperature/, accessed on 5th of June 2019.

[7] "Electrification of Road Transport Roadmap 2nd Version," *ERTRAC, EPoSS, and SmartGrids*, available at: http://www.ertrac.org/index.php?page=ertrac-roadmap, June 2012.

[8] "Monthly Energy Review, Anual Energy Outlook Reports 2018," *U.S Energy Information Administration*, available at: https://www.eia.gov/

[9] J. V. Mierlo and G. Maggetto, "Views on Hybrid Drivetrain Power Management Strategies," p. 17, available at: https://etecmc10.vub.ac.be/publications/evs17jvm.pdf

[10] "Hybridisation of Road Transport," *ERTRAC*, available at: http://www.ertrac.org/index.php?page=ertrac-roadmap , June 2011.

[11] M. A. Melliger, O. P. R. van Vliet, H. Liimatainen, "Anxiety vs reality – Sufficiency of Battery Electric Vehicle Range in Switzerland and Finland," *Transportation Research part D: Transport and environment,* vol. 65, pp. 101 - 115, December 2018.

[12] "Passenger Car Low Carbon Technology Roadmap," *UK Automotive Council*, available:

http://www.automotivecouncil.co.uk/2013/09/automotive-technology-roadmaps/, September 2013.

[13] R. Fisher, "Dedicated Hybrid Transmission: A New Category of Transmissions," *14th CTI Symposium Berlin*, Graz, p. 14. , 2015.

[14] T. Pfund, "The Schaeffler eDrive platform," presented at the *Shaeffler Symposium 2018: Mobility for Tomorrow*, Baden-Baden, 2018.

[15] T. Eckenfels, F. Kolb, S. Lehmann, W. Neugebauer, and M. Calero, "48V Hybridisation," presented at *Schaeffler Symposium 2018: Mobility for Tomorrow*, Baden-Baden, 2018.

[16] M. Bassett, A. Cooper, J. Hall, A. Harrington, S. Reader, J. Hartland, J. Harris, A. Taylor, "HyPACE - Hybrid Petrol Advance Combustion Engine - Advacned Boosting System for Extended Stoichiometric Operation and Improved Dynamic Response," *WCX SAE World Congress Experience*, SAE, p. 14. , 2019.

[17] M. Olszewski, C. W. Ayers, T. A. Burress, S. L. Campbell, C. L. Coomer, A. A. Wereszczak, J. P. Cunningham, L. E. Seiber, and H. T. Lin, "Evaluation of 2010 Toyota Prius Hybrid Synergy Drive System," ed. http://www.osti.gov/bridge: Oak Ridge National Laboratory, 2011.

[18] J. German, "Hybrid Vehicles: Technology Development and Cost Reduction," A Series on Technology Trends in Passagner Vehicles in the USA ,*International Council on Clean Transportation*, p. 18. , June 2015.

[19] D. Greenwood, "Hybridisation for Performance and Economy," *Future Powertrain Conference*, 19th of February 2014

[20] R. Hodkinson and J. Fenton, "Lightweight Electric/Hybrid Vehicle Design," Butterworth-Heinemann, p. 280. , 2001.

[21] E. Mehrdad, G. Yimin, G. E. Sebastien, and A. Emadi, "Modern Electric, Hybrid Electric and Fuel Cell Vehicles", *Power Electronics and Application Series*, USA, CRC press LLC, p. 419., 2005.

[22] K. Atallah and D. Howe, "A Novel High-performance Magnetic Gear," *IEEE Transactions on Magnetics*, vol. 37, pp. 2844-2846. , 2001.

[23] B. McGilton, M. Mueller, and A. McDonald, "Review of Magnetic Gear Technologies and Their Applications in Marine Energy," *5th IET International Conference on Renewable Power Generation (RPG) 2016*, pp. 1-6, 2016.

[24] K. Atallah, S. D. Calverley, and D. Howe, "Design, analysis and realisation of a high-performance magnetic gear," *IEE Proceedings - Electric Power Applications*, vol. 151 pp. 135-143, 2004.

[25] P. O. Rasmussen, T. O. Andersen, F. T. Jorgensen, and O. Nielsen, "Development of a High-performance Magnetic Gear," *IEEE Transactions on Industry Applications*, vol. 41, pp. 764-770., 2005.

[26] E. Gouda, S. Mezani, L. Baghli, and A. Rezzoug, "Comparative Study Between Mechanical and Magnetic Planetary Gears," *IEEE Transactions on Magnetics*, vol. 47, pp. 439-450., 2011.

[27] N. W. Frank and H. A. Toliyat, "Analysis of the Concentric Planetary Magnetic Gear with Strengthened Stator and Interior Permanent Magnet (IPM) Inner Rotor," *IEEE Energy Conversion Congress and Exposition*, pp. 2977-2984., 2010.

[28] D. J. Evans and Z. Q. Zhu, "Influence of Design Parameters on Magnetic Gear's Torque Capability," *2011 IEEE International Electric Machines and Drives Conference (IEMDC)*, pp. 1403-1408., 2011.

[29] S. J. Kim, E. J. Park, S. Y. Jung, and Y. J. Kim, "Transfer Torque Performance Comparison in Coaxial Magnetic Gears with Different Flux-Modulator Shapes," *IEEE Transactions on Magnetics*, vol. 53, no.6, pp. 1-4, June 2017.

[30] Z. Q. Zhu and D. Howe, "Influence of Design Parameters on Cogging Torque in Permanent Magnet Machines," in *IEEE Transactions on Energy Conversion*, vol. 15, no. 4, pp. 407-412, Dec. 2000.

[31] G. Jungmayr, J. Loeffler, B. Winter, F. Jeske, and W. Amrhein, "Magnetic Gear: Radial Force, Cogging Torque, Skewing, and Optimization," *IEEE Transactions on Industry Applications*, vol. 52, pp. 3822-3830., 2016

[32] O. Molokanov, P. Dergachev, S. Osipkin, and P. Kurbatov, "Study on Cogging Torque in Coaxial Planetary Magnetic Gear," *2016 IEEE 2nd Annual Southern Power Electronics Conference (SPEC)*, pp. 1-5., 2016

[33] S. Gerber and R. J. Wang, "Analysis of the End-effects in Magnetic Gears and Magnetically Geared Machines," *2014 International Conference on Electrical Machines (ICEM)*, pp. 396-402., 2014.

[34] M. Fukuoka, K. Nakamura, and O. Ichinokura, "Experimental Tests of Surface Permanent Magnet Magnetic Gear," *2012 15th International Conference on Electrical Machines and Systems (ICEMS)*, pp. 1-6., 2012.

[35] J. Lee and J. Chang, "Analysis of the Vibration Characteristics of Coaxial Magnetic Gear," *IEEE Transactions on Magnetics*, vol. 53, no. 6, pp. 1-4, June 2017.

[36] X. Yin, P. D. Pfister, and Y. Fang, "A Novel Magnetic Gear: Toward a Higher Torque Density," *IEEE Transactions on Magnetics*, vol. 51, pp. 1-4, 2015.

[37] Y. Chen, W. N. Fu, and W. Li, "Performance Analysis of a Novel Triple-Permanent-Magnet- Excited Magnetic Gear and Its Design Method," *IEEE Transactions on Magnetics*, vol. 52, pp. 1-4, 2016.

[38] K. Atallah, J. Rens, S. Mezani, and D. Howe, "A Novel "Pseudo" Direct-Drive Brushless Permanent Magnet Machine," *IEEE Transactions on Magnetics*, vol. 44, pp. 4349-4352, 2008.

[39] K. Atallah, J. Wang, S. D. Calverley, and S. Duggan, "Design and Operation of a Magnetic Continuously Variable Transmission," *IEEE Transactions on Industry Applications*, vol. 48, pp. 1288-1295, 2012.

[40] L. Sun, M. Cheng, and H. Jia, "Analysis of a Novel Magnetic-Geared Dual-Rotor Motor With Complementary Structure," *IEEE Transactions on Industrial Electronics*, vol. 62, pp. 6737-6747, 2015.

[41] L. Sun, M. Cheng, J. Zhang, and L. Song, "Analysis and Control of Complementary Magnetic-Geared Dual-Rotor Motor," *IEEE Transactions on Industrial Electronics*, vol. 63, pp. 6715-6725, 2016.

[42] L. Sun, M. Cheng, H. Wen, and L. Song, "Motion Control and Performance Evaluation of a Magnetic-Geared Dual-Rotor Motor in Hybrid Powertrain," vol. 64, *IEEE Transactions on Industrial Electronics*, pp. 1863-1872, 2017.

[43] A. Rahman, "Advances in Ecological Modern Electric and Hybrid Electric Vehicles," *8th International Conference and Exhibition on Ecological Vehicles and Renewable Energies (EVER)*, 2013.

[44] K. Takashi, K. Ryoji, and M. Hiroyuki, "Advanced technologies of traction motor for automobile," *ECCE Asia Downunder (ECCE Asia*), pp. 147-152, 2013.

[45] A. Tutu, "Bosch Parallel Full Hybrid System Explained," *Can be accessed on: www.autoevolution.com,* 8th of April 2010.

[46] S. Jurkovic, K. Rahman, B. Bae, N. Petel, and P. Savagian, "Next generation chevy volt electric machines; design, optimization and control for performance and rare-earth mitigation," *Energy Conversion Congress and Exposition (ECCE)*, Montreal, pp. 5219-5226, 2015.

[47] K. Rahman, S. Jurkovic, J. P. Savagian, N. Patel, and R. Dawsey, "Retrospective of electric machines for EV and HEV traction applications at general motors," *IEEE Energy Conversion Congress and Exposition (ECCE)* , Milwaukee, WI, pp. 1-8, 2016.

[48] D. G. Dorrell, A. M. Knight, and M. Popescu, "Performance Improvement in High-Performance Brushless Rare-Earth Magnet Motors for Hybrid Vehicles by Use of High Flux-Density Steel," *IEEE Transactions on Magnetics*, vol. 47, pp. 3016-3019, Oct. 2011.

[49] N. J. Stannard, J. G. Washington, and G. J. Atkinson, "A comparison of axial field topologies employing SMC for traction applications," *2016 19th International Conference on Electrical Machines and Systems (ICEMS)*, Chiba, pp. 1-6, 2016.

[50] K.-F. Hsueh, J.-H. Cheng, Y.-S. Chen, and A. Lu, "Study of Different Arrangement of Magnets for the Purpose of Reducing Magnet Usage in Designing an Integrated Starter/Generator for Hybrid Vehicles," *SAE International,* pp. 1-8, 2013.

[51] T. Nakada, S. Ishikawa, and S. Oki, "Development of an Electric Motor for a Newly Developed Electric Vehicle," *SAE International*, pp. 1-7, 2014.

[52] R. Yang, N. Schofield, and A. Emadi, "Comparative study between interior and surface permanent magnet traction machine designs," *IEEE Transportation Electrification Conference and Expo (ITEC)* , Dearborn, MI, pp. 1-6, 2016.

[53] X. Ge, Z. Q. Zhu, G. Kemp, D. Moule, and C. Williams, "Optimal Step-Skew Methods for Cogging Torque Reduction Accounting for Three-Dimensional Effect of Interior Permanent Magnet Machines," *IEEE Transactions on Energy Conversion*, vol. 32, pp. 222-232, March 2017.

[54] Z. Yang, F. Shang, and P. I. Brown, "Comparative Study of Interior Permanent Magnet, Induction, and Switched Reluctance Motor Drives for EV and HEV Applications," *IEEE Transactions on Transportation Electrification*, vol. 1, pp. 245-254, 2015.

[55] M. Burwell, J. Goss, and M. Popescu, "Performance/cost comparison of Induction-Motor and Permanent-Magnet-Motor in a Hybrid Electric Vehicle," availabel at: http://www.coppermotor.com/design-resources/: International Copper Association, 2013.

[56] Z. Yang, F. Shang, I. P. Brown, and M. Krishnamurthy, "Comparative Study of Interior Permanent Magnet, Induction, and Switched Reluctance Motor Drives for EV and HEV Applications," *IEEE Transactions on Transportation Electrification*, vol. 1. , pp. 245-254, Oct. 2015.

[57] J. Pyrhonen, T. Jokinen, and V. Hrabovcova, "Design of Rotating Electrical Machines″. John Wiley & Sons, Ltd., p. 512, 2008.

[58] S. M. Raziee, O. Misir and B. Ponick, "Winding Function Approach for Winding Analysis," in *IEEE Transactions on Magnetics*, vol. 53, no. 10, pp. 1-9, Oct. 2017

[59] R. Cipin and M. Patocka, "New infinitesimal method for the analysis and synthesis of AC machines winding," presented at the *International Aegean Conference on Electrical Machines and Power Electronics and Electromotion*, Istanbul, 2011.

[60] R. Cipin and M. Patocka, "AC fractional winding design by the new method," presented at the *International Symposium on Power Electronics Power Electronics, Electrical Drives, Automation and Motion*, Sorrento, 2012.

[61] M. S. Islam, S. Mir, and T. Sebastian, "Effect of Paralleling the Stator Coils in a Permanent-Magnet Machine," *IEEE Transactions on Industry Applications,* vol. 42, no. 6, pp. 1429-1436, 2006.

[62] D.G. Dorrell, M. Popescu, C. Cossar, and D. Ionel, "Unbalanced Magnetic Pull in Fractional-Slot Brushless PM Motors," presented at the *IEEE Industry Applications Society Annual Meeting*, Edmonton, Alta, 2008.

[63] T. Burress, "Benchmarking State-of-the-Art Technologies," in *2013 U.S. DOE Hydrogen and Fuel Cells Program and Vehicle Technologies Program Annual Merit Review and Peer Evaluation Meeting*, Oak Ridge National Laboratory, 2013, p. 21. Available at: https://www.energy.gov/sites/prod/files/2014/03/f13/ape006_burress_2013_o.pdf

[64] A. Penzkofer, "Analytical Modelling and Analysis of Magnetic Gears and Pseudo Direct Drives for Large Wind Turbines," PhD, Electrical and Electronic Engineering, University of Sheffield, Sheffield, uk.bl.ethos.706027, 2016. [Online]. Available: http://etheses.whiterose.ac.uk/id/eprint/16452

[65] T. Reichert, T. Nussbaumer and J. W. Kolar, "Split Ratio Optimization for High-Torque PM Motors Considering Global and Local Thermal Limitations," in *IEEE Transactions on Energy Conversion*, vol. 28, no. 3, pp. 493-501, Sept. 2013.

[66] *Catalogue of NdFeB permanent magnets*, Arnold Magnetics, 2019. [Online]. Available at: https://www.arnoldmagnetics.com/wp-content/uploads/2017/10/Catalog-151021.pdf.

[67] W. Hua, M. Cheng, Z. Q. Zhu and D. Howe, "Design of Flux-Switching Permanent Magnet Machine Considering the Limitation of Inverter and Flux-Weakening Capability," *Conference Record of the 2006 IEEE Industry Applications Conference Forty-First IAS Annual Meeting*, Tampa, FL, 2006, pp. 2403-2410.

[68] N. Bianchi, *Electrical Machine Analysis Using Finite Elements*, 1 ed. Boca Raton: CRC Press (in English), 2005, p. 304.

[69] T. V. Frandsen and P. O. Rasmussen, "Practical investigation of end effect losses in a Motor Integrated Permanent Magnet Gear," *2015 IEEE Energy Conversion Congress and Exposition (ECCE)*, Montreal, QC, 2015, pp. 4425-4432.

[70] A. Kenny, A. Palazzolo, G. T. Montague, and A. F. Kascak, "Theory and Test Correlation for Laminate Stacking Factor Effect on Homopolar Bearing Stiffness," *Transactions of the ASME,* vol. 126, p. 4, 2004.

[71] M. L. Barton, "Loss Calculation in Laminated Steel Utilizing Antisotropic Magnetic Permeability," *IEEE Transactions on Power Apparatus and Systems,* vol. PAS-99, pp. 1280-1287, 1980.

[72] M. Popescu and D. G. Dorrell, "Skin effect and proximity losses in high speed brushless permanent magnet motors," *2013 IEEE Energy Conversion Congress and Exposition*, Denver, CO, 2013, pp. 3520-3527.

[73] G. Volpe, M. Popescu, F. Marignetti and J. Goss, "Modelling AC Winding Losses in a PMSM with High Frequency and Torque Density," *2018 IEEE Energy Conversion Congress and Exposition (ECCE)*, Portland, OR, 2018, pp. 2300-2305.

[74] M. Popescu, T. J. E. Miller, M. McGilp, D. M. Ionel, S. J. Dellinger, and R. J. Heidemann, "On the Physical Basis of Power Losses in Laminated Steel and Minimum-Effort Modeling in an Industrial Design Environment," presented at the *2007 IEEE Industry Applications Annual Meeting*, New Orleans, LA, 2007.

[75] D. Kowal, P. Sergeant, L. Dupré, and H. Karmaker, "Comparison of Frequency and Time-Domain Iron and Magnet Loss Modeling Including PWM Harmonics in a PMSG for a Wind Energy Application," *IEEE Transactions on Energy Conversion,* vol. 30, pp. 476-486, 2015.

[76] Y. F. a. M. S. K. Yamazaki, "Loss Analysis of Permanent-Magnet Motors With Concentrated Windings—Variation of Magnet Eddy-Current Loss Due to Stator and Rotor Shapes," *IEEE Transactions on Industry Applications,* vol. 45, pp. 1334-1342, July-Aug. 2009.

[77] M. Paradkar and J. Bocker, "2D analytical model for estimation of eddy current loss in the magnets of IPM machines considering the reaction field of the induced eddy currents," *2015 IEEE International Electric Machines & Drives Conference (IEMDC)*, Coeur d'Alene, ID, 2015, pp. 1096-1102.

[78] N. Boubaker, D. Matt, P. Enrici, F. Nierlich and G. Durand, "Measurements of Iron Loss in PMSM Stator Cores Based on CoFe and SiFe Lamination Sheets and Stemmed From Different Manufacturing Processes," in *IEEE Transactions on Magnetics*, vol. 55, no. 1, pp. 1-9, Jan. 2019.

Appendix A: Derivation of modulated air gap flux density function

Considering air gap flux density distribution expressed by the equation (2-1) and modulating function representing the array of pole pieces in the equation (2-2), the resultant modulated function is a product of the two aforementioned functions:

$$B_{r\_mod}(\vartheta) = \delta_{ppr}(\vartheta) \cdot B_{r\_pm}(\vartheta) \tag{A-1}$$

Considering only the fundamental harmonic of both functions, i.e. coefficients m and n in equations (2-1) and (2-2) are equal to 1, the equation (A-1) can be rewritten as follows:

$$\begin{aligned} B_{r\_mod}(\vartheta) = \frac{4 \cdot B_r}{\pi} \cdot sin\big(p_{in}(\vartheta + \omega_{in} \cdot t)\big) \\ \cdot \left(\frac{1}{2} + \frac{2}{\pi} sin\left(p_{ppr}\big(\vartheta + \omega_{ppr} \cdot t\big)\right)\right) \end{aligned} \tag{A-2}$$

After multiplication, the equation (A-2) takes the following form:

$$\begin{aligned} B_{r\_mod}(\vartheta) = \frac{2 \cdot B_r}{\pi} \\ \cdot \sin\big(p_{in}(\vartheta + \omega_{in} \cdot t)\big) + \frac{8 \cdot B_r}{\pi^2} \cdot \sin\big(p_{in}(\vartheta + \omega_{in} \cdot t)\big) \\ \cdot \sin\left(p_{ppr}\big(\vartheta + \omega_{ppr} \cdot t\big)\right) \end{aligned} \tag{A-3}$$

The equation (A-3) can be further rearranged using trigonometric product identity so that amplitudes and velocities of all individual space harmonics become apparent:

$$B_{r\_mod}(\vartheta) = \frac{2 \cdot B_r}{\pi} \cdot \sin\left(p_{in}(\vartheta + \omega_{in} \cdot t)\right)$$
$$+ \frac{4 \cdot B_r}{\pi^2} cos\left[\left(p_{ppr} - p_{in}\right)\left(\vartheta + t\frac{\left(p_{ppr}\omega_{ppr} - p_{in}\omega_{in}\right)}{\left(p_{ppr} - p_{in}\right)}\right)\right] \quad \text{(A-4)}$$
$$- \frac{4 \cdot B_r}{\pi^2} cos\left[\left(p_{ppr} + p_{in}\right)\left(\vartheta + t\frac{\left(p_{ppr}\omega_{ppr} + p_{in}\omega_{in}\right)}{\left(p_{ppr} + p_{in}\right)}\right)\right]$$